SCUOLA NORMALE SUPERIORE

PH.D. THESIS

Quantum Information Processing and Quantum Spin Systems

Davide Rossini

SUPERVISOR

Prof. Rosario Fazio

Pisa, 2007

Contents

Introduction

Since the second half of the past century, the application of quantum mechanical principles to large scale technology has caused an enormous social impact. It is sufficient to consider the use of laser and transistor in our everyday's life: for instance, the latter represents the cornerstone which made possible the enormous growing of computer potentialities. More recently, the synergy between quantum physics and computer science is developing at a more fundamental level: quantum mechanical principles can be used to process and transmit information [1, 2, 3, 4]. The ultimate aim is to build a "quantum machine" based on a completely different logic, namely a "quantum logic", so that it processes information and performs logical operations by exploiting the laws of quantum mechanics. The power of quantum computers essentially consists on the possibility of superposing quantum states and having entanglement (i.e., non-local quantum correlations between well separated systems [14]), so that a large number of classical inputs can be processed in a single run. Quantum algorithms exploit this inherent parallelism, in order to efficiently highlight the desired output.

Technological efforts needed to build such a computer are very demanding [10]; the key point resides in the ability to control the evolution of a large number of *qubits* (the quantum counterparts of classical bits, i.e., two-level quantum systems) for the time necessary to perform many *quantum gates*. One of the main obstacles is *decoherence*: the decay of quantum information stored on a quantum computer, due to unavoidable interaction with the environment [13]. Decoherence obviously introduces errors in the computation, thus affecting its performance. Another source of errors that must be considered is the presence of *imperfections* in the quantum computer hardware. Even though further technological breakthroughs are probably required, the first demonstrative experiments in this direction are remarkable [11], since at least they allow to test the theoretical principles of quantum mechanics and to control individual quanta [12].

The idea of building quantum computers can be traced back to the early Eighties: namely, Feynman was the first who speculated on the possibility of using a quantum computer in order to simulate quantum-mechanical systems [17]; this spawned an active area of research in physics. The simulation of quantum systems is indeed an extremely hard task for classical computers, as the size of the Hilbert space increases exponentially with the number of constituents of the system. The growth in memory requirement would be only linear in quantum computers, since they are themselves quantum many-body systems. Therefore a quantum computer operating with only a few tens of qubits could outperform a classical computer [9]; finding efficient quantum algorithms, as well as extracting useful information from the output are a crucial issue.

At present, together with quantum cryptography, the simulation of quantum dynamics of complex systems promises to become the first application in quantum data processing: on one hand, quantum algorithms for simulating the quantum evolution of classically chaotic dynamical systems, like the baker's map [18], the kicked rotator [19], and the sawtooth map [20], have been found. On the other hand, the baker's map [23] and sawtooth map [24] have been already implemented on a three-qubit NMR-based quantum computer. These systems are highly non trivial and are paradigmatic for the study of quantum chaos; moreover important physical quantities could be extracted already with less than 10 qubits [3, 21, 22]. For these reasons, we believe that understanding effects of decoherence and quantum noise onto these types of algorithms will be of crucial importance in the near-future experimental realizations of quantum computers. In chapter 2 we give a detailed analysis on effects of quantum imperfections in the simulation of the sawtooth map. In particular we show that the stability of quantum computation is essentially independent of the chaotic or integrable behavior of the simulated dynamics [74].

Despite the first experimental advances in building quantum information processors, the realization of quantum computers outperforming present classical supercomputers is still far from being accessible. For this reason, numerical study of quantum mechanical systems still relies on few exceptional cases of quantum dynamics that can be efficiently simulated on classical computers. Efficient classical simulations are generally possible only for slightly entangled systems [126], nonetheless they embrace several interesting quantum many-body systems. Amongst them, we mention strongly correlated one-dimensional quantum lattice models at zero temperature [114], whose static,

as well as dynamic evolution can be simulated by means of the *Density Matrix Renormalization Group* (DMRG) algorithm [141, 110] [1]. The dynamic version of DMRG is used in chapter 5, in order to simulate the time evolution of a qubit coupled to a anisotropic Heisenberg spin chain, for which an analytic solution is not available. In chapter 7 we exploit the static DMRG algorithm in the study of the phase diagram and magnetic properties of the spinorial *Bose-Hubbard model* [127]. This system plays a crucial role in condensed matter, as it is the benchmark lattice model in order to study Josephson-junction arrays [133] and superconducting films [134]. More recently, emphasis has been put on its importance in the study of strongly correlated systems that can be realized with cold atomic gases in optical lattices [129]: the dynamics of such systems can indeed be mapped into Hubbard-type models [132]. Atomic physics on optical lattices provides a whole toolbox to engineer various types of interacting Bose and Fermi systems, that may also have direct application in quantum computation, since interatomic controlled interactions can be tuned with great accuracy, and therefore used to create and manipulate entanglement with high fidelity [130, 131].

Quantum mechanics allows not only to perform faster operations, but also operations intrinsically inaccessible to classical means. In particular, it provides a unique contribution to *cryptography* [5], enabling two communicating parties to detect whether the transmitted message has been intercepted by an eavesdropper. This is not the case in the realm of classical physics, as it would always be possible, in principle, to copy classical information without affecting the original message. In con

even for quantum computation: it is necessary, for example, to link several small quantum processors for large-scale quantum computing. Thus it is of fundamental importance to have physical systems which can serve as data bus for quantum communication. The ideal channel for long distance quantum communication is an optical fiber; in this case the carriers of information are photons, which can be addressed and transmitted with high control and with a low level of decoherence [6]. A major problem with this type of channel would be the interfacing of a quantum computer, such as solid-state quantum devices like arrays of spins or Josephson junctions, to optical systems [27]. For this reason, for short distance communication, alternatives to interfacing different kinds of physical systems are preferred. A possibility consists in realizing quantum channels by using condensed-matter systems, like *spin chains*: even without modulating the couplings between the spins, it is possible to transfer a generic quantum state from one end to the opposite end of the chain with reliable fidelity for up to a few tens of spins [29]. Moreover, the efficiency of the state transfer can be greatly improved either by tailoring the system Hamiltonian, or by performing complex local encoding and decoding operations on the spins at the ends of the chain: a proper choice of the modulation of the coupling strengths, for example, is sufficient to admit perfect state transfer at some given times [30, 31]. These protocols are especially appealing for experimentalists, as they require no dynamical control on the physical system during the state transfer, therefore they are believed to be less vulnerable to decoherence. It thus remains to be seen their robustness against unavoidable static imperfections. Particularly remarkable is the case when, in the ideal situation, perfect state transfer is obtained: this problem is analyzed in chapter 3, where we show that it is possible, at least in principle, to tolerate or correct errors induced by static noise [94].

Apart from experimental inaccuracies, the intrinsic dispersive nature of the information propagation along a spin chain inevitably reduces the fidelity of the state transfer [29, 34]. Without using Hamiltonians engineered "ad hoc", or complex encoding and decoding operations, perfect transfer is generally not possible: feedback and memory effects naturally arise in the quantum communication, thus preventing a sharp definition of transmission times. Nonetheless, efficient mechanisms of information transfer can be devised by carefully exploiting the dispersive dynamics of the chain, as it is discussed in chapter 4, where we analyze the asymptotic number of qubits that can be transmitted per second along unmodulated spin chains [101].

Spin chains can also serve as realistic models in order to describe the surrounding environment: typically the dynamics of mesoscopic or macroscopic systems is complicated by their coupling with environmental modes; at low temperatures, these environmental effects are dominated by localized modes, such as nuclear and paramagnetic spins, that are well described by *spin bath* models [52]. Of course, understanding decoherence induced by this class of baths is a crucial issue for every successful implementation of quantum information processing: in the near future, research on quantum computation will have to focus both on practical implementations, paying attention to the decoherence characteristics of the relevant materials, and on general studies of decoherence for systems of qubits coupled to spin baths [1]. The study developed in chapter 5 can be brought back to this framework: we consider a pure dephasing model for a qubit system coupled to an interacting spin bath, providing results that go beyond the case of a central spin uniformly coupled to all the spins of the bath. We also show how this bath can be experimentally engineered, by using atoms in optical lattices [67].

A fairly different approach in studying decoherence is adopted in chapter 6: instead of modelling the environment as a many-body object, we have considered a single-particle deterministic system in the chaotic regime; despite its apparent simplicity, it is able to mimic the effects of a pure dephasing many-body bath, with infinitely many degrees of freedom [73]. This demonstrates that the dynamical complexity, rather than the number of degrees of freedom, seems to be the crucial required property for decoherence.

This thesis is organized as follows. In the first chapter we introduce the basic concepts of quantum information and computation processing, that may serve as a background for the subsequent chapters. Chapter 2 is focused on the stability of quantum computation of complex chaotic dynamics, anticipated by a brief introduction to classical and quantum chaos. In the next two chapters we deal with the transmission of quantum information both along modulated chains (Chap. 3) and unmodulated chains (Chap. 4). Then we focus on the problem of decoherence in quantum information, by considering two rather different types of environment, namely a many-body spin bath (Chap. 5) and a one-degree-of-freedom chaotic bath (Chap. 6). Finally, in chapter 7 we concentrate ourselves on the classical simulation of a quantum mechanical system: we use the numerical DMRG algorithm in order to simulate the spinorial Bose-Hubbard model. In appendix C we include a rather detailed description of this numerical technique.

Chapter 1

Quantum Computation and Quantum Communication

The recent application of quantum mechanical principles to the theory of information and computation has opened new and fascinating perspectives in both fundamental science and technological applications [1, 2, 3, 4]. Perhaps one of the earliest discoveries in quantum information processing is that quantum mechanics can be used to perform key distribution between two distant parties in a completely secure way. This procedure, also known as *quantum key distribution*, relies on the principle that observation in general disturbs the system being observed [5]. Experimental advances in the field of quantum cryptography are impressive, and quantum-cryptographic protocols have been demonstrated, using optical fibers, over distances of a few tens of kilometers at rates of the order of a thousand bits per second [6].

Another very remarkable theoretical issue is the discovery of fast computation algorithms, that are based on quantum logic. The most famous one, that was developed by Shor in 1994, admits the factorization of a large integer number with time and memory requirements that are polynomial in the problem size, thus exponentially smaller as compared to any known classical algorithm [7]. Further evidence for the power of quantum computers comes from Grover's algorithm, that accomplishes the task of conducting a search through an unstructured database quadratically faster [8]; despite the less pronounced speedup, the widespread applicability of this problem has excited considerable interest. The simulation of quantum physical systems is known to be another generally hard task for classical computers; quantum computers would considerably speed-up the simulation, making this problem

tractable [9]. Actually, the technological challenge needed to build quantum computers is very demanding [10], even if some quantum algorithms have been already put on working prototypes (see, e.g, Refs. [11]); as an example, we quote the implementation of the Shor's algorithm on a seven-qubit NMR-based quantum computer.

The experimental realization of reliable quantum information processing devices is strongly hindered by internal quantum hardware imperfections and unwanted coupling with the external environment. Entangling interactions with the environment are thought to be the ultimate obstacle in engineering of nanodevices for reliable quantum information processing and computing. Indeed, every quantum superposition typically rapidly evolves into a complex entangled state involving the environment, which appears, to the system alone, as a statistical mixture. This process is known as *decoherence* [13]. The study of the effects induced by internal imperfections, as well as the decoherence, is crucial for the development of control and error-correction strategies in every quantum information processing.

In this chapter we briefly introduce the basics of quantum computation and quantum communication theory, focusing on the simulation of quantum physical systems (Sec. 1.2), the transmission of quantum information in spin chains (Sec. 1.3), and the problem of decoherence (Sec. 1.4). These notions will be subsequently used in the remaining chapters of this Thesis.

1.1 Quantum computation

Quantum computation refers to information processing by means of a quantum system [1, 2, 3, 4]. In the theory of classical data processing, the fundamental unit of information is called *bit*. A classical bit is generally a macroscopic system, described by one or more continuous parameters, such as voltages. Within this parameter space two well separated regions are chosen in order to represent the two possible states 0 and 1. An n-bit memory can exist in any of 2^n logical states, labelled from $000\ldots0$ to $111\ldots1$. Besides storing binary data, classical computers manipulate it; the most general operation they can do on n bits of input is to evaluate a function f that produces m bits of output which are uniquely determined by the input:

$$\{0,1\}^n \xrightarrow{f} \{0,1\}^m \,. \tag{1.1}$$

It can be shown that a sequence of boolean operations acting on the bits one or two at a time (like, for example, NOT and AND) plus a COPY operation, that takes one bit to two bits, are sufficient to realize any deterministic transformation of the type in Eq. (1.1).

On the other hand, the fundamental unit of quantum information is a two-level quantum system, which is commonly called *qubit*. Contrary to a classical bit, a qubit is typically codified by a microscopic system, such as an atom, a nuclear spin, or a photon. The analog of the boolean states 0 and 1 are now two orthogonal states of the qubit, like horizontal and vertical photon polarizations: $|0\rangle \equiv |\leftrightarrow\rangle$, $|1\rangle \equiv |\updownarrow\rangle$. A qubit can also exist in a continuum of intermediate states or superpositions, mathematically represented as complex linear combinations of the basis states $|0\rangle$ and $|1\rangle$. These intermediate states cannot be reliably distinguished, even in principle, from the basis states: with regard to any measurement, the superposition $\alpha\,|0\rangle + \beta\,|1\rangle$ behaves like $|0\rangle$ with probability $|\alpha|^2$ and like $|1\rangle$ with probability $|\beta|^2$.

1.1.1 Quantum parallelism and entanglement

In general, while a string of n classical bits can be in any of 2^n boolean configurations ($x = 000\ldots0$ through $x = 111\ldots1$), a string of n qubits can exist in any state of the form:

$$|\Psi\rangle = \sum_{x=00\ldots0}^{11\ldots1} c_x\,|x\rangle\ , \tag{1.2}$$

where the c_x are complex numbers such that $\sum_x |c_x|^2 = 1$. The *quantum superposition principle* clearly emerges from Eq. (1.2): while n classical bits can store only a single integer x, a n-qubit state can be prepared in any superposition of the 2^n quantum states $|x\rangle$. The superposition principle opens up new possibilities for computation: when performing a classical computation, different inputs require separate runs. In contrast, exploiting this huge parallelism, a quantum computer can perform a computation for exponentially many inputs on a single run.

The other quantum feature at the basis of the quantum computational speedup is *entanglement* [14]. Entanglement is the most spectacular and counterintuitive manifestation of quantum mechanics, that is observed in composite quantum systems: it signifies the existence of non-local correlations between measurements performed on well-separated particles. After

two classical systems have interacted, they are in well-defined individual states; in contrast, after two quantum particles have interacted, they can no longer be described independently of each other. The prototypes of two-qubit entangled states are the so called "Bell states":

$$\begin{cases} |\phi^{\pm}\rangle = \frac{1}{\sqrt{2}} \left(|00\rangle \pm |11\rangle \right), \\ |\psi^{\pm}\rangle = \frac{1}{\sqrt{2}} \left(|01\rangle \pm |10\rangle \right) . \end{cases} \tag{1.3}$$

They are characterized by the fact that the reduced density matrix of each of the two particles is a multiple of the identity: $\rho_A = \rho_B = \frac{1}{2}\hat{\mathbb{1}}_2$. This means that any local measurement performed by Alice or Bob cannot give any information on the global state of the system: it completely resides in non-local correlations between the two parties.

The key role of entanglement in quantum computation can be understood by the following heuristic argument. There is no entanglement in classical physics, therefore, in order to represent the superposition of 2^n levels by means of classical waves, these levels must belong to the same system (classical states of separate systems can never be superposed). Thus, in order to classically describe the generic n-qubit state (1.2), we need a single 2^n-level system. Hence, the amount of physical resources needed for the computation grows exponentially with n. In contrast, due to entanglement, in quantum physics a generic superposition of 2^n levels may be represented by means of n qubits. Thus, the amount of physical resources grows only linearly with n. The ability to preserve and manipulate entangled states is eventually responsible both for their power and for the difficulty of building them.

1.1.2 Quantum gates

Any classical computation can be expressed as a sequence of one- and two-bit operations; similarly any quantum computation can be expressed as a sequence of one- and two-qubit quantum gates, that is unitary operations acting on one or two qubits [15]. The most general one-qubit gate is described by the following 2×2 unitary matrix, written in the standard computational basis $\{|0\rangle, |1\rangle\}$:

$$\hat{U}_1 = \begin{pmatrix} \alpha & \beta \\ \gamma & \delta \end{pmatrix} . \tag{1.4}$$

The parameters $\alpha, \beta, \gamma, \delta$ are complex numbers such that $\hat{U}\hat{U}^{\dagger} = \hat{U}^{\dagger}\hat{U} = \hat{\mathbb{1}}$. Important examples are the Hadamard gate, in which $\alpha = \beta = \gamma = -\delta = \frac{1}{\sqrt{2}}$,

and the phase shift gate, where $\alpha = 1$, $\beta = \gamma = 0$, $\delta = e^{i\phi}$. One qubit gates can be easily implemented, for example by quarter- and half-wave plates acting on polarized photons, or by radio frequency tipping pulses acting on nuclear spins in a magnetic field.

An example of a two-qubit quantum gate is the controlled-NOT (or XOR) gate, which flips its second input (called "target") if its first input (called "control") is $|1\rangle$ and does nothing if it is $|0\rangle$:

$$\begin{array}{ll} |0\rangle \otimes |0\rangle \rightarrow |0\rangle \otimes |0\rangle & |1\rangle \otimes |0\rangle \rightarrow |1\rangle \otimes |1\rangle \\ |0\rangle \otimes |1\rangle \rightarrow |0\rangle \otimes |1\rangle & |1\rangle \otimes |1\rangle \rightarrow |1\rangle \otimes |0\rangle \end{array} . \tag{1.5}$$

This gate is of primary importance in quantum computation, since, together with one-qubit quantum gates, form a universal set of quantum operations: any unitary operator acting on n qubits can be implemented with a quantum circuit involving only these gates [15]. Unlike one-qubit gates, two-qubit gates are typically difficult to realize experimentally, because they require two separated quantum information carriers to be brought into strong and controlled interactions.

The XOR gate is particularly useful to illustrate the impossibility of cloning an unknown quantum state. Indeed if XOR is applied to boolean data in which the second qubit is $|0\rangle$, the effect is to copy the first qubit into the second: $|x, 0\rangle \rightarrow |x, x\rangle$ for $x = 0, 1$. One might suppose that XOR does the same for superpositions, such as $|\psi\rangle = \alpha |0\rangle + \beta |1\rangle$, so that $|\psi, 0\rangle \rightarrow |\psi, \psi\rangle$, but this is not the case: the result of applying XOR to $|\psi, 0\rangle$ is the entangled state $\alpha |00\rangle + \beta |11\rangle$ in which neither output qubit alone has a definite state. This behavior is characteristic not only of this gate, but of any unitary interaction (thus leading to the famous "quantum no-cloning theorem" [16]): its typical effect is to map most unentangled initial states of interacting systems into entangled final states, which, from the viewpoint of either system alone, causes an unpredictable disturbance.

1.2 Quantum simulation of physical systems

Apart from solving certain problems faster, quantum computers working with quantum gates and wires, seem to provide exponential speedup in the simulation of quantum physical systems [17, 9]. This is believed to be of primary importance in first-future realizations of quantum computer hardware. Indeed, while thousands of qubits and billions of quantum logic operations

are needed to solve classically difficult factoring problems, or to appreciably speed up the searching from unstructured databases, it would be possible to use a quantum computer with only a few tens of qubits and a few thousand operations to perform simulations that would be classically intractable.

The first hypothetical quantum computer devised by Feynman in 1982 is simply a quantum system which evolves exactly as the physical system to be simulated, thus following its dynamics [17]. In this way, at the end of the "calculation" one would find the quantum computer in a state $|\psi_t\rangle$ from which it would be possible, at least in principle, to recover all the relevant information of the simulated system. In fact, the quantum measurement is intrinsically a statistical process which inevitably modifies the state $|\psi_t\rangle$, therefore many runs of the same simulation are typically needed in order to extract the required information. Feynman conjectured that this quantum computer was an universal one, in the sense that it could simulate any quantum system which evolves under local interactions. This conjecture has been proved years later by Lloyd in Ref. [9], where he showed that it is possible to simulate any local quantum evolution by a quantum computer in a time proportional to the simulation time t, and memory size proportional to the number of system's variables. On the other hand, it is clear that the simulation of quantum mechanical systems on classical computers requires time and memory resources which typically grow exponentially with the number of constituents of the system. For instance, if we wish to simulate a chain of n spin-$\frac{1}{2}$ particles, the size of the Hilbert space is 2^n. Namely, the state of this system is determined by 2^n complex numbers. Nonetheless, a n-qubit quantum computer hardware would be sufficient to run such a simulation.

Present-day quantum computers sufficiently powerful to perform complex simulations of generic quantum systems are far from being experimentally built up; nonetheless, an important class of algorithms for the simulation of some highly non trivial quantum kicked systems [18, 19, 20] would only require a few-tens-qubits quantum computer in order to extract information otherwise inaccessible to classical supercomputers [21, 22, 3]. For this reason, these quantum algorithms are believed to constitute the ideal software for short- and medium-term quantum computers operating with a small number of qubits, and the most suitable testing ground for investigating the limits of quantum computation due to imperfections and decoherence effects. Experimental implementations of some small-size chaotic models have been already performed, like the simulation on a three-qubit NMR-based quantum processor of the baker's map [23] and the sawtooth map [24].

1.3 Quantum transmission

Quantum communication protocols generally require the ability to reliably transfer a quantum state between distant parties. For example, *quantum teleportation* [25] and *quantum dense coding* [26] require a pair of particles in a maximally entangled state, such as one of the four Bell states (1.3), to be shared between the two communicating parties A and B, which will be hereafter referenced to as Alice and Bob. In a second stage, this shared entanglement is used to achieve, respectively, transmission of a qubit with two classical bits or transmission of two classical bits with a qubit. Transferring a quantum state from one qubit to another is also required in scalable quantum computing based on the quantum network, in order to link several small quantum processors for large-scale computation.

In view of the great potentialities of solid-state quantum computing, attention is recently focusing on the possibility to realize quantum channels by using condensed-matter systems. In particular, *spin chains* are being considered as coherent data buses: the quantum transmission of state is achieved between two spins at the two ends of the chain [29]. The crucial problem is the dependence of transferring efficiency on communication distance. Usually, in plain transmission schemes, the efficiency is inversely proportional to the distance of the two spins, therefore such quantum state transmission can only work efficiently over short distances. In order to improve the efficiency of the state transfer, two different strategies are usually adopted: a certain class of schemes achieves efficient communication by tailoring the system Hamiltonian [30, 31, 32, 33], with a corresponding minimal (if not null) cost in terms of encoding and decoding operations. In the second approach, communication efficiency is obtained through complex encoding and decoding operations, but with minimal requirements on the Hamiltonian of the chain [34, 35, 36, 37, 38, 39, 40]. As in all situations in quantum information, the reliability of such spin-chain protocols relies on the capability of isolating the experimental setup from the external world, and on the possibility to reduce all static imperfections. Since they typically require no dynamical control on the physical system during the state transfer, the coupling to the environment is supposed to be weak, therefore they are believed to be less vulnerable to decoherence.

In the following subsections we will briefly discuss two paradigmatic cases of quantum state transmission: the first along a Heisenberg spin-1/2 unmodulated chain (that is the first example of a quantum spin-chain communication

protocol, proposed by Bose in Ref. [29]), the second through a XY modulated chain (with a protocol admitting a perfect state transfer along arbitrary distances [30]).

1.3.1 Communication in unmodulated spin chains

In Ref. [29] Bose showed that an unmodulated Heisenberg one-dimensional spin chain is able to act as a quantum data bus over reasonable distances ($\sim 10^2$ lattice sites). The communication is achieved by placing a spin encoding the state to be transferred at one end of the chain, and waiting for a specific amount of time to let this state propagate to the other end. This scheme helps to avoid interfacing, since both quantum computers and quantum channels can then be made by the same physical systems. Moreover a great advantage of this approach is that state transfer occurs due to the interaction between the spins of the chain, and *no dynamical control* is required (except for the preparation and the detection of the state). Proposals to implement this scheme with superconducting nanocircuits have been already put forward [32, 41, 42] and very likely these implementations can also be extended to other solid-state systems [43, 44, 45].

Consider a ferromagnetic isotropic Heisenberg chain composed of N spins 1/2 in a transverse magnetic field, described by the Hamiltonian:

$$\hat{H}_{XYZ} = -J \sum_{i=1}^{N-1} \hat{\vec{\sigma}}_i \cdot \hat{\vec{\sigma}}_{i+1} - B \sum_{i=1}^{N} \hat{\sigma}_i^z \tag{1.6}$$

where $\hat{\vec{\sigma}}_i = (\hat{\sigma}_i^x, \hat{\sigma}_i^y, \hat{\sigma}_i^z)$ are the Pauli matrices of the i-th spin. Assume that the sender Alice is close to the first spin (the "sender spin", $i = 1$) at one end of the chain, while the receiver Bob is located close to the last spin (the "receiver spin", $i = N$) at the opposite end of the chain; all the other spins in between act as channel spins. In order to transfer an unknown state to Bob, Alice replaces the existing sender spin with a spin encoding the state to be transferred. After waiting for a specific amount of time, the unknown state placed by Alice travels to the receiver spin with some "fidelity"; then Bob picks up the receiver spin to obtain a state close to the one Alice wanted to send.

Suppose that the system is initially frozen in its ground state $|\mathbf{0}\rangle \equiv |00\ldots0\rangle$, where $|0\rangle$ ($|1\rangle$) denotes the spin down (respectively up) state of a spin. To start the protocol, Alice places a spin in the unknown state

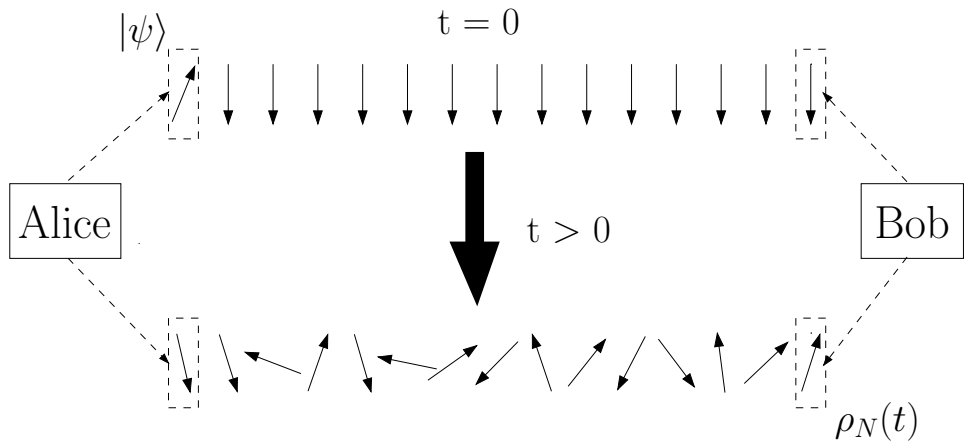

Figure 1.1: Quantum communication through a one-dimensional spin chain: Alice and Bob are at the two opposite ends. The spin chain is initially set in the ferromagnetic ground state. Alice places her quantum state she wants to communicate on the leftmost spin; then, after time t, Bob receives this state with some fidelity $f = \langle\psi|\,\rho_N(t)\,|\psi\rangle$ on the rightmost spin.

$|\psi\rangle = \cos(\theta/2)\,|0\rangle + e^{i\varphi}\sin(\theta/2)\,|1\rangle$ at the first site of the chain. The state of the whole chain at $t = 0$ is thus

$$\begin{aligned} |\Psi_0\rangle &= \big(\cos(\theta/2)\,|0\rangle + e^{i\varphi}\sin(\theta/2)\,|1\rangle\big) \otimes |0\rangle^{\otimes(N-1)} \\ &\equiv \cos(\theta/2)\,|\mathbf{0}\rangle + e^{i\varphi}\sin(\theta/2)\,|\mathbf{1}\rangle \end{aligned} \tag{1.7}$$

where $|\mathbf{j}\rangle \equiv |00\ldots010\ldots0\rangle$ denotes the chain state in which the spin at site j has been flipped to $|1\rangle$. Bob then lets the system evolve until the initial state $|\Psi_0\rangle$ is mapped to a final state which is as close as possible to $\cos(\theta/2)\,|\mathbf{0}\rangle + e^{i\varphi}\sin(\theta/2)\,|\mathbf{N}\rangle$, and finally reads out the N-th spin. Since the system Hamiltonian of Eq. (1.6) commutes with the total spin component along the z direction, i.e.

$$\left[\,\hat{H}_{XYZ}\,,\,\sum_{i=1}^{N}\hat{\sigma}_i^z\,\right] = 0\,, \tag{1.8}$$

the state transfer is completely determined by the evolution in the N-dimensional Hilbert subspace $\mathcal{H}_1$ spanned by the basis vectors $\{|\mathbf{j}\rangle\}_{j=1\ldots N}$, corresponding to spin configurations in which all spins are down apart from one

spin up at site j. Thus the initial state of the network evolves in time as:

$$|\Psi_t\rangle = \cos\frac{\theta}{2}\,|\mathbf{0}\rangle \;+\; e^{i\varphi}\sin\frac{\theta}{2}\sum_{j=1}^{N} g_j(t)\,|\mathbf{j}\rangle \tag{1.9}$$

where we set $g_j(t) = \langle \mathbf{j}|\, e^{-i\hat{H}t}\,|\mathbf{1}\rangle$.

The accuracy of the state transfer can be determined through the analysis of the fidelity (see Sec. A for details):

$$f(t,\theta,\varphi) = \langle\psi|\,\rho_N(t)\,|\psi\rangle\ , \tag{1.10}$$

where $\rho_N(t)$ is the reduced density matrix of the N-th spin at time t. The fidelity in Eq. (1.10) expresses a generalized overlap between a pure state and a mixture. This quantity, like the overlap of two pure states, is a real number between zero and one; values close to one mean that the state transfer has been reliably transferred from one to the other end of the chain. The matrix $\rho_N(t)$ is obtained by tracing out all but the receiver spin from $|\Psi_t\rangle$:

$$\rho_N(t) = P(t)\,|\psi_N(t)\rangle\,\langle\psi_N(t)| + \big(1-P(t)\big)\,|0\rangle\,\langle 0| \tag{1.11}$$

with

$$|\psi_N(t)\rangle = \frac{1}{\sqrt{P(t)}}\left(\cos\frac{\theta}{2}\,|0\rangle + e^{i\phi}\sin\frac{\theta}{2}\,g_N(t)\,|1\rangle\right), \tag{1.12}$$

where $P(t) = \cos^2(\theta/2) + \sin^2(\theta/2)\,|g_N(t)|^2$, and $g_N(t) = \langle \mathbf{N}|\, e^{-i\hat{H}t}\,|\mathbf{1}\rangle$ is the transition amplitude of an excitation from the first to the last site. The fidelity averaged over all pure input states $|\psi\rangle$ in the Bloch sphere is then given by

$$f(t) \equiv \langle f(t,\vartheta,\varphi)\rangle_{\vartheta,\varphi} = \frac{|g_N(t)|\cos\gamma}{3} + \frac{|g_N(t)|^2}{6} + \frac{1}{2}\,, \tag{1.13}$$

where $\gamma = \arg\{g_N(t)\}$. The magnetic fields B_i can be chosen such that $\gamma = 2\pi k$, thus maximizing $f(t)$ with respect to the phase of $g_N(t)$.

In Ref. [29] some outputs of numerical simulations are presented. It is shown that for $N = 2$ and $N = 4$ the Heisenberg chain gives perfect quantum state transfer (up to three decimal places), while for $N = 8$ nearly perfect transfer is achieved ($f \sim 0.994$). The fidelity also exceeds 0.9 for many chain lengths smaller than 20. It is also shown that a chain of $N \leq 80$ exceeds the highest fidelity for classical transmission of the state, i.e. 2/3 (see Fig. 1.2).

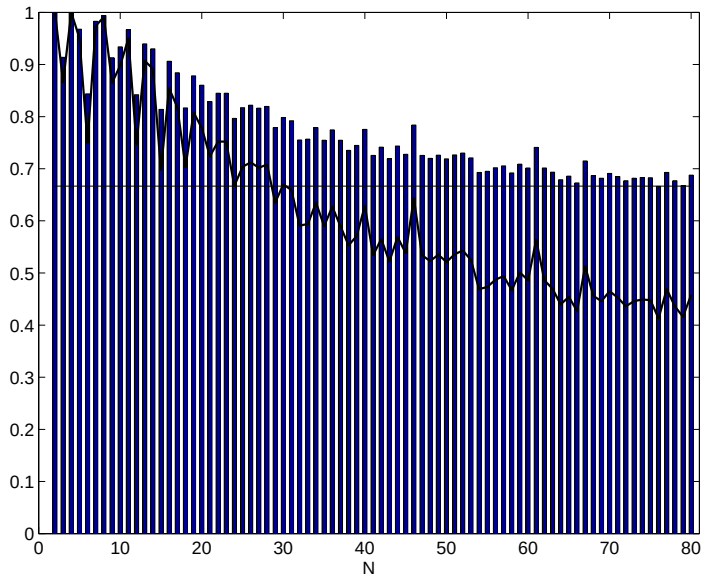

Figure 1.2: Maximum fidelity of quantum communication through a Heisenberg chain achieved in a fixed time interval $[0, 4000/J]$ as a function of the chain length N. The time t_0 at which these maxima are achieved varies with N. The straight line shows the highest fidelity for classical transmission of a quantum state. (figure quoted from Ref. [29]).

1.3.2 Perfect communication in modulated spin chains

The fidelity of quantum communication can be significantly incresed by admitting the possibility of modulating the coupling strenghts between the various spins of the chain. In Ref. [30] it has been shown that perfect state transfer can be achieved over arbitrary distances by means of the following modulated XY spin chain:

$$\hat{H}_{XY} = \sum_{n=1}^{N-1} J_n \left(\hat{\sigma}_n^x \hat{\sigma}_{n+1}^x + \hat{\sigma}_n^y \hat{\sigma}_{n+1}^y\right), \qquad \text{with} \quad J_n = J\sqrt{n(N-n)}\,. \tag{1.14}$$

As for the Heisenberg chain, the XY spin chain commutes with the total spin component along the z direction (see Eq. (1.8)). So, even in this case, the state transfer dynamics is completely determined by the evolution in the N-dimensional Hilbert subspace $\mathcal{H}_1$. For a dynamics governed by Eq. (1.14),

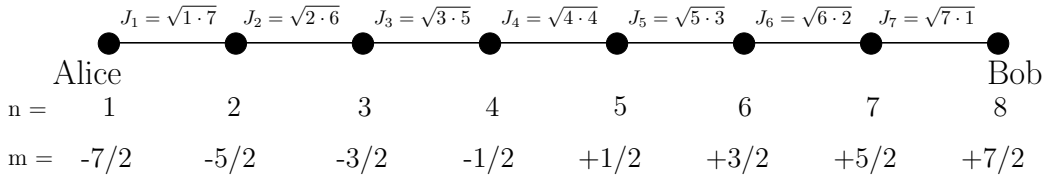

Figure 1.3: Couplings J_n in a $N = 8$ spin XY chain, which admits a perfect state transfer from Alice to Bob. Relabeling of the basis vectors $|\mathbf{j}\rangle$ in terms of the eigenvalues $|m\rangle$ of a fictitious spin-$\frac{7}{2}$ particle is also shown.

there exist many times t_n at which the matrix element $g_N = \langle \mathbf{N}| e^{-i\hat{H}t} |\mathbf{1}\rangle$ is equal to one, thus producing perfect state transfer.

In order to see this, we first relabel the spins of the chain. One can indeed associate a fictitious spin-$\frac{N-1}{2}$ particle with a N-spin chain and relabel the basis vectors as $|m\rangle$, where $m = -\frac{N-1}{2} + n - 1$. The sender qubit can thus be labeled both as $|n = 1\rangle$ and $\left|m = -\frac{N-1}{2}\right\rangle$, while the receiver qubit both as $|n = N\rangle$ and $\left|m = +\frac{N-1}{2}\right\rangle$. The Hamiltonian in Eq. (1.14), when restricted to the subspace $\mathcal{H}_1$, is of the form:

$$\hat{H}_{XY}|_{\mathcal{H}_1} = \begin{pmatrix} 0 & J_1 & 0 & 0 & \cdots & 0 \\ J_1 & 0 & J_2 & 0 & \cdots & 0 \\ 0 & J_2 & 0 & J_3 & \cdots & 0 \\ 0 & 0 & J_3 & 0 & \cdots & 0 \\ \vdots & \vdots & \vdots & \vdots & \ddots & J_{N-1} \\ 0 & 0 & 0 & 0 & J_{N-1} & 0 \end{pmatrix} \tag{1.15}$$

This matrix is the representation of the Hamiltonian $\hat{H} \equiv 4J\,\hat{S}^x$ of a fictitious spin $\vec{S} = (N-1)/2$ particle. The time evolution of the network: $\hat{U}(t) = \exp(-4iJ\hat{S}^x t)$ is then a rotation of this fictitious particle. The matrix elements $U_l^k(t) = \langle \mathbf{l}| e^{-i\hat{H}t} |\mathbf{k}\rangle$ are well known [46] and, in particular, the probability amplitude for the state transfer $|\mathbf{1}\rangle \to |\mathbf{N}\rangle$ is

$$\langle \mathbf{N}| \hat{U}(t) |\mathbf{1}\rangle \equiv U_N^1 = \big[-i \sin(2Jt) \big]^{N-1}. \tag{1.16}$$

Thus, since the state $|\mathbf{0}\rangle$ does not evolve in time, perfect transfer of a generic quantum bit $|\psi\rangle$ between the sender and the receiver is obtained at every time $t_n = (2n+1)\pi/4J$ (n integer).

This protocol has already been experimentally implemented in Ref. [47] using a three qubit nuclear magnetic-resonance quantum computer. We also underline that the crucial point for having perfect transfer is not the type of interaction, but the ability to modulate the couplings between spins. Indeed in [30] it is also shown that an Heisenberg chain like the one of Eq. (1.6) in a transverse magnetic field can admit perfect transfer, provided that:

$$J_n = J\sqrt{n(N-n)}\,; \qquad B_n = (J_n + J_{n-1}) - \frac{1}{N-2}\sum_{k=1}^{N-1} J_k\,. \tag{1.17}$$

Finally, we stress the fact that these protocols for quantum state transmission through spin chains are especially appealing, as they do not require the ability to switch on and off the interactions between spins during the state transfer (they however require limited switching of interactions of the sender spin and the receiver spin with the rest of the chain at the beginning and the end of the protocol, respectively). For this reason the coupling to the environment is generally supposed to be weak.

1.4 Decoherence

Real physical systems are never isolated, therefore each exhaustive model of a quantum system has also to include the unavoidable coupling with the surrounding environment. These typically unwanted interactions are the source of *decoherence*: quantum information initially present in the state of the system gets irreversibly lost into non-classical correlations between the system and the environment [13].

Though decoherence relies on fundamental principles of quantum mechanics, a comprehensive characterization of it is a relatively recent subject. In this direction, the first works are dated the 1980's, and concern the emergence of classicality in a world governed by the laws of quantum mechanics [48, 49]. Until that time, classical macroscopic world and microscopic quantum realm were considered as strictly distinct, therefore studied within separate fields. The boundary between classical and quantum was thought as a purely philosophical problem, intangible by physical analysis. This changed with the understanding that there is no need for denying quantum mechanics to hold even macroscopically, if one is able to understand, within the framework of quantum mechanics, why the macro-world appears to be classical.

The physics of decoherence became very popular in the last decade: due to advances in experimental engineering of quantum nanodevices, it has been possible to observe the gradual emergence of classical properties in microscopic quantum systems, in perfect agreement with the principles of quantum mechanics [50]. Moreover, a deeper understanding of the decoherence phenomenon seems to be essential to develop quantum computation technologies, since it is the main threat for the source of the potential power of any quantum algorithm: quantum superpositions [1, 3].

1.4.1 Dynamics of a system coupled to an environment

The dynamics of a *closed* quantum system is described by a unitary operator $\hat{U}(t) = e^{-\frac{i}{\hbar}\hat{H}t}$, where $\hat{H}$ is the Hamiltonian of the system (without losing in generality, we suppose here that $\hat{H}$ is time-independent). A natural way to describe the dynamics of an *open* system is to regard it as arising from the interaction between the system of interest S, and its surrounding environment E, which together form a closed quantum system. The dynamics of the composite system $S+E$ will then be described by the unitary time evolution operator $\hat{U}_{SE}$ corresponding to the global Hamiltonian $\hat{H}_{SE} = \hat{H}_S + \hat{H}_E + \hat{H}_{\rm int}$, where $\hat{H}_S$ and $\hat{H}_E$ are the Hamiltonians of S and E respectively, while $\hat{H}_{\rm int}$ is the interaction term between them.

Suppose now that the system is initially in state $\rho_S(0)$, disentangled from the environment input state $\rho_E(0)$. After the interaction, the final state of the system alone $\rho_S(t)$ may not be related by a unitary transformation to $\rho_S(0)$. Indeed, the composite system $S+E$ evolves under the unitary operator $\hat{U}_{SE}$; then we have to perform a partial trace over the environmental degrees of freedom, in order to find the final density matrix state of S:

$$\rho_S(t) = {\rm Tr}_E\left\{\hat{U}_{SE}(t)\left[\rho_S(0)\otimes\rho_E(0)\right]\hat{U}^\dagger_{SE}(t)\right\} \tag{1.18}$$

If we perform the trace in the eigenbasis of $\rho_E(0) = \sum_k p_k |\psi_k\rangle_E\langle\psi_k|$, we get:

$$\begin{aligned}\rho_S(t) &= \sum_{j,k} p_k \, {}_E\langle\psi_j|\hat{U}_{SE}(t)|\psi_k\rangle_E \; \rho_S(0) \; {}_E\langle\psi_k|\hat{U}^\dagger_{SE}(t)|\psi_j\rangle_E \\ &\equiv \sum_l \hat{M}_l \; \rho_S(0) \; \hat{M}_l^\dagger \,, \end{aligned} \tag{1.19}$$

where we have defined the so called *Kraus operators*

$$\hat{M}_l = \sqrt{p_{k_l}} \; {}_E\langle\psi_{j_l}|\hat{U}^\dagger_{SE}(t)|\psi_{k_l}\rangle_E \,. \tag{1.20}$$

From unitarity of $\hat{S}$ it follows that the Kraus operators satisfy $\sum_l \hat{M}_l^\dagger \hat{M}_l = \hat{\mathbb{1}}$. Eq. (1.19) defines the most general linear map $\$: \rho_S \to \rho'_S$ that takes density operators to density operators, which is usually called *superoperator*, or *quantum channel* [1, 2].

An example of decoherence process

We discuss here a particularly instructive case of quantum channel, that provides a typical example of decoherence in realistic situations. Suppose that it is possible to find a number of distinct orthogonal system states that are left unchanged by the environmental interaction (this happens, for example, if the system Hamiltonian $\hat{H}_S$ commutes with the interaction term $\hat{H}_{\rm int}$). Denoting this set of states as $\{|n\rangle_S\}$, then $\hat{U}_{SE}$ has the form:

$$\hat{U}_{SE}(t) = \sum_n |n\rangle_S\langle n| \otimes \hat{U}_n^{(E)}(t) \tag{1.21}$$

where $\hat{U}_n^{(E)}(t)$ are unitary operators acting on the environment. We also suppose for simplicity that the bath is initially in the pure state $|\psi_0\rangle_E$. Therefore, from Eq. (1.19) we get:

$$\rho_S(t) = \sum_{m,n} [\rho_S(0)]_{m,n} |m\rangle_S\langle n| \ \otimes \ {}_E\langle\psi_0|\hat{U}_n^{(E)\dagger}(t)\, \hat{U}_m^{(E)}(t)\, |\psi_0\rangle_E \,. \tag{1.22}$$

Since the $\hat{U}_n^{(E)}$ are unitary, the diagonal elements of $\rho_S(t)$ (also called "populations") are left unaffected, while the off-diagonal terms (or "coherences") are multiplied by the overlap $\langle\psi_n|\psi_m\rangle$, where $|\psi_n\rangle = \hat{U}_n^{(E)}\,|\psi_0\rangle_E$:

$$(\rho'_S)_{m,m} = (\rho_S)_{m,m} \qquad (\rho'_S)_{m,n} = (\rho_S)_{m,n}\,\langle\psi_n|\psi_m\rangle \,. \tag{1.23}$$

The modulus of this overlap is less than one, therefore the coherences, which characterize the ability of the system state to display quantum superpositions, get suppressed. Notice that, after the interaction, the joint quantum state $S + E$ is no longer separable; part of the coherence initially located in the system now resides in non-local correlations with the environment, and it is irremediably lost, once the environment is disregarded.

1.4.2 Models of environment

Although desirable, it is not always possible to fully characterize the environment, therefore it is necessary to resort to appropriate modelizations.

Paradigmatic models represent the bath as a many-body system, such as a set of bosonic harmonic oscillators [51] or of spin-1/2 particles [52]. Indeed, what typically happens is that the environmental effects are dominated either by delocalized modes such as electrons, photons, phonons, or by localized modes, such as nuclear spins and defects; in the first case the environment maps into an *oscillator bath* model, while in the second case a *spin bath* model is obtained.

The best known and studied oscillator bath model is due to Caldeira and Leggett [53]: the environment consists of infinitely many uncoupled harmonic oscillators at thermal equilibrium. This model is well suited for describing a central system weakly coupled to N environmental modes. Since the mapping to an oscillator bath can be made rigorous only if the coupling is weak, this model is best adapted to N *delocalized modes*, where the coupling is $\sim 1/\sqrt{N}$ and thus small for large N. An example of coupling with a Caldeira-Leggett bath is given by the Hamiltonian

$$\hat{H} = \frac{\hbar\omega_0}{2}\hat{\tau}^z + \hbar\hat{\tau}^z \sum_k (g_k\, \hat{b}_k^\dagger + g_k^*\, \hat{b}_k) + \sum_k \hbar\omega_k\, \hat{b}_k^\dagger \hat{b}_k \tag{1.24}$$

which represents a qubit, described by the Pauli matrices $\hat{\tau}^\alpha$, coupled to a collection of harmonic modes, described by the bosonic field modes $\{\hat{b}_k^\dagger, \hat{b}_k\}$, via coupling constants g_k. In this case the system Hamiltonian commutes with the interaction, therefore there is no energy exchange between the qubit and the bath, and a purely decohering mechanism happens, as in Eq. (1.22). The model of decoherence described by Eq. (1.24) is a particular case in which the dynamics of the system can be calculated analytically, nonetheless it has been widely used to model decoherence in quantum computers [54, 55].

The coupling to environmental modes cannot be always described by a bosonic bath: at low energies, the entropy and heat capacity of almost all real physical systems are dominated by *local modes* such as defects, impurity spins, and nuclear spins, which give rise to completely different environmental interactions. Typically local modes relax very slowly at low temperatures, because little phase space is available in their coupling to any delocalized modes. However they often couple strongly to any mesoscopic or macroscopic collective coordinate; this coupling is of course independent of N (rather than exhibiting the $\sim 1/\sqrt{N}$ dependence typical of oscillator baths). This environment is well described by a *spin bath* model. As an example, here we quote a central-spin model Hamiltonian, that is a direct reformulation of

Eq. (1.24) in terms of a spin bath:

$$\hat{H} = \frac{\hbar\omega_0}{2}\hat{\tau}^z + \hbar\hat{\tau}^z \sum_k \vec{\epsilon}_k \cdot \hat{\vec{\sigma}}_k + \hbar \sum_k \vec{\lambda}_k \cdot \hat{\vec{\sigma}}_k + \hbar \sum_{k,l} V_{kl}^{\alpha\beta}\, \hat{\sigma}_k^{\alpha}\, \hat{\sigma}_l^{\beta}\,, \qquad (1.25)$$

where the Pauli matrices $\hat{\sigma}^{\alpha}$ describe the spin bath degrees of freedom.

The study of decoherence due to spin baths has been recently given much interest [49, 56, 57, 58, 59, 60, 61, 62, 63, 64, 65, 66, 67], even if most of the works done so far are still based on the central-spin model, which may entail fictitious symmetries that are absent in realistic systems. We also mention that recently, first studies of the role played by chaotic dynamics in the decoherence process have been carried out [68, 69, 70, 71, 72, 73]. It has been shown that, in some cases, it is also possible to recover the effects of a many-body bosonic or fermionic environment, via the coupling to only a single-particle bath, provided its dynamics is chaotic [73].

Chapter 2

Stability of Quantum Simulation

As stated in Sec. 1.2, the simulation of quantum dynamics of some simple, though non trivial, classically chaotic systems promises to become the first experimental evidence of exponential speedup of quantum computing, with respect to classical one. Quantum algorithms for the simulation of such systems may therefore be a valid testing ground for investigating the effects of hardware imperfections, as well as those of decoherence on the quantum computation.

In this chapter we study the stability of quantum simulation of the sawtooth map, when subjected to internal hardware imperfections. The quantum sawtooth map is a one-degree-of-freedom periodically driven system, whose underlying classical dynamics can be chaotic or not, depending on system's parameters; it exhibits a highly non trivial dynamics and can be efficiently simulated on a quantum computer [20] (see Subsec. 2.2.1). We outline the effects of classical and quantum unitary perturbations (Hamiltonian perturbations in the system's parameters and errors introduced in quantum gates, respectively), by studying the temporal behavior of the fidelity: we show that the decay of fidelity in presence of perturbations in the quantum gates is almost independent of the dynamical regime of the simulated system, in sharp contrast with the effects of classical perturbations [74].

The chapter is organized as follows: in Sec. 2.1 we give an introduction to the notions of classical and quantum chaos. We describe some prototype chaotic dynamical systems, including the kicked rotator and the sawtooth map, and briefly analyze the fidelity decay in presence of dynamical chaos. In

Sec. 2.2 we focus on an efficient quantum algorithm for simulating the quantum sawtooth map, and introduce our quantum and classical error models. Finally, in Sec. 2.3 we present our results concerning the fidelity decay.

2.1 Quantum chaos

Quantum chaos [75, 76] is a field of investigation of great importance for fundamental physics, as well as in different research areas like atomic physics, condensed matter, nuclear physics and, more recently, quantum computers [3]: it is the study of quantum systems whose classical analogs are chaotic. Before considering quantum systems, we start from the conception of dynamical chaos in classical mechanics [77]; hereafter we will restrict our attention to non-dissipative Hamiltonian systems.

Dynamical chaos destroys the deterministic image of classical physics, in the sense that, typically, for chaotic systems the trajectories of the deterministic equations of motion are, in some sense, random and unpredictable. The mechanism of such surprising property of classical dynamics is rooted in the *local exponential instability* of motion. The local dynamics is described by the linearized equations of motions:

$$\begin{cases} \dot{\xi} = \dfrac{\partial^2 H}{\partial q \partial p}\,\xi + \dfrac{\partial^2 H}{\partial p^2}\,\eta \\ \dot{\eta} = -\dfrac{\partial^2 H}{\partial q^2}\,\xi - \dfrac{\partial^2 H}{\partial q \partial p}\,\eta \end{cases} \tag{2.1}$$

where $H = H(q, p; t)$ is the Hamiltonian, (q, p) are the coordinates of the $2N$ dimensional phase space and $\xi = dq$, $\eta = dp$ are the N-dimensional vectors in the tangent space. The coefficients of the linear equations are taken on the reference trajectory and therefore they depend explicitly on time.

An important quantity which characterizes the stability of the motion on the reference trajectory is the so called *Lyapunov exponent* λ, which is defined as the limit:

$$\lambda = \lim_{|t|\to\infty} \frac{1}{|t|} \ln\, d(t)\,, \tag{2.2}$$

where $d^2 = \xi^2 + \eta^2$ is the length of the tangent vector ($d(0) = 1$). Positivity of the Lyapunov exponent $\lambda > 0$ means exponential instability of motion. As it is seen from Eq. (2.2), the exponential instability in Hamiltonian systems

does not depend on the direction of time. The reason why the exponentially unstable motion is called "chaotic" is that almost all orbits, though deterministic, are unpredictable. This means that, in order to predict a new segment of a chaotic trajectory, one needs an additional information proportional to the length of this segment and independent of the previous length of the trajectory. In this situation information cannot be extracted from the observation of past history of motion. Instead if the instability is not exponential, for example a power law, then the required information for unit time is inversely proportional to the previous length of the trajectory and, asymptotically, prediction becomes possible.

The exponential instability implies a continuous spectrum of the motion and correlations decay. This property, in the theory of dynamical systems, is called "mixing" and provides statistical independence of different parts of a dynamical trajectory thus allowing a statistical description in terms of few macroscopic variables. Dynamical chaos represents a limiting case of chaotic motion. The opposite limiting case is given by completely integrable systems, which possess N integrals of motion (where N is the number of degree of freedom). Integrable systems are characterized by discrete spectrum, and quasi-periodicity of motion (i.e. no statistical relaxation).

The problem of *quantum chaos* originated from the necessity of understanding the classical chaos in terms of quantum mechanics. Let us first remind that quantum mechanics can be considered as divided in two qualitative different parts: the proper quantum dynamics of the system wavefunction $|\psi_t\rangle$, governed by the deterministic Schrödinger equation, and the measurement process, which is fundamentally a random process. The possible relationship with classical chaos refers to the above mentioned first part only. One of the main difficulties is that the energy spectrum of finite, bounded, quantum Hamiltonian systems is discrete. This would correspond to the case of regular motion, which is the opposite of dynamical chaos. It therefore appears that the conditions for dynamical chaos are always absent in quantum mechanics! This conclusion would contradict the correspondence principle, which requires transition from quantum to classical mechanics for all phenomena, including dynamical chaos.

The apparent contradiction between the discrete spectrum of quantum motion and the correspondence principle is reconciled by the fact that there exist characteristic *time scales* of quantum motion. Indeed, the distinction between discrete and continuous spectrum becomes non ambiguous only in

the limit $t \to \infty$. In order to clarify the existence of different time scales it is useful to compare classical and quantum evolution starting from the same initial conditions. According to Ehrenfest theorem, a quantum wave packet follows a beam of classical orbits until it remains narrow. During this time interval t_E, which is called *Ehrenfest time*, the quantum motion is exponentially unstable and "random" as the classical one. After this time scale, the quantum relaxation process takes place in absence of exponential instability, until the *Heisenberg time* t_R. The lack of exponential instability does not prevent exponential decay of dynamical quantities, like correlation functions or survival probability. This second time scale is related to the fundamental uncertainty principle: in continuous time t the discrete spectrum cannot be resolved for $t < t_R$, where $t_R \sim \rho_0$ and ρ_0 is the level density of the eigenstates which enter the initial condition $|\psi_0\rangle$ and therefore control the quantum dynamics. Typically $t_E \ll t_R$, so quantum relaxation takes place in absence of exponential instability. For larger times the quantum energy enters a steady-state oscillatory regime, correspondingly the momentum distribution reaches a steady state which has approximately an exponential form of characteristic length ξ, which can be shown to be approximated by the classical diffusion coefficient. This typical feature of quantum chaos is known as *quantum dynamical localization* [78].

2.1.1 Periodically driven dynamical systems

Time-dependent perturbations, especially periodic ones, are of central attention in the study of chaotic dynamical systems, since they provide the simplest examples of classical non-integrability: systems with a single degree of freedom are classically integrable if autonomous, but may be non-integrable if subjected to periodic driving. Of special interest are cases for which the temporal modulation takes the form of a periodic train of delta kicks:

$$H(\theta, n, t) = \frac{n^2}{2} + kV(\theta) \sum_{j=-\infty}^{+\infty} \delta(t - jT)\,, \tag{2.3}$$

where (n, θ) are the conjugated action-angle variables ($0 \leq \theta < 2\pi$). These maps characterize a point-particle which is in a circular motion, and is periodically subjected to external driving forces V of period T, and of strength depending on its position. Due to the periodicity of the system, the Hamilton equations of motion can be straightforwardly integrated along one period.

The time evolution $t \to t+T$ is then classically described by the map:

$$\begin{cases} n_{t+T} = n_t - k\,\mathrm{d}V/\mathrm{d}\theta|_{\theta_t} \\ \theta_{t+T} = \theta_t + T n_{t+T} \qquad (\mathrm{mod}\ 2\pi) \end{cases} \tag{2.4}$$

where (θ_t, n_t) denote the values of the action-angle variables at time t, immediately before the t-th kick.

The corresponding quantum evolution in one map iteration is described by the unitary operator $\hat{U}$:

$$|\psi_{t+T}\rangle = \hat{U}|\psi_t\rangle = e^{-iT\hat{n}^2/2}\, e^{-ikV(\hat{\theta})}|\psi_t\rangle\,, \tag{2.5}$$

where $|\psi_t\rangle$ is the system wavefunction at time t ($|\psi_t(\theta+2\pi)\rangle = |\psi_t(\theta)\rangle$), immediately before the t-th kick; $\hat{\theta} = \theta\,\cdot$, $\hat{n} = -i\partial/\partial\theta$ are the canonically conjugated angular position and impulse operators, which obey the commutation rule $[\hat{\theta}, \hat{n}] = i$. Hereafter we set $\hbar = 1$.

The kicked rotator

A fairly complete understanding has been achieved for both classical and quantum dynamics of the so called "kicked rotator" [79], which is described by the Hamiltonian of Eq. (2.3) with $V(\theta) = \cos(\theta)$. By inserting the potential $V(\theta) = \cos(\theta)$ in Eqs. (2.4), and rescaling $n \to p = Tn$, one notices that the classical equations of motion depend only on the parameter $K \equiv kT$:

$$\begin{cases} p_{t+T} = p_t + K\sin\theta_t \\ \theta_{t+T} = \theta_t + p_{t+T} \qquad (\mathrm{mod}\ 2\pi)\,. \end{cases} \tag{2.6}$$

The classical kick-to-kick description of Eqs. (2.6) is the famous Chirikov standard map, and it is usually referred to as the prototype of chaotic systems. For $K = 0$ the motion is integrable; when K increases, a transition to chaos of the Kolmogorov-Arnold-Moser (KAM) type is observed. The last invariant KAM torus is broken for $K \approx 0.97$. If $K \sim 1$ the phase space is mixed (simultaneous presence of integrable and chaotic components). If K increases further, the stability islands progressively reduce their size; for $K \gg 1$ they are not visible any more. On the torus $0 \le \theta < 2\pi$, $-\pi \le p < \pi$, the Chirikov standard map describes the stroboscopic dynamics of a conservative dynamical system with two degrees of freedom which, in the fully chaotic regime $K \gg 1$, relaxes to the uniform distribution on the torus.

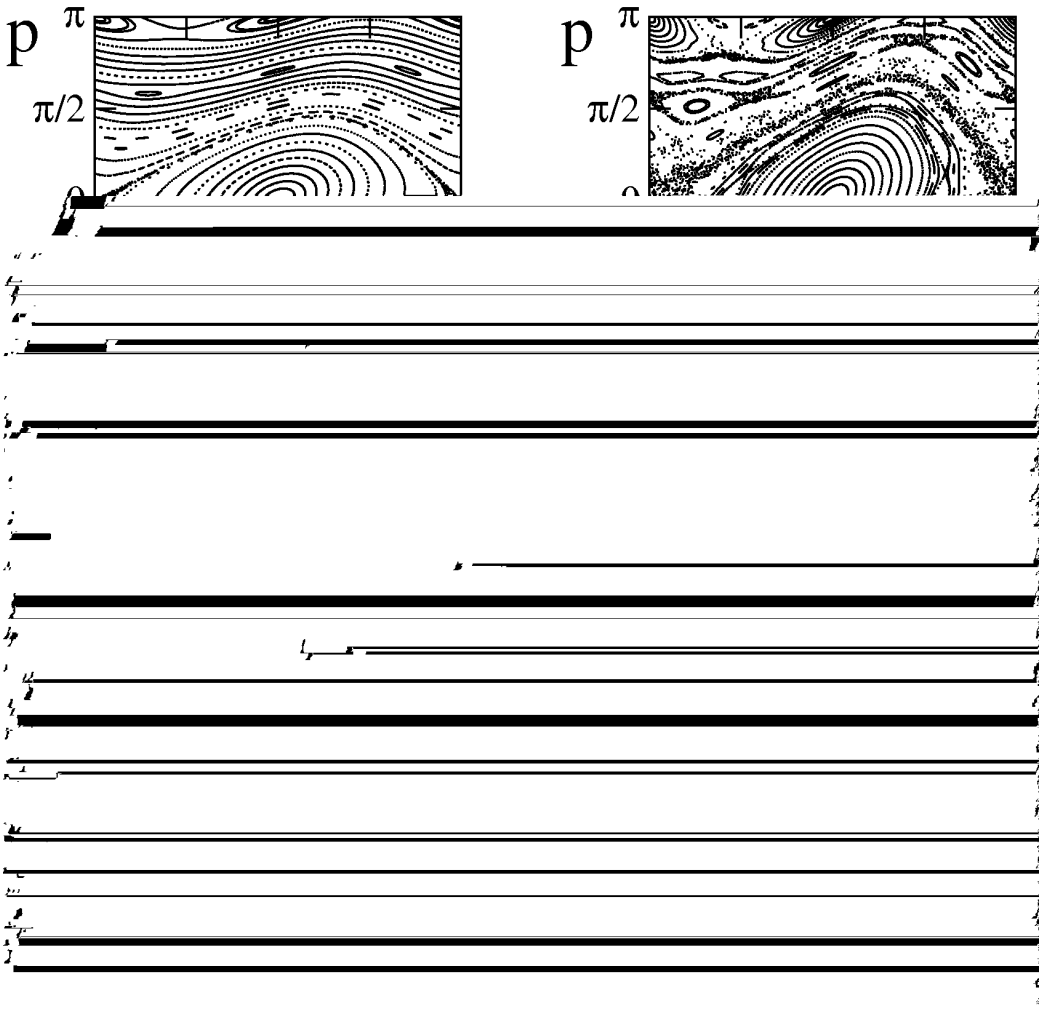

Figure 2.1: Phase space portrait of the Chirikov standard map, for different values of K: $K = 0.5$ (up left), 1 (up right), 2 (down left), 5 (down right).

From Eq. (2.5), the quantum evolution in one map iteration is obtained:

$$|\psi_{t+T}\rangle = \hat{U}|\psi_t\rangle = e^{-iT\hat{n}^2/2}\, e^{-ik\cos(\hat{\theta})}|\psi_t\rangle\,. \tag{2.7}$$

The effective Planck constant is given by $\hbar_{\text{eff}} = T$. Indeed, if we consider the operator $\hat{p} = T\hat{n}$ ($\hat{p}$ is the quantization of the classical rescaled action p), we have

$$[\hat{\theta}, \hat{p}] = T[\hat{\theta}, \hat{n}] = iT = i\hbar_{\text{eff}}. \tag{2.8}$$

The classical limit $\hbar_{\text{eff}} \to 0$ is obtained by taking $k \to \infty$ and $T \to 0$, while keeping $K = kT$ constant. One typically deals with Hilbert spaces of dimension N, thus fixing the value of $T = 2\pi L/N$ (assuming that $-\pi L \leq p < \pi L$, L being the number of considered angular momentum cells).

The sawtooth map

Another important delta-kicked system is the so called "sawtooth map", which corresponds to Hamiltonian (2.3) with $V(\theta) = -\frac{1}{2}(\theta - \pi)^2$. The time evolution $t \to t + T$ is classically described by the map:

$$\begin{cases} p_{t+T} = p_t + K(\theta_t - \pi) \\ \theta_{t+T} = \theta_t + p_{t+T} \end{cases} \tag{2.9}$$

where, as before, we set $p = Tn$ and $K = kT$. The classical motion is stable for $-4 \leq K \leq 0$ and completely chaotic over all the phase space for $K < -4$ and $K > 0$, the maximum Lyapunov exponent being:

$$\lambda = \begin{cases} \ln\left|\frac{1}{2}\left(2 + K - \sqrt{K^2 + 4K}\right)\right| & \text{for} \quad K < -4 \\ 0 & \text{for} \quad -4 \leq K \leq 0 \\ \ln\left[\frac{1}{2}\left(2 + K + \sqrt{K^2 + 4K}\right)\right] & \text{for} \quad K > 0 \end{cases}. \tag{2.10}$$

As shown on the left of Fig. 2.2, in the stable, quasi-integrable regime, the phase space has a complex structure of elliptic islands down to smaller and smaller scales. Note that the integrable islands are surrounded by a non-integrable region, and that each trajectory diffuses (anomalously) in this region. The cases $K = 0, -1, -2, -3, -4$ are integrable. On the contrary, in the chaotic region (see right of Fig. 2.2) no stability island is present, and every trajectory can generate all the points of the phase space; in this case the system is said to be *ergodic*.

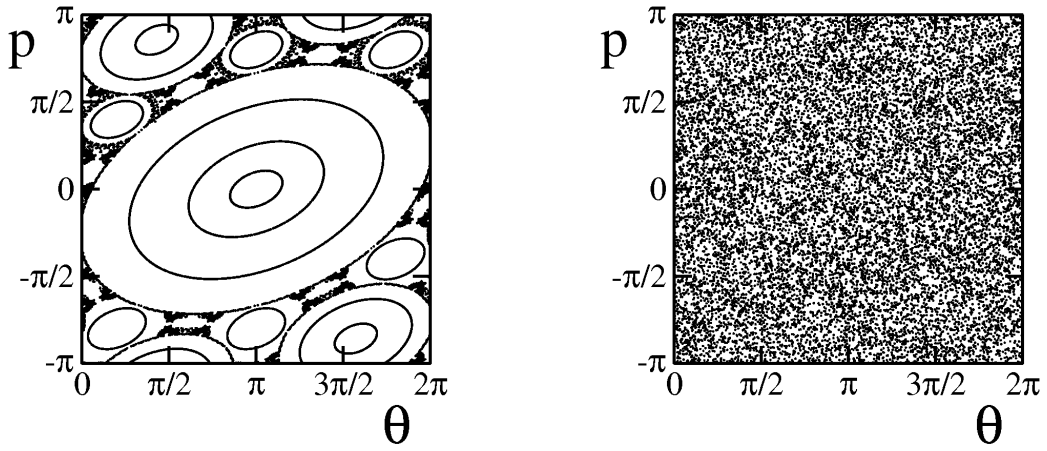

Figure 2.2: Phase space portrait of the classical sawtooth map for different dynamical regimes: quasi-integrable at $K = -0.5$ (left side); chaotic at $K = 0.1$ (right side). For $K = -0.5$ we show 7 trajectories inside the integrable islands and a single trajectory filling the anomalously diffusive region. For $K = 0.1$ we just show one trajectory.

The corresponding quantum evolution in one map iteration is described by the unitary operator

$$\hat{U} = e^{-iT\hat{n}^2/2}\, e^{ik(\hat{\theta}-\pi)^2/2}\,, \tag{2.11}$$

where, as before, $|\psi_t(\theta + 2\pi)\rangle = |\psi_t(\theta)\rangle$; $[\hat{\theta}, \hat{n}] = i$; $\hbar_{\rm eff} = T$. The classical limit $\hbar_{\rm eff} \to 0$ is again obtained by taking $k \to \infty$ and $T \to 0$, while keeping $K = kT$ constant. In this chapter we study this map on the torus $0 \leq \theta < 2\pi$, $-\pi \leq p < \pi$, and consider Hilbert spaces of dimension N, thus setting $T = 2\pi/N$.

2.1.2 The fidelity in quantum chaotic systems

There are some tools which are typically used to investigate quantum chaotic systems. Among them, probably the most important ones are the fidelity [80] (see App. A), the level spacing statistics (see App. B), the local density of states, the von Neumann entropy, and the Husimi functions [76]. Here we focus on the various fidelity decay behaviors in quantum chaotic system. Let us recall that the fidelity $f(t)$ is the squared overlap of two wave vectors

$|\psi(t)\rangle$ and $|\psi_\epsilon(t)\rangle$ that are obtained by evolving the same initial state $|\psi_0\rangle$ with unperturbed and perturbed evolutions $\hat{U}(t)$ and $\hat{U}_\epsilon(t)$, according to the Hamiltonians $\hat{H}$ and $\hat{H} + \epsilon\hat{V}$ respectively:

$$f(t) = |\, \langle\psi_0|\, \hat{U}_\epsilon^\dagger(t)\, \hat{U}(t)\, |\psi_0\rangle\, |^2 \,. \tag{2.12}$$

The study of the temporal decay of quantum fidelity in classically chaotic systems has recently received great interest [81]; a rich variety of different behaviors has been found, ranging from Gaussian to exponential or power-law decay, depending on the chaotic or integrable nature of the system under investigation, on the initial state, and on the shape of the perturbation. For classically chaotic systems, under quite general circumstances, three distinct characteristic regimes of fidelity decay have been identified:

- *Perturbative regime* - Let V be the typical matrix element of the perturbation operator $\hat{V}$ connecting the eigenvectors of $\hat{U}$, and let Δ be the average level spacing of the unperturbed system. Then, if the perturbation is small enough, such that $\epsilon < \Delta/V$, a *Gaussian decay* of the fidelity takes place:

  $$f(t) \sim e^{-\epsilon^2 V^2 t^2} \,. \tag{2.13}$$

  This can be seen by expanding Eq. (2.12) on the eigenbasis $\{|\phi_m\rangle\}$ of $\hat{U}$:

  $$f(t) = \Big| \sum_m \langle\phi_m|\psi_0\rangle\, e^{-i\epsilon\langle\psi_0|\hat{V}|\phi_n\rangle\, t} \Big|^2 \,, \tag{2.14}$$

  and then using stationary perturbation theory techniques. Notice that, provided $|\psi_0\rangle$ is a superposition of a large number of eigenvectors $|\phi_m\rangle$, for very short times $t \ll (\epsilon\, \delta V)^{-1}$ the fidelity decay is always quadratic, independently of $\hat{U}$ (here δV indicates the standard deviation of the matrix elements of $\hat{V}$).

- *Fermi Golden Rule regime* - For stronger perturbations, $\epsilon > \Delta/V$, stationary perturbation theory no longer applies and the fidelity decay becomes *exponential* [82]:

  $$f(t) \sim e^{-\epsilon^2 V^2\, t/\Delta} \,. \tag{2.15}$$

  This behavior persists up to a given threshold: $\epsilon < \epsilon_c$. From Eqs. (2.13), (2.15) it follows that there exists a crossover time $\tilde{t} \sim 1/\Delta$ between the

exponential and the Gaussian regime, which turns out to be equal to the Heisenberg relaxation time t_R. For a sufficiently strong perturbation, fidelity completely decays within t_R according to Eq. (2.15). In the opposite case, if ϵ is sufficiently small, no significant decay of fidelity takes place during the Heisenberg time, and therefore one observes the Gaussian decay of Eq. (2.13) after time t_R.

- *Semiclassical regime* - For a localized initial state (such as a coherent Gaussian wave packet), the short-time quantum dynamics follows the corresponding classical evolution of a narrow beam of classical orbits until the Ehrenfest time t_E, as predicted by the Ehrenfest theorem. Therefore, for times shorter than t_E, the quantum fidelity follows the classical behavior, that is characterized by an exponential decay with a *perturbation independent rate* equal to the largest Lyapunov exponent λ of the system [83]:
$$f(t) \sim e^{-\lambda t} . \tag{2.16}$$
In typical situations with a sufficiently strong perturbation $\epsilon > \epsilon_c$, fidelity decays to the saturation value in times shorter than t_E; this explains the observed perturbation-independent decay rate of fidelity.

The fidelity is central in the study of the stability of dynamical systems under Hamiltonian perturbations (classical errors), but can also be a useful tool in order to characterize the stability of quantum computation. In this last case perturbations can be modeled by unitary errors in the quantum gates implementing the quantum algorithm (quantum errors). In Sec. 2.3 we will show that, whereas the decay of fidelity with Hamiltonian perturbations is very sensitive to the dynamical regime, errors on quantum gates induce a Fermi Golden Rule exponential decay that is substantially independent of the dynamics of the underlying system [74]. Finally we also notice that the fidelity can be efficiently evaluated on a quantum computer, as discussed in appendix A.

2.2 Simulation of chaotic systems

We now turn to the problem of the simulation of dynamical systems. From the viewpoint of computational complexity, the following question naturally arises: given a generic dynamical system, is it possible to find its solution at time t efficiently, taking into account unavoidable computational errors?

the backward evolution, we do not recover the initial distribution at time $2t$ (see Fig. 2.3). This is because any amount of numerical error in computer simulations rapidly effaces the memory of the initial conditions. On the contrary, the same numerical simulations in the quantum case show that time reversibility is preserved in the presence of small errors. This is a clear signature of the fact that quantum motion is very stable, in sharp contrast to the classical extreme sensitivity to initial conditions and rapid loss of memory.

In view of the above considerations, it is natural to inquire about the stability of quantum computation in the presence of unavoidable imperfections in the quantum computer hardware. In the remaining part of this section, we describe the quantum algorithm we want to study, and a model of perturbations whose effects we are going to investigate.

2.2.1 Quantum algorithm for the sawtooth map

The quantum evolution of the sawtooth map in one map iteration from time t to time $t+T$ is given by the unitary operator $\hat{U}$ in Eq. (2.11). There exists an efficient quantum algorithm that simulates the action of $\hat{U}$ on a N-dimensional Hilbert space by using a register of $n_q = \log_2 N$ qubits; this is based on the forward-backward "Quantum Fourier Transform" (QFT) between the canonically conjugate θ and n representations [20]. Such an approach is rather convenient, since $\hat{U}$ is the product of two operators $\hat{U}_k \equiv e^{ik(\hat{\theta}-\pi)^2/2}$ and $\hat{U}_T \equiv e^{-iT\hat{n}^2/2}$, where $\hat{U}_k$ is diagonal in the θ representation, while $\hat{U}_T$ is diagonal in the n representation. In brief, the quantum algorithm for one map iteration requires the following steps:

- The unitary operator $\hat{U}_k$ is decomposed in n_q^2 two qubit gates:

$$e^{ik(\hat{\theta}-\pi)^2/2} = \prod_{j,l=1}^{n_q} \exp\left[2\pi^2 ik\left(\alpha_j 2^{-j} - \frac{1}{2n_q}\right)\left(\alpha_l 2^{-l} - \frac{1}{2n_q}\right)\right] \quad (2.17)$$

  where $\theta = 2\pi\sum \alpha_j 2^{-j}$, with $\alpha_j \in \{0,1\}$. Each two qubit gate can thus be written in the $\{|00\rangle, |01\rangle, |10\rangle, |11\rangle\}$ basis, in θ representation, as $\exp(ik\pi^2\hat{D})$, where $\hat{D}$ is a diagonal matrix with elements:

$$\left\{\frac{1}{2n_q^2}, \frac{1}{n_q}\left(\frac{1}{2n_q} - \frac{1}{2^l}\right), \frac{1}{n_q}\left(\frac{1}{2n_q} - \frac{1}{2^j}\right), 2\left(\frac{1}{2^j} - \frac{1}{2n_q}\right)\left(\frac{1}{2^l} - \frac{1}{2n_q}\right)\right\};$$

- The change from the θ to the n representation is obtained by means of the QFT, which requires n_q Hadamard gates and $n_q(n_q-1)/2$ controlled-phase shift gates [85];
- In the new representation, the operator $\hat{U}_T$ has essentially the same form as $\hat{U}_k$ in the first step, therefore it can be decomposed in n_q^2 two-qubit gates, similarly to Eq. (2.17);
- Finally we return to the initial θ representation via an inverse QFT.

On the whole, the algorithm requires $3n_q^2 + n_q$ one- and two-qubit gates per map iteration, and it is exponentially efficient with respect to any known classical algorithm. This exponential speedup eventually resides on the quantum computer's ability to vastly parallelize the performance of a classical discrete Fourier transform: the best classical algorithm for computing it on 2^n elements is the Fast Fourier Transform, which requires $O(n\,2^n)$ elementary operations. On the contrary the corresponding Quantum Fourier Transform, only neeads $O(n^2)$ quantum elementary gates (see, e.g., Ref. [85]). Moreover, we stress the fact that the quantum algorithm does not require any auxiliary work-space qubit, as both the "kick operator" $\hat{U}_k$ and the "free rotation operator" $\hat{U}_T$ have the same quadratic form [19].

2.2.2 Classical and quantum perturbations

Here we introduce our models of "classical" and "quantum" perturbations, whose effects will be analyzed in detail in the following section (Sec. 2.3). With the name of "classical" perturbations we refer to Hamiltonian perturbations of the dynamical system's parameters that have a classical limit, while "quantum" perturbations are intended to be unitary memoryless errors introduced at each quantum gate. These quantum errors have no classical analogue and are unavoidable during a quantum computation.

We will limit ourselves to consider unitary errors modeled by *noisy gates*, neglecting unwanted coupling with the external environment; such noise results from the imperfect control of the quantum computer. For instance, in a NMR quantum computer the logic gates on qubits are simulated by applying magnetic fields to the system. If the direction or the intensity of the fields are not correct, a slightly different gate is applied, though it remains unitary. In ion-trap quantum processors, laser pulses are used to implement sequences of quantum gates [86]. Fluctuations in the duration of each pulse induce unitary

errors, which accumulate during a quantum computation. We also assume that the errors affecting different quantum gates are completely *uncorrelated*: every time a noisy gate is applied, the dephasing parameters randomly fluctuate, without keeping trace of the previous implemented gates [87, 88, 89, 90].

We give a quantitative characterization of the two types of errors in the context of the quantum sawtooth map model, that we are going to simulate:

- *Classical errors* - We perturb the kicking strength k in Eq. (2.11) as follows: at each map step, k is slightly changed by a small amount $\delta k(t)$, which is randomly chosen in the interval $[-\delta k, \delta k]$. Consequently, $\delta K(t) \equiv T\delta k(t) \in [-\delta K, +\delta K]$, where $\delta K \equiv T\delta k$. This kind of perturbation, when applied to the classical motion, disturbs a given orbit by a small amount at each map step and therefore, to some extent, mimics the presence of round-off errors in a classical computer.

- *Quantum errors* - As stated in the previous subsection, the quantum algorithm for simulating the one-kick operator of the sawtooth map, Eq. (2.11), requires $2n_q$ Hadamard gates and $3n_q^2 - n_q$ controlled-phase shift gates [19, 20], where $n_q = \log_2 N$, and N is the dimension of the Hilbert space. As quantum errors, we choose to perturb the implemented quantum gates in the following way:
  − Controlled-phase shift gates are diagonal in the computational basis and act non-trivially only on the four-dimensional Hilbert subspace spanned by two qubits. In this subspace, we write each controlled-phase shift gate as $\tilde{C} = \mathcal{E}C$, where C is the ideal gate and the diagonal perturbation $\mathcal{E}$ is given by $\mathcal{E} = \mathrm{diag}(e^{i\epsilon_0}, e^{i\epsilon_1}, e^{i\epsilon_2}, e^{i\epsilon_3})$. Therefore, the unitary error operator $\mathcal{E}$ introduces unwanted phases.
  − Each one-qubit gate can be seen as a rotation of the Bloch sphere about some axis $\hat{u}_0$. In particular, the Hadamard gate is a rotation through an angle π about $\hat{u}_0 = (\sin\theta_0\cos\phi_0, \sin\theta_0\sin\phi_0, \cos\theta_0)$, where $\theta_0 = \pi/4$ and $\phi_0 = 0$. Unitary errors tilt the rotation angle $\hat{u_0} \to \hat{u} = (\sin\theta\cos\phi, \sin\theta\sin\phi, \cos\theta)$, with $\theta = \theta_0 + \nu_1$ and $\phi = \phi_0 + \nu_2$. We assume that the dephasing parameters $\{\epsilon_i\}_{i=1\ldots4}$, $\{\nu_j\}_{j=1,2}$ are randomly and uniformly distributed in the interval $[-\epsilon, \epsilon]$. We also assume that errors affecting different quantum gates are completely *uncorrelated*: every time we apply a noisy gate, the dephasing parameters randomly fluctuate in the (fixed) interval $[-\epsilon, +\epsilon]$.

2.2.3 Initial conditions

As initial state $|\psi_0\rangle$ for the quantum simulations we consider:

- A *coherent Gaussian wave packet*:

$$|\psi_0\rangle_G = A \sum_{n=0}^{N-1} e^{\frac{-(n-n_0)^2}{2\sigma^2} + i\left(n-\frac{n_0}{2}\right)\theta_0} |n\rangle, \tag{2.18}$$

  where (θ_0, n_0) is the center of the wave packet ($\langle\hat{\theta}\rangle = \theta_0$, $\langle\hat{n}\rangle = n_0$), A a normalization constant, and $\sigma^2 = (\Delta n)^2 \equiv \langle(\hat{n} - \langle\hat{n}\rangle)^2\rangle$ the variance in the momentum representation. We choose $\sigma^2 = N/(2\pi L)$ in order to obtain an equal value for the variances in p and in θ, namely $\Delta\theta\,\Delta p = \hbar_{\text{eff}}$, with $\Delta\theta = \Delta p = \sqrt{\hbar_{\text{eff}}}$. The wave vector (2.18) is the closest quantum analog of a classical probability density, localized in a small region of the phase space, centered in (θ_0, p_0) and of width σ. This type of states can be prepared efficiently on a quantum computer [91].

- A *random wave vector*: $|\psi_0\rangle_R = \sum_{n=1}^{N} c_n |n\rangle$, where the coefficients c_n have amplitudes of the order of $1/\sqrt{N}$ and random phases. This state has no classical analogue.

2.3 Results and discussion

In this section we compare the effect of noisy gates, "quantum errors", with that of *randomly fluctuating perturbations* in the system's parameters, "classical errors", by analyzing the fidelity decay. Hereafter we will call $f_c(t)$ and $f_q(t)$ the fidelity for classical or quantum errors, respectively.

2.3.1 Fidelity with classical errors

Let us consider the fidelity decay $f_c(t)$, obtained under fluctuating perturbations in the parameter k of the sawtooth map. We show that $f_c(t)$ exhibits a marked dependence on the simulated dynamics, by observing qualitatively different behaviors, depending on the chaotic or non-chaotic motion.

We first analyze the *quasi-integrable regime* $-4 \leq K \leq 0$. In this case the sawtooth map behaves, inside the main integrable island with fixed point

$(\theta, p) = (\pi, 0)$ (see Fig. 2.2), as a harmonic oscillator, with characteristic frequency $\nu_K = \omega_K/2\pi = \sqrt{-K}/2\pi$. Therefore, in the semiclassical regime the quantum motion of coherent wave packets residing inside integrable islands closely follows the harmonic evolution of the corresponding classical trajectories. In the central island this motion has period $T = 2\pi/\sqrt{-K}$, while in the outer islands the period is multiplied by a factor which depends on the order of the corresponding resonances (for example, the two upper islands in Fig. 2.2 correspond to a second order resonance, and inside them the period is doubled). Since the chosen perturbation affects the parameter K, the fidelity $f_c(t)$ is obtained as the overlap of two wave packets which move inside an integrable island with slightly different frequencies.

For a static perturbation, $\delta K(t) = \delta K$, the centers of the two wave packets separate ballistically (linearly in time) and a very fast decay of quantum fidelity is expected, as far as the distance between the centers of the two packets becomes larger than their width σ [92, 93]. The type of decay is related to the shape of the initial wave packet. In particular, for a Gaussian wave packet a Gaussian decay is expected. If $\delta\nu_K \equiv \nu_{K+\delta K} - \nu_K$ denotes the frequency separation between perturbed and unperturbed motion, the Gaussian decay takes place after a time $t_s \propto \sigma/\delta\nu_K$. In the case of a randomly fluctuating perturbation, $\delta K(t) \in [-\delta K, \delta K]$, the frequency $\nu_{K+\delta K(t)}$ of a classical trajectory following the perturbed dynamics is not constant. The relative displacement of this orbit with respect to the one described by the unperturbed dynamics (with a frequency ν_K) is approximately given by a Brownian motion. The separation between the two orbits is proportional to the frequency difference $\delta\nu_K$. In this case the fidelity decay is again Gaussian, but in general it shows large random fluctuations from the Gaussian profile (see for example the upper curve in Fig. 2.4), which depend on the noise realization. Moreover, the distance between the centers of the two wave packets grows $\propto \sqrt{\delta\nu_K t}$, and therefore the Gaussian decay starts after a time scale $t_s \propto \sigma^2/\delta\nu_K$. We also notice that the fidelity decay depends not only on the shape of the initial state, but also on its position. Indeed, inside any integrable island the frequency's perturbation $\delta\nu_K = \nu_{K+\delta K} - \nu_K \approx \frac{\delta K}{4\pi\sqrt{-K}}$ is independent of the position of the wave packet in phase space. Since larger orbits imply a larger velocity, and consequently a larger relative ballistic motion of the two wave packets, the fidelity drops faster when we move far from the center of the integrable islands.

In the *chaotic regime*, the fidelity $f_c(t)$ always decays exponentially; an example of such decay is given in Fig. 2.4, lower curve. For small pertur-

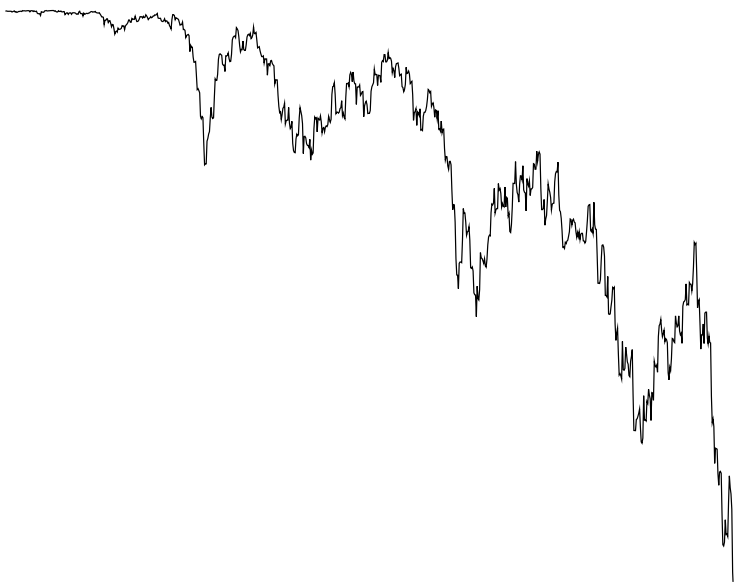

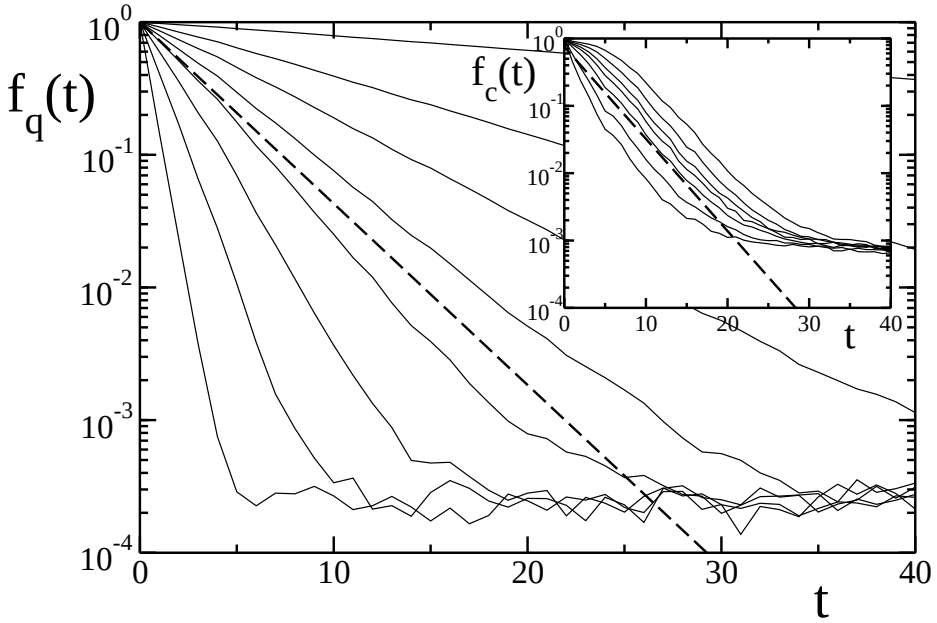

Figure 2.5: Fidelity decay for noisy gates in the sawtooth map with $K = 0.1$, $n_q = 12$. From right to left: $\epsilon = 1.5 \times 10^{-2}$, 3×10^{-2}, 4×10^{-2}, 5×10^{-2}, 6×10^{-2}, 7.5×10^{-2}, 10^{-1}, 1.5×10^{-1}. Inset: fidelity decay for uncorrelated perturbations in the parameter k. From right to left $\delta K = T\delta k = 3 \times 10^{-3}$, 5×10^{-3}, 7.5×10^{-3}, 10^{-2}, 1.5×10^{-2}, 3×10^{-2}, 5×10^{-2}. In both graphs, data are averaged over 50 initial Gaussian wave packets. Dashed lines show the Lyapunov exponential decay: $f(t) = e^{-\lambda t}$, where $\lambda \approx 0.315$ is the classical Lyapunov exponent at $K = 0.1$.

litatively different behaviors (exponential or Gaussian decay) are shown in Fig. 2.4. Notice also that the regular dynamics turns out to be much more stable than the chaotic one (to represent both cases on the same figure, the perturbation value chosen in the chaotic case is 20 times smaller than the one chosen in the integrable case).

2.3.2 Fidelity with quantum errors

We now analyze the fidelity behavior in the presence of natural errors for quantum computation, namely *random unitary perturbations* of amplitude ϵ on *quantum gates*, following the noise model described in Subsec 2.2.2.

As shown in Figs. 2.5-2.6, in the *chaotic regime* the fidelity $f_q(t)$ drops

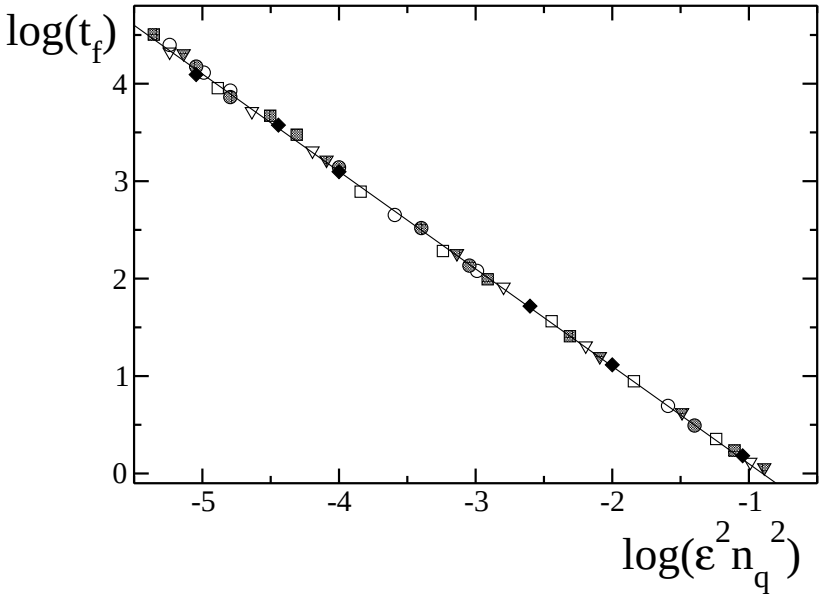

Figure 2.6: Characteristic time scale t_f for the fidelity decay, determined by the condition $f(t_f) = 0.9$, in the sawtooth map at $K = 5$ with noisy gates. Data are obtained for different perturbation strengths ϵ and number of qubits: $n_q = 4$ (empty circles), 5 (filled circles), 6 (empty squares), 7 (filled squares), 8 (empty triangles), 9 (filled triangles), and 10 (filled diamonds). The straight line shows the dependence $t_f \simeq 0.126/\epsilon^2 n_q^2$, corresponding to the exponential fidelity decay (2.19), with $C \approx 0.28$. The initial state is in all cases a Gaussian wave packet and data are averaged over 50 noise realization. Logarithms are decimal.

exponentially, with a rate $\Gamma \propto \epsilon^2 n_q^2$. The exponential decay stops when the fidelity approaches the saturation value $f_q(\infty) = 1/N$, given by the inverse of the size of the Hilbert space (it reflects the finiteness of the system). This decay can be understood from the Fermi Golden Rule: each noisy gate transfers a probability of order ϵ^2 from the ideal unperturbed state to other states. Due to the fact that perturbations acting on two different gates are completely uncorrelated, an exponential decay rate proportional to ϵ^2 and to the number of gates $n_g \equiv 3n_q^2 + n_q$ required to implement one step of the sawtooth map is expected:

$$f_q(t) \simeq e^{-\Gamma t} \simeq e^{-C\epsilon^2 n_g t}, \tag{2.19}$$

where $C \approx 0.28$ is a constant that we have computed from our numerical

data. We have determined the characteristic time scale t_f for fidelity decay from the condition $f_q(t_f) = A = 0.9$ (note that the value chosen for A is not crucial). Our numerical calculations, shown in Fig. 2.6, clearly demonstrate that:

$$t_f \propto \frac{1}{\epsilon^2 n_q^2}, \tag{2.20}$$

in agreement with Eq. (2.19).

The fidelity decay in the chaotic regime always follows the exponential behavior predicted by the Fermi golden rule. Therefore, in contrast with the case of classical errors, there is no saturation of the decay rate to the largest Lyapunov exponent of the system (see Fig. 2.5). This result can be understood from the *non-locality* of quantum errors: each noisy gate can make direct transfer of probability on a large distance in phase space. This is a consequence of the binary encoding of the discretized angle and momentum variables. For instance, we represent the momentum eigenstates $|n\rangle$ ($-N/2 \leq n < N/2$) in the computational basis as $|\alpha_{n_q} \cdots \alpha_2 \alpha_1\rangle$, where $\alpha_j \in \{0, 1\}$ and $n = -N/2 + N \sum_{j=1}^{n_q} \alpha_j 2^{-j}$. If we take, say, $n_q = 6$ qubits ($N = 2^6 = 64$), the state $|000000\rangle$ corresponds to $|n = -32\rangle$ ($p = -\pi$), $|000001\rangle$ to $|n = -31\rangle$ ($p = -\pi + 2\pi(1/2^6)$), and so on until $|111111\rangle$, corresponding to $|n = 31\rangle$ ($p = -\pi + 2\pi(63/2^6)$). Let us consider the simplest quantum error, the bit flip: if we flip the less significant qubit ($\alpha_1 = 0 \leftrightarrow 1$), we exchange $|n\rangle$ with $|n + 1\rangle$ (mod N), while, if we flip the most significant qubit ($\alpha_{n_q} = 0 \leftrightarrow 1$), we exchange $|n\rangle$ with $|n + 32\rangle$ (mod N). It is clear that this latter error transfers probability very far in phase space and cannot be reproduced by classical local errors. Therefore, no semiclassical regime for the fidelity decay is expected with quantum errors. In particular, the non locality of perturbations makes the fidelity insensitive to the rate of local exponential instability, given by the Lyapunov exponent.

The most striking feature of the fidelity decay induced by quantum errors is its substantial independence of the chaotic or non-chaotic nature of the underlying classical dynamics. An example of this behavior is shown in Fig. 2.7 and strongly contrasts with what obtained by perturbing the system's parameters (see Fig. 2.4); in particular, the fidelity decay for integrable dynamics is exponential. The only dependence on the dynamics is found when starting from a Gaussian wave packet; in that case integrable dynamics turns out to be a little more stable than chaotic dynamics: we numerically obtained a ratio of the decay rates in the chaotic and in the integrable case which oscillates between 1.15 and 1.4, for different values of n_q between 5 and 16,

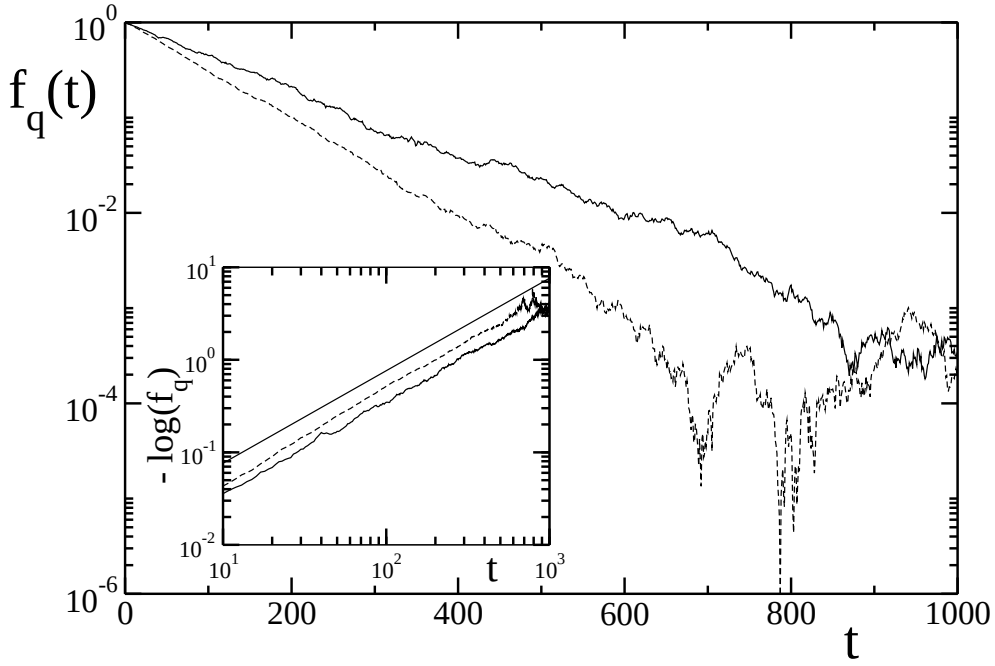

Figure 2.7: Fidelity decay for the quantum sawtooth map simulated with $n_q = 12$ qubits, in the presence of uncorrelated unitary quantum errors with maximum perturbation strength $\epsilon = 10^{-2}$. As initial condition we consider a Gaussian wave packet peaked in $(\theta_0, p_0) = (1, 0)$. The upper curve is for the quasi-integrable regime $K = -0.5$, while the lower one is for the chaotic case $K = 0.5$. In the inset we plot the same curves, showing $-\log(f_q)$ versus time. The solid line corresponds to exponential fidelity decay, that is $-\log f_q \propto t$. Logarithms are decimal.

and for various ϵ ranging from 10^{-5} to 10^{-1}. Anyway, the smaller decay rate obtained when we evolve a Gaussian wave packet inside an integrable island is not due to the lack of exponential instability, but simply to the fact that the dynamics preserves the coherence of the wave packet. This can be clearly seen from the data of Fig. 2.8.

Summarizing, we can conclude that the decay of fidelity due to noisy gates does not depend on the value of the Lyapunov exponent, and is independent of the presence or lack of exponential instability [1]:

[1] A further confirmation of our statements comes from the analysis of the fidelity decay when implementing the quantum algorithm without dynamical evolution, i.e. by putting $T = 0$ and $k = 0$ in Eq. (2.11). In such a situation, we found that the fidelity drops again

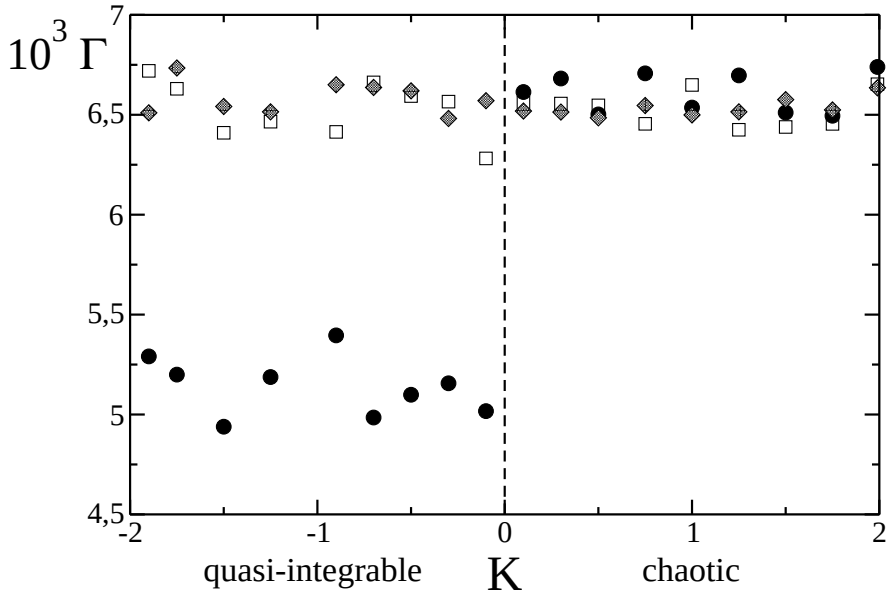

Figure 2.8: Fidelity decay rate for noisy gates as a function of K ($n_q = 9$, $\epsilon = 10^{-2}$). As initial condition we choose: (i) a Gaussian wave packet centered in $(\theta_0, p_0) = (1, 0)$ (circles) (note that for $-4 < K < 0$ this packet is inside the main integrable island); (ii) a Gaussian packet centered in $(\theta_0, p_0) = (0, 0)$ (squares), that is residing in the diffusive region; (iii) a random wavefunction (diamonds). Data obtained after averaging over 25 noise realizations.

- In the *chaotic regime* $K > 0$ (Lyapunov exponent $\lambda > 0$), the fidelity decay rate is independent of the initial state (Gaussian packet or random state) and of the rate of exponential instability. Indeed, the decay rate is independent of K, while λ depends on K.

- In the *quasi-integrable regime* $-4 < K < 0$ (Lyapunov exponent $\lambda = 0$), only in the case in which we choose as initial state a Gaussian packet placed inside an integrable island we obtain a fidelity decay rate smaller than in the chaotic case. On the other hand, if we start from a random state of if we place the Gaussian wave packet inside the anomalously diffusive region, we obtain the same decay rate as in the chaotic case.

exponentially and the ratio between the decay rates starting from a random or a Gaussian state is the same as in the quasi-integrable regime.

The rich variety of behaviors found in the study of the stability of quantum motion under Hamiltonian perturbations has no correspondence in the fidelity of quantum computation under its natural perturbations. In this latter case, insensitivity to the dynamics is eventually due to the intrinsic non locality of the quantum errors; we therefore expect that this scenario remains valid also in the case of non-unitary quantum noise and/or when errors, correlated or memoryless, act not only on the qubits on which we apply a quantum gate but on all the qubits that constitute the quantum computer.

Chapter 3

Stability of Quantum Transmission

In the previous chapter we analyzed the stability of quantum computation when corrupted by noisy gates; this type of errors is due to internal imperfections in the computer hardware. In the field of quantum information processing, besides quantum computing, quantum communication also covers a great importance. Moreover, experiments implementing quantum transmission protocols are much further feasible than the ones implementing quantum algorithms, since they typically require manipulation of simple quantum states, rather than complicated sequences of non local quantum gates [1]. Theoretical efforts in developing communication protocols and inquiring about their stability with respect to similar internal imperfections of the quantum devices would therefore be particularly suitable.

Actually, several protocols have been proposed which would allow distant parties to exchange and/or share quantum information over chains of permanently coupled spins (see Sec. 1.3 and references therein). The ultimate aim of these protocols is to achieve perfect transfer of any quantum state in a given period of time. High degrees of efficiency also require the capability of isolating the experimental setup from the external world, preventing it from decoherence, and to reduce all static internal imperfections. In this chapter we focus on the stability of a quantum transmission protocol, introduced in Ref. [30], through a modulated spin 1/2 chain that admits perfect state transfer of any quantum state in a fixed period of time (see Subsec. 1.3.2 for details), when subjected to static internal imperfections [94]. Namely, we are interested in the robustness of this communication protocol in presence of

disorder both in the exchange couplings between the spins of the chain and in the local magnetic field. Since no dynamical control on the spin chain is required, decoherence is supposed to play a minor role, with respect to static imperfections in the engineered chain.

The structure of the chapter is the following: in Sec. 3.1 we introduce the communication spin-chain model we have explicitly studied, that is basically the protocol proposed by Christandl *et al.* in Ref. [30], perturbed with static imperfections in the exchange couplings and in the local magnetic field strengths of the spin chain Hamiltonian. We then analyze the fidelity of the transferred state (Sec. 3.2), and the level spacing statistics of the system Hamiltonian (Sec. 3.3). In Sec. 3.4 we take a closer look at the behavior of the fidelity as a function of time: the presence of static imperfections leads to a fractal temporal signal; its fractal dimension can be related to the amount of disorder present in the chain.

3.1 The model

As a model of static imperfections on the Hamiltonian hardware of the exact quantum communication protocol proposed in Ref. [30], we insert in the XY Hamiltonian of Eq. (1.14) a random perturbation both in the exchange couplings and in the local variations of the magnetic field. Namely, we consider a quantum spin 1/2 chain described by:

$$\hat{H} = \sum_{n=1}^{N} B_n \hat{\sigma}_n^z + \sum_{n=1}^{N-1} J_n \left(\hat{\sigma}_n^x \hat{\sigma}_{n+1}^x + \hat{\sigma}_n^y \hat{\sigma}_{n+1}^y\right). \tag{3.1}$$

The coefficients B_n and J_n are chosen such that:

$$B_n = b_n\,, \qquad\qquad J_n = J\sqrt{n(N-n)} \cdot (1+\delta_n) \tag{3.2}$$

where δ_n and b_n are random variables with uniform distribution in the intervals $\delta_n \in [-\epsilon_J, \epsilon_J]$ and $b_n \in [-\epsilon_B, \epsilon_B]$. Obviously, for $\epsilon_J = \epsilon_B = 0$, perfect state transfer is recovered at times $t_n = (2n+1)\pi/4J$, with n integer (see Subsec. 1.3.2 for details).

In the following, we study the sensitivity of the state transfer to the random perturbations (i.e., $\epsilon_J, \epsilon_B > 0$). In view of the possible applications with solid-state systems [42], we will also discuss a case of correlated disorder. Similar questions for quantum computation algorithms in realistic

modelizations of quantum computer hardware have been already analyzed in Refs. [20, 95]. In that case, the loss of efficiency of the algorithm was related to the appearance of quantum chaos in the quantum computer register. This relation has been characterized studying the *Level Spacing Statistics* (LSS) (see App. B for details). Following these lines we have considered the transition of the LSS of the spin chain in the presence of static imperfections. Even though it is not possible to frame this problem within the random matrix theory [96], we show that the LSS is still a convenient tool to describe the system efficiency in performing the state transfer. The presence of static imperfections leads to another clear signature of the modified properties of the spectrum in the fidelity. The degradation of the state transfer corresponds to the emergence of a fractal signal: the fidelity changes from a periodic function of time to a fractal time series. This behavior has the same origin as the one found in the probability densities of the quantum evolution in tight-binding lattices [97, 98].

3.2 Stability of the communication: fidelity

We first analyze the behavior of the optimal fidelity for the state transfer as a function of static imperfection strengths, averaged over N_{av} different disorder realizations. As we said in Subsec. 1.3.1, the fidelity $f(t) = \langle\psi|\,\rho_N(t)\,|\psi\rangle$ of the state $|\psi\rangle$ transfer along a chain which conserves the total spin z component, averaged over the initial state distributed uniformly over the Bloch sphere, is given by Eq. (1.13), that is:

$$f(t) = \frac{|g_N(t)|\cos\gamma}{3} + \frac{|g_N(t)|^2}{6} + \frac{1}{2}, \tag{3.3}$$

where $g_N(t) = \langle\mathbf{N}|\,e^{-i\hat{H}t}\,|\mathbf{1}\rangle$ is the transition amplitude of an excitation from the first to the last site; the phase factor $\gamma = \arg\{g_N(t)\}$ can be gauged away by a proper choice of the external field. An average over N_{av} different imperfection realizations is then performed, thus obtaining

$$\overline{f}(t) \equiv \langle f(t)\rangle_{\mathcal{D}is}\,. \tag{3.4}$$

We numerically solved the Schrödinger equation for the dynamical evolution and computed the fidelity of the rightmost spin with respect to the input state. In Fig. 3.1 we plot typical results of this evolution both for the ideal

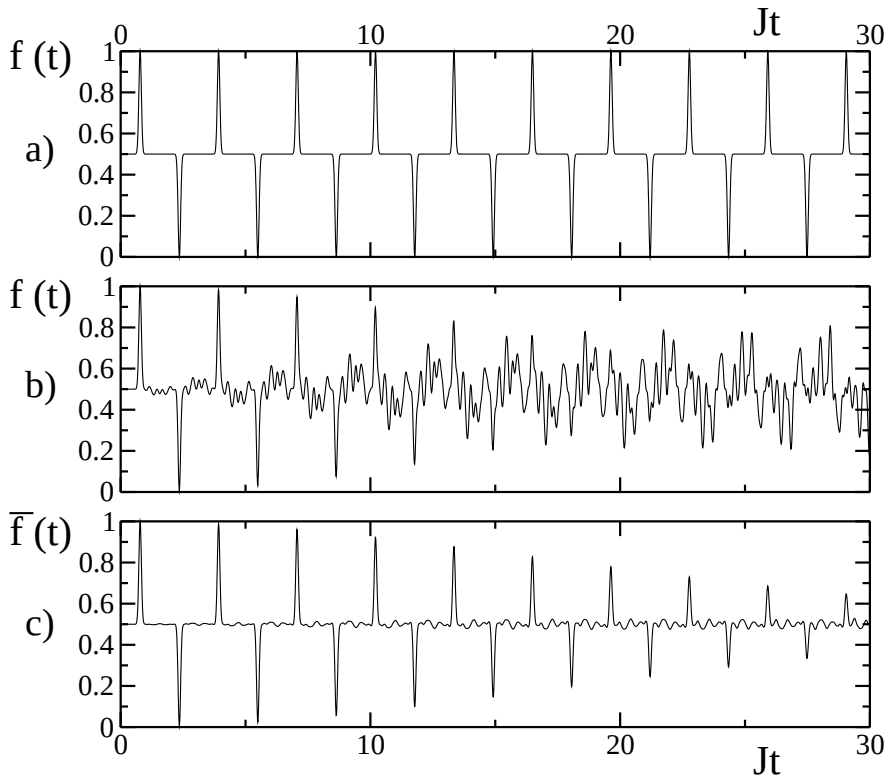

Figure 3.1: Fidelity of the N-th spin in a $N = 100$ chain as a function of time.
a) Without imperfections: $\varepsilon_J = \varepsilon_B = 0$.
b) With imperfections: $\varepsilon_J = 10^{-2}$, $\varepsilon_B = 0; N_{av} = 1$.
c) With imperfections: $\varepsilon_J = 10^{-2}$, $\varepsilon_B = 0$; averaged over $N_{av} = 10^2$ realizations.

case (Fig. 3.1A) and in presence of imperfections (Fig. 3.1B.). Figure 3.1C is the result of an average over different disorder realizations. In the presence of disorder the simple periodicity of the fidelity oscillation is lost. Moreover, the maximal value of the fidelity is less than unity (it is reached at slightly different time intervals, as compared to the ideal case). Thus the optimal time for state transfer should be inferred for each experimental sample. The original (in the ideal case) periodicity of the signal is recovered averaging over different disorder realizations, however, the maxima are progressively suppressed on increasing time. Therefore the optimal state transfer, in presence of imperfections, is obtained in correspondence of the first peak at time $t_1 = \pi/4J$.

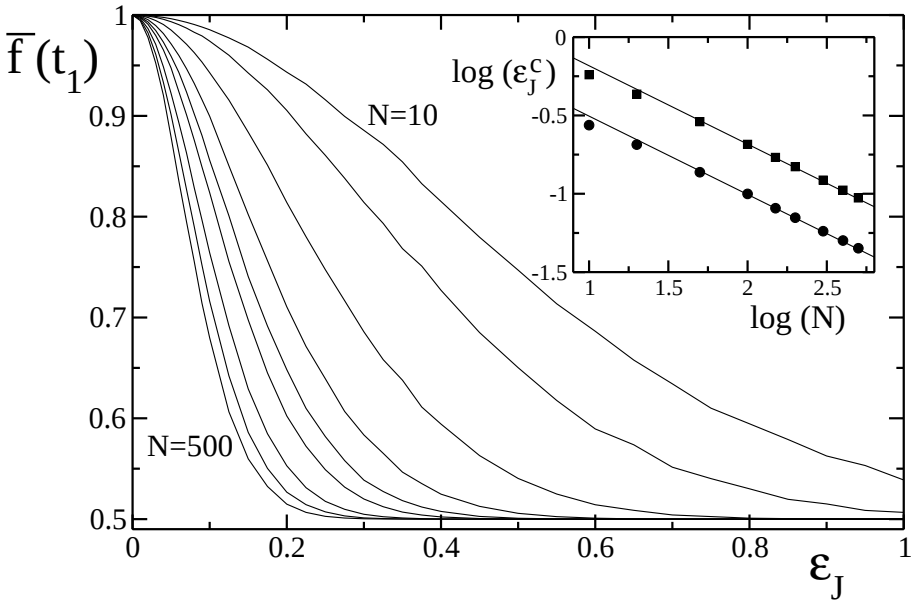

Figure 3.2: Averaged fidelity at time t_1 as a function of the disorder ε_J for different chain lengths and $\epsilon_B = 0$, $N_{av} = 10^3$. From right to left $N =$ 10, 20, 50, 100, 150, 200, 300, 400, 500. Inset: ε_J^c as a function of N obtained from the condition $\overline{f}(t_1) = 0.9$ (circles) and $\overline{f}(t_1) = 0.7$ (squares). Straight lines are proportional to $N^{-0.5}$. Here and in the following figures logarithms are decimal.

We now concentrate on the dependence of the optimal fidelity ($\overline{f}$ at time t_1) as a function of static imperfection strength and of the chain length. In Fig. 3.2 we plotted the fidelity as a function of ϵ_J for different chain lengths, assuming that there is no disorder in the local field ($\epsilon_B = 0$); the opposite situation, with disordered local magnetic field ($\epsilon_B \neq 0$) and ideal nearest neighbor interaction ($\epsilon_J = 0$) is shown in Fig. 3.3. These sources of disorder lead to a striking different behavior. While in the first case the error introduced by the imperfections increases with N, the effect of the disorder on local magnetic field decreases, becoming less effective on increasing the chain length. For completeness we also show the case where both ϵ_B and ϵ_J are different from zero in Fig. 3.4. The almost independence of the two effects can be traced back to the fact that the we are working in the sector with one spin up.

The behavior of the fidelity obeys a simple scaling law. We verified nu-

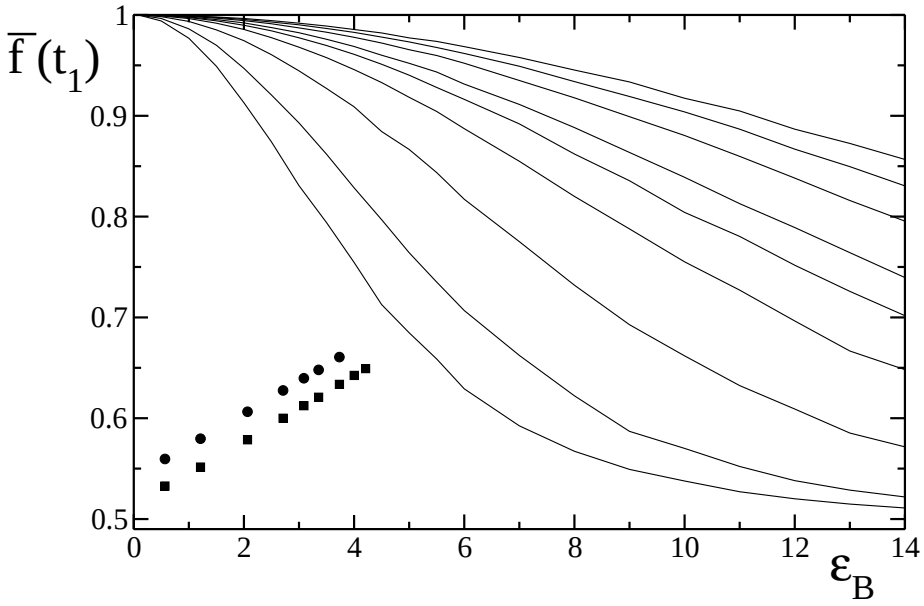
$\overline{f}(t_1)$
1
0.9
0.8
0.7
0.6
0.5
0
2
4
6
8
10
12
14
ε_B

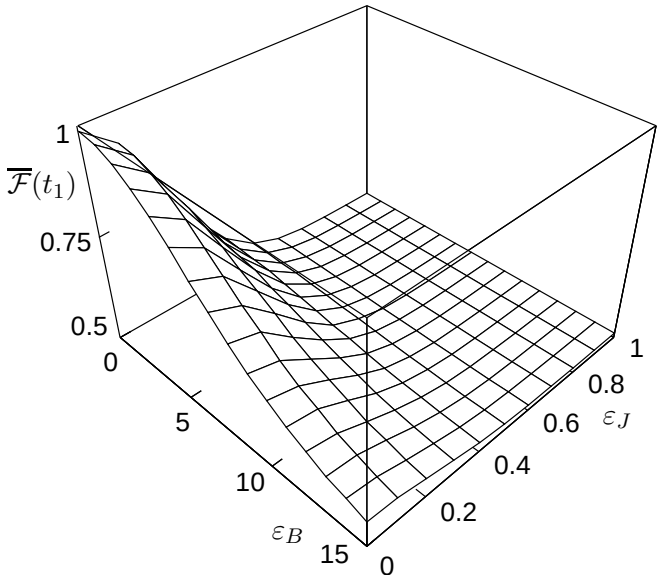

Figure 3.4: Average fidelity at time t_1 as a function of both amplitudes of the disorder ϵ_J, ϵ_B for a $N = 50$ spin network; $N_{av} = 100$.

The scaling given in Eq. (3.5) can be justified, in the limit of very small disorder, by means of perturbation theory: in the limit $\epsilon_J t, \epsilon_B t \ll 1$, the fidelity reads:

$$\overline{f}(t) \approx 1 - \frac{\varepsilon_B^2}{3} \sum_{k=1}^{N} \frac{2\,\mathrm{Re}[D_{k,k}(t)] - C_k^2(t)}{3} - \frac{\varepsilon_J^2}{3} \sum_{k=1}^{N} \frac{2\,\mathrm{Re}[F_{k,k}(t)] - E_k^2(t)}{3}\,. \quad (3.8)$$

The evaluation of the coefficients C_k, $D_{k,k}$, E_k, and $F_{k,k}$ is postponed to Subsec. (3.2.2).

Within our model of disorder, strong fluctuations of the exchange couplings lead to a degradation of the signal, while the same protocol is not very sensitive (especially for long chains) to fluctuations in the local magnetic fields: the disorder in the local magnetic field eventually averages out in the limit of infinite spin. In view of the little effect of random fields on the quantum communication over long chains, from now on we will consider only the effect of disordered exchange coupling between spins.

3.2.1 Correlated imperfections

The presence of spatial correlation in the disorder is a concrete possibility in experimental realizations of this protocol, as, for example, with Josephson-junction chains [41, 32]. We model correlated disorder as follows: the sign of any single δ_k (the error on the k-th coupling) is correlated with the previous one following the rule:

$$\begin{aligned} &\delta_i\delta_{i-1} > 0 \quad \text{with probability } \mathcal{P}, \\ &\delta_i\delta_{i-1} < 0 \quad \text{otherwise.} \end{aligned}$$

- 7.fΩ5.16001 -1.8 dΩ(0.Ω

3.2.2 Perturbation theory

We show here how to evaluate the fidelity $\overline{f}(t)$ of Eq. (3.4) averaged over different disorder realizations by means of a perturbation theory in ϵ_J, ϵ_B. Eq. (3.3) shows that $\overline{f}(t)$ depends only on the matrix element

$$\begin{aligned} g_N(t) &= \langle \boldsymbol{N}|e^{-i(\hat{H}+\hat{H}_I)t}|\mathbf{1}\rangle \\ &= \langle \boldsymbol{N}|e^{-i\hat{H}t}\mathcal{T}\left[\exp\left(-i\int_0^t dt\, e^{i\hat{H}t}\hat{H}_I e^{-i\hat{H}t}\right)\right]|\mathbf{1}\rangle \\ &= 1+\mathcal{O}(H_I)+\mathcal{O}(H_I^2) \end{aligned} \tag{3.10}$$

where $\mathcal{T}$ is the time ordered product, $\hbar = 1$, and $\hat{H}_I$ is the part of the Hamiltonian that describes the static imperfections b_n, δ_n. We first consider the case where $\delta_n = 0$, that is, only random local magnetic fields are present. We develop the time ordered product up to the second order in H_I. The first order term reads

$$\begin{aligned} \mathcal{O}(H_I) &= -i\int_0^t dt\, \langle \mathbf{1}|\, e^{i\hat{H}t}\hat{H}_I e^{-i\hat{H}t}\,|\mathbf{1}\rangle \\ &= -i\sum_{\ell=1}^N b_\ell \int_0^t dt(1-2|U_\ell^1(t)|^2) \equiv -i\sum_{\ell=1}^N b_\ell C_\ell(t), \end{aligned} \tag{3.11}$$

where $U_\ell^k(t) \equiv \langle \boldsymbol{\ell}|e^{-i\hat{H}t}|\boldsymbol{k}\rangle$ (explicit expressions for these matrix elements can be found in [46]). The second order is given by:

$$\begin{aligned} \mathcal{O}(H_I^2) &= -\int_0^t\int_0^t dt\, dt'\, \langle \mathbf{1}|e^{i\hat{H}t}\hat{H}_I e^{-i\hat{H}(t-t')}\hat{H}_I e^{-i\hat{H}t'}|\mathbf{1}\rangle \\ &= -\sum_{\ell=1}^N\sum_{m=1}^N b_\ell b_m \int_0^t\int_0^t dt\, dt' \Big[1-2\left|U_m^1(t)\right|^2 \\ &\quad -2\left|U_\ell^1(t')\right|^2 + 4U_m^{1*}(t)U_\ell^1(t')\sum_{k=1}^N U_m^k(t)U_k^{\ell *}(t')\Big] \\ &\equiv -\sum_{\ell=1}^N\sum_{m=1}^N b_\ell b_m D_{\ell,m}(t). \end{aligned} \tag{3.12}$$

The fidelity $\overline{f}(t)$ is given by the average over different disorder realization of the coefficient $g_N(t)$ and of its modulus square:

$$\begin{aligned} \overline{f(t)} &= \frac{1}{2} + \left\langle \frac{|g_N(t)|}{3} + \frac{|g_N(t)|^2}{6} \right\rangle_{\mathcal{D}} \\ &\approx 1 - \frac{\varepsilon_B^2}{3} \sum_{k=1}^{N} \frac{2\,\mathrm{Re}[D_{k,k}(t)] - C_k^2(t)}{3}. \end{aligned} \tag{3.13}$$

The case for $\delta_n \neq 0$ is obtained following the same steps; the final result is analogous to Eq. (3.8):

$$\overline{f}(t) = 1 - \frac{\varepsilon_B^2}{3} \sum_{k=1}^{N} \frac{2\,\mathrm{Re}[D_{k,k}(t)] - C_k^2(t)}{3} - \frac{\varepsilon_J^2}{3} \sum_{k=1}^{N} \frac{2\,\mathrm{Re}[F_{k,k}(t)] - E_k^2(t)}{3} \tag{3.14}$$

where the coefficients $E_k, F_{m,\ell}$ are given by

$$E_\ell = 4 \int_0^t dt\, \mathrm{Re}\left[U_\ell^1(t) U_{\ell+1}^{1*}(t)\right], \tag{3.15}$$

$$\begin{aligned} F_{m,\ell} &= 4 \int_0^t \int_0^t dt\, dt' \sum_{k=1}^{N} \left[U_m^{1*}(t) U_k^{m+1}(t) + U_{m+1}^{1*}(t) U_k^m(t)\right] \\ &\quad \times \left[U_\ell^{1*}(t') U_k^{\ell+1*}(t') + U_{\ell+1}^{1*}(t') U_k^{\ell*}(t')\right]. \end{aligned} \tag{3.16}$$

The effects of the two different kind of perturbations in Eq. (3.14), namely the local magnetic fields b_ℓ and the couplings δ_k, are decoupled because they fluctuate independently from each other.

3.3 Level spacing statistics

The behavior of the fidelity is essentially dictated by the time dependence of the amplitude $g_N = \langle \mathbf{N} | \, e^{-i\hat{H}t} \, | \mathbf{1} \rangle$ (see Eq. (3.3)). A deeper insight of its characteristics in disordered chains can be understood by analyzing the Statistics of the Level Spacing (LSS) of the spin-chain Hamiltonian in presence of disorder. Indeed this tool is widely used in the study of quantum perturbed systems with classically chaotic counterparts, especially in connection with the formalism of the Random Matrix Theory (see App. B for a brief introduction). Strictly speaking, the Hamiltonian of Eq. (3.1) cannot be considered as a random matrix, since it is tridiagonal; however, the

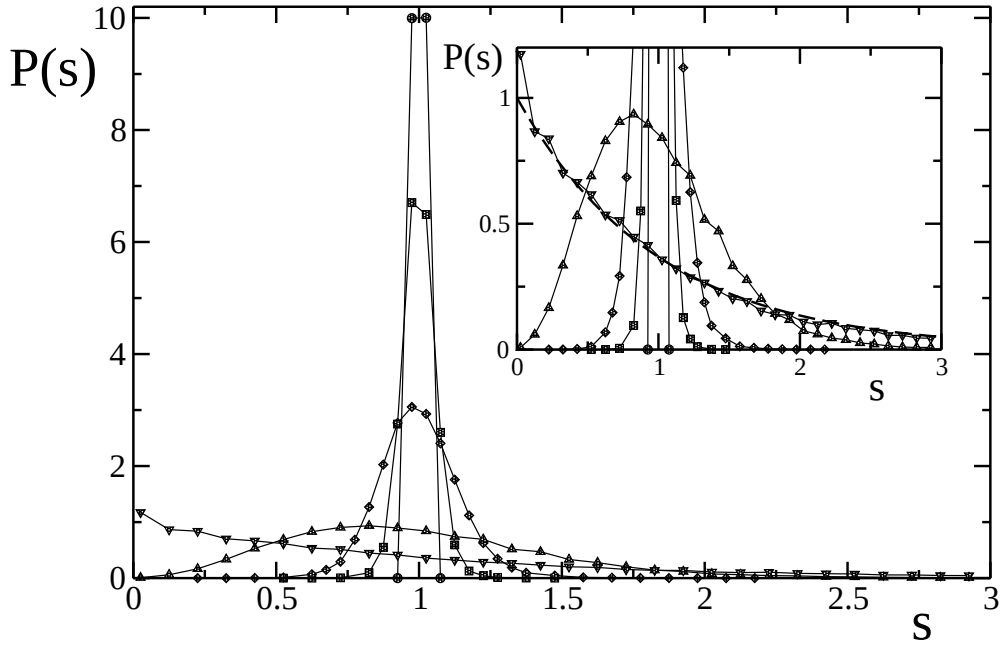

Figure 3.6: Level spacing statistics $P(s)$ for $N = 100$, $\epsilon_B = 0$, $N_{av} = 10^3$ and different values of ϵ_J: $\epsilon_J = 10^{-3}$ (circles), $\epsilon_J = 2 \times 10^{-2}$ (squares), $\epsilon_J = 5 \times 10^{-2}$ (diamonds), $\epsilon_J = 2 \times 10^{-1}$ (triangles up), $\epsilon_J = 1$ (triangles down). Inset: magnification of the same figure around $s = 1$. The dashed line corresponds to the Poissonian $P_P(s)$.

LSS can still be used to characterize the crossover that static imperfections induce in the spectrum of the Hamiltonian. Therefore this analysis helps in understanding the behavior of the disordered chain.

We recall that the Hamiltonian $\hat{H}$ of Eq. (3.1) is a tridiagonal matrix with zero entries on the diagonal, and $H_{k,k+1} = H_{k+1,k} = \lambda\sqrt{k(N-k)}$, where N is the chain length and λ a constant. Without any perturbation ($\epsilon_J = \epsilon_B = 0$) the energy levels are then equally spaced, while in presence of strong random perturbations ($|\epsilon_J| \sim 1$) its eigenvalues are completely uncorrelated. This crossover is detected by the level spacing statistics: it changes from a delta function P_D to a Poisson distribution P_P, given by the formulas:

$$P_D(s) = \delta(s-1) \quad \text{no disorder} \tag{3.17}$$

$$P_P(s) = \exp(-s) \quad \text{strong disorder.} \tag{3.18}$$

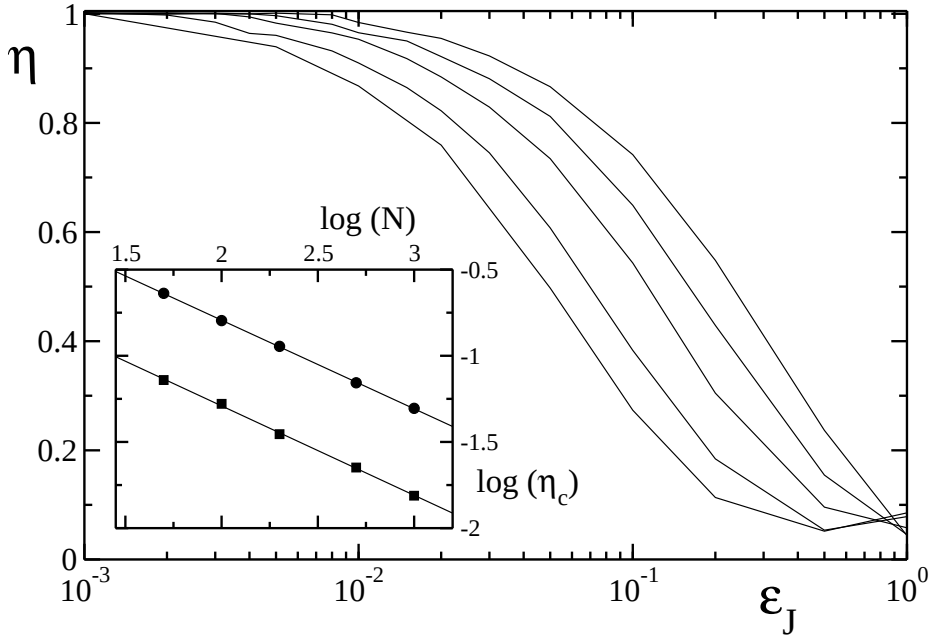

Figure 3.7: The parameter η as a function of the strength of the static imperfections ϵ_J. Different curves correspond to different spin chain length: from right to left $N = 50$, $N = 100$, $N = 200$, $N = 500$. We averaged over N_{av} disorder realizations with $N_{av} = 10^4$. Inset: scaling of the parameter η_c as a function of the chain length N obtained from the condition $\eta = 0.5$ (circles) and $\eta = 0.8$ (squares). Straight lines are proportional to $N^{-0.5}$.

Figure 3.6 shows this crossover: $P(s)$ changes from one limiting case to the other as a function of static imperfection strength. This crossover can be quantitatively characterized by the parameter:

$$\eta = \frac{\int_0^1 |P(s) - P_P(s)| ds}{\int_0^1 |P_D(s) - P_P(s)| ds} \,, \tag{3.19}$$

which varies from $\eta = 1$ (in the case of a delta function) to $\eta = 0$ (for a Poisson distribution) [95]. In Fig. 3.7 we show the dependence of η on the strength of the perturbation. The crossover starts at $\epsilon_J \sim 10^{-3} - 10^{-2}$, depending on the length of the chain. In the inset of Fig. 3.7 we report the dependence of the imperfection strength η_c at which the parameter η reaches a given constant value ($\eta = 0.5$, 0.8). The threshold η_c drops with the spin

length as

$$\eta_c \sim N^{-0.5} \ . \tag{3.20}$$

Thus it follows the same law found in the previous section regarding the fidelity of the state transfer, Eq. (3.6).

3.4 Fractal dimension of the fidelity

An interesting consequence of the modification of the spectrum, and hence of the fidelity, in presence of static imperfections emerges in the time dependence of the fidelity. In this section we will not look for the optimal time for the state transfer, but rather analyze its behavior as a function of time. It appears that the time signal of the fidelity has a fractal behavior.

In order to measure the fractal dimension of the signal, we used the modified box counting algorithm [99]. In the standard box counting algorithm the fractal dimension D of the signal is obtained by covering the data with a grid of square boxes of size L^2. The number $M(L)$ of boxes needed to cover the curve is recorded as a function of the box size L. The (fractal) dimension D of the curve is then defined as

$$D = -\lim_{L\to 0} \log_L M(L). \tag{3.21}$$

One finds $D = 1$ for a straight line, while $D = 2$ for a periodic curve. Indeed, for times much larger than the period, a periodic curve covers uniformly a rectangular region. Any given value of D in between of these integer values is a signal of the fractality of the curve. The modified algorithm of Ref.[99] follows the same lines but uses rectangular boxes of size $L \times \Delta_i$ (Δ_i is the largest excursion of the curve in the region L). Then, the number

$$M(L) = \frac{\sum_i \Delta_i}{L} \tag{3.22}$$

is computed (time boxes L are expressed in units of the exchange coupling J). For any curve, a region of box lengths $L_{\min} < L < L_{\max}$ exists where $M \propto L^D$. Outside this region one either finds $D = 1$ or $D = 2$: the first equality ($D = 1$) holds for $L < L_{\min}$ and it is due to the coarse grain artificially introduced by numerical simulations. The second one ($D = 2$) is obtained for $L > L_{\max}$ and it is due to the finiteness of the analyzed time series. The boundaries $L_{\min}, L_{\max}$ have to be chosen properly for any signal.

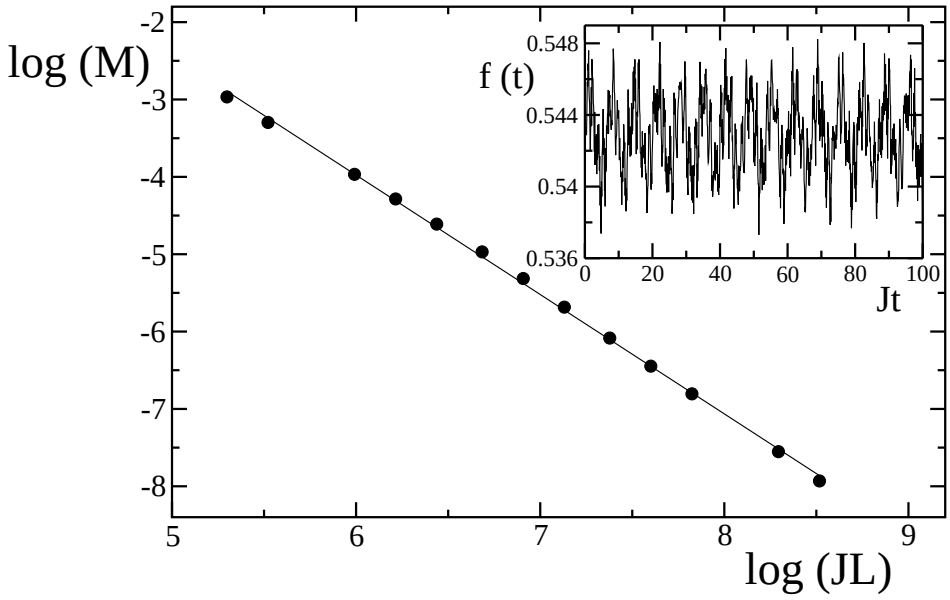

Figure 3.8: M as a function of the interval JL. A numerical fit gives a fractal dimension $D = 1.52$. Inset: temporal evolution of the fidelity up to time $T = 10^4/J$ in the presence of disorder for $\epsilon_J = 0.26$, $\epsilon_B = 0$, $N_{av} = 1$, $N = 500$.

We apply the modified algorithm to the signal of the fidelity for a single realization of disorder after a transient regime needed to reach the average value of $f = 0.5$; the inset of Fig. 3.8 shows a typical fluctuating signal, while Fig. 3.8 shows the numerically computed function $M(L)$ which gives a fractal dimension $D = 1.52$. It is natural to investigate the dependence of the fractal dimension with the static imperfection strengths: the results of numerical simulations are given in Fig. 3.9. The curve changes gradually its dimension from $D \approx 2$ (periodic curve) to $D = 1$ for very large imperfection strengths. This last result is due to the fact that for very large disorder the fidelity drops almost immediately to 0.5, corresponding to a complete loss of the initial state information (the fidelity remains constant, thus having dimension $D = 1$). However, the most general situation in presence of static imperfections is a fractal fidelity: defining, as before, a threshold of disorder strength D_c at which the fidelity has a given fractal dimension between two and one, we find that this threshold drops as

$$D_c \sim N^{-0.5} \, . \tag{3.23}$$

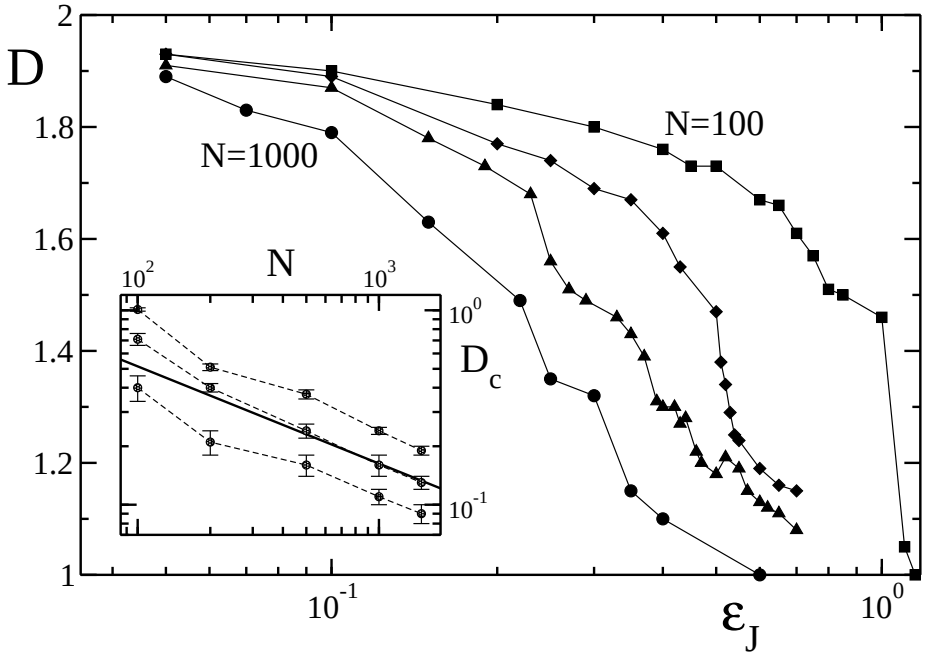

Figure 3.9: Fractal dimension D of the signal $f(t)$ as a function of the perturbation strength ϵ_J for $\epsilon_B = 0$, $N_{av} = 1$ and, from right to left, $N = 100$, 200, 500, 1000. The error on the fractal dimension is of the order of three percent. For $\epsilon_J < 5{\times}10^{-2}$ the error on D increases significantly as $L_{min} \lesssim L_{max}$. Inset: scaling parameter D_c as a function of the chain length N from the condition $D = 1.76$, 1.6, 1.4 (from bottom to the top). The full straight line is proportional to $N^{-0.5}$.

This behavior is shown in the inset of Fig. 3.9 and follows exactly the same scaling as the parameters η_c and ϵ_J^c (Eqs. (3.6) and (3.20)).

The fact that the three distinct critical thresholds follow the same scaling as a function of the chain length and imperfection strength, independently from the chosen critical value, reflects the profound changes in the quantum system induced by the presence of static imperfections. The threshold drops as the square root of the chain length: this is a behavior similar to the one found in Ref. [20] in a different system, where it was a consequence of the two-body nature of the interactions. Here, the dependence is mainly due to the fact that the system is confined to the subspace of one excitation. The conclusion of this analysis is that it is possible, at least in principle, to tolerate or correct errors introduced by static imperfections.

Chapter 4

Information Transfer Rates in Spin Chains

Apart from unavoidable experimental imperfections, which inevitably reduce the fidelity of the state transfer, even the theoretical analysis of quantum communication spin-chain channels may be problematic, because of the dispersive nature of the information propagation [34, 29]. The protocol proposed in Ref. [30], whose stability has been studied in the previous chapter, represents an exception, since, in that case, the system dynamics can be seen as a simple rotation of a fictitious spin (see Sec. 1.3.2). Without using Hamiltonians engineered *ad hoc*, or complex encoding and decoding operations, Bob is generally not able to perfectly recover Alice's information, due to the dispersive free evolution of the chain. Therefore, on one hand, dispersion does not permit a sharp definition of transmission times; on the other hand, it is also responsible for the presence of feedback and memory effects in the quantum communication [100]: part of the information previously injected by Alice into the chain typically interferes with subsequent data sent. Nevertheless, in some cases it is possible to evaluate the transmission rates even in presence of such memory effects [101].

In this chapter we analyze the performances of communication protocols along unmodulated spin chains. By studying the asymptotic number of qubits transmitted per second, we show that efficient mechanisms of information transfer can be devised by carefully exploiting the dispersive dynamics of the chain. In Sec. 4.1 we introduce a prototypical class of spin chain communication protocols in which a single quantum channel is used in order to admit multiple-qubit transfer in time between two distant parties. In Sec. 4.2

we focus on the simplest not-trivial solvable case: a chain with only two intermediate spins. We show that, despite the fact that a two-spin channel can act as a simple swapper, thus making it possible to obtain a perfect state transfer from Alice to Bob, the maximum achievable transfer rate is not obtained in correspondence of perfect transfer. In Sec. 4.3 instead we analyze numerically the case of arbitrarily long chains: here a lower bound on the maximum attainable communication rates is provided by using the dual-rail protocol of Ref. [36].

4.1 Spin channel for multiple qubit communication

The spin communication channel we consider is an array C of N permanently coupled spin 1/2 that interact through an Hamiltonian $\hat{H}$. The total spin component $\hat{S}_z$ of the system is supposed to be a constant of motion. The chain C constitutes the physical channel along which quantum information is transmitted. As shown in Fig. 4.1, we assume that the sender (Alice) and the receiver (Bob) of the messages have access to two distinct subsets C_A and C_B of the spins of the chain (typically the first and the last spin) and to two distinct sets of ancillary qubits (i.e. Alice's memories $A \equiv \cdots A_3\ A_2\ A_1$ and Bob's memories $B \equiv B_1\ B_2\ B_3\ \cdots$). Such subsets and memories are used to "write" and "read" the information into and from the chain, and constitute areas of *complete control* for the communicating parties (namely Alice has total control on $A + C_A$, while Bob has total control on $B + C_B$).

In the communication scenario we are considering here the spins of the chain and Bob's memories B are initially set up in the $\hat{\sigma}_z$ "down" state $|0\rangle \equiv |\downarrow\rangle$ (analogously we indicate the $\hat{\sigma}_z$ "up" vector with $|1\rangle \equiv |\uparrow\rangle$). On the other hand Alice's memories A are in some (possibly entangled) input states $|\Psi\rangle_A$ which encode the information she wants to transmit. At time $t = 0$ the global state of the composite system $A + C + B$ is thus

$$|\Psi\rangle_A \otimes |\mathbf{0}\rangle_C \otimes |\mathbf{0}\rangle_B \ , \tag{4.1}$$

which is an eigenstate of the Hamiltonian of the chain $\hat{H}$. Ideally, Alice's and Bob's goal is to transform (4.1) into the state

$$|\mathbf{0}\rangle_A \otimes |\mathbf{0}\rangle_C \otimes |\Psi\rangle_B \ , \tag{4.2}$$

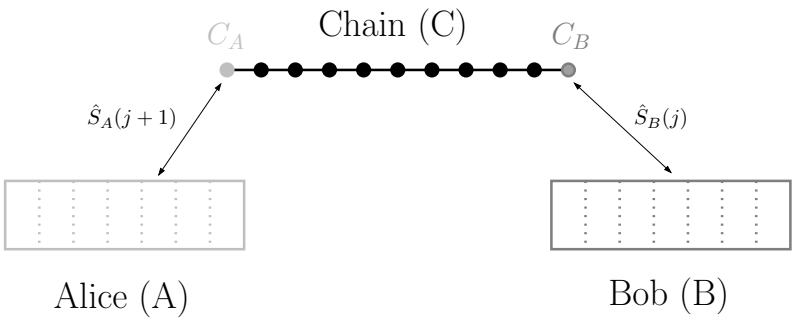

Figure 4.1: Communication scenario. Alice (A) and Bob (B) control their memory, and have access respectively to the first and the last qubit of the chain (C). The intermediate spins of the chain act as a quantum channel for quantum communication between Alice and Bob. At regular time intervals both Alice and Bob perform a SWAP gate between one of her/his memory qubit and the spin of the chain to whom each of them has access. During the time between two consecutive swaps the chain is let freely evolve, according to the Hamiltonian $\hat{H}$.

by performing local operations on $A+C_A$ and $B+C_B$ and by cleverly exploiting the transport properties of the chain free evolution. In this context the efficiency of the communication can be characterized through the transmission rate r of the protocol. This is an asymptotic quantity which describes the maximum number of qubits one can transfer per unit of time with average fidelity converging to 1 in the limit of large transmission times (see for instance Refs. [100]). However, we will mostly focus on protocols for which the average time T it takes to pass from (4.1) to (4.2) is a finite quantity. In this case r is given by

$$r = M/T \ , \tag{4.3}$$

where M is the number of qubits encoded into the states $|\Psi\rangle_A$ of Eq. (4.1). In what follows, T will be computed by considering only the spin chain free evolution, thus neglecting the time intervals employed by Alice and Bob to perform their local operations. This is legitimate by the fact that in the model the only dynamical constraint is imposed by $\hat{H}$.

Even in the ideal case when the coupling with the environment and the presence of imperfections is neglected, the evaluation of the transmission rate of Eq. (4.3) is typically complicated by the dispersive free evolution of the

chain [29, 34, 36, 37, 38, 102]. To better understand this point, it is sufficient to focus on the case in which $|\Psi\rangle_A$ is a separable vector of the form

$$|\Psi\rangle_A = |\cdots\ \psi_3\ \psi_2\ \psi_1\rangle_A \tag{4.4}$$

where the j-th memory element of Alice's memory is initialized in $|\psi_j\rangle_{A_j} \equiv \alpha_j|0\rangle_{A_j} + \beta_j|1\rangle_{A_j}$. Suppose now that Alice starts the transfer protocol at time $t = 0$ by coupling her first memory element A_1 with the chain spin C_A through an instantaneous SWAP gate [1] $\hat{S}_A(1)$. This resets the memory element A_1 to $|0\rangle_{A_1}$ while "copying" its initial state into the first chain element, i.e.

$$|\mathbf{\Psi\, 0\, 0}\rangle_{ACB} \rightarrow |\cdots\ \psi_3\, \psi_2\, 0\rangle_A \otimes \Big[\alpha_1\, |00\cdots 0\rangle_C + \beta_1\, |10\cdots 0\rangle_C\Big] \otimes |\mathbf{0}\rangle_B\,. \tag{4.5}$$

The system then evolves freely for a time interval τ in order to allow the "perturbation" ψ_1 introduced locally by Alice in C_A to spread along the whole chain. Since the Hamiltonian $\hat{H}$ commutes with $\hat{S}_z$, the state (4.5) becomes [29]:

$$|\cdots\psi_3\psi_2 0\rangle_A \otimes \left(\ \alpha_1|\mathbf{0}\rangle_C + \beta_1 \sum_{n=1}^{N} \gamma_{1n}(\tau)|\mathbf{n}\rangle_C\ \right) \otimes |\mathbf{0}\rangle_B\,, \tag{4.6}$$

where $|\mathbf{n}\rangle_C$ is the state of the chain with all spins down but the n-th, and

$$\gamma_{1n}(\tau) = {}_C\langle \mathbf{n}|e^{-i\hat{H}\tau}|\mathbf{1}\rangle_C \tag{4.7}$$

is the probability amplitude of finding the spin up in the n-th chain location. By applying the instantaneous SWAP gate $\hat{S}_B(1)$ which couples his first memory B_1 and the last chain element C_B, Bob has now a chance to transfer Alice's information into B. If the chain Hamiltonian $\hat{H}$ is engineered such that there exists a certain time τ_* at which the amplitude $\gamma_{1N}(\tau_*)$ is unitary [30, 31] (i.e. $\gamma_{1N}(\tau_*) = e^{i\varphi_*}$), then the excitation sent by Alice has been perfectly traveled to the spin C_B. Bob can thus safely transfer the exact state ψ_1 into B_1 with a simple swap operation, followed by a proper phase shift gate on B_1 to compensate $e^{i\varphi_*}$. This process can be iterated to the remaining memories A: at the j-th run Alice will move the memory A_j into the chain by means of the SWAP $\hat{S}_A(j)$ which couples A_j with C_A while, after a time interval τ_*, Bob will extract it from C by applying the SWAP $\hat{S}_B(j)$ which couples B_j with C_B. Assuming perfect timing, the scheme guarantees the transfer of one qubit every τ_* seconds, yielding a rate (4.3) equal to $1/\tau_*$.

Unfortunately, for a generic Hamiltonian $\hat{H}$ and time τ the amplitude $\gamma_{1N}(\tau)$ is not unitary; in this case Bob's SWAP will not succeed in perfectly extracting Alice's information ψ_1 out of the chain. The excitation which codifies ψ_1, that has been previously put into the chain, is in general spread out over all the sites of the chain. Therefore, at each run only a fraction of Alice's information is transferred in B: the rest remains into the chain and has a chance of interfering with the subsequent operations of the communicating parties. In particular, every time Alice couples her memories with the chain, there is a finite probability that part of the information which was previously injected into C, will re-enter into A. In this case she will never send it back through the chain, so that Bob will never be able to reconstruct the state with perfect fidelity. The net result is the arising of memory effects [100] in the communication which require a proper handling.

4.2 Two-spins chain channel

In this section we focus on the simplest non trivial spin channel model. It is given by a chain C of only $N = 2$ spins, the first being controlled by Alice and the second by Bob. We will see that, despite its simplicity, the model retains sufficient structure to permit the analysis of memory effects. In particular it will allow us to compare the transmission rates of protocols which exploit memory effects with protocols which do not.

4.2.1 Plain scheme

We begin by considering a communication scheme where, every τ seconds, Alice and Bob simultaneously[1] perform sequences of SWAPs operations which couple the A memories with C_A and the B memories with C_B (namely, at the j-th step they both apply $\hat{S}_A(j)$ and $\hat{S}_B(j-1)$, respectively). This is the simplest approach, in which the communicating parties try to squeeze their messages through the chain by repetitively tempering with it, without taking into account its internal dynamics. After m steps the global state of the system is described by the vector

$$\hat{\mathcal{W}}_m|\Psi\,\mathbf{0}\,\mathbf{0}\rangle_{ACB}\ , \tag{4.8}$$

[1]Simultaneity between Alice and Bob operations and the assumption of having uniform time intervals are not fundamental in our analysis: these hypotheses are considered only to simplify the problem and to compact the notation.

where $\hat{\mathcal{W}}_m$ is the unitary transformation

$$\hat{\mathcal{W}}_m = \hat{S}_B(m-1)\,\hat{S}_A(m)\,\hat{U}\cdots\hat{S}_B(2)\,\hat{S}_A(3)\,\hat{U}\,\hat{S}_B(1)\,\hat{S}_A(2)\,\hat{U}\,\hat{S}_A(1)\,, \quad (4.9)$$

with $\hat{U} \equiv e^{-i\hat{\mathcal{H}}\tau}$. Consequently the reduced density matrix of Bob's memories can be expressed as

$$\rho_B(m) = \mathrm{Tr}_{AC}\Big[\,\hat{\mathcal{W}}_m\,\Big(\,|\Psi\,\mathbf{0}\,\mathbf{0}\rangle_{ACB}\langle\Psi\,\mathbf{0}\,\mathbf{0}|\,\Big)\,\hat{\mathcal{W}}_m^{\dagger}\,\Big]\,. \quad (4.10)$$

Despite the complexity of the correlations introduced by the concatenated SWAPs, for $N = 2$ Eq. (4.10) can be reduced to a tensor product form $\mathcal{D}_\eta^{\otimes m}(|\Psi\rangle\langle\Psi|)$, for which standard memoryless quantum channel analysis [103] can be used to compute the rate (4.3). Here $\mathcal{D}_\eta$ denotes the single qubit amplitude damping channel map [1, 29, 102], that is defined by the two Kraus operators

$$\hat{M}_0 = \begin{pmatrix} 1 & 0 \\ 0 & \sqrt{\eta} \end{pmatrix}\,, \quad \hat{M}_1 = \begin{pmatrix} 0 & \sqrt{1-\eta} \\ 0 & 0 \end{pmatrix}\,, \quad (4.11)$$

with $0 \le \eta \le 1$ (see Sec 1.4.1). Suppose indeed that Alice's memories A have been prepared in the separable state form of Eq. (4.4). From Eq. (4.8) one obtains

$$\sum_{j_1\ldots j_m=0}^{1} \bar{\beta}_1^{j_m}\ldots\bar{\beta}_n^{j_1}|j_m\ldots j_1\rangle_A \otimes |\psi_{m+1}0\rangle_C \otimes |\tilde{\psi}_1^{(j_1)}\ldots\tilde{\psi}_m^{(j_m)}\rangle_B\,, \quad (4.12)$$

where $\bar{\beta}_k = \beta_k\,\gamma_{11}(\tau)$, and

$$|\tilde{\psi}_k^{(j_k)}\rangle = \begin{cases} |0\rangle & \text{if} \quad j_k = 1 \\ |\psi_k'\rangle \equiv \alpha_k|0\rangle + \beta_k\gamma_{12}(\tau)|1\rangle & \text{if} \quad j_k = 0 \end{cases}\,,$$

with $\gamma_{11}(\tau)$ and $\gamma_{12}(\tau)$ defined as in Eq. (4.7) and satisfying the constraint $|\gamma_{11}(\tau)|^2+|\gamma_{12}(\tau)|^2 = 1$. From (4.12) we notice that, at each time after having applied the two SWAP operations, the chain is always disentangled from Alice and Bob memories. This permits to express Eq. (4.10) as a product of m amplitude damping channels $\mathcal{D}_\eta$, with quantum efficiency $\eta = |\gamma_{12}(\tau)|^2$ equal to the transfer probability of one excitation from the first to the second spin of the chain. Indeed, neglecting a phase shift component that can always be compensated by Bob through a local operation on B, one has

$$\rho_B(m) = \bigotimes_{k=1}^{m}\Big(|\bar{\beta}_k|^2\,|0\rangle\langle 0| + |\psi_k'\rangle\langle\psi_k'|\Big) = \bigotimes_{k=1}^{m}\mathcal{D}_\eta\left(|\psi_k\rangle_{A_k}\langle\psi_k|\right)\,. \quad (4.13)$$

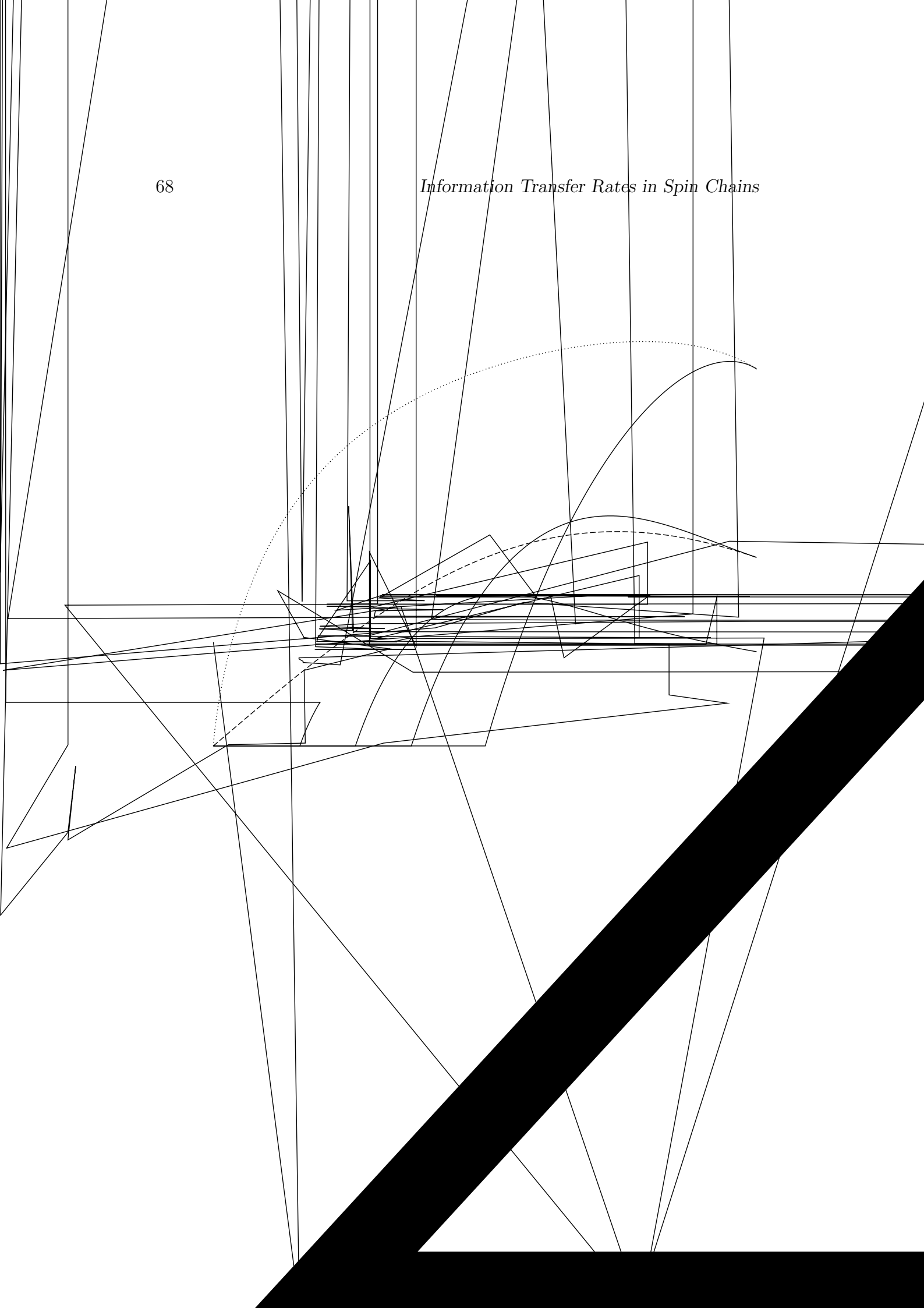

Exploiting the linearity of Eq. (4.10) this identity can then be generalized to all (non necessarily separable) input states $|\Psi\rangle_A$.

The transmission rate (4.3) associated with the protocol in Eq. (4.9) can be now easily computed by considering the quantum channel capacity [103] of the memoryless channel map $\mathcal{D}_\eta$. This has been derived in Ref. [102]: it is null for $\eta \leqslant 0.5$ and equal to

$$Q(\eta) = \max_{p\in[0,1]} \{H_2(\eta p) - H_2\left((1-\eta)p\right)\} \tag{4.14}$$

otherwise (here $H_2(x) = -x\log_2 x - (1-x)\log_2(1-x)$ is the binary entropy function). Equation (4.14) gives the maximum number of qubits which can be reliably transmitted per use of the channel $\mathcal{D}_\eta$ in the asymptotic limit of $m \gg 1$ uses. Considering that in a time interval $T = m\,\tau$ the protocol (4.10) accounts for m uses of the $\mathcal{D}_\eta$, we can estimate its rate as follows:

$$r \equiv \lim_{m\to\infty} \frac{m\,Q(\eta)}{m\,\tau} = \frac{Q(\eta)}{\tau}\,. \tag{4.15}$$

It should be stressed that the possibility of achieving the rate (4.15) relays on the identification of an optimal encoding space [103] which, in the general case, requires infinitely many uses of the map $\mathcal{D}_\eta$ (i.e. infinitely long transmission time). In this respect, Eq. (4.15) should be considered more as an indication of the efficiency of the protocol (4.10) rather than a realistic communication rate of the chain.

In order to provide an explicit expression for the rates (4.15), we consider the $\hat{S}_z$-preserving spin chain Hamiltonian of the form

$$\hat{H} = J(\hat{\sigma}_1^x\hat{\sigma}_2^x + \hat{\sigma}_1^y\hat{\sigma}_2^y) + \Delta\,\hat{\sigma}_1^z\hat{\sigma}_2^z\,, \tag{4.16}$$

for which the excitation transfer amplitude is just a sinusoidal periodic function of τ of period $\pi/(2J)$, i.e.

$$\eta = |\gamma_{12}(\tau)|^2 = \sin^2(2J\,\tau)\,. \tag{4.17}$$

For $\tau = \tau_* \equiv \pi/(4J)$ the free evolution operates a SWAP between the spins, thus achieving perfect transmission of a generic quantum state. Correspondingly in this case the quantum capacity (4.14) of the channel is optimal and equal to one, while the rate (4.15) is $1/\tau_*$. Given the periodicity of Eq. (4.17), for $\tau > \tau_*$ the rate (4.15) can never be higher than this quantity. However,

there exists a value $\tau_{\max} < \tau_*$ such that $r(\tau_{\max}) > r(\tau_*)$ (see Fig. 4.2): i.e. τ_* is not the optimal time transfer for the plain scheme (4.10). Notice also that the quantum capacity of the amplitude damping channel is strictly zero for $\eta \leqslant \eta_c = 0.5$, thus meaning that for $\tau \leqslant \tau_0 \equiv \pi/8J$, the channel does not transmit any quantum information.

In order to reduce the time τ_0, a slightly different version of the protocol can be implemented, in which we suppose that Bob has at his disposal n additional memories for each qubit that Alice sends. The protocol goes on exactly as before, except that, after each double swap, (performed from both Alice and Bob) Bob runs n additional SWAP operations at regular time intervals τ. The unitary transformation in Eq. (4.9) then modifies into:

$$\begin{aligned} \hat{\mathcal{W}}_m &= \left[\hat{S}_B(m_n)\hat{U}\cdots\hat{S}_B(m_1)\hat{U}\right]\hat{S}_A(m)\,\hat{U}\cdots \\ &\quad \cdots\left[\hat{S}_B(2_n)\hat{U}\cdots\hat{S}_B(2_1)\hat{U}\right]\hat{S}_A(2)\,\hat{U}\cdot \\ &\quad \cdot\left[\hat{S}_B(1_n)\hat{U}\cdots\hat{S}_B(1_1)\hat{U}\right]\hat{S}_A(1)\,. \end{aligned} \tag{4.18}$$

In this way Bob can enhance the transfer fidelity [38], at the price that both time and memory requirements are increased by a factor n for each qubit sent by Alice. The capacity of such a channel can be evaluated exactly as before, except that the quantum efficiency η is now dependent of n, and it is given by:

$$\eta_n \equiv \sum_{k=0}^{n} |\gamma_{11}(\tau)|^{2k}|\gamma_{12}(\tau)|^2 = 1-(1-\eta)^{n+1}\,, \tag{4.19}$$

where $\eta = |\gamma_{12}(\tau)|^2$ is the quantum efficiency for $n = 0$. In Fig. 4.2 we plotted the corresponding quantum transmission rates as a function of the time between two successive swaps τ for different values of n. Notice that the time τ_0 is reduced, as one increases n.

4.2.2 Exploiting the internal dynamics of the chain

In this section we show how memory effects induced by the free evolution of the chain can be exploited in order to simplify encoding and decoding procedures. In particular, differently from the cases discussed in the previous section, the schemes analyzed here allow one to achieve optimal transmission rate by encoding the information in only a finite number of memory elements.

The simplest version of these new classes of protocols is a variation of the *dual-rail encoding* of Ref. [36]. The idea is to assume that Alice uses her

first two memory qubits (i.e. A_1 and A_2) to codify a single information qubit $|\psi\rangle = \alpha|0\rangle + \beta|1\rangle$, while keeping the third memory element into the reference state $|0\rangle_{A_3}$, i.e., following the notation of Eq. (4.4),

$$|\psi\rangle \to \alpha|010\rangle_A + \beta|001\rangle_A \,. \tag{4.20}$$

As in the plain scheme, every τ seconds Alice and Bob are then required to perform a sequence of SWAPs gates between their memories and the chain. In this case however, we will show that after the second SWAP by Bob (i.e. after the third SWAP by Alice) a simple magnetization measurement on their memories allow both the communicating parties to establish, independently, whether the state $|\psi\rangle$ has been exactly transmitted to Bob, or it has returned to Alice's memory. Indeed, assume that at $t = 0$ the global system is in the state

$$\big(\alpha|010\rangle_A + \beta|001\rangle_A\big) \otimes |00\rangle_C \otimes |00\rangle_B \,. \tag{4.21}$$

After the first two SWAPs of Bob and the first three SWAPs of Alice (i.e. after 2τ seconds from the beginning of the transmission), it is transformed into a superposition where with probability $|\gamma_{11}(\tau)|^2$ the information has been returned into A (encoded in A_3A_2), while with probability $|\gamma_{12}(\tau)|^2$ the information has been moved into B (encoded in B_1B_2), i.e.

$$\begin{aligned} &\gamma_{11}(\tau)\,\big(\alpha|100\rangle_A + \beta|010\rangle_A\big) \otimes |00\rangle_C \otimes |00\rangle_B \\ &+ \gamma_{12}(\tau)\,|000\rangle_A \otimes |00\rangle_C \otimes \big(\alpha|10\rangle_B + \beta|01\rangle_B\big)\,. \end{aligned} \tag{4.22}$$

These two possibilities can be distinguished by Alice and Bob by performing independent magnetization measurements on their respective memories B and A. For instance, the first possibility (i.e. information in A) will yield, respectively, the outcome 0 (null total magnetization of B) and 1/2 (a single spin up in A) for Bob and Alice measurements. Analogously, when the information is in B the measurements will yield, respectively, the outcome 1/2 and 0. In the latter case the communicating parties can proceed by sending another qubit (encoded by Alice in $A_6A_5A_4$ and received by Bob in B_3B_4), while in the former case, first the information is locally moved back from A_3A_2 into A_2A_1 and the protocol is repeated until Bob is certain to receive the state. The iteration of this procedure is trivial.

To compute the transmission rate of this communication scheme we note that the probability that Bob will receive Alice's state $|\psi\rangle$ exactly at the j-th

iteration of the protocol is $P_j = |\gamma_{12}(\tau)|^2 \, (1-|\gamma_{12}(\tau)|^2)^{j-1}$. The average time required to transfer the qubit is then:

$$T = \sum_{j=1}^{+\infty} 2\tau j P_j = \frac{2\tau}{|\gamma_{12}(\tau)|^2} \, , \tag{4.23}$$

from which we get

$$r = \frac{1}{T} = \frac{|\gamma_{12}(\tau)|^2}{2\tau} \, . \tag{4.24}$$

Assuming that the transferring spin chain C is described by the Hamiltonian in Eq. (4.16), this expression has been plotted in Fig. 4.2 (dashed line) for a comparison with the protocols of the previous section. Notice that, for $\tau \leqslant \tau_0$, contrary to the standard plain encoding, the transmission rate is not zero; the maximal transfer rate however is achieved with a standard encoding.

Alice and Bob can use slightly more complicated types of encodings, in order to optimize the transfer rate. For instance Alice can fix the number E of excitations she employs to codify her input qubit messages in $\mathcal{N}$ spins of A. The case discussed before corresponds to $E = 1$, $\mathcal{N} = 2$; the generalization to a generic number of spins, with $E = 1$ fixed, is trivial: Alice can send a number $\log_2(\mathcal{N})$ of qubits, provided she employs $\mathcal{N} + 1$ memories (the extra memory play the same role of A_3 in the simple version of the scheme). The protocol then proceeds exactly as before, where Bob swaps on his $\mathcal{N}$-states memory. He then has to measure the magnetization at every time interval $\mathcal{N}\tau$. The success probabilities P_j are the same as before, while the transfer rate is then given by:

$$r = \frac{|\gamma_{12}(\tau)|^2 \, \log_2 \mathcal{N}}{\mathcal{N}\tau} \, . \tag{4.25}$$

The case $E = 2$ is slightly more complicated by the fact that, after a time $\mathcal{N}\tau$, Bob can measure two excitations with probability $|\gamma_{12}(\tau)|^4$ (in that case he has perfectly received the state), no excitations with probability $|\gamma_{11}(\tau)|^4$ (the state has perfectly returned to Alice, therefore they have to restart the protocol), or one excitation. In this last case, only one excitation is returned to Alice and she has then to retransmit it, by using the same procedure for $E = 1$ described before. It can be shown that the transfer rate for the case $E = 2$ is given by:

$$r = \frac{\log_2 \binom{\mathcal{N}}{2}}{\mathcal{N}\tau} \cdot \frac{(1 - |\gamma_{11}(\tau)|^4)^2}{1 - |\gamma_{11}(\tau)|^4 + 2|\gamma_{11}(\tau)|^2 - 2|\gamma_{11}(\tau)|^6} \, . \tag{4.26}$$

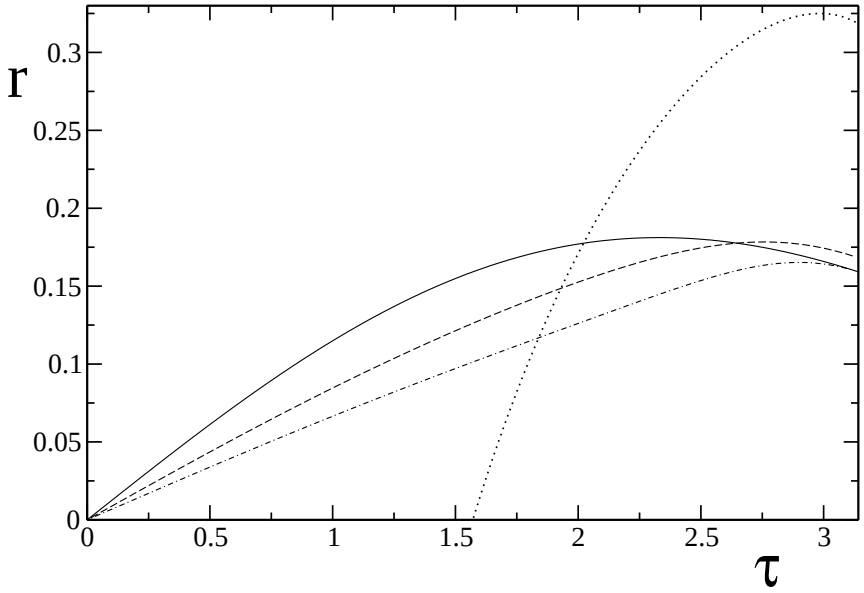

Figure 4.3: Quantum transmission rates for a two-qubit channel driven by Hamiltonian in Eq. (4.16) with $J = 1/4$ for different qubit encodings: standard encoding (one spin per qubit, dotted line), one qubit in two spins (full line), two excitations in three spins (dashed line), three excitations in four spins (dotted-dashed line).

Similar expressions for the transfer rate with higher E can be obtained. The only difference is that an increasing number of possibilities appears: after a time $\mathcal{N}\tau$, Bob can receive a number of excitations $E_B \leqslant E$, consequently a number $E_A = E - E_B$ of excitations return to Alice. According to the value of E_A, she then has to apply a sub-protocol for the transfer of E_A excitations, with $E_A \leqslant E$. This procedure has to be iterated until $E_B = E$.

In Fig. 4.3 we show the theoretical values of the transmission rates in a two-qubit channel for different values of E and $\mathcal{N}$, as a function of the time τ (continuous lines); the asymptotic rate for the standard encoding, Eq. (4.15), is also shown for reference. Moreover we have explicitly simulated these types of communication protocols between Alice and Bob with a standard Monte Carlo numerical technique. To this end, an instantaneous transmission rate $r(t)$ can be defined as the ratio between the number of transmitted qubits M until time t and the actual transmission time t. The value of M has been evaluated stochastically, following the theoretical probability distributions P_j

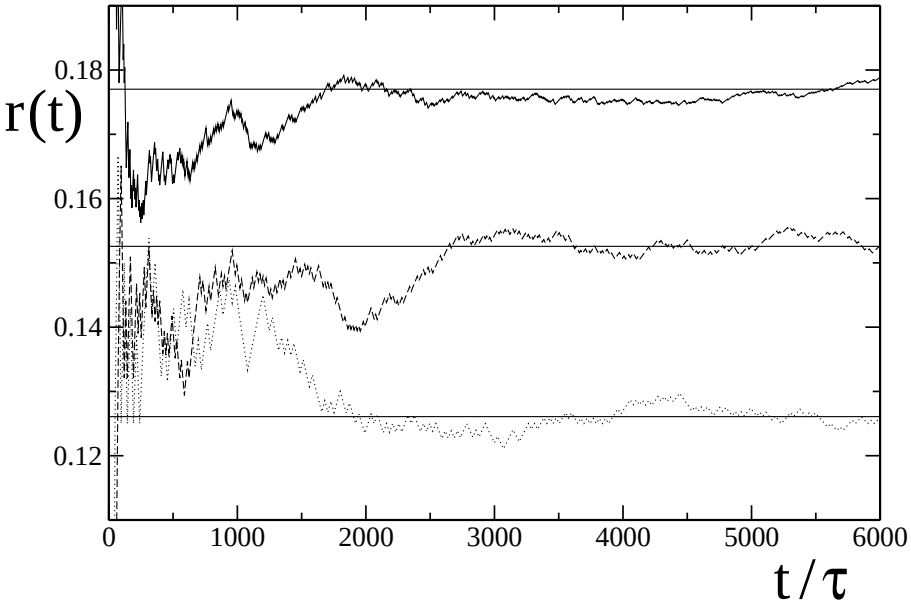

Figure 4.4: Instantaneous quantum transmission rates for a two-qubit channel described by the Hamiltonian in Eq. (4.16) with $J = 1/4$ for $\tau = 2$. The various curves correspond to different qubit encodings: one qubit in two spins (continuous line), two excitations in three spins (dashed line), three excitations in four spins (dotted line). Straight lines correspond to the rates obtained after averaging over an infinite time, that are evaluated analytically from Eqs. (4.25), (4.26) and similar.

of the state transfer. In Fig. 4.4 we explicitly show the dependence of such computed instantaneous transmission rate as a function of the elapsed time t, for different types of encodings; notice that, by definition of transmission rate (4.3), the instantaneous transfer rate $r(t)$ correctly converges to the asymptotic value given by Eqs. (4.25), (4.26) and similar (straight lines).

4.3 Dual-rail channel

In the previous section we analyzed the simplest spin chain model ($N = 2$). The results we obtained were indicative of the possibility of exploiting memory effects to devise better communication procedures (e.g., having simpler encoding and decoding protocols). These results also showed that transmission rates could easily be computed also in the presence of such effects. In

this section we would like to derive a lower bound for the maximum achievable transmission rate that can be reached in the case of an arbitrarily long spin chain. This is not a simple task [100], due to the presence of the memory correlations in the evolution of the spins chain. The point is that, at present, given a single spin chain of $N > 2$ elements, we do not have communication schemes which permit Alice and Bob to verify independently that the transferring of a signal succeeded, allowing, on one hand, to move to the transmission of the next one, while, on the other hand, determining the average qubit transmission time T. A simple way to address these issues, is to consider the case in which the channel C is composed by three *identical* uncoupled spin 1/2 chains, each of them governed by an Hamiltonian $\hat{H}$ that conserves the total magnetization.

As before, we suppose that Alice has access to the leftmost spin of each of the three chains, while Bob can manipulate the spin at the opposite end of the chains. We also assume that, at time $t = 0$, all the chains are set up in the ferromagnetic ground state $|\mathbf{0}\rangle^{(i)} \equiv |0_1 \dots 0_N\rangle^{(i)}$ (where $i = \{1, 2, 3\}$ is the index that labels the chain). The communication strategy we want to analyze is the following. Alice use the chains 1 and 2 to transfer her first message to Bob by means of a dual-rail encoding [36]. Since this is a "conclusive" strategy, it allows Bob to know exactly at what instant Alice's message has been loaded in his memory. When this happens, he will use the third chain to signal back to Alice that he is ready to receive a new qubit of information (e.g. he does so by sending a spin up message to Alice). The whole procedure is then reiterated for the transmission of the second Alice's message.

To see how this works in details let us first consider a simplified version of the above scheme, where the feed-back message by Bob is transmitted to Alice through a side classical communication line (e.g. a telephone line). In this case we need only to consider the information transfer along the spin chains 1 and 2 from Alice to Bob. Assume that the first message Alice wants to transmit is the qubit $|\psi\rangle = \alpha|0\rangle + \beta\,|1\rangle$. The chains 1 and 2 are then prepared into the following superposition:

$$|\mathbf{s}(1)\rangle \equiv \alpha\,|\mathbf{0}\rangle^{(1)} \otimes |\mathbf{1}\rangle^{(2)} + \beta\,|\mathbf{1}\rangle^{(1)} \otimes |\mathbf{0}\rangle^{(2)}\ . \tag{4.27}$$

The system is then let freely evolve, such that the excitation in Eq. (4.27)

will propagate along the two chains:

$$|\mathbf{s}(1)\rangle \xrightarrow{\hat{U}(\tau)} \sum_{n=1}^{N} \gamma_{1n}(\tau)\,|\mathbf{s}(n)\rangle\,, \tag{4.28}$$

where $\gamma_{ij}(\tau)$ is the same as in Eq. (4.7). Following Ref. [36], at regular time intervals τ Bob performs a magnetization measurement on the last spins of the chain 1 and 2, in order to check if the state $|\psi\rangle$ has traveled to him. In the meantime Alice does nothing and waits until she receives Bob's "OK" feedback message on the phone. At the first Bob's measurement, which happens after a time τ, if he measures a non-zero magnetization, he concludes that the qubit $|\psi\rangle$ is located on the last spins of the chain: therefore he can safely SWAP it into his memory B. According to Eq. (4.28), such event happens with probability $\pi_1 \equiv |\gamma_{1N}(\tau)|^2$. In this case he communicates to Alice via the classical channel the success of information transfer, and she will proceed by sending another qubit through the chains 1 and 2 following the same procedure.

Vice-versa, if the first outcome of Bob's measurement is zero, then he knows that the system has been projected in the state

$$\frac{1}{\sqrt{1-\pi_1}} \sum_{n=1}^{N-1} \gamma_{1n}(\tau)|\mathbf{s}(n)\rangle\,, \tag{4.29}$$

where Alice's qubit of information $|\psi\rangle$ is still contained in the chains 1 and 2. Bob has then another possibility to receive the state $|\psi\rangle$: he can wait for another time τ, before performing the second magnetization measurement. Just before the measurement, the system will be in the state:

$$\frac{1}{\sqrt{1-\pi_1}} \sum_{n=1}^{N} \Big(\gamma_{1n}(2\tau) - \gamma_{Nn}(\tau)\gamma_{1N}(\tau)\Big)|\mathbf{s}(n)\rangle\,. \tag{4.30}$$

Correspondingly Bob's probability to receive the qubit at the second measurement is then:

$$\pi_2 = \frac{1}{\pi_1}|\gamma_{1N}(2\tau) - \gamma_{NN}(\tau)\gamma_{1N}(\tau)|^2\,. \tag{4.31}$$

If the transfer has been still unsuccessful, then he can repeat this strategy, until he is sure the state has been transferred. After each time $k\tau$ he has a

probability π_k to receive the state that can be obtained by simply iterating this scheme:

$$\pi_k = \left[\prod_{j=1}^{k-1} \frac{1}{1-\pi_j}\right] \cdot |c_k|^2 \,, \tag{4.32}$$

where

$$c_k = \gamma_{1N}(k\tau) - \sum_{j=1}^{k-1} \gamma_{NN}(j\tau)\, c_{k-j} \,. \tag{4.33}$$

The probability of having $k-1$ failures and a success at the k-th measurement is thus expressed by:

$$\begin{aligned} P(k) &= \pi_k \cdot (1-\pi_{k-1}) \cdot (1-\pi_{k-2}) \cdot \ldots \cdot (1-\pi_1) \\ &= \left| \gamma_{1N}(k\tau) - \sum_{j=1}^{k-1} \gamma_{NN}(j\tau)\, c_{k-j} \right|^2 . \end{aligned} \tag{4.34}$$

The total probability of success after k steps is given by the sum of all $P(j)$, with $j = 1, \ldots, k$. It can be shown that, under a very general hypothesis on the system Hamiltonian $\hat{H}$, the probability of success converges to 1 in the limit $k \to \infty$ [37].

By knowing all the probabilities (4.34) it is possible to evaluate the average time T needed for the transfer of the first qubit from Alice to Bob. Indeed, since $P(k)$ is exactly the transfer probability after k steps, and since each step takes τ seconds, we get

$$T = \sum_{k=1}^{+\infty} k\,\tau\, P(k) \,. \tag{4.35}$$

If we suppose that Bob can instantaneously communicate to Alice the fact that he effectively received the qubit (for example via a classical communication channel), and that, immediately after having known the transfer success, she sends another qubit, we than obtain the transfer rate $r = 1/T$. In Fig. 4.5 we plot this quantity for a dual-rail channel composed of two identical isotropic spin 1/2 Heisenberg chains of the form $\hat{H} = -J \sum_{j=1}^{N} \hat{\vec{\sigma}}_j^{(i)} \hat{\vec{\sigma}}_{j+1}^{(i)}$ for which the amplitudes $\gamma_{ij}(\tau)$ have been explicitly computed in Ref. [29] (dashed line). As discussed at the beginning of the section, the requirement of a classical communication channel needed as a feedback from Bob to Alice can be relaxed, provided that there is a third spin chain connecting them.

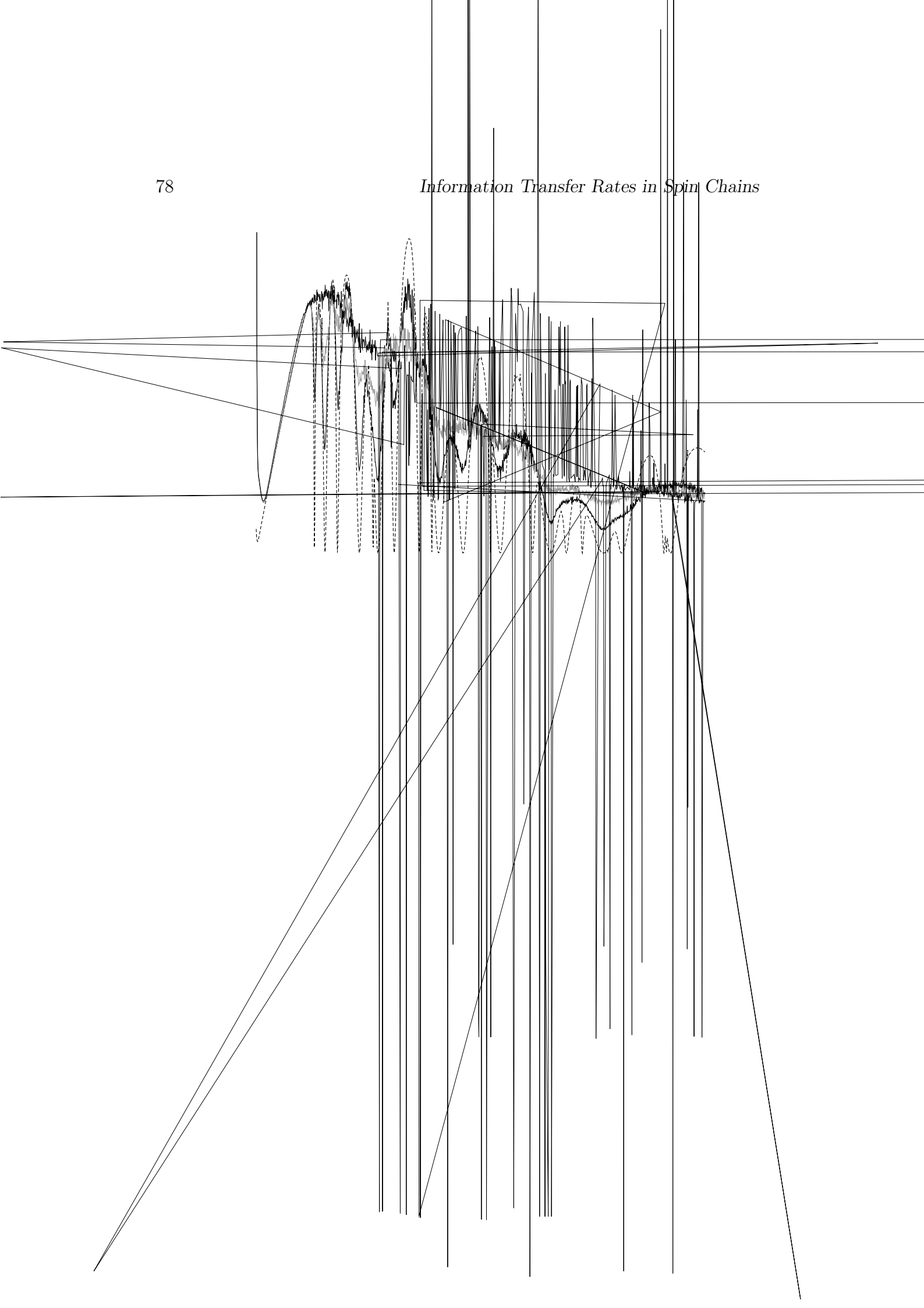

Chapter 5

Decoherence by Interacting Quantum Spin Baths

The study of the stability of quantum information processing with respect to internal hardware imperfections is believed to be a crucial task for the development of control and error-correction strategies [1]. Actually, this is not the only source of errors: unwanted coupling with the environment is also a threat to the actual implementation of any quantum computation and communication protocol; an exhaustive characterization of decoherence in experimental devices well suited for such protocols is therefore crucial. Even before, adequate modelizations of the bath are necessary; in this direction, paradigmatic models are many-body quantum systems such as bosonic harmonic oscillators [51] or spin baths [52]. The following two chapters are focused on the problem of decoherence in quantum information. Two completely different models of environment will be taken into account: here we study dynamical dephasing of a two-level system locally coupled to a many-body spin bath [67]; in the subsequent chapter we will consider the disentangling properties of a single-particle chaotic system to whom a Bell pair is coupled [73].

In this chapter we focus on a setup constituted by a single qubit coupled to a one-dimensional array of spin-1/2 particles, whose free evolution is driven by a Hamiltonian which embraces Ising, XY and Heisenberg universality classes. This model of quantum baths can be of fundamental importance to understand decoherence in open quantum systems, since it can be experimentally engineered by using cold bosons in optical lattices. As an example, we show how to implement a pure dephasing model for a qubit coupled to

an interacting spin bath, thus providing a way to employ optical lattices as *open quantum system simulators* [67]. This analysis can be framed in the context of the recently growing interest in the study of decoherence due to spin baths [49, 56, 57, 58, 59, 60, 61, 62, 63, 64, 65, 66]. Most of the works done so far are based on the so called *central spin model*, where the two-level system is coupled isotropically to all the spins of the bath (see Sec. 1.4.2, Eq. (1.25) with $\vec{\lambda}_k = \vec{\lambda}$). This assumption tremendously simplifies the derivation, but, at the same time, it may introduce some fictitious symmetries which are absent in realistic systems. Moreover it can be very hard to simulate it with engineered baths. A crucial feature of our setup is that the two-level system interacts with only *few* spins of the bath. As we will show, this introduces qualitative differences as compared to the central spin model, moreover it is amenable to an experimental implementation with optical lattices.

The chapter is organized as follows. In the next section we introduce our system-plus-bath model Hamiltonian and describe how it is possible to quantify the decoherence rate in the system by means of the so called "Loschmidt echo". We then show in Sec. 5.2 how optical lattices can be used to simulate this type of open systems. The following sections are devoted to the derivation and the analysis of our results, both for a single system-bath link (Sec. 5.3), and for multiple links (Sec. 5.4). When the two-level system is coupled to an XY model, it is possible to derive an exact result for the Loschmidt echo. This is explained in Subsec. 5.3.1, where we also discuss in detail its short- and long-time behavior, and relate it to the critical properties of the chain. Further insight is obtained by perturbative calculations which agree very well, in the appropriate limits, with the exact results. In Subsec. 5.3.2 we present our results for the Heisenberg bath. In this case an analytic approach is not possible, therefore we solved the problem by means of the time-dependent Density Matrix Renormalization Group (see appendix C for details). In Subsec. 5.3.3 we analyze the possible relation between decoherence and entanglement properties of the environment: we relate the short-time decay of coherences to the two-site nearest-neighbor concurrence inside the bath. Finally, in Sec. 5.4 we extend our results to the case in which the system is coupled to an arbitrary number of bath spins; a regime in which the decoherence is substantially independent of the coupling strength between the system and the environment is discussed in Subsec. 5.4.1.

5.1 The model

The model we consider consists of a two-level quantum object, i.e., a qubit S coupled to an *interacting* spin bath E composed by N spin-1/2 particles (see Fig.5.1a): the idea is to study how the internal dynamics of E affects the decoherent evolution of S. The global system $S+E$ is fully characterized by a standard Hamiltonian of the form

$$\hat{H} = \hat{H}_S + \hat{H}_E + \hat{H}_{\rm int}\,, \tag{5.1}$$

with $\hat{H}_{S,E}$ being the free Hamiltonians of S and E, and $\hat{H}_{\rm int}$ being the coupling term. Without loss of generality we assume the free Hamiltonian of the qubit to be of the form

$$\hat{H}_S = \frac{\omega_e}{2}\left(\mathbb{1} - \hat{\tau}_z\right) = \omega_e \left|e\right\rangle \left\langle e\right|\,, \tag{5.2}$$

with $\hat{\tau}_\alpha$ being the Pauli matrices of S ($\alpha = x, y, z$), and $|e\rangle$ its excited state (the ground state is represented by the vector $|g\rangle$). On the other hand, the environment is modeled by a one-dimensional quantum spin-1/2 chain described by the Hamiltonian

$$\hat{H}_E = -\frac{J}{2}\sum_j \Big[\left(1+\gamma\right)\hat{\sigma}_j^x\hat{\sigma}_{j+1}^x + \left(1-\gamma\right)\hat{\sigma}_j^y\hat{\sigma}_{j+1}^y + \Delta\hat{\sigma}_j^z\hat{\sigma}_{j+1}^z + 2\lambda\hat{\sigma}_j^z\Big]\,, \tag{5.3}$$

where $\hat{\sigma}_i^\alpha$ ($\alpha = x, y, z$) are the Pauli matrices of the i-th spin. The sum over j goes from 1 to $N-1$ for open boundary conditions, or from 1 to N for periodic boundary conditions (where we assume that $\hat{\sigma}_{N+1}^\alpha \equiv \hat{\sigma}_1^\alpha$). The constants J, Δ, γ and λ respectively characterize the interaction strength between neighboring spins, the anisotropy parameter along z and in the xy plane, and an external transverse magnetic field. The Hamiltonian (5.3) has a very rich structure [104]. For the sake of simplicity, we shall consider the two following paradigmatic cases:

- the XY model in a transverse field (see Sec. 5.3.1). Here one has $\Delta = 0$ and λ, γ generic. For $0 < \gamma \leq 1$, Eq. (5.3) belongs to the Ising universality class, and it has a critical point at $|\lambda_c| = 1$; for $\gamma = 0$ it reduces to the XX universality class, which is critical for $|\lambda| \leq 1$.

- the XXZ anisotropic Heisenberg model (see Sec. 5.3.2). Here one has $\lambda, \gamma = 0$ and Δ generic. In this case the Hamiltonian (5.3) is critical for $-1 \leq \Delta \leq 1$ while it has ferromagnetic or anti-ferromagnetic order for $\Delta > 1$ or $\Delta < -1$ respectively.

Finally, the qubit S is coupled to the spin bath through a dephasing interaction of the form

$$\hat{H}_{\rm int} = -\epsilon \sum_{j=j_1}^{j_m} |e\rangle \langle e| \, \hat{\sigma}_j^z \,, \tag{5.4}$$

where ϵ is the coupling constant, and the *link number* m counts the number of environmental spins (labelled by $j_1 \ldots j_m$) to which S is coupled (Fig.5.1a refers to the case where S is interacting with the first spin of an open-boundary chain, i.e. $m = 1$, $j_1 = 1$).

By varying the parameters $m, \Delta, \gamma, \lambda$ and ϵ, the above Hamiltonians allow us to analyze several non-trivial $S + E$ scenarios. Moreover we will see in Sec. 5.2 that it is possible to use optical lattices manipulation techniques [44, 45] to experimentally simulate the resulting dynamical evolution.

Decoherence in the system

With the choice of the coupling (5.4), the populations of the ground and excited states of the qubit do not evolve in time, since $[\hat{\tau}^z, \hat{H}_{\rm int}] = 0$. Consequently, no dissipation takes place in the model and the qubit evolution is *purely decoherent*: the system S loses its coherence without exchanging energy with the bath

where the two branches of the environment are $|\varphi_g(t)\rangle_E = e^{-i\hat{H}_g t}\,|\varphi(0)\rangle_E$ and $|\varphi_e(t)\rangle_E = e^{-i\hat{H}_e t}\,|\varphi(0)\rangle_E$. Therefore the evolution of the reduced density matrix $\rho \equiv \mathrm{Tr}_E\,|\Psi\rangle\,\langle\Psi|$ of the two-level system corresponds to a pure dephasing process. In the basis of the eigenstates $\{|g\rangle, |e\rangle\}$, the diagonal terms ρ_{gg} and ρ_{ee} do not evolve in time. Instead the off-diagonal terms decay according to:

$$\rho_{eg}(t) = \rho_{eg}(0)\, e^{-i\omega_e t} D(t)\,, \tag{5.8}$$

where

$$D(t) \equiv \langle\varphi_g(t)|\varphi_e(t)\rangle = \langle\varphi(0)|e^{i\hat{H}_g t}e^{-i\hat{H}_e t}|\varphi(0)\rangle \tag{5.9}$$

is the decoherence factor. The decoherence of S can then be characterized by the fidelity (or the "Loschmidt echo")

$$\mathcal{L}(t) \equiv |D(t)|^2 = |\langle G|e^{-i(\hat{H}_E + \langle e|\hat{H}_{\rm int}|e\rangle)t}|G\rangle|^2\,, \tag{5.10}$$

where we used the fact that $|\varphi(0)\rangle = |G\rangle$ is the ground state of $\hat{H}_E$ (see also App. A). On one hand, values of $\mathcal{L}(t)$ close to 1 indicate a weak interaction between the environment and the qubit (the case $\mathcal{L}(t) = 1$ corresponds to total absence of interaction, i.e., $\epsilon = 0$). On the other hand, values of $\mathcal{L}(t)$ close to 0 correspond instead to a strong suppression of the qubit coherence due to the interaction with E (for $\mathcal{L}(t) = 0$ the qubit is maximally entangled with the environment, and its density matrix ρ becomes diagonal).

5.2 Simulation of open quantum systems by optical lattices

Here we present a method which would allow one to experimentally simulate the dynamics induced by the Hamiltonian of Eq. (5.1) in a realistic setup. The $S+E$ system introduced in Sec. 5.1 can be seen as an "inhomogeneous" spin network with $N+1$ sites, where one of the spins (say, the first) plays the role of the system of interest S, while the remaining N play the role of the environment E. This immediately suggests the possibility of simulating the dynamical evolution of such a system on optical lattices by employing the techniques recently developed in Ref. [44] (see also Sec. 7.1). An important aspect of our scheme is the fact that we assume the coupling between the system S and E to be independent from the couplings among the N spins which compose the environment. Analogously, the free Hamiltonian of S is

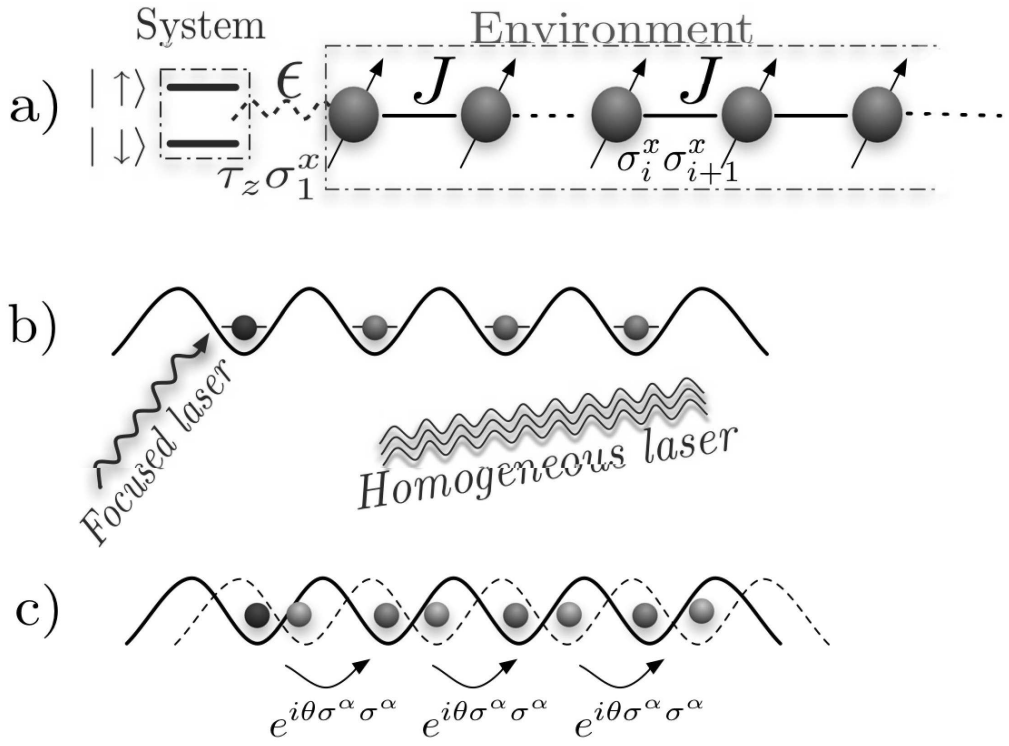

Figure 5.1: a) A sketch of the system-plus-bath model we consider in this work. The two-level system (at position zero) is coupled to the σ^z component of the first spin of the chain that acts as a spin bath. Atoms in an optical lattice can simulate this controlled decoherence by means of series of lasers b) and lattice displacements c), which allow to realize both the interaction of the bath with an external magnetic field and the anisotropic exchange coupling present in Eq. (5.3).

assumed to be different from the on-site terms of the free Hamiltonian of E. On one hand this allows us to study different environment Hamiltonians without affecting the coupling between E and S. On the other hand, this also allows us to analyze different $S+E$ coupling regimes (e.g. strong, weak) without changing the internal dynamics of the bath.

The key advantage of our method is that we can realize the system-plus-bath setup by using a single one-dimensional lattice in which the quantum system is placed on a given lattice site (for example the first one, as in Fig. 5.1b). The different Hamiltonians for the system and for the bath are

realized by specific pulse sequences which simulate the dynamics of the model. The same holds for the coupling Hamiltonian of the two-level system with the bath, which is different from the couplings within the bath. In Fig. 5.1 the leftmost atom simulates the two-level system, the coupling to the second site is the interaction between the quantum system and the environment, the rest of the chain is the interacting spin environment.

Jané *et al.* showed in Ref. [44] that atoms loaded in an optical lattice can simulate the evolution of a generic spin Hamiltonian in a stroboscopic way when subjected to appropriate laser pulses, Fig. 5.1b, and controlled displacements, Fig. 5.1c, which allow to implement the single-site and two-site contributions to the Hamiltonian. The key point is that in our case the sequences of gates need to allow for discriminating between the system and the bath. The types of baths that one can simulate by these means embrace Ising, XY and Heisenberg exchange Hamiltonian. Therefore, by varying the parameters of the optical lattice, it is possible to test the impact of the different phases (critical, ferromagnetic, anti-ferromagnetic, etc...) of the environment on the decoherence of the two-level system.

The time evolution operator associated with the Hamiltonian $\hat{H}$ in Eq. (5.1) over a time t can be simulated by decomposing it into a product of operators acting on very short times $\tau \ll t$, via a Trotter expansion [159]:

$$\begin{aligned} e^{-i\hat{H}t} &= \lim_{n\to\infty} \Bigg[\hat{U}_0^z(\omega_e\tau)\, \hat{U}_{0,1}^{zz}(\epsilon\tau) \prod_{j=1}^{N} \hat{U}_j^z\big(\tfrac{J\lambda\tau}{2}\big) \\ &\quad \times \hat{U}_{j,j+1}^{xx}\big(\tfrac{J(1+\gamma)\tau}{2}\big)\, \hat{U}_{j,j+1}^{yy}\big(\tfrac{J(1-\gamma)\tau}{2}\big)\, \hat{U}_{j,j+1}^{zz}\big(\tfrac{J\Delta\tau}{2}\big) \Bigg]^n \end{aligned} \tag{5.11}$$

where $\tau = t/n$, $\hat{U}_j^z(\theta) \equiv e^{i\theta\hat{\sigma}_j^z}$, $\hat{U}_{j,k}^{\alpha\beta}(\theta) \equiv e^{i\theta\hat{\sigma}_j^\alpha\hat{\sigma}_k^\beta}$, and the index 0 labels the two-level system S. For $\alpha \in \{x, y\}$ one can write $\hat{U}_{j,k}^{\alpha\alpha} = \hat{V}_j^\alpha\, \hat{V}_k^\alpha\, \hat{U}_{j,k}^{zz}\, \hat{V}_k^{\alpha\dagger}\, \hat{V}_j^{\alpha\dagger}$, where $\hat{V}_j^\alpha = (\hat{\mathbb{1}} - i\hat{\sigma}_j^\alpha)/\sqrt{2}$ are fast homogeneous local unitary operations. These can be realized with single atoms trapped in an optical lattice [44], each having two relevant electronic levels $(|0\rangle_j\,, |1\rangle_j)$ interacting with a resonant laser according to:

$$\hat{H}_j^L = \Omega\left(e^{i\phi}|1\rangle_j\langle 0| + e^{-i\phi}|0\rangle_j\langle 1|\right). \tag{5.12}$$

The evolution under the Hamiltonian in Eq. (5.12), $\hat{U}_j^L(t,\phi) \equiv e^{-i\hat{H}_j^L t}$, yields the single-qubit operations $\hat{V}_j^x = \hat{U}_j^L(\frac{\pi}{4\Omega}, 0)$, $\hat{V}_j^y = \hat{U}_j^L(\frac{\pi}{2\Omega}, 0)\, \hat{U}_j^L(\frac{3\pi}{4\Omega}, \frac{\pi}{2})$

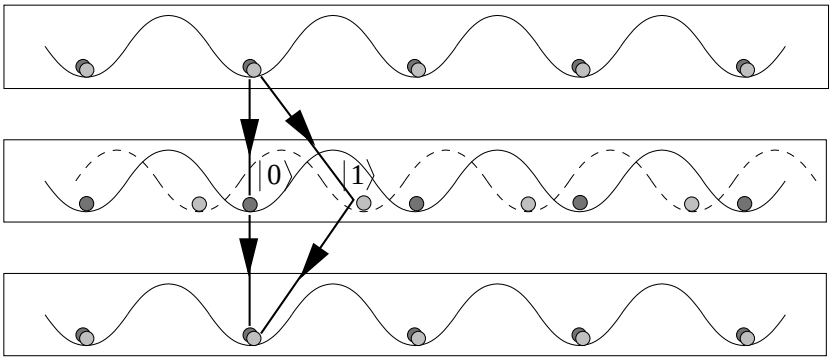

Figure 5.2: Atoms in a double optical lattice. Interaction between adjacent qubits is obtained by displacing one of the lattice (e.g. the one which traps the atoms when their electronic level is in $|1\rangle$, here depicted with light balls) with respect to the other (that traps atoms in $|0\rangle$ state, dark balls). In this way the $|1\rangle$ component of atom j approaches in space the $|0\rangle$ component of atom $j+1$, and these collide in a controlled way. Finally the two components of each atom are brought back together (figure quoted from Ref. [44]).

and $\hat{U}_j^z(\theta) = \hat{U}_j^L(\frac{\pi}{2\Omega}, \pi+\theta)\,\hat{U}_j^L(\frac{\pi}{2\Omega}, 0)$, whence $\hat{U}_j^z(-\frac{\pi}{2}) = i\hat{\sigma}_j^z$, while $\hat{U}_j^L(\frac{\pi}{2\Omega}) = i\hat{\sigma}_j^x$. These operation can be made very fast by simply increasing the laser intensity and thereby the Rabi frequency. They can be performed either simultaneously on all qubits, by shining the laser homogeneously onto all atoms, or selectively on some of them, by focusing it appropriately (see Fig. 5.1b). For our purposes the individual addressing is needed only for the atom in position 0, which represents the quantum system; this is anyway the minimal physical requirement for being able to monitor its state during the evolution.

Two-qubit operations can be performed by displacing the lattice in a state-selective way [105], so that state $|0\rangle_j|1\rangle_{j+1}$ acquires a phase factor $e^{-i\varphi}$, as experimentally realized in [106]. Namely, one builds up two identical periodic optical lattices, each formed by the standing wave of two interfering laser beams that are superimposed in space. The lattices are such that they trap the atoms depending on their internal electronic levels, $|0\rangle$ and $|1\rangle$. By adjusting the phases of the interfering laser beams, the two lattices can be easily displaced with respect to each other, therefore displacing the atoms conditionally to their internal state. Performing this process adiabatically, such that the trapped atoms remain in the motional ground state, and choosing a relative displacement of one lattice period, the $|1\rangle$ component of atom

in position j meets the $|0\rangle$ component of atom in position $j+1$, and the two atoms interact through controlled collisions for a time t_1. Then the lattices are adiabatically returned to their initial positions. The result of the interaction process is that the $|1\rangle_j |0\rangle_{j+1}$ component of the wave functions picks up a certain phase shift which depends on the interaction time t_1. Notice that interactions between more distant qubits can be achieved by larger relative displacements of the two lattices; notice also that the whole process moves all the atoms at the same time, so that interactions that are produced are invariant under translations.

The resulting gate $\hat{G}_{j,j+1}(\varphi)$ can be composed with $\hat{\sigma}^x$ rotations to yield $\hat{U}^{zz}_{j,j+1}(\theta) = e^{i\theta}[\hat{G}_{j,j+1}(2\theta)\,\hat{\sigma}^x_j\hat{\sigma}^x_{j+1}]^2$. This will affect all atoms from 0 to N. Since we want a different coupling for the $\{01\}$ pair than for all others, we need to erase the effect of the interaction for that specific pair using only local operations on atom 0, as in the sequences $[\hat{\sigma}^z_0\,\hat{U}^{xx}_{01}(\theta)]^2 = [\hat{\sigma}^z_0\,\hat{U}^{yy}_{01}(\theta)]^2 = [\hat{\sigma}^x_0\,\hat{U}^{zz}_{01}(\theta)]^2 = \hat{\mathbb{1}}$. Defining $\hat{U}^{\alpha\alpha}_{\otimes}(\theta) \equiv \prod_{j=1}^{N}\hat{U}^{\alpha\alpha}_{j,j+1}(\theta)$, we can generate each simulation step in Eq. (5.11) as

$$\begin{aligned}\hat{\mathcal{U}}_n \;\equiv\; & \left[\hat{\sigma}^x_0\,\hat{U}^{zz}_{\otimes}\big((\epsilon-\tfrac{J\Delta}{2})\tfrac{\tau}{2}\big)\right]^2\left[\hat{\sigma}^z_0\,\hat{U}^{xx}_{\otimes}\big(-\tfrac{J(\gamma+1)\tau}{4}\big)\right]^2 \\ & \left[\hat{\sigma}^z_0\,\hat{U}^{yy}_{\otimes}\big(\tfrac{J(\gamma-1)\tau}{4}\big)\right]^2\hat{U}^{zz}_{\otimes}(-\epsilon\tau)\,\hat{U}^{z}_{0}(\omega_e\tau)\,\hat{U}^{z}_{\otimes}\big(\tfrac{J\lambda\tau}{2}\big)\end{aligned} \tag{5.13}$$

involving only global lattice displacements, global laser-induced rotations and local addressing of atom 0.

We note that, apart from 1D spin baths, this approach can be straightforwardly extended to environments with higher dimensionality. For example, it would be quite interesting to consider a 3D optical lattice; besides being feasible from an experimental point of view, this could be useful in studying for instance the situation found in solid-state NMR [107]. Here we focus on one-dimensional baths since, in several cases, they admit an exact solution.

5.3 The single-link scenario

In this section we analyze the time evolution of the Loschmidt echo (5.10) for several distinct scenarios where the qubit S is coupled to just one spin of the chain, i.e. $m = 1$ in Eq. (5.4). In this case, in the thermodynamic limit the interaction $\hat{H}_{\rm int}$ between the system S and the environment E does not affect the description of the bath Hamiltonian $\hat{H}_E$, since it is local; therefore it can be considered in all senses as a small perturbation of the environment. The

bath is effectively treated as a reservoir, which is in contact with the system through just one point. In the following we study the cases in which the bath is described by a one dimensional spin-1/2 Ising, an XY (Subsec. 5.3.1) and a Heisenberg (Subsec. 5.3.2) chain.

5.3.1 XY bath

Here we focus on the case of a spin bath E characterized by a free Hamiltonian (5.3) of the XY form, i.e., with null anisotropy parameter along z ($\Delta = 0$). In this case the environment is a one-dimensional spin-1/2 XY model, which is analytically solvable [108]. Below we show that also the Loschmidt echo can be evaluated exactly [67], both for open and for periodic boundary conditions.

In the case $m < N$ in which the system S is coupled to just some of the spins of the bath E, the perturbed Hamiltonian $\hat{H}_e$ of Eq. (5.6) is the Hamiltonian of an XY chain in a non-uniform magnetic field. In this circumstance one cannot employ the approach of Ref. [63], and in general the dynamical evolution of the system has to be solved numerically. The derivation we present here instead is analytical and it applies for all values of $m = 1, \cdots, N$. In the following we will present it for the case of a generic m but, in the remaining of the section, we will explicitly discuss its results only for the single-link case (i.e. $m = 1$).

The first step of the analytical derivation is a Jordan-Wigner transformation (JWT), in order to map both Hamiltonians $\hat{H}_g$ and $\hat{H}_e$ onto a free-Fermion model, described by the quadratic form [108]

$$\hat{\mathcal{H}} = \sum_{i,j} \left[\hat{c}_i^\dagger \, A_{i,j} \, \hat{c}_j + \frac{1}{2} (\hat{c}_i^\dagger \, B_{i,j} \, \hat{c}_j^\dagger + \text{h.c.}) \right] + \frac{1}{2} \sum_i A_{i,i} \, , \tag{5.14}$$

where $\hat{c}_i, \hat{c}_i^\dagger$ are the annihilation and creation operators for the spinless Jordan-Wigner fermions, defined by

$$\hat{c}_k = \exp \left(i\pi \sum_{j=1}^{k-1} \hat{\sigma}_j^+ \hat{\sigma}_j^- \right) \hat{\sigma}_k^- \, , \tag{5.15}$$

where $\hat{\sigma}^\pm = \hat{\sigma}^x \pm i\hat{\sigma}^y$. The two matrices $\mathbf{A}$, $\mathbf{B}$ are given by

$$[\mathbf{A}]_{j,k} = -J\big(\delta_{k,j+1} + \delta_{j,k+1}\big) - 2(\lambda + \epsilon_j)\delta_{j,k}, \tag{5.16}$$

$$[\mathbf{B}]_{j,k} = -\gamma J\big(\delta_{k,j+1} - \delta_{j,k+1}\big) \, , \tag{5.17}$$

where $\epsilon_j = 0$ for $\hat{H}_g$, while

$$\epsilon_j = \begin{cases} \epsilon & \text{if S is coupled to the } j\text{-th spin} \\ 0 & \text{elsewhere} \end{cases} \tag{5.18}$$

for $\hat{H}_e$. A generic quadratic form, like Eq. (5.14) (where $\mathbf{A}$ is a Hermitian matrix, due to the Hermiticity of $\mathcal{H}$, and $\mathbf{B}$ is antisymmetric, due to the anti-commutation rules among the $\hat{c}_i$), can be diagonalized in terms of the normal-mode spinless Fermi operators $\{\hat{\eta}_k, \hat{\eta}_k^\dagger\}$:

$$\mathcal{H} = \sum_k E_k \left(\hat{\eta}_k^\dagger \hat{\eta}_k - \frac{1}{2} \right), \tag{5.19}$$

where $\hat{\eta}_k = \sum_i (g_{k,i}\hat{c}_i + h_{k,i}\hat{c}_i^\dagger)$, or in matrix form:

$$\hat{\vec{\eta}} = \mathbf{g} \cdot \hat{\vec{c}} + \mathbf{h} \cdot \hat{\vec{c}}^{\,\dagger}\,. \tag{5.20}$$

If we rewrite the two change-of-basis matrices $\mathbf{g}$ and $\mathbf{h}$ as $g_{k,i} \equiv \frac{1}{2}(\phi_{k,i} + \psi_{k,i})$ and $h_{k,i} \equiv \frac{1}{2}(\phi_{k,i} - \psi_{k,i})$, we eventually arrive at the following coupled linear equations, whose solution permits to find the eigenbasis of the non-uniform Hamiltonian in Eq. (5.14):

$$\begin{cases} \vec{\phi}_k(\mathbf{A} - \mathbf{B}) &= E_k \vec{\psi}_k, \\ \vec{\psi}_k(\mathbf{A} + \mathbf{B}) &= E_k \vec{\phi}_k. \end{cases} \tag{5.21}$$

Since $\mathbf{A}$ is symmetric and $\mathbf{B}$ is antisymmetric, all of the E_k are real; also the $g_{k,i}$ and the $h_{k,i}$ can be chosen to be real. The canonical commutation rules for the normal-mode operators impose the constraints: $\mathbf{g}\,\mathbf{g}^{\mathbf{T}} + \mathbf{h}\,\mathbf{h}^{\mathbf{T}} = \mathbb{1}$; $\mathbf{g}\,\mathbf{h}^{\mathbf{T}} - \mathbf{h}\,\mathbf{g}^{\mathbf{T}} = 0$.

It is convenient to rewrite the bath Hamiltonian-plus-interaction $\hat{H}_e$ as:

$$\hat{H}_e = \frac{1}{2} \hat{\mathbf{\Psi}}^\dagger \, \mathbf{C} \, \hat{\mathbf{\Psi}}\,, \tag{5.22}$$

where $\hat{\mathbf{\Psi}}^\dagger = \left(\hat{c}_1^\dagger \ldots \hat{c}_N^\dagger \, \hat{c}_1 \ldots \hat{c}_N \right)$ ($\hat{c}_i$ are the corresponding spinless Jordan-Wigner Fermion operators) and $\mathbf{C} = \hat{\sigma}^z \otimes \mathbf{A} + i\hat{\sigma}^y \otimes \mathbf{B}$ is a tridiagonal block matrix. The Loschmidt echo, Eq. (5.10), can then be evaluated by means of the following formula [109]:

$$\mathcal{L}(t) = \left| \left\langle e^{-it \sum_{i,j} C_{i,j} \hat{\Psi}_i^\dagger \hat{\Psi}_j} \right\rangle \right| = \left| \det \left(1 - \mathbf{r} + \mathbf{r}\, e^{-i\mathbf{C}t} \right) \right|\,, \tag{5.23}$$

where the elements of the matrix $\mathbf{r}$ are simply the two-point correlation functions of the spin chain: $r_{ij} = \langle G|\hat{\Psi}_i^\dagger \hat{\Psi}_j|G\rangle$, where $|G\rangle$ is the ground state of $\hat{H}_g$. Details about the explicit expression of the correlators r_{ij} as well as of the matrix $e^{-i\mathbf{C}t}$ are given in the following subsection.

Equation (5.23) provides an explicit formula for the Loschmidt echo in terms of the determinant of a $2N \times 2N$ matrix, whose entries are completely determined by the diagonalization of the two linear systems given by Eq. (5.21). This is one of the central results of our work. It allows us to go beyond the central spin model where all the spins of E are uniformly coupled with S ($m = N$), whose solution (at least for periodic boundary conditions) was discussed in [63, 64] and, for the sake of completeness, has been reviewed below (see Eq. (5.35)). Notice that, similarly to the central spin model, this formula allows to study a system composed of a large number of spins in the bath $N \sim 10^2 - 10^3$, as it only requires manipulations of matrices whose size scales linearly, and not exponentially, with N.

Fermion correlation functions

Below we provide an explicit expression for the two-point correlation matrix $(\mathbf{r})_{ij} = \langle \hat{\Psi}_i^\dagger \hat{\Psi}_j \rangle$ of the operators $\hat{\mathbf{\Psi}}^\dagger = \left(\hat{c}_1^\dagger \dots \hat{c}_N^\dagger \, \hat{c}_1 \dots \hat{c}_N\right)$ on the ground state of the system Hamiltonian $\hat{H}_g$. The $2N \times 2N$ matrix $\mathbf{r}$ is written in terms of the Jordan Wigner fermions $\{\hat{c}_k, \hat{c}_k^\dagger\}$ as:

$$\mathbf{r} = \begin{pmatrix} \left\langle \hat{c}_i^\dagger \, \hat{c}_j \right\rangle_{i,j=1,N} & \left\langle \hat{c}_i^\dagger \, \hat{c}_j^\dagger \right\rangle_{i,j=1,N} \\ \left\langle \hat{c}_i \, \hat{c}_j \right\rangle_{i,j=1,N} & \left\langle \hat{c}_i \, \hat{c}_j^\dagger \right\rangle_{i,j=1,N} \end{pmatrix} . \tag{5.24}$$

Therefore it is sufficient to express $\{\hat{c}_k, \hat{c}_k^\dagger\}$ in terms of the normal mode operators $\{\hat{\eta}_k^{(g)}, \hat{\eta}_k^{(g)\dagger}\}$ which diagonalize Hamiltonian $\hat{H}_g$, since $< \hat{\eta}_j^{(g)} \hat{\eta}_k^{(g)\dagger} >= \delta_{jk}$, the other expectation values of the $\hat{\eta}$'s on the ground state being zero. By inverting Eq. (5.20) we get

$$\hat{\vec{c}} = \mathbf{g}^{\mathbf{T}} \cdot \hat{\vec{\eta}} + \mathbf{h}^{\mathbf{T}} \cdot \hat{\vec{\eta}}^\dagger \, , \tag{5.25}$$

from which it directly follows that

$$\mathbf{r} = \begin{pmatrix} \mathbf{h}^{(g)\mathbf{T}} \, \mathbf{h}^{(g)} & \mathbf{h}^{(g)\mathbf{T}} \, \mathbf{g}^{(g)} \\ \mathbf{g}^{(g)\mathbf{T}} \, \mathbf{h}^{(g)} & \mathbf{g}^{(g)\mathbf{T}} \, \mathbf{g}^{(g)} \end{pmatrix} . \tag{5.26}$$

The superscript $^{(g)}$ stands for the change-of basis-matrices $\mathbf{g}$ and $\mathbf{h}$ relative to the Hamiltonian $\hat{H}_g$.

The last ingredient for the evaluation of the Loschmidt echo, Eq. (5.23), is the exponential $e^{i\mathbf{C}t}$. We introduce the vector $\hat{\mathbf{\Gamma}}^\dagger = \left(\hat{\eta}_1^{(g)\dagger} \dots \hat{\eta}_N^{(g)\dagger} \hat{\eta}_1^{(g)} \dots \hat{\eta}_N^{(g)}\right)$, so that $\hat{\mathbf{\Psi}} = \mathbf{U}^\dagger \hat{\mathbf{\Gamma}}$, where

$$\mathbf{U} = \begin{pmatrix} \mathbf{g^{(e)}} & \mathbf{h^{(e)}} \\ \mathbf{h^{(e)}} & \mathbf{g^{(e)}} \end{pmatrix} . \tag{5.27}$$

We can therefore rewrite Eq. (5.22) as

$$\hat{H}_e = \frac{1}{2} \hat{\mathbf{\Psi}}^\dagger \, \mathbf{C} \, \hat{\mathbf{\Psi}} = \frac{1}{2} \hat{\mathbf{\Gamma}}^\dagger \, \mathbf{U} \, \mathbf{C} \, \mathbf{U}^\dagger \, \hat{\mathbf{\Gamma}} \equiv \frac{1}{2} \hat{\mathbf{\Gamma}}^\dagger \, \mathbf{D} \, \hat{\mathbf{\Gamma}}, \tag{5.28}$$

where $\mathbf{D}$ is a $2N \times 2N$ diagonal matrix, whose elements are the energy eigenvalues of $\hat{H}_e$ and their opposites:

$$\mathbf{D} = \begin{pmatrix} \mathbf{E^{(e)}} & \mathbf{0} \\ \mathbf{0} & -\mathbf{E^{(e)}} \end{pmatrix} . \tag{5.29}$$

It then follows that $\mathbf{C} = \mathbf{U}^\dagger \, \mathbf{D} \, \mathbf{U}$, from which one can easily calculate the exponential $e^{i\mathbf{C}t}$.

Central spin model

If the qubit is uniformly coupled to all the spins of the chain, the effect of the interaction in Eq. (5.4) is simply of renormalizing the transverse field strength in the bath Hamiltonian: for $\Delta = 0$ both Hamiltonians $\hat{H}_g$ and $\hat{H}_e$ correspond to an XY model with anisotropy γ, uniform couplings J and local magnetic field λ and $\lambda + \epsilon$ respectively. They can be diagonalized via a standard JWT, followed by a Bogoliubov rotation [108]. The normal mode operators that diagonalize $\hat{H}_e$, satisfying the fermion anti-commutation rules, are given by

$$\hat{\eta}_k^{(e)} = \sum_j \frac{e^{-2\pi i j k/N}}{\sqrt{N}} \prod_{l<j} \hat{\sigma}_l^x \left(u_k^{(e)} \hat{\sigma}_j^+ - i v_k^{(e)} \hat{\sigma}_j^- \right) , \tag{5.30}$$

where the coefficients $u_k^{(e)} = \cos(\theta_k/2)$, $v_k^{(e)} = \sin(\theta_k/2)$ depend on the angle

$$\theta_k(\epsilon) = \arctan \left[\frac{-\sin(2\pi k/N)}{\cos(2\pi k/N) - (\lambda + \epsilon)} \right] . \tag{5.31}$$

The corresponding single quasi-excitation energy is given by $E_k^{(e)} \equiv \mathcal{E}_k(\epsilon)$:

$$\mathcal{E}_k(\epsilon) = 2J\sqrt{\left[\cos\left(\frac{2\pi k}{N}\right) - (\lambda+\epsilon)\right]^2 + \gamma^2 \sin^2\left(\frac{2\pi k}{N}\right)}\,. \tag{5.32}$$

The Hamiltonian $\hat{H}_g$ can be diagonalized in a similar way; the corresponding normal-mode operators are connected to the previous ones by a Bogoliubov transformation:

$$\hat{\eta}_{\pm k}^{(g)} = \cos(\alpha_k)\,\hat{\eta}_{\pm k}^{(e)} - i\sin(\alpha_k)\,\hat{\eta}_{\mp k}^{(e)\dagger}\,, \tag{5.33}$$

with $\alpha_k = [\theta_k(0) - \theta_k(\epsilon)]/2$.

The spin chain is initially in the ground state $|G\rangle$ of $\hat{H}_g$; this state can be rewritten as a BCS-like state:

$$|G\rangle = \prod_{k>0}\left[\cos(\alpha_k) - i\sin(\alpha_k)\,\hat{\eta}_k^{(e)\dagger}\,\hat{\eta}_{-k}^{(e)\dagger}\right]|G_e\rangle \tag{5.34}$$

where $|G_e\rangle$ is the ground state of $\hat{H}_e$. This expression allows one to rewrite the Loschmidt echo $\mathcal{L}(t)$ in Eq. (5.10) in a simple factorized form:

$$\mathcal{L}_{m=N}(t) = \prod_{k=1}^{N/2}\left[1 - \sin^2(2\alpha_k)\,\sin^2(\mathcal{E}_k t)\right]\,. \tag{5.35}$$

Eq. (5.35) provides a straightforward formula in order to calculate the Loschmidt echo for a central spin coupled uniformly to all the spins of the bath. Nonetheless this model, although in some circumstances it can reveal the emergence of a quantum phase transition in the environment [63, 64], does not provide an effective physical description of a standard reservoir, since the coupling with the system is highly non-local and it can drive the evolution of the bath itself. However in the following section we will use it to test the convergence of our results to the ones presented in [63, 64], in the limit $m \to N$.

Ising bath: general features

The generic behavior of $\mathcal{L}$ as a function of time for different values of λ, and fixed coupling constant ϵ, is shown in Fig. 5.3. For $\lambda < 1$ the echo oscillates with a frequency proportional to ϵ, while for $\lambda > 1$ the oscillation amplitudes

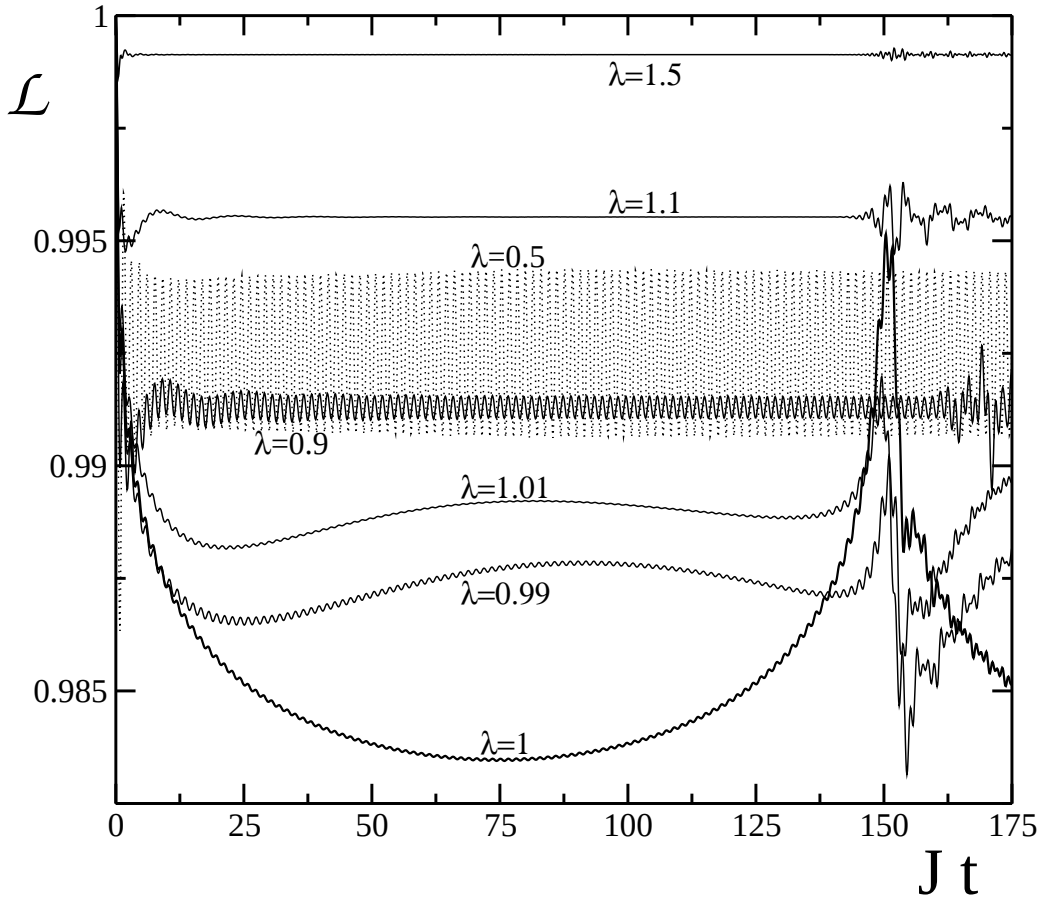

Figure 5.3: Single-link Ising model ($m = 1, \Delta = 0, \gamma = 1$): Loschmidt echo of Eq. (5.23) as a function of time for a qubit coupled to a $N = 300$ spin chain with periodic boundary conditions (here $\epsilon = 0.25$). The various curves are for different values of the transverse magnetic field (corresponding values of λ are indicated in the figure). The critical point corresponds to $\lambda = 1$ (thick line). Notice the revivals of quantum coherence at $t^* \sim 150$, due to the finite size of the chain.

are drastically reduced. The Loschmidt echo reaches its minimum value at the critical point $\lambda_c = 1$, thus revealing that the decoherence is enhanced by the criticality of the environment. Since the chain is finite, at long times there are revivals of coherence [1]; in the thermodynamic limit $N \to \infty$ they completely disappear. In any case, as it can be seen from the figure, already for $N = 300$ spins there is a wide interval where the asymptotic behavior at long times can be analyzed.

Short-time behavior

At short times the Loschmidt echo $\mathcal{L}$ decays as a Gaussian [80]:

$$\mathcal{L}(t) \sim e^{-\alpha t^2}\,, \tag{5.36}$$

as it can be seen in Fig. 5.4a, which shows a magnification of the curves from Fig. 5.3 for small times. This behavior can be predicted within a second-order time perturbation theory in the coupling ϵ between the system and the bath: if ϵ is small as compared to the interaction J between neighboring spins in the bath ($\epsilon \ll J$), the decoherence factor $D(t)$ of Eq. (5.9) can be expanded in series of ϵ:

$$\begin{aligned} \langle e^{i\hat{H}_g t}\, e^{-i\hat{H}_e t}\rangle &= \left\langle \mathcal{T}\left[\exp\left(-i\int_0^t dt' e^{i\hat{H}_g t'}\hat{\mathcal{W}} e^{-i\hat{H}_g t'}\right)\right]\right\rangle \\ &\simeq 1 + \epsilon\lambda_1 + \epsilon^2\lambda_2\,, \end{aligned} \tag{5.37}$$

where $\mathcal{T}$ is the time ordered product and $\hat{\mathcal{W}} = \epsilon\,\hat{\sigma}_1^z$ accounts for the interaction of the two-level system with the spin chain. The above expression has to be evaluated on the ground state of $\hat{H}_g$, therefore it is useful to rewrite the interaction $\hat{\mathcal{W}}$ in terms of the normal mode operators $\hat{\eta}_k^{(g)}$ of $\hat{H}_g$:

$$\hat{\mathcal{W}} = \epsilon\left[2\sum_{i,j}\left(g_{i,1}\hat{\eta}_i^{(g)\dagger} + h_{i,1}\hat{\eta}_i^{(g)}\right)\left(g_{j,1}\hat{\eta}_j^{(g)} + h_{j,1}\hat{\eta}_j^{(g)\dagger}\right) - 1\right].$$

The first-order term then reads

$$\lambda_1 = -it\left(2\sum_i |h_{i,1}|^2 - 1\right), \tag{5.38}$$

[1] A rough estimate of the revival times is given by $t^* = N/\bar{v}_\lambda$, where $\bar{v}_\lambda$ is the maximum phase velocity of the spin chain over all the normal mode velocities, in units of sites. Given the dispersion relation $\mathcal{E}_k$, then $\bar{v}_\lambda = \mathrm{Max}_{\bar{k}}(\partial_k \mathcal{E})|_{\bar{k}}$. As an example, for the Ising chain (whose dispersion relation is given by Eq. (5.32) with $\gamma = \epsilon = 0$) we have $\bar{v}_\lambda = 2\min(\lambda, 1)$.

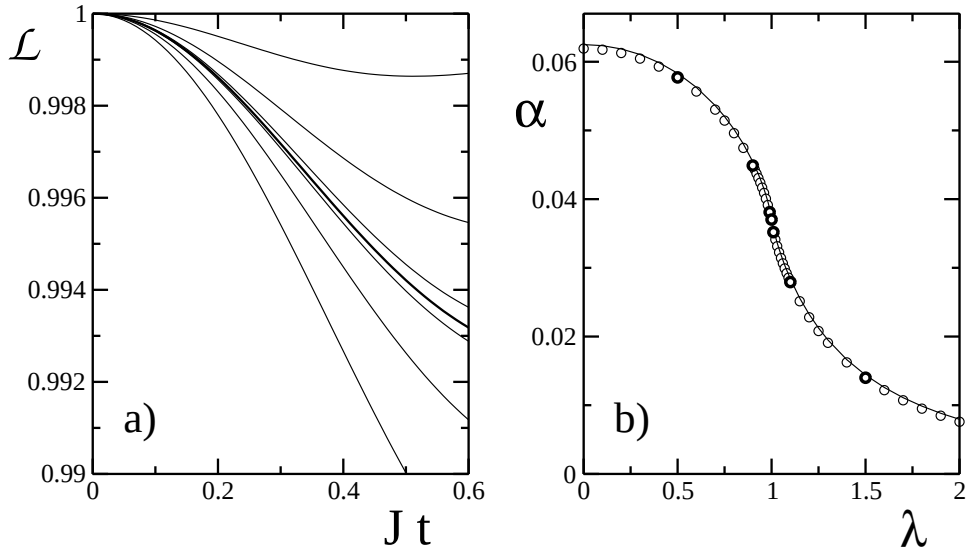

Figure 5.4: Short-time behavior of the Loschmidt echo: a) magnification of the plot in Fig. 5.3 for $t \leq 0.6$, where a Gaussian decay $L \sim e^{-\alpha t^2}$ is visible (various curves are for different values of λ: from bottom to top $\lambda = 0.5$, 0.9, 0.99, 1, 1.01, 1.1, 1.5); b) dependence of α on λ (the solid line shows the perturbative estimate given by Eq. (5.40)).

while the second-order term is given by

$$\lambda_2 = -\int_0^t dt' \int_0^{t'} dt'' \Bigg[4 \sum_{i \neq j} \Big((g_{i,1} h_{j,1})^2 - g_{i,1} g_{j,1} h_{i,1} h_{j,1} \Big) e^{-i(E_i + E_j)(t' - t'')} + \Big(2 \sum_i |h_{i,1}|^2 - 1 \Big)^2 \Bigg]. \tag{5.39}$$

The Loschmidt echo is then evaluated by taking the square modulus of the decoherence factor:

$$\mathcal{L}(t) \simeq 1 - 4\epsilon^2 t^2 \sum_{i \neq j} \Big[(g_{i,1} h_{j,1})^2 - g_{i,1} g_{j,1} h_{i,1} h_{j,1} \Big]. \tag{5.40}$$

In Fig. 5.4b the initial Gaussian rate α is plotted as a function of λ; circles represent numerical data, while the solid red curve is the perturbative estimate obtained from second-order perturbation theory, given by Eq. (5.40).

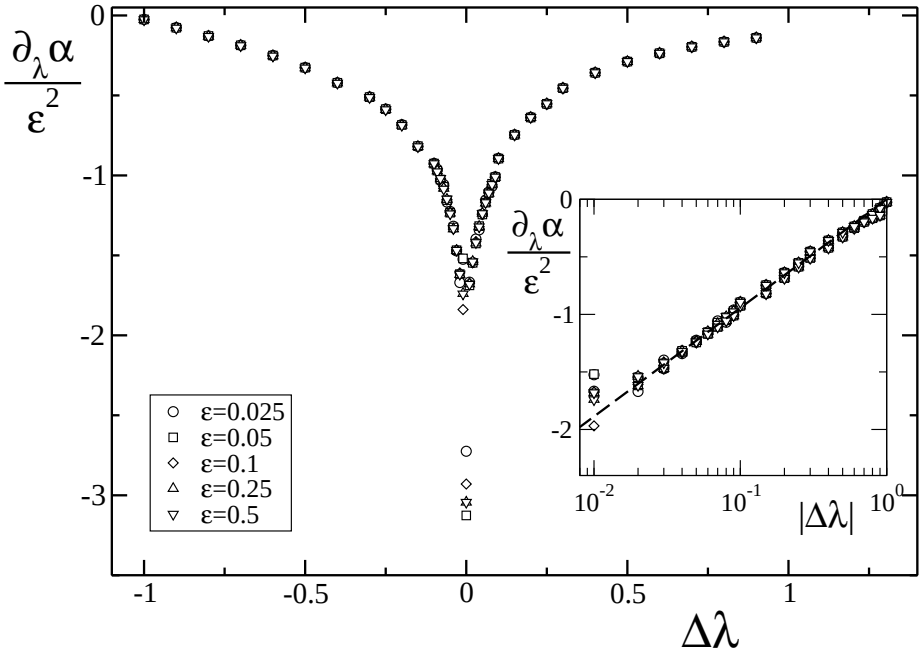

Figure 5.5: Single-link Ising model ($m = 1, \Delta = 0, \gamma = 1$): Loschmidt echo at short times. The plot shows the rescaled parameter $\partial_\lambda \alpha/\epsilon^2$ as a function of λ for a periodic chain ($N = 200$). Various symbols are for different values of the coupling strength ϵ. Inset: plot in a semi-logarithmic scale. The dashed line indicates a fit of numerical data: $\partial_\lambda \alpha/\epsilon^2 = \tilde{c}_1 \log|\Delta\lambda| + \tilde{c}_2$, with $\tilde{c}_1 \approx 0.40983$ and $\tilde{c}_2 \approx 0.000108$.

In Fig. 5.5 we analyze the behavior of the first derivative of the rate $\alpha(\lambda, \epsilon)$ as a function of the distance from criticality $\Delta\lambda \equiv \lambda - \lambda_c$, for a fixed number N of spins in the chain. As predicted by the perturbative estimate, α scales like ϵ^2; most remarkably, its first derivative with respect to the transverse field diverges if the environment is at the critical point λ_c. In the inset we show that $\partial_\lambda \alpha$ diverges logarithmically on approaching the critical value, as:

$$\frac{\partial \alpha}{\partial \lambda} = c_1 \ln|\lambda - \lambda_c| + \text{const.} \tag{5.41}$$

This is a universal feature, entirely due to the underlying criticality of the Ising model. Our results show that at short times the Loschmidt echo is regular even in the presence of a bath undergoing a phase transition. The critical properties manifest in the *changes* of $\mathcal{L}$ when the bath approaches the critical point.

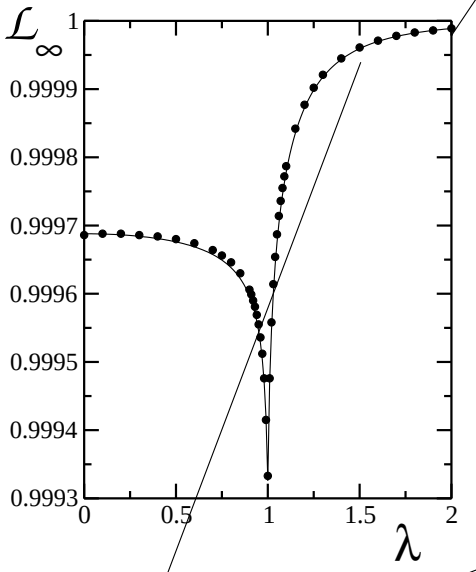
$\mathcal{L}_\infty$
1
0.9999
0.9998
0.9997
0.9996
0.9995
0.9994
0.9993
0
0.5
1
1.5
2
λ

1

1

Here, c_k are the coefficients of the expansion $|\psi_0^{(g)}\rangle = \sum_k c_k |\psi_k^{(e)}\rangle$, where $\hat{H}_e|\psi_k^{(e)}\rangle = E_k^{(e)}|\psi_k^{(e)}\rangle$ and $|\psi_0^{(g)}\rangle \equiv |G\rangle$. An integration of the ansatz Eq. (5.42) from time $T > t_0$ to time $T + \Delta$ thus gives:

$$\mathcal{L}_\infty = \left| \sum_k |c_k|^2 e^{-iE_k^{(e)}\left(T+\frac{\Delta}{2}\right)} \operatorname{sinc}\left(\frac{E_k^{(e)}\Delta}{2}\right) \right|^2 , \tag{5.44}$$

where $\operatorname{sinc}(x) = \sin(x)/x$. If the ground state in the perturbed Hamiltonian $\mathcal{H}_e$ is not degenerate, we can just retain the term in the sum corresponding to $k = 0$, thus obtaining $\mathcal{L}_\infty \approx |c_0|^4$. Therefore a rough estimate of the Loschmidt echo is given by the overlap between the ground state of $\hat{H}_g$ and the ground state of $\hat{H}_e$. This can be evaluated via second-order perturbation theory in ϵ:

$$c_0 = 1 - \frac{1}{2} \sum_{k\neq 0} \frac{\left| \langle \psi_k^{(g)}| \, \hat{\mathcal{W}} \, |\psi_0^{(g)}\rangle \right|^2}{\left(E_k^{(g)} - E_0^{(g)}\right)^2} \tag{5.45}$$

where $|\psi_k^{(g)}\rangle$ are excited states of $\hat{H}_g$ with energies $E_k^{(g)}$ and $\hat{\mathcal{W}} = \epsilon \sum_{j=j_1}^{j_m} \hat{\sigma}_1^z$. The expression in Eq. (5.45) can be easily computed for the case $m = 1$ following the same steps used to evaluate Eq. (5.37). The final result is:

$$\mathcal{L}_\infty \approx \left[1 - 2\epsilon^2 \sum_{i\neq j} \left(\frac{g_{i1}\, h_{j1}}{\tilde{E}_i^{(g)} + \tilde{E}_j^{(g)}} \right)^2 \right]^4 , \tag{5.46}$$

where the energies $\tilde{E}_k^{(g)}$ are rescaled on the ground state energy, $\tilde{E}_k^{(g)} = E_k^{(g)} - E_0^{(g)}$. In Fig. 5.6 we plotted these results for two different values of the perturbation strength (solid lines); they can be compared with the exact numerical results (circles). Notice that analytic estimates are more accurate for small ϵ, and far from the critical region.

Ising bath: scaling with the size

As one could expect, contrary to the case of a non-local system-bath coupling [63], if the environment is not at the critical point, the decay of the coherences is independent of the number of spins in the bath. This is due to the fact that correlations away from criticality decay exponentially, while they decay as a power law at the critical point. In particular, we checked

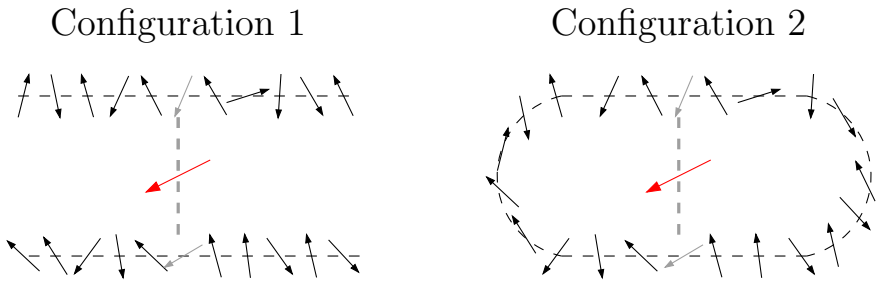

Figure 5.7: Qubit coupled to two non-communicating N-sites chains (configuration 1) and to two spins of a $2N$-sites chain (configuration 2). Here we set $N = 11$.

that both the initial rate α and the saturation value $\mathcal{L}_\infty$ do not depend significantly on N for $\lambda \neq \lambda_c$. We present here a simple argument as a confirmation of this statement. Far from the critical region, independently of the bath size (for sufficiently large baths), a qubit simultaneously coupled to two non-communicating N-sites chains via a one-spin link (configuration 1) should decohere in the same way as if it was coupled to two sufficiently distant spins of a $2N$-sites chain (configuration 2). A pictorial representation of the two configurations described above is shown in Fig. 5.7, where the central spin represents the system, the grey ones are the bath spins directly coupled to the system. We numerically checked that, far from the critical region, the two configurations leave the decoherence unchanged. In particular we chose an $N = 200$ chain, and obtained that, if $|\lambda - \lambda_c| \gtrsim 10^{-2}$, the Loschmidt echo evaluated in the two configurations is the same, up to a discrepancy of 10^{-5}, as it can be seen from Fig. 5.8.

At the critical point instead the behavior dramatically changes: in Fig. 5.9 we plot the decay of $\mathcal{L}$ in time at λ_c for different sizes of the chain and fixed perturbation strength, $\epsilon = 0.25$. The minimum value $\mathcal{L}_0^c$ reached by the Loschmidt echo decays with the size N as

$$\mathcal{L}_0^c = \frac{\mathcal{L}_0}{1 + \beta \ln(N)}. \tag{5.47}$$

Notice also that revivals are due to the finiteness of the environmental size (as in Fig. 5.3). We expect that the coherence loss should go to zero at the thermodynamic limit $N \to \infty$; this is hard to see numerically, since the decay is logarithmic, and the actual value of $\mathcal{L}_0^c$ is still quite far from zero, even for $N = 2000$ spins.

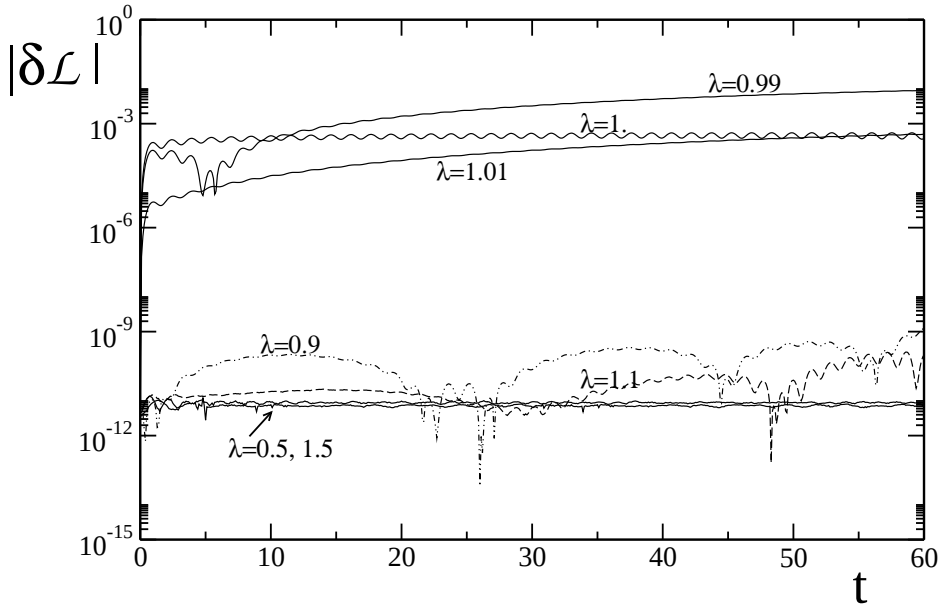

Figure 5.8: Absolute differences in the Loschmidt echo decay between configuration 1 (qubit coupled to two non communicating open $N = 200$ spin Ising chains) and configuration 2 (qubit coupled to two opposite spins of a periodic $N = 400$ spin Ising chain). Different curves are for various values of the transverse field λ.

XY baths with arbitrary xy-anisotropy γ

The properties described in the previous subsections are typical of the Ising universality class, indeed they remain qualitatively the same as far as $\Delta = 0, \gamma \neq 0$ in Eq. (5.3): in particular this class of models has one critical point at $\lambda = 1$. Following our previous analysis of the Ising model ($\gamma = 1$), we focus on the two distinct regions of short- and long-time behavior, whose features are depicted in Fig. 5.10.

At small times the decay is again Gaussian, as in Eq. (5.36), and the first derivative of the decay rate α with respect to λ diverges at λ_c (see Fig 5.10a). As far as the xy anisotropy decreases, the system approaches a limiting case in which $\partial_\lambda^- \alpha = -\infty$, while $\partial_\lambda^+ \alpha = 0$. The asymptotic value $\mathcal{L}_\infty$ at long times shows a cusp at $\lambda = 1$; notice that, as the anisotropy γ decreases, despite the fact that the decay of coherences at short times is always reduced, their saturation value $\mathcal{L}_\infty$ becomes lower for $\lambda < 1$, while gets higher for $\lambda > 1$.

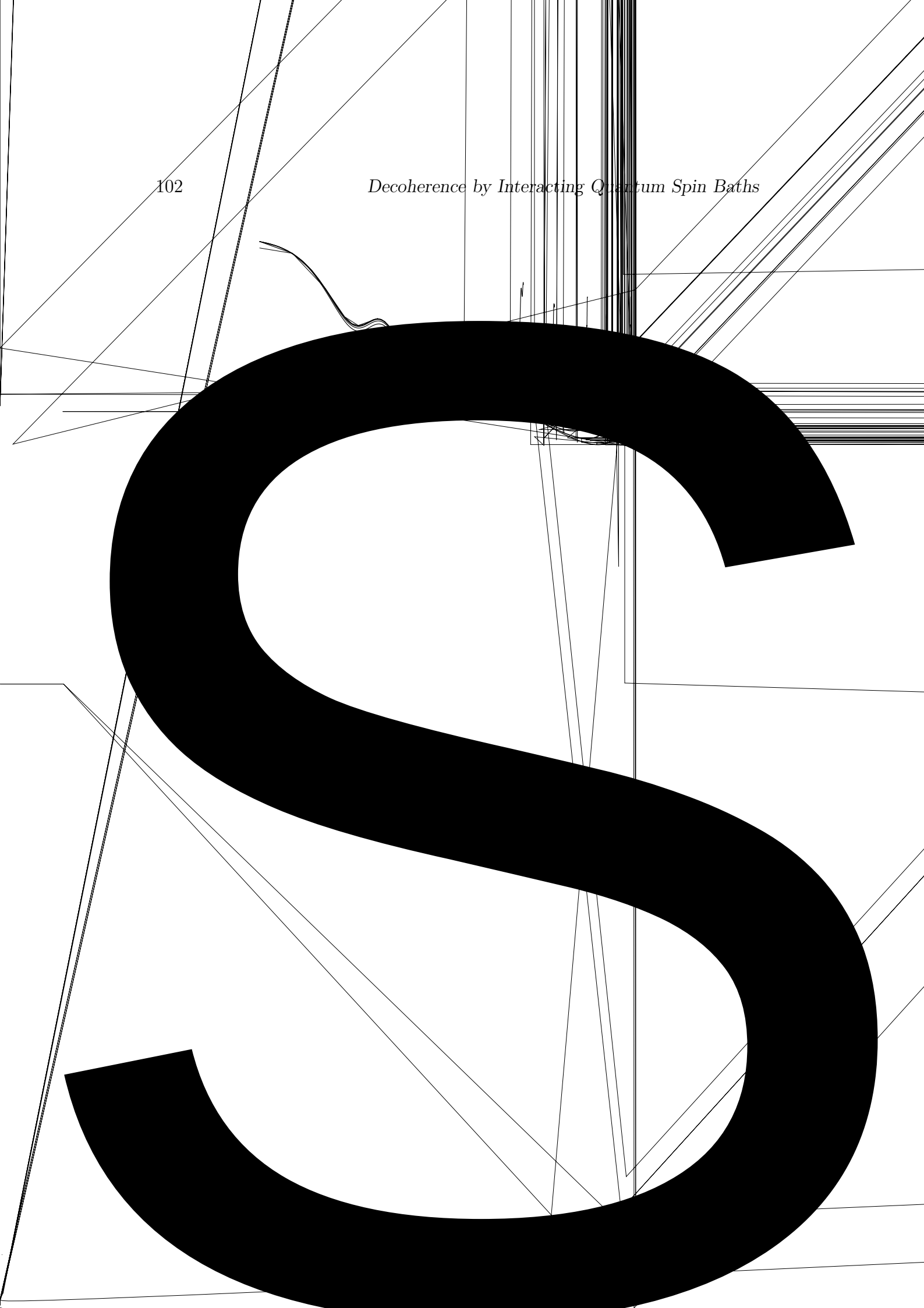

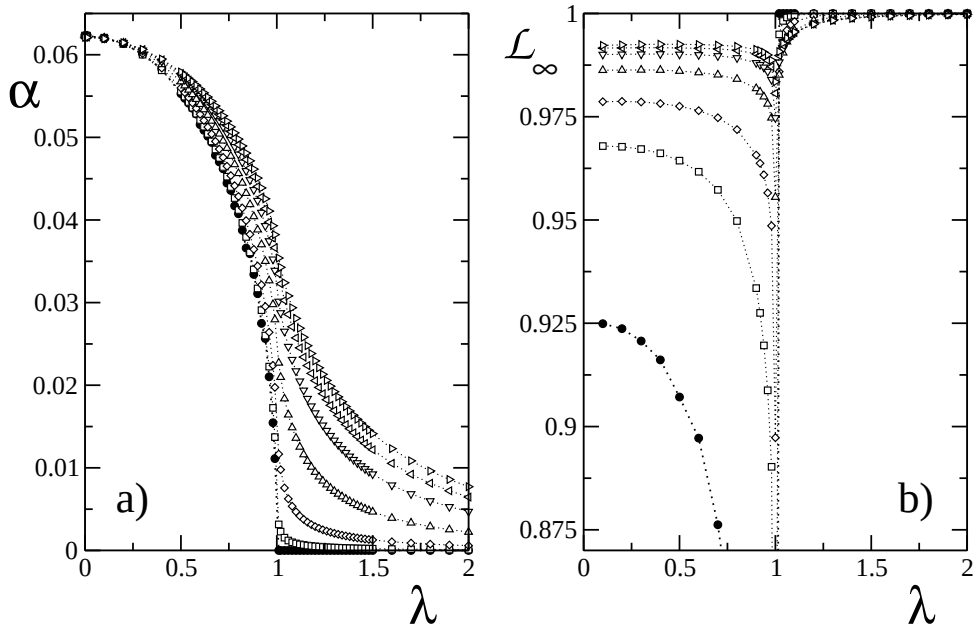

Figure 5.10: Single-link XY models ($m = 1, \Delta = 0$): Short- and long-time behavior of the Loschmidt echo for a qubit coupled to a periodic $N = 300$ spin XY chain, with a coupling strength $\epsilon = 0.25$.
a) Small times (initial Gaussian decay rate α);
b) Long times (saturation values $\mathcal{L}_\infty$). The various curves correspond to different anisotropy values: $\gamma = 0$ (XX-model, full circles), 0.1 (squares), 0.25 (diamonds), 0.5 (triangles up), 0.75 (triangles down), 0.9 (triangles left), 1 (Ising, triangles right).

exhibits a critical behavior over the whole parameter range $|\lambda| \leq 1$, while it is ferromagnetic (anti-ferromagnetic) for $\lambda > 1$ ($\lambda < -1$). The decay of the Loschmidt echo (shown in Fig. 5.11) reflects its critical properties: indeed we found that it behaves as in Eq. (5.47) over the whole range $|\lambda| \leq 1$. In the ferromagnetic case instead the coupled qubit does not decohere at all (i.e. $\mathcal{L}(t) = 1$), since the ground state of the XX-model for $\lambda > 1$ is the fully polarized state with all spins parallel to the external field. The first derivative of the initial decay rate $\partial_\lambda \alpha$ is monotonically negative in the critical region by increasing λ and diverges for $\lambda \to 1^-$, while it is strictly zero for $\lambda > 1$. Also the plateau $\mathcal{L}_\infty$ as a function of λ presents a discontinuity in $\lambda = 1$, since it drops to zero for $\lambda \to 1^-$, and it equals one for $\lambda > 1$.

5.3.2 XXZ Heisenberg bath

In this section we consider a single-link ($m = 1$) XXZ anisotropic Heisenberg chain ($\lambda = \gamma = 0$ in Eq. (5.3)) with anisotropy parameter Δ. We resort to the numerical t-DMRG [110] to compute the Loschmidt echo (5.10), since this specific spin model is not integrable (for details about the static and time-dependent DMRG algorithms see appendix C). Namely, we have to evaluate the overlap between the ground state $|G\rangle$ of $\hat{H}_g$ and the time evolution of the same state under the Hamiltonian $\hat{H}_e$. First, we run the static DMRG algorithm in order to evaluate the ground state $|G\rangle$ of $\hat{H}_g$. The t-DMRG is then subsequently used, to simulate the dynamics of $|G\rangle$ under the Hamiltonian $\hat{H}_e$. We also keep track of the state $|G\rangle$ in the new truncated basis of $e^{-i\hat{H}_e t}|G\rangle$ (see Subsec. C.1.2), so that we can straightforwardly evaluate the

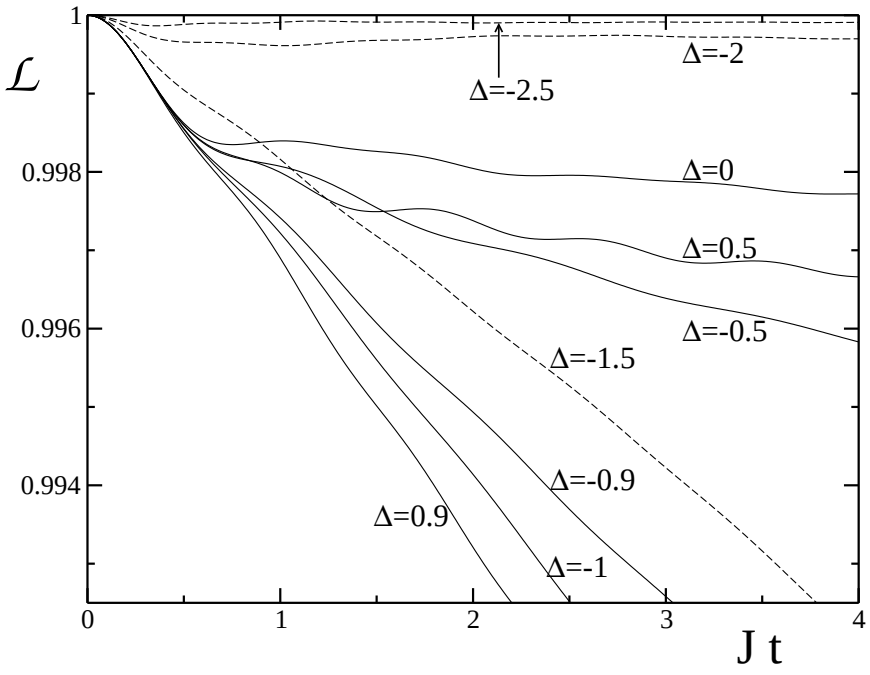

Figure 5.12: Single-link XXZ model ($m = 1, \lambda = \gamma = 0$): Loschmidt echo as a function of time for a qubit coupled to the central spin of an open ended $N = 100$ spin XXZ Heisenberg chain, with coupling strength $\epsilon = 0.1$. The various curves are for different values of the anisotropy $\Delta = 0.9$; curves corresponding to non-critical situations are dashed.

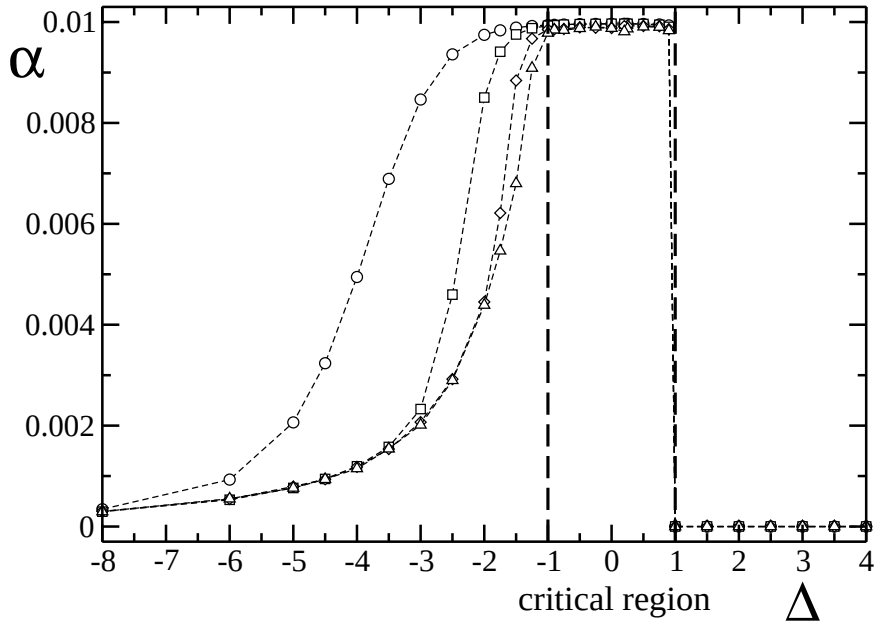

Figure 5.13: Scaling of the decay rate α at short times for an open ended XXZ Heisenberg chain as a function of Δ. The various symbols are for different sizes of the chain: $N = 10$ (circles), 20 (squares), 50 (diamonds), 100 (triangles). The coupling strength between the qubit and the chain is kept fixed at $\epsilon = 0.1$.

overlap in Eq. (5.10). We focus on open boundary conditions, since DMRG with periodic boundaries intrinsically gives much less accurate results [111].

The evaluation of the Loschmidt echo with the t-DMRG is more time- and memory-consuming than its exact calculation in the solvable cases, therefore at present we could not study the behavior of $\mathcal{L}(t)$ at long times. Nonetheless we are able to fully analyze the short-time behavior in systems with environment size of up to $N \sim 10^2$ spins, setting a Trotter slicing $J\,\delta t = 10^{-3}$ and a truncated Hilbert space of dimension $M = 100$. In the following we show the results concerning the coupling of the two-level system to one spin in the middle of the chain: this corresponds to the case with less border effects. We numerically checked that the results are not qualitatively affected from this choice, but changing the system-environment link position results in a faster appearance of finite size effects due to the open boundaries.

In Fig. 5.12 we plot the decay of the Loschmidt echo as a function of time, for various values of the anisotropy Δ and fixed coupling strength $\epsilon = 0.1$. In

the ferromagnetic zone outside of the critical region ($\Delta \geq 1$) $\mathcal{L}$ does not decay at all, as a consequence of the ground state full polarization. In the critical region and for long times, the Loschmidt echo decay is proportional to the modulus of Δ and for $\Delta > -1$ it slows down until it is completely suppressed in the perfectly anti-ferromagnetic regime ($\Delta \to -\infty$). The short time decay is again Gaussian at short times and the rate α is shown in Fig. 5.13 for various sizes of the bath. We notice two qualitatively different behaviors at the boundaries of the critical region: at $\Delta = +1$ there is a sharp discontinuity, while at $\Delta = -1$ the curve is continuous. In the critical region $-1 \leq \Delta \leq 1$ the initial decay rate α is constant and reaches its maximum value due to the presence of low energy modes, while in the ferromagnetic phase $\Delta \geq 1$ it is strictly zero. In the figure, finite size effects are evident: indeed, contrary to the XY model, the decay rate α changes with the bath size N outside the critical region. However, as the system approaches the thermodynamic limit ($N \to \infty$), the dependence on N weakens and, while at $\Delta = -1$ the curve $\alpha(\Delta)$ appears to remain continuous, its first derivative with respect to Δ tends to diverge. On the contrary, the ferromagnetic transition $\Delta = 1$ is discontinuous independently of N.

5.3.3 Decoherence and entanglement

We propose here to establish a link between decoherence effects on the system and entanglement inside the environment. This study can be justified by the fact that decoherence properties of the qubit system seem to be intrinsically related to quantum correlations of the bath, as the proximity to critical points reveals. On the other hand, entanglement quantifies the amount of these correlations that do not have classical counterparts, and it has been widely studied in the recent years, especially in connection with the onset of quantum phase transitions [112, 113, 114, 115].

In Ref. [62] it was shown that two-party entanglement in the environmental bath of a central spin model can suppress decoherence; this effect has been explained as a consequence of entanglement sharing, and it was supposed to be common to any system whose environment maintains appreciable internal entanglement, while evolving in time. We now characterize a more complex case of system-plus-bath coupling, given by Eq. (5.1), with a richer structure in the ground state entanglement which suggests the following picture, valid at short times for $Jt \ll 1$: We expect that when the decay of coherences is quadratic, only short range correlations in the bath are important, therefore

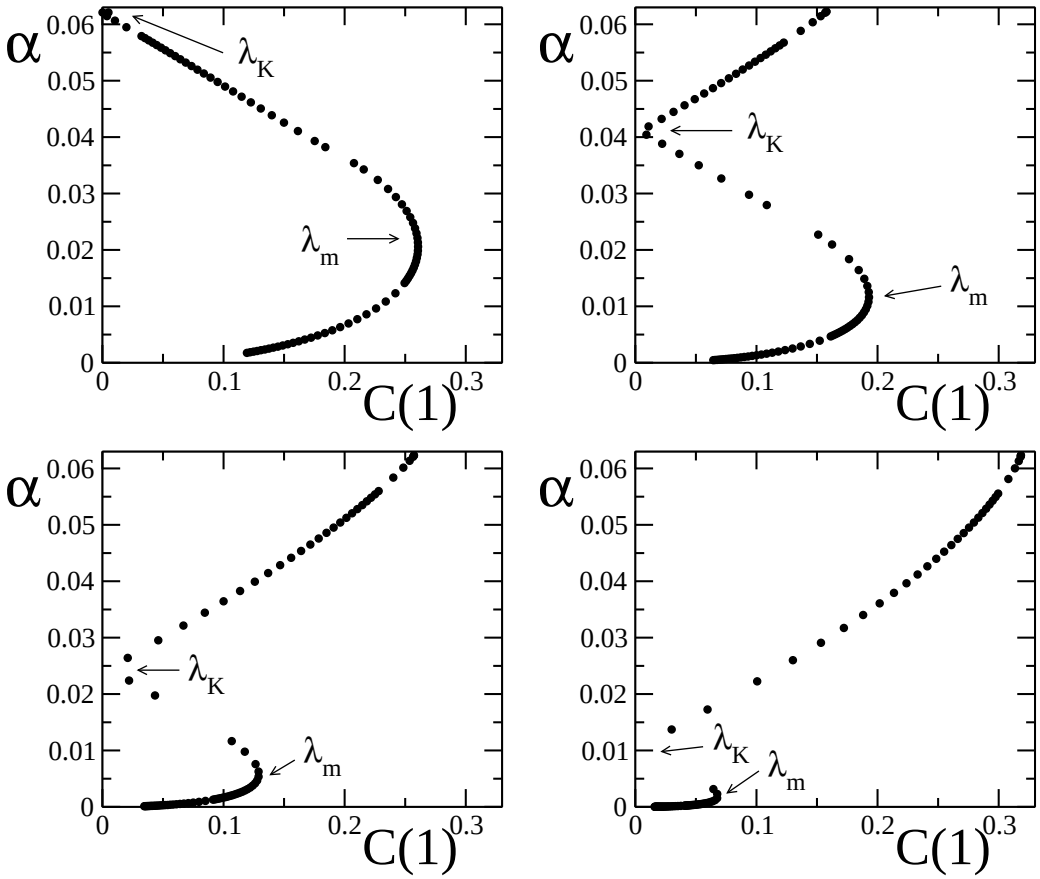

Figure 5.14: Dependence of the Loschmidt echo decay rate α on the nearest-neighbor concurrence $C(1)$ in the XY model, for $\epsilon = 0.25$ and different anisotropy values: $\gamma = 1$ (upper left), 0.5 (upper right), 0.25 (lower left), 0.1 (lower right). Data have been evaluated for an $N = 301$ spin chain.

it seems natural to relate the short-time decay rate α to the two-site nearest neighbor entanglement of the chain, that is measured by the concurrence $C(|i-j|)$ [116], i and $j \equiv i \pm 1$ denoting the positions of two spins inside the chain (see App. D.2.1, Eq. (D.14)).

We start our analysis by considering again the XY spin bath: in this case, the concurrence $C(k)$ can be analytically evaluated in terms of one-point and two-point spin-correlation functions [117, 118]. As long as $\gamma \neq 0$, this system belongs to the Ising universality class, for which it has been shown that the concurrence between two spins vanishes unless the two sites are at most next-to-nearest neighbor [112, 113]. The nearest-neighbor concurrence $C(1)$ presents a maximum that occurs at $\lambda = \lambda_m > 1$, and it is not related to the critical properties of the model. For $\lambda > \lambda_m$ it monotonically decreases to zero, as the ground state goes towards the ferromagnetic product state. For $\lambda < \lambda_m$ the concurrence decreases and precisely reaches zero at the so called "Kurmann point": $\lambda_K = \sqrt{(1+\gamma)(1-\gamma)}$, where the ground state exactly factorizes [119]. In the proximity of the quantum phase transition, the entanglement obeys a scaling behavior [112]; in particular, at the thermodynamic limit the critical point is characterized by a logarithmic divergence of the first derivative of the concurrence: $\partial_\lambda C(1) \sim \ln|\lambda - \lambda_c|$. A similar divergence has been found for the first derivative of the decay rate α of the Loschmidt echo (see the inset of Fig. 5.5). In Fig. 5.14 we analyzed the dependence of α as a function of the nearest-neighbor concurrence $C(1)$. The behavior $\alpha(C)$ is not monotonic, since α monotonically decreases with λ (see Fig. 5.4b), while $C(1)$ has a non-monotonic behavior. Indeed, for $\lambda > \lambda_m$ and $\lambda < \lambda_K$ the two quantities are correlated, while they become anti-correlated for $\lambda_m > \lambda > \lambda_K$.

A similar scenario has been found in the case of the Heisenberg chain as a spin bath, reported in Fig. 5.15. As for the Ising model, the behavior of $\alpha(C)$ is not monotonic, following the concurrence behavior: Indeed $C(1)$ is zero for $\Delta \geq 1$ (in the fully polarized ground state), it monotonically increases while decreasing Δ up to $\Delta = -1$, and then starts to decrease again, vanishing in the perfect anti-ferromagnetic limit $\Delta \to -\infty$ [120]. In conclusion, the behavior $\alpha = \alpha(C)$ is monotonically increasing in the anti-ferromagnetic region, is constant at the criticality, and is strictly zero for the ferromagnetic phase (see Figs. 5.12b, 5.13), resulting in a direct correlation of α and $C(1)$ in the anti-ferromagnetic phase.

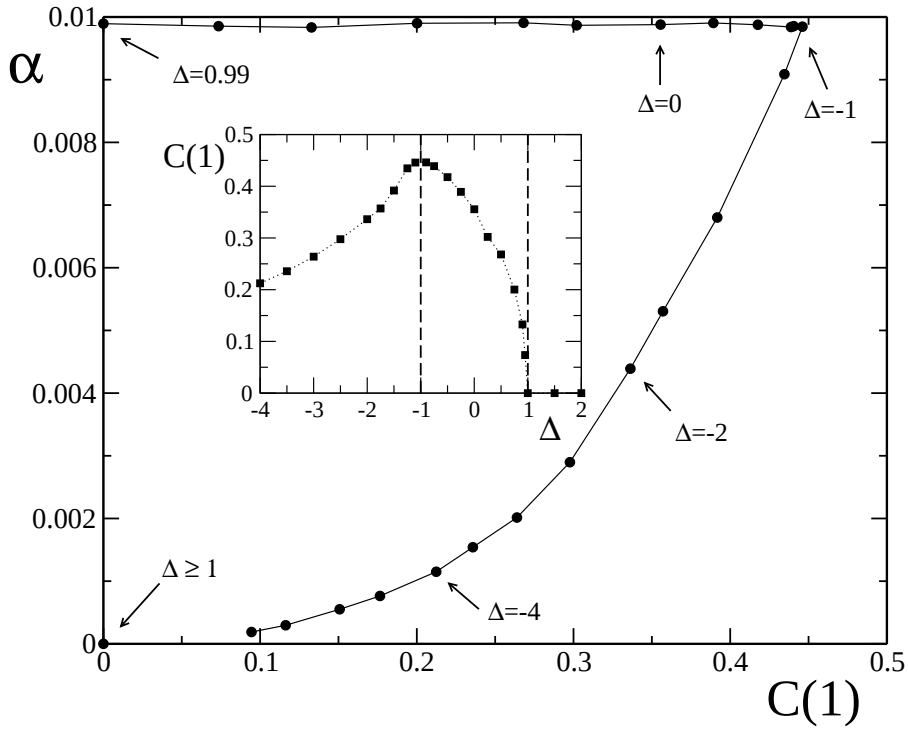

Figure 5.15: Decay rate α as a function of the nearest-neighbor concurrence $C(1)$ in the Heisenberg model for $N = 100$, $\epsilon = 0.1$. Inset: nearest-neighbor concurrence as a function of the anisotropy Δ. The two dashed lines isolate the critical region.

5.4 The multiple-links scenario

In this section we study the case in which the system S is non-locally coupled to more than one spin of the bath E, namely we choose $m \neq 1$ in the interaction Hamiltonian Eq. (5.4). In general, given a number m of links, there are many different ways to couple the two-level system with the bath spins. In the following we will consider two geometrically different setups: a spin-symmetric configuration (type A) where the qubit is linked to some spins of the chain which are equally spaced, and a non-symmetric configuration (type B) where the spins to which the qubit is linked are nearest neighbor. We will also suppose that the interaction strength ϵ between the qubit and each spin of the bath is kept fixed and equal for all the links. A schematic picture of the two configurations is given in Fig. 5.16. We will present results concerning

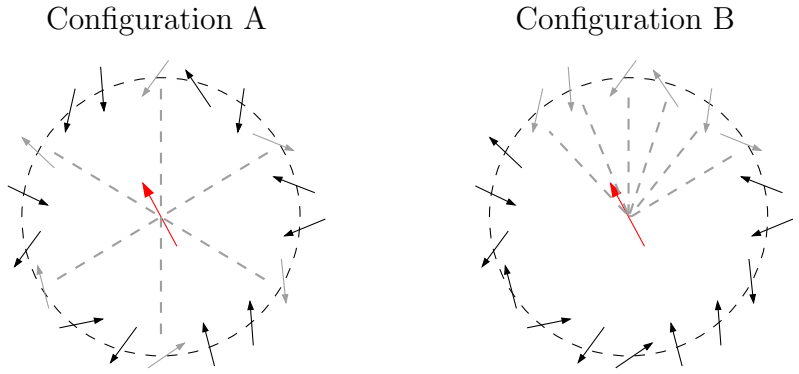

Figure 5.16: Different setups for the coupling of the two-level system (red spin) with the spin chain. The qubit is linked to the spins of the chain depicted in grey. Configuration A shows a star-symmetric setup, while configuration B is a non-symmetric packed setup. As a pictorial example, here we set $N = 18$, $m = 6$.

an environment constituted by an Ising spin chain with periodic boundary conditions. Notice that this system-environment coupling can induce the emergence of criticality in E even for small couping $\epsilon \ll J$ in the central spin scheme, i.e. $m = N$ [63, 64]. Indeed, in this case, a perturbation ϵ results in a change of the external magnetic field of the chain from λ to $\lambda + \epsilon$. If the environment is characterized by $\lambda < 1$, at $\epsilon > 1 - \lambda$ the coupling drives a quantum phase transition in the bath [64].

Short-time behavior

At short times the Loschmidt echo exhibits a Gaussian decay, as in Eq. (5.36), for both configurations. For the setup A the decay rate α, far from the critical region, scales as

$$\alpha \propto m\,\epsilon^2, \tag{5.48}$$

as it can be seen from Fig. 5.17a. The scaling with the number of links m is a consequence of the fact that the short-time behavior is dominated by the dynamics of the environment spins close to those linked to the qubit (see also Sec. 5.3.3). Therefore, if the linked spins are not close to each other, they do not interact among them on the short time scale $Jt \ll 1$. Near the critical point this picture is not valid, since long-range correlations between spins of the bath become important, even at small times. In this region indeed the

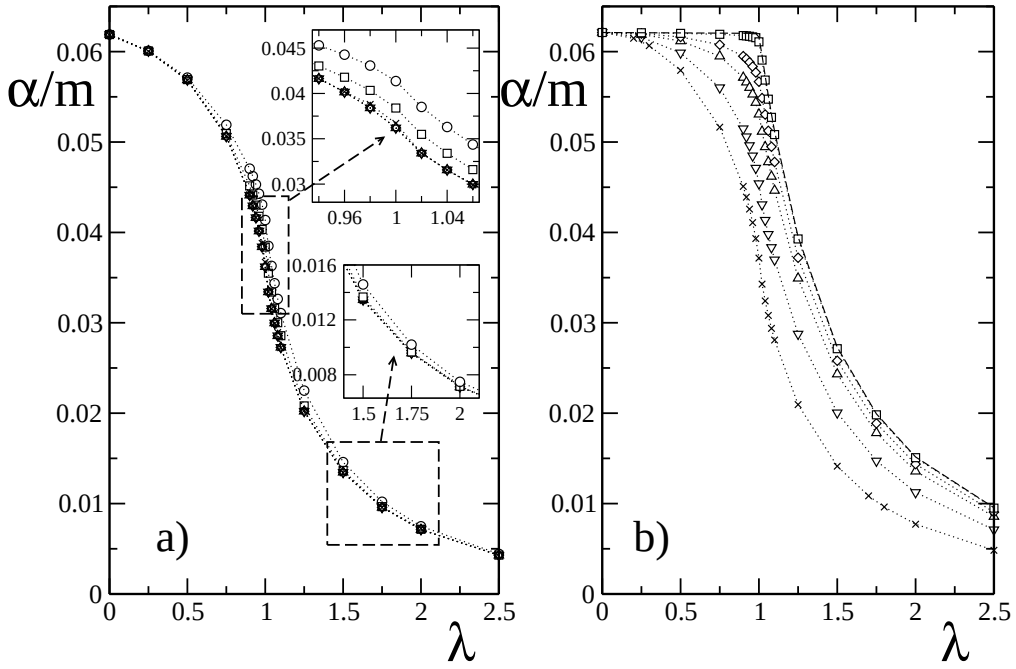

Figure 5.17: Decay rate α rescaled with respect to the number of links m, in a star symmetric configuration (type A) on the left, and in a non-symmetric configuration (type B) on the right. The environment is an $N = 300$ spin Ising chain with periodic boundary conditions. The interaction strength ϵ is kept fixed for all the links between the qubit and the environment spins: $\epsilon = 0.25$. Various symbols stand for different values of m: 1 (crosses), 2 (triangles down), 5 (triangles up), 10 (diamonds), 100 (squares), 150 (circles), 300 (dashed line, right figure). The inset on the left figure shows a magnification of the same plot, centered in proximity of the critical point $\lambda_c = 1$.

scaling $\alpha \sim m$ is less appropriate, as it can be seen in the inset of Fig 5.17a.

The scaling of Eq.(5.48) does not hold any more in the setup B, as in this case collective modes influence the dynamics of the system even at short times, since the spins linked to the central spin are close to each other and they are not independent any more. This is clearly visible in Fig. 5.17b. We notice also that, as m/N increases, α tends to remain constant for $\lambda \leq 1$ and then decreases for $\lambda > 1$. In the limiting case $m = N$, α is positive and strictly constant for $\lambda \leq \lambda_c$; the first derivative $\partial_\lambda \alpha$ presents a discontinuity at λ_c, showing a divergence from the ferromagnetic zone $\lambda \to 1^+$.

Long-time behavior

Here we concentrate on the setup B, since the configuration A is less interesting: indeed for long times the Loschmidt echo behaves as if the qubit was coupled to an environment with a smaller number of spins. In Fig. 5.18 we plotted the asymptotic value of the Loschmidt echo $\mathcal{L}_\infty$ for the setup B. We observe that, as m increases, the coherence loss enhances, and the valley around the critical point λ_c deepens and gets broader. Notice also that, when approaching the central spin limit, the asymptotic value $\mathcal{L}_\infty$ reaches values very close to zero, even far from criticality. This situation is completely different from what occurs in the single-link scenario where, away from criticality, the Loschmidt echo remains very close to one even for non negligible system-bath coupling strengths (e.g., for $\epsilon = J/4$ we found $\mathcal{L}_\infty \sim 0.99$, as it can be seen, for example, from Figs. 5.3, 5.6).

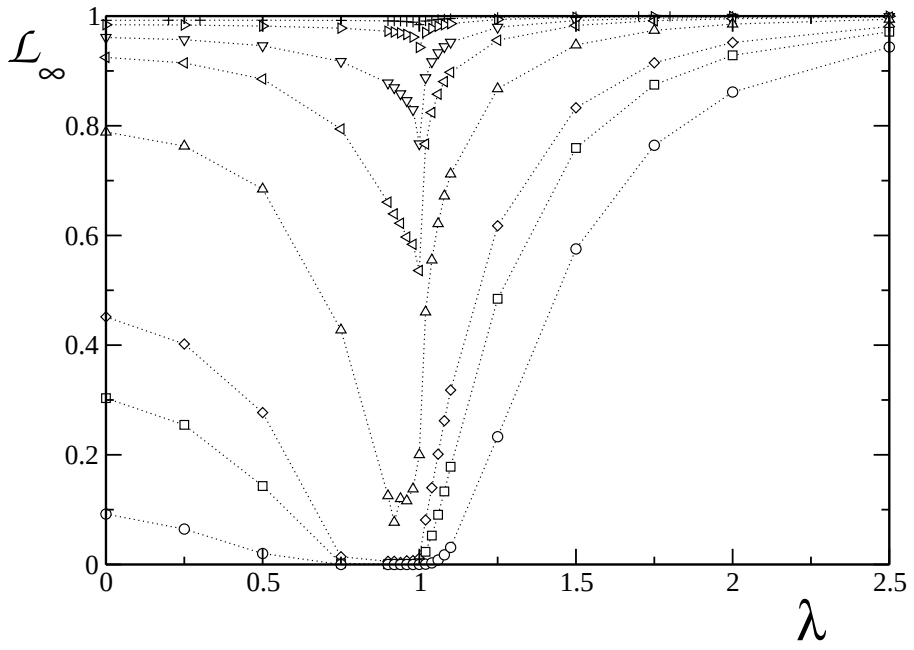

Figure 5.18: Asymptotic value of the Loschmidt echo for setup B; the environment is a 300 spin Ising chain, with $\epsilon = 0.25$. Various symbols stand for different values of m: from top to bottom $m = 1$ (plus), 2 (triangles right), 5 (triangles down), 10 (triangles left), 30 (triangles up), 100 (diamonds), 150 (squares), 300 (circles).

5.4.1 Strong coupling to the bath

Under certain conditions decoherence induced by the coupling with a bath manifests universal features [64]: in Ref. [64] it has been shown that when the coupling to the system drives a quantum phase transition in the environment, the decay of coherences in the system is Gaussian in time, with a width independent of the coupling strength. In particular, for a central spin coupled to an N-spin Ising chain, the Loschmidt echo in Eq. (5.35) is characterized by a Gaussian envelope modulating an oscillating term:

$$\mathcal{L}(t) = |\cos(\epsilon t)|^{N/2}\, e^{-S_N^2 t^2}\,, \tag{5.49}$$

provided that

$$\lambda < 1 \qquad \text{and} \quad \lambda + \epsilon \gg 1\,. \tag{5.50}$$

The oscillations are not universal, but the Gaussian width S_N^2 depends only on the properties of the environment Hamiltonian, in particular it is independent of the coupling strength ϵ and of the transverse magnetic field λ, while it is proportional to the number N of spins in the bath. The case of the central spin model is illustrated in Fig. 5.19a, where the different curves stand for various values of ϵ.

This universal behavior for strong couplings is present in more general qubit-environment coupling, different from the central spin limit, provided that the same conditions in Eq. (5.50) on λ and ϵ hold. In the Ising bath model, we checked that it remains valid also for a number of system-bath links $m \neq N$ and for different geometries, as it can be seen in Fig. 5.19 (panels b-d). The fast oscillations remain proportional to ϵ, since they are a consequence of the interaction $\propto \epsilon\, \tau_z \sigma_j^z$ between the qubit and the spins of the bath. Instead in general the envelope is Gaussian only for small times, but its width S_N^2 is independent of ϵ.

We found that, for the non-symmetric configuration B, S_N^2 depends only on the number of links m, being proportional to it. No dependence from the perturbation strength ϵ, the size N of the bath, or the transverse magnetic field λ has been observed, provided that $m \gtrsim 10$, as it can be seen from Fig. 5.20b. Indeed in the setup B the qubit behaves like in the central spin model: in the regime of strong coupling, the effect of the environment spins not directly linked to the qubit can be neglected since they interact weakly, as compared to the system-bath interactions. Therefore a system strongly coupled to m neighbour spins of an N-spin chain decoheres in the same way as if it was coupled to all the spins of an m-spin chain.

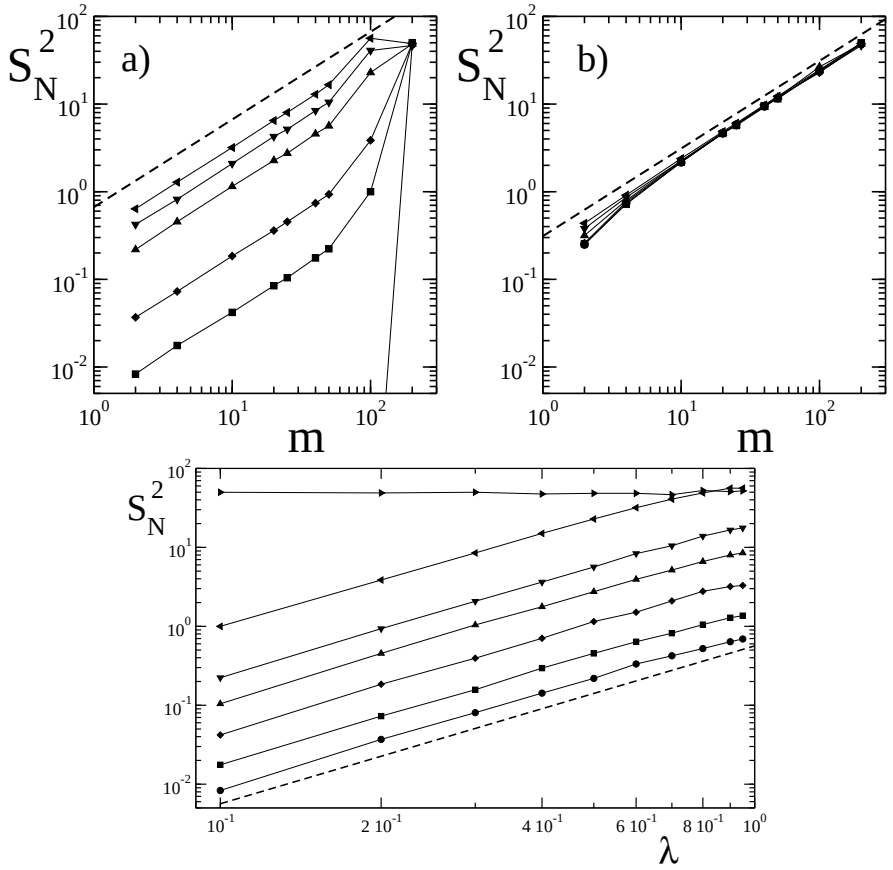

Figure 5.20: Upper: Width of the Gaussian envelope S_N^2 as a function of the number of system-bath links m, for different values of the transverse field: $\lambda = 0$ (circles), 0.1 (squares), 0.2 (diamonds), 0.5 (triangles up), 0.7 (triangles down), 0.9 (triangles left). The two panels correspond to: a) star-symmetric configuration (type A); b) non-symmetric configuration (type B). Dashed curves represent a linear behavior $S_N^2 \sim m$ and are plotted as guidelines. Lower: S_N^2 as a function of λ, for different values of m in setup A: $m = 2$ (circles), 4 (squares), 10 (diamonds), 25 (triangles up), 50 (triangles down), 100 (triangles left), 200 (triangles right). The bath is modeled as an $N = 200$ Ising chain with periodic boundary conditions ($m = 200$ corresponds to the central spin model); the coupling strength is kept fixed and equal to $\epsilon = 80$.

transmitting quantum information: in this system the density matrix of two non-neighbouring spins evolves independently of the other spins.

Chapter 6

Conservative Chaotic Map as a Model of Environment

In this chapter we address the following question: could the many-body environment be substituted, without changing the effects on system's dynamics, by a closed deterministic system with a small number of degrees of freedom yet chaotic? In other words, can the complexity of the environment arise not from being many-body, but from chaotic dynamics? We will give a positive answer, showing that the kicked rotator, which is a single-particle deterministic dynamical system (see Subsec. 2.1.1), can reproduce, in the chaotic regime, the effects of a pure dephasing many-body bath. When the kicked rotator is coupled to a two-entangled-qubits system, the entropy of the system increases, while the entanglement between the two qubits decays, thus illustrating the loss of quantum coherence. In the semiclassical limit, the interaction with the environment can be approximated by a random phase-kick on the two qubits, thus admitting an analytic treatment of the evolution in time of entanglement between them. Our results are in good agreement with the evolution obtained in a pure dephasing stochastic model. Since this pure dephasing decoherence mechanism can be derived in the framework of the Caldeira-Leggett model [55], we have established a direct link between the effects of a many-body environment and of a chaotic single-particle environment. Finally we show that our model, that can be efficiently simulated on a quantum computer, naturally displays memory effects. This may be relevant in the study of non-Markovian environments, since non-Markovian effects, apart from some exceptions [121], are usually hard for analytic treatment.

The chapter is organized as as follows: we first introduce in Sec. 6.1

our model of two qubits coupled to a chaotic environment; in Sec. 6.2, we investigate both the entropy production and the entanglement decay rates, and compare our results with those obtained in the phase-kick model; a Bloch representation of the phase-kick map is also explicitly derived and discussed in Subsec 6.2.1. Finally, in Sec. 6.3, we analyze non-Markovian effects, that are related to the decay of the relevant correlation functions inside the bath.

6.1 The model

We consider a system composed by two qubits that are coupled to an environment modeled by a quantum kicked rotator (see Subsec. 2.1.1 for a brief overview). The global system is governed by the Hamiltonian

$$\hat{H} = \hat{H}_1 + \hat{H}_2 + \hat{H}_{\rm kr} + \hat{H}_{\rm int}\,, \tag{6.1}$$

where $\hat{H}_i = \omega_i\,\hat{\sigma}_i^x$ $(i = 1, 2)$ describes the free evolution of the two qubits,

$$\hat{H}_{\rm kr} = \frac{\hat{n}^2}{2} + k\cos(\hat{\theta})\sum_j \delta(\tau - jT) \tag{6.2}$$

the quantum kicked rotator (see Sec. 2.1.1), and

$$\hat{H}_{\rm int} = \epsilon\,(\hat{\sigma}_1^z + \hat{\sigma}_2^z\cos(\hat{\theta})\sum_j \delta(\tau - jT) \tag{6.3}$$

the interaction between the qubits and the kicked rotator; $\hat{\sigma}_i^\alpha$ $(\alpha = x, y, z)$ denote the Pauli matrices of the i-th qubit. Both the cosine potential in $\hat{H}_{\rm kr}$ and the interaction $\hat{H}_{\rm int}$ are switched on and off instantaneously (kicks) at regular time intervals T. We consider the two qubits as an open quantum system and the kicked rotator as their *common* environment. Note that we choose noninteracting qubits as we want their entanglement to be affected exclusively by the coupling to the environment.

The Hilbert space of the global system is given by

$$\mathcal{H} = \mathcal{H}_1 \otimes \mathcal{H}_2 \otimes \mathcal{H}_{\rm kr}\,, \tag{6.4}$$

where $\mathcal{H}_1$ and $\mathcal{H}_2$ are the two-dimensional Hilbert spaces associated to the two qubits, and $\mathcal{H}_{\rm kr}$ is the N-dimensional space for the kicked rotator.

The time evolution generated by Hamiltonian (6.1) in one kick, i.e., from time tT (prior to the t-th kick) to time $(t+1)T$ (prior to the $(t+1)$-th kick), is described by the operator

$$\hat{U} = e^{-i(k+\epsilon(\hat{\sigma}_1^z+\hat{\sigma}_2^z))\cos(\hat{\theta})}\, e^{-iT\hat{n}^2/2}\, e^{-i\,\delta_1\,\hat{\sigma}_1^x}\, e^{-i\,\delta_2\,\hat{\sigma}_2^x}. \tag{6.5}$$

The effective Planck constant of the system is $\hbar_{\text{eff}} = T = 2\pi/N$, where N is the number of quantum levels used to describe the kicked rotator (the classical limit of the environment is obtained by taking $T \to 0$ and $k \to \infty$, such that $K = kT$ is fixed); $\delta_i = \omega_i T$; ϵ is the coupling strength between the qubits and the environment. Hereafter $t = \tau/T$ denotes the discrete time, measured in number of kicks. The kicked rotator will be always considered on the torus $0 \leq \theta < 2\pi$, $-\pi \leq p < \pi$, where the corresponding classical map describes the stroboscopic dynamics of a *conservative* dynamical system with two degrees of freedom (the phase space portrait is sketched in Fig. 2.1, for different values of K).

6.2 Loss of coherence induced by a chaotic environment

We are interested in the case in which the environment is chaotic (therefore we consider the kicked rotator with $K \gg 1$). The two qubits are initially prepared in a maximally entangled state, such that they are disentangled from the environment. Namely, we suppose that at $t = 0$ the system is in the state

$$|\Psi_0\rangle = \left|\phi^+\right\rangle \otimes |\psi_0\rangle\ , \tag{6.6}$$

where $|\phi^+\rangle = \frac{1}{\sqrt{2}}(|00\rangle + |11\rangle)$ is a Bell state (the particular choice of the initial maximally entangled state is not crucial for our purposes), and $|\psi_0\rangle = \sum_n c_n |n\rangle$ is a generic state of the kicked rotator, with c_n random coefficients such that $\sum_n |c_n|^2 = 1$, and $|n\rangle$ eigenstates of the momentum operator. The evolution in time of the global system (kicked rotator plus qubits) is described by the unitary operator $\hat{U}$ defined in Eq. (6.5). Therefore, any initial pure state $|\Psi_0\rangle$ evolves into another pure state $|\Psi(t)\rangle = \hat{U}^t |\Psi_0\rangle$. The reduced density matrix $\rho_{12}(t)$ describing the two qubits at time t is then obtained after tracing $|\Psi(t)\rangle\langle\Psi(t)|$ over the kicked rotator's degrees of freedom.

In the following we will focus our attention on the time evolution of the entanglement E_{12} between the two qubits, which is directly related to the

concurrence [116] of the reduced density matrix ρ_{12}, (Sec. D.2.1, Eq. (D.14)), and between them and the kicked rotator, measured by the von Neumann entropy S_{12} (Sec. D.1.2, Eq. (D.5)). Clearly, for states like the one in Eq. (6.6), we have $E_{12}(0) = 1$, $S_{12}(0) = 0$. As the total system evolves, we expect that E_{12} decreases, while S_{12} grows up, thus meaning that the two-qubit system is progressively losing coherence.

If the kicked rotator is in the chaotic regime and in the semiclassical region $\hbar_{\text{eff}} \ll 1$, it is possible to drastically simplify the description of the system in Eq. (6.1) by using the *random phase-kick* approximation, in the framework of the Kraus representation formalism. Since, to a first approximation, the phases between two consecutive kicks in the chaotic regime can be considered as uncorrelated, the interaction with the environment can be simply modeled as a phase-kick rotating both qubits through *the same* random angle about the z-axis of the Bloch sphere. This rotation is described by the unitary matrix

$$\hat{R}(\theta) = \begin{bmatrix} e^{-i\epsilon\cos\theta} & 0 \\ 0 & e^{i\epsilon\cos\theta} \end{bmatrix} \otimes \begin{bmatrix} e^{-i\epsilon\cos\theta} & 0 \\ 0 & e^{i\epsilon\cos\theta} \end{bmatrix}, \tag{6.7}$$

where the angle θ is drawn from a uniform random distribution in $[0, 2\pi)$. The one-kick evolution of the reduced density matrix ρ_{12} is then obtained after averaging over θ:

$$\bar{\rho}_{12} \approx \frac{1}{2\pi} \int_0^{2\pi} d\theta\, \hat{R}(\theta)\, e^{-i\delta_2\hat{\sigma}_2^x} e^{-i\delta_1\hat{\sigma}_1^x} \rho_{12}\; e^{i\delta_1\hat{\sigma}_1^x} e^{i\delta_2\hat{\sigma}_2^x} \hat{R}^\dagger(\theta)\,; \tag{6.8}$$

hereafter overbars denote values of the variables at time $t + T$.

Fig. 6.1 shows that in the region $\hbar_{\text{eff}} \ll 1$, in which the environment is a semiclassical object, the time evolution of the entanglement can be accurately predicted by the random phase model. Even though differences between the two models remain at long times due to the finite number N of levels in the kicked rotator, such differences appear at later and later times when $N \to \infty$ ($\hbar_{\text{eff}} \to 0$). The parameter K has been chosen much greater than one, so that the classical phase space of the kicked rotator can be considered as completely chaotic. The actual value $K \approx 99.72676$ approximately corresponds to a zero of the Bessel function $J_2(K)$. This is to completely wipe off memory effects between consecutive and next-consecutive kicks (see Sec. 6.3, Eqs. (6.21)-(6.22) for details).

We point out that the random phase model can be derived from the Caldeira-Leggett model with a pure dephasing coupling $\propto (\hat{\sigma}_1^z + \hat{\sigma}_2^z) \sum_k g_k \hat{q}_k$,

entanglement E_{12} in time, for different values of the oscillation frequencies δ_1 and δ_2 of the two qubits, at a fixed value of the coupling strength ϵ with the environment. The short time decay of E_{12} is always exponential and superimposed to oscillations whose frequency is determined by the internal dynamics of the two qubits [2]. Such oscillations can be clearly seen for $\delta_1 = \delta_2/\sqrt{2} = 10^{-3}$ (dashed curve), while their amplitude and period are too small to be seen on the scale of the figure for $\delta_1 = \delta_2/\sqrt{2} = 10^{-1}$ (solid curve). Finally, oscillations are absent at $\delta_1 = \delta_2/\sqrt{2} = 10^{-4}$ (dotted curve), as in this case their period is longer than the time scale for entanglement decay. Analogous remarks can be done about the oscillations in the entanglement production, measured by the reduced von Neumann entropy plotted in the inset of Fig. 6.2.

An analytic estimate of the entanglement decay rate and of the entropy production can be derived from the random phase-kick model, in the limiting case $\delta_1, \delta_2 \ll \epsilon \ll 1$, that is, when the internal dynamics of the two qubits can be neglected on the time scale for entanglement decay. Starting from Eq. (6.8), it is possible to explicitly write down the map $\rho_{12} \to \bar{\rho}_{12}$ in the Bloch representation (see Subsec. 6.2.1, Eqs. (6.16)). Though in general these equations have to be solved numerically, we provide an explicit analytic solution valid for $\delta_1, \delta_2 \ll \epsilon \ll 1$. In that case, for $\epsilon^2 t \ll 1$ we obtain:

$$E_{12}(t) \simeq 1 - \frac{4\epsilon^2 t}{\ln 2}, \tag{6.10}$$

$$S_{12}(t) \simeq \frac{2\epsilon^2 t}{\ln 2}\left(1 - \ln(2\epsilon^2 t)\right), \tag{6.11}$$

consistently with the numerically obtained behavior of Eq. (6.9) for small times, with $\alpha \approx 4/\ln 2$. The analytic estimates (6.10) for E_{12} and (6.11) for S_{12} are shown as thick dashed curves in Fig. 6.2. A very good agreement with numerical data can be clearly seen for $\delta_1, \delta_2 \ll \epsilon \ll 1$.

In Fig. 6.3 the decay rate Γ of entanglement as a function of ϵ is shown; circles represent numerical data, while the dashed line is the analytic estimate of Eq. (6.10). A dependence $\Gamma \propto \epsilon^2$ is found in both cases. In

[2] In the limit in which one of the two qubits' oscillation frequencies is much smaller than the other, the period $T_{\rm osc}$ of entanglement oscillations is given by $T_{\rm osc} \sim \pi/\max(\delta_1, \delta_2)$. When the two frequencies are comparable ($\delta_1 \sim \delta_2$), then $T_{\rm osc} \sim \pi/\bar{\delta}$, where $\bar{\delta} = (\delta_1+\delta_2)/2$. In general $T_{\rm osc}$ is a non linear function of δ_1 and δ_2; this feature is contained in Eqs. (6.16), which have to be solved numerically for each specific case.

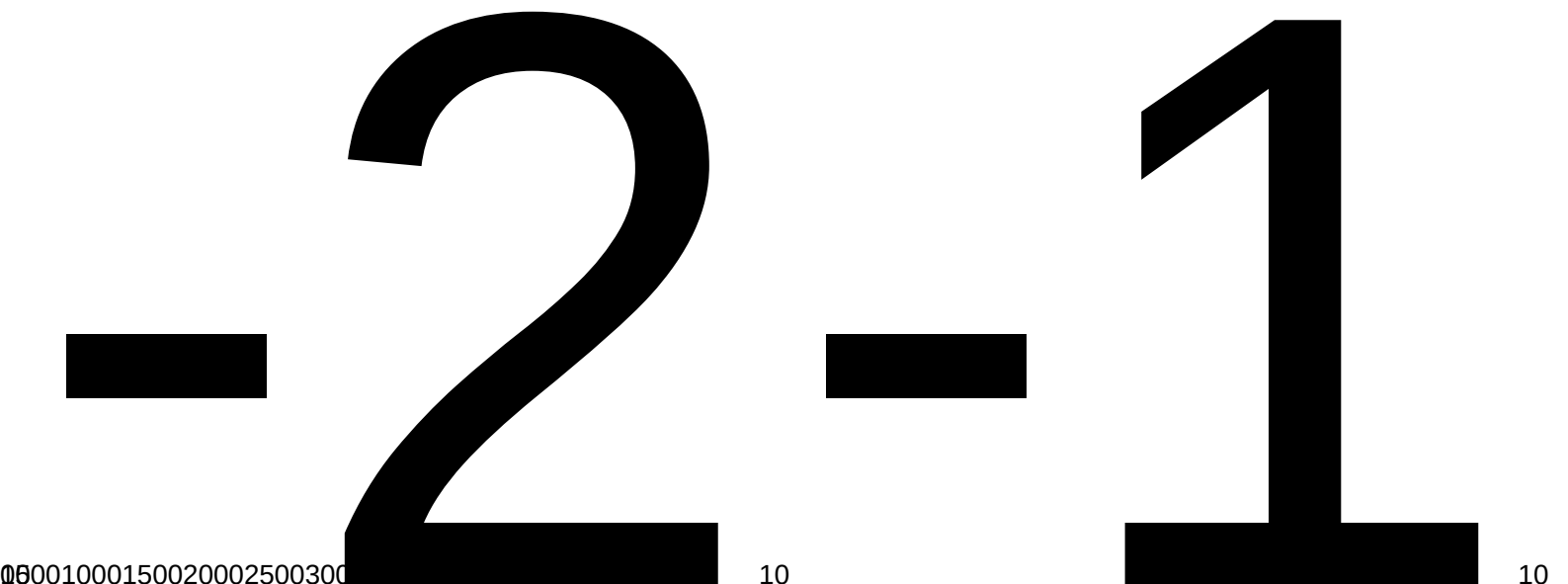
-2
-1
0
10
10

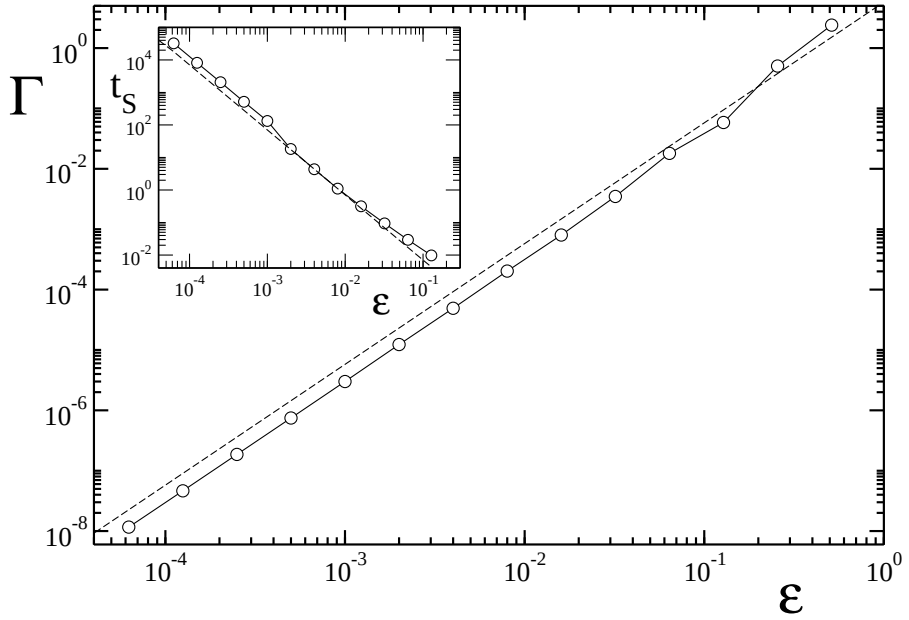

Figure 6.3: Decay rates Γ of the entanglement E_{12} (main figure) and time scales t_S for the Von Neumann entropy (obtained from $S_{12}(t_S) = 0.002$) (inset) as a function of the coupling strength ϵ for $N = 2^{14}$, $K \approx 99.73$, $\delta_1 = \delta_2/\sqrt{2} = 10^{-2}$. Both numerical data (circles) and the analytic predictions (dashed curves) given by Eq. (6.10) (main figure) and Eq. (6.11) (inset) are shown.

We would like to stress that the results discussed in this section do not depend on the initial condition $|\psi_0\rangle$ in (6.6), provided that the kicked rotator is in the chaotic regime. On the other hand, we have found that both the entanglement decay and the entropy production strongly depend on $|\psi_0\rangle$ in the integrable region $K < 1$. This implies that only in the chaotic regime a single particle can behave as a dephasing environment.

Finally we notice that, contrary to other bath models [122], the random phase-kick model is not capable of generating entanglement between the two qubits system. This has been numerically checked both for initial pure separable states and for separable mixtures. We also checked that, starting from a generic two qubit entangled state, the interaction with a chaotic memoryless environment cannot increase entanglement. Namely, we considered 10^7 random initial conditions with $E_{12}(0) \neq 0$ and we found that, already after $t \sim 100$ kicks, entanglement has been always lowered: $E_{12}(t) < E_{12}(0)$.

6.2.1 The random phase model

We provide here an explicit set of equations describing map (6.8) in the Bloch representation, where a generic two-qubit mixed state can be written as:

$$\rho_{12} = \frac{1}{4}\hat{\mathbb{1}} \otimes \hat{\mathbb{1}} + \sum_{i=1}^{3} \alpha_i (\hat{\sigma}^i \otimes \hat{\mathbb{1}}) + \sum_{j=1}^{3} \beta_j (\hat{\mathbb{1}} \otimes \hat{\sigma}^j) + \sum_{i,j=1}^{3} \gamma_{ij} (\hat{\sigma}^i \otimes \hat{\sigma}^j)\,. \quad (6.12)$$

We insert this expansion into Eq. (6.8) and evaluate the commutators between ρ_{12} and the terms that multiply ρ_{12} on the right in (6.8) ($e^{i\delta_1 \hat{\sigma}_1^x}$, $e^{i\delta_2 \hat{\sigma}_2^x}$, and $\hat{R}^\dagger(\theta)$). For this purpose, we use the standard commutation rules for the Pauli matrices:

$$\left[\hat{\sigma}^i, \hat{\sigma}^j\right] = 2i\,\epsilon_{ijk}\,\hat{\sigma}^k\,, \quad (6.13)$$

where ϵ_{ijk} is the Levi-Civita tensor, which is equal to $+1$ if ijk is an even permutation of 123, to -1 for odd permutations, and 0 otherwise. We also use the identity

$$e^{i\delta\hat{\sigma}^x} = (\cos\delta)\,\hat{\mathbb{1}} + i\,(\sin\delta)\,\hat{\sigma}^x \quad (6.14)$$

and expand the exponentials in $\hat{R}^\dagger(\theta)$ to the second order in ϵ. The average over θ is then performed by using

$$\langle \cos^{2n+1}\theta \rangle_\theta = 0\,, \qquad \langle \cos^2\theta \rangle_\theta = \tfrac{1}{2}\,, \qquad \langle \cos^4\theta \rangle_\theta = \tfrac{3}{8}. \quad (6.15)$$

In this way we arrive at the following one-kick map, valid for $\epsilon, \delta_1, \delta_2 \ll 1$:

$$\begin{cases} \bar{\alpha}_x = \alpha_x(1-\epsilon^2) \\ \bar{\alpha}_y = \alpha_y(1-\epsilon^2) - 2\delta_1\alpha_z \\ \bar{\alpha}_z = \alpha_z + 2\delta_1\alpha_y \end{cases} \qquad \begin{cases} \bar{\beta}_x = \beta_x(1-\epsilon^2) \\ \bar{\beta}_y = \beta_y(1-\epsilon^2) - 2\delta_2\beta_z \\ \bar{\beta}_z = \beta_z + 2\delta_2\beta_y \end{cases}$$

$$\begin{cases} \bar{\gamma}_{xx} = \gamma_{xx}(1-2\epsilon^2) + 2\epsilon^2\gamma_{yy} \\ \bar{\gamma}_{yy} = \gamma_{yy}(1-2\epsilon^2) + 2\epsilon^2\gamma_{xx} - 2\delta_1\gamma_{zy} - 2\delta_2\gamma_{yz} \\ \bar{\gamma}_{zz} = \gamma_{zz} + 2\delta_1\gamma_{yz} + 2\delta_2\gamma_{zy} \\ \bar{\gamma}_{xy} = \gamma_{xy}(1-2\epsilon^2) - 2\epsilon^2\gamma_{yx} - 2\delta_2\gamma_{xz} \\ \bar{\gamma}_{yx} = \gamma_{yx}(1-2\epsilon^2) - 2\epsilon^2\gamma_{xy} - 2\delta_2\gamma_{zx} \\ \bar{\gamma}_{xz} = \gamma_{xz}(1-2\epsilon^2) + 2\delta_2\gamma_{xy} \\ \bar{\gamma}_{zx} = \gamma_{zx}(1-2\epsilon^2) + 2\delta_1\gamma_{yx} \\ \bar{\gamma}_{yz} = \gamma_{yz}(1-2\epsilon^2) - 2\delta_1\gamma_{zz} + 2\delta_2\gamma_{yy} \\ \bar{\gamma}_{zy} = \gamma_{zy}(1-2\epsilon^2) + 2\delta_1\gamma_{yy} - 2\delta_2\gamma_{zz}\,. \end{cases} \quad (6.16)$$

These equations can be immediately generalized to the continuous time limit.

We now focus on the

simulate important quantum noise models such as random telegraphic or $1/f$ noise.

In this section, we show that memory effects naturally appear in our model, beyond the random phase approximation [124]. First of all, we point out that, given the coupling $\hat{H}^{(\mathrm{int})} \propto \cos\hat{\theta}$, the bath correlation function relevant for the study of memory effects is $\langle\cos[\theta(t)]\cos[\theta(t')]\rangle$. Even in the chaotic regime, the phases are not completely uncorrelated: in the classical Chirikov standard map (2.6) correlations between cosines of the phases in two consecutive kicks are zero, but the same correlations between phases of two next-consecutive kicks do not vanish. Indeed, as shown in Subsec. 6.3.1, we have:

$$\langle\cos\theta\cos\bar{\theta}\rangle = 0, \tag{6.21}$$

$$\langle\cos\theta\cos\bar{\bar{\theta}}\rangle = \frac{J_2(K)}{2}, \tag{6.22}$$

where, given $\theta = \theta(t)$, $\bar{\theta} = \theta(t+1)$ and $\bar{\bar{\theta}} = \theta(t+2)$, $J_2(K)$ is the Bessel function of the first kind of index 2 and K is the classical chaos parameter. Correlations between more distant kicks, $\langle\cos[\theta(t)]\cos[\theta(t')]\rangle$, with $t'-t>2$, though non vanishing, are very weak for $K \gg 1$, therefore hereafter we will neglect them. Correlations in the kicked rotator dynamics eventually result in a modification of the decay rate Γ of entanglement, as it is clearly shown in Fig. 6.4, where we plot the dependence of Γ as a function of K.

In order to include these memory effects in a phase-kick model, we use the following conditional probability distribution for the angle $\bar{\theta}$ at time $t+1$, given the angle θ at time t:

$$p(\bar{\theta}|\theta) = \begin{cases} \sqrt{J_2}\,\delta\Big[\bar{\theta}-\theta+\dfrac{\pi}{2}(-1)^t\Big] + \dfrac{1-\sqrt{J_2}}{2\pi}, & (J_2>0), \\ \sqrt{-J_2}\,\delta\Big[\bar{\theta}-\theta-\dfrac{\pi}{2}\Big] + \dfrac{1-\sqrt{-J_2}}{2\pi}, & (J_2<0). \end{cases} \tag{6.23}$$

This distribution corresponds to having a $\bar{\theta}$ angle which is correlated with θ (i.e. $\bar{\theta} = \theta \pm \pi/2$) with probability $p_{\mathrm{c}} = \sqrt{|J_2|}$, and completely uncorrelated with probability $p_{\mathrm{nc}} = 1 - p_{\mathrm{c}}$. For our purposes, the relevant properties of the probability distribution $p(\theta,\bar{\theta}) = p(\theta)p(\bar{\theta}|\theta)$ are: $\int d\theta \int d\bar{\theta}\, p(\theta,\bar{\theta}) = 1$; $\int d\theta \int d\bar{\theta}\, p(\theta,\bar{\theta})\cos\theta\cos\bar{\theta} = 0$; $\int d\theta \int d\bar{\theta}\, p(\theta,\bar{\bar{\theta}})\cos\theta\cos\bar{\bar{\theta}} = J_2/2$. Therefore, Eq. (6.23) is a convenient distribution probability leading to a decay

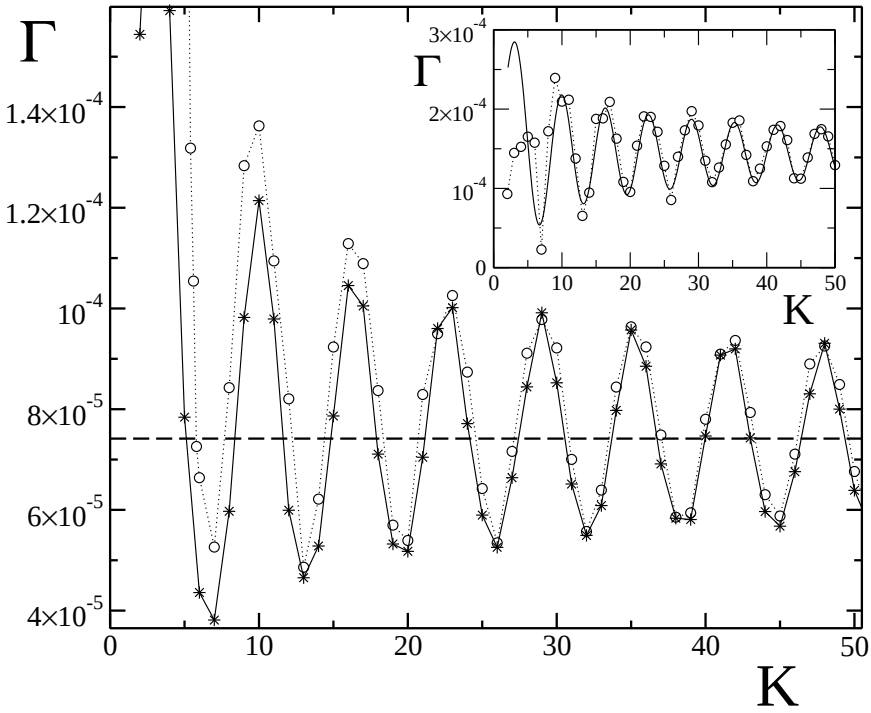

Figure 6.4: Oscillations of the entanglement decay rate Γ as a function of the classical chaos parameter K, at $\epsilon = 5\times10^{-3}, \delta_1 = \delta_2/\sqrt{2} = 10^{-2}$, $N = 2^{14}$ (circles). Stars show the results obtained from a quantum trajectory approach (with average over 5000 trajectories) applied to the phase-kick model (6.24). Inset: entanglement decay rates as a function of K for $\epsilon = 5 \times 10^{-3}$, $\delta_1 = \delta_2 = 0$, $N = 2^{14}$ (circles). The solid curve shows the analytic estimate (6.26).

of the bath correlation function as in Eqs. (6.21) - (6.22) for the kicked rotator model. Of course, other probability distributions could equally well reproduce such decay.

Given the probability distribution $p(\bar{\theta}|\theta)$, it is possible to give a simple generalization of the phase-kick model, taking into account the correlations of Eqs. (6.21) - (6.22). We replace (6.8) with the following two-kicks time evolution map:

$$\bar{\bar{\rho}}_{12} \approx \int_0^{2\pi} d\theta \int_0^{2\pi} d\bar{\theta}\, p(\theta,\bar{\theta})\, \hat{R}(\bar{\theta})\hat{R}(\theta)\, \rho_{12}\, \hat{R}^\dagger(\theta)\hat{R}^\dagger(\bar{\theta}), \tag{6.24}$$

where ρ_{12} and $\bar{\bar{\rho}}_{12}$ are the two-qubit density matrix at times t and $t+2$ and

$p(\theta, \bar{\theta})$ is the joint probability to have a rotation through an angle θ at a time t and an angle $\bar{\theta}$ at time $t+1$. Therefore, $p(\theta, \bar{\theta})$ accounts for correlations between angles at subsequent kicks. Clearly, if angles are completely uncorrelated we have $p(\theta, \bar{\theta}) = 1/4\pi^2$, thus recovering the random phase-kick model (6.8). Note that, for sake of simplicity, map (6.24) has been written for $\delta_1 = \delta_2 = 0$ (the generalization to $\delta_1, \delta_2 \neq 0$ is straightforward).

The phase-kick model (6.24) can be simulated by using the quantum trajectories approach [125]. This method is very convenient in the study of dissipative systems: instead of solving a master equation, one stochastically evolves a state vector, and then averages over many runs. At the end, we get the same probabilities as the ones directly obtained through the density matrix. In our case, the effect of the kicked rotator on the two-qubits wave function is simply that of a rotation through an angle whose value is drawn according to the probability distribution (6.23). Numerical data obtained with the quantum trajectories method are plotted in Fig. 6.4 (stars); notice that, at $K \gg 1$, they are in good agreement with data from simulation of the Hamiltonian model (6.1) (circles).

It is also possible to give an analytic estimate of the decay rate $\Gamma(K)$ in the limit in which the free evolution of the two qubits can be neglected (i.e., we take $\delta_1, \delta_2 \ll \epsilon \ll 1$). As for the random phase model (6.8), in this limit the effect of map (6.24) is pure dephasing. At every map step the density matrix ρ_{12} is of the form of Eq. (6.19). The coherences D_t can be computed by iterating Eq. (6.24). We obtain what follows for the first time steps:

$$\begin{cases} D_1 = 1 - 4\epsilon^2, \\ D_2 = 1 - 8\epsilon^2, \\ D_3 = 1 - \big[12 + 8J_2(K)\big]\epsilon^2, \\ D_4 = 1 - \big[16 + 16J_2(K)\big]\epsilon^2. \end{cases} \tag{6.25}$$

Assuming an exponential decay of entanglement, $E_{12}(t) \sim e^{-\Gamma t}$, we can evaluate Γ starting from D_3 and D_4: $\Gamma \approx \ln(E_3/E_4)$. Thus, from Eqs. (6.25) we obtain the following analytic estimate:

$$\Gamma \approx \frac{4\epsilon^2}{\ln 2}\left(1 + 2J_2(K)\right). \tag{6.26}$$

In the inset of Fig. 6.4 we compute the entanglement decay rates as a function of K in the case $\delta_1 = \delta_2 = 0$. This figure shows that the rates obtained from numerical data for the chaotic bath model (circles) are in good agreement, when $K \gg 1$, with the analytic estimate (6.26) (solid curve).

6.3.1 Angular correlations in the standard map

In this subsection we provide a simple proof of Eqs. (6.21) - (6.22), namely we evaluate correlations between the cosines of the phases of two consecutive and next-consecutive kicks. Averages are performed over all the input phase space:

$$\langle f(\theta,p)\rangle \equiv \lim_{P\to\infty}\left\{\int_{-P}^{P}\frac{\mathrm{dp}}{2P}\int_0^{2\pi}\frac{f(\theta,p)}{2\pi}\,\mathrm{d}\theta\right\} \tag{6.27}$$

We recall that, after a rescaling of the angular momentum: $n \to p = Tn$, the Chirikov standard map (2.6) becomes

$$\begin{cases} \bar{p} = p + K\sin\theta, \\ \bar{\theta} = \theta + \bar{p}, \qquad (\mathrm{mod}\ 2\pi), \end{cases} \tag{6.28}$$

depending only on the parameter $K = kT$ (overbars denote variables at time t+1). Starting from Eq. (6.28), we obtain the following equalities for correlations between two consecutive kicks:

$$\begin{aligned} \left\langle \cos\theta\cos\bar{\theta}\right\rangle &= \langle\cos\theta\cos\left(\theta+p+K\sin\theta\right)\rangle \\ &= \langle\cos p\rangle\,\langle\cos\theta\cos\left(\theta+K\sin\theta\right)\rangle \\ &- \langle\sin p\rangle\,\langle\cos\theta\sin\left(\theta+K\sin\theta\right)\rangle = 0, \end{aligned} \tag{6.29}$$

where we have used some trivial trigonometric identities, and $\langle\cos x\rangle = \langle\sin x\rangle = 0$.

Correlations between two next-consecutive kicks are evaluated by considering values at times $t+1$ (denoted by an overbar) and $t-1$ (denoted by an underbar). The map in Eq. (6.28) can be straightforwardly inverted to give backward evolution:

$$\begin{cases} \underline{p} = p - K\sin(\theta - p), \\ \underline{\theta} = \theta - p, \qquad (\mathrm{mod}\ 2\pi). \end{cases} \tag{6.30}$$

Therefore, from Eqs. (6.28) and (6.30), after some simple algebra we obtain:

$$\begin{aligned} &\left\langle \cos\bar{\theta}\cos\underline{\theta}\right\rangle = \langle\cos\left(\theta+p+K\sin\theta\right)\cos\left(\theta-p\right)\rangle \\ &= \frac{1}{2}\,\langle\cos\left(2\theta+K\sin\theta\right)\rangle = \frac{1}{2}J_{-2}(K) = \frac{1}{2}J_2(K), \end{aligned} \tag{6.31}$$

where

$$J_n(K) = \frac{1}{2\pi}\int_0^{2\pi}\cos\left(K\sin\theta - n\theta\right)\mathrm{d}\theta \tag{6.32}$$

is the Bessel function of the first kind of index 2.

Chapter 7

Spin-1 Bosons on One-Dimensional Lattices

In this chapter we return to the problem of the simulation of quantum physical systems. As already stated in Sec 1.2, the simulation of quantum many-body systems is generally a very demanding task, since the size of the Hilbert space grows exponentially with the number of particles. It is believed that quantum computation would be particularly helpful in this direction: the mere growth in memory requirement would be only linear, since a quantum computer is itself a many-body quantum system. Unfortunately, technological requirements in order to build such machines are very demanding [10], and at present they are still far from being fulfilled.

Nonetheless, it is possible to efficiently simulate important classes of low dimensional systems by means of advanced numerical techniques, provided only ground state and low-lying states properties are investigated [126]. These systems include models that cover a primary role in the theory of condensed matter, like spin-1/2 chains or Hubbard-like models with nearest neighbor interactions. In Chap. 5 we simulated the short-time dynamics of an anisotropic Heisenberg chain (a model that is not analytically solvable) by means of the time-dependent Density Matrix Renormalization Group algorithm (see Subsec. 5.3.2). In this chapter we focus on the one-dimensional spin-1 Bose-Hubbard model: we present a quantitative characterization of its phase diagram and magnetic properties of the first insulating lobe [127], obtained by means of static DMRG numerical investigations (details about the DMRG algorithm are given in appendix C).

The chapter is organized as follows: in Sec. 7.1 we introduce the spinless

Bose-Hubbard model, and also describe its extension to the spinorial model. In Sec. 7.2 we present a quantitative phase diagram of the one-dimensional Bose-Hubbard spin-1 model. Finally, in Sec. 7.3 we move to a comprehensive characterization of the magnetic properties of its first Mott insulating lobe.

7.1 The Bose-Hubbard model

Bose-Einstein condensation (BEC) is a purely quantum phenomenon consisting in the collapse of a boson gas into a macroscopic quantum state, when cooled under a critical temperature T_c which depends on the gas density [128]. Recently, the usage of standing waves from couples of counter-propagating laser beams has opened the possibility to create an optical lattice with several wells inside an harmonic trap [129]. Atoms in a condensate can be confined to different lattice sites, and by varying the depth of the periodic potential, i.e., the intensity of the laser beams, it is possible to tune interatomic interactions with great accuracy. In particular, the experimental realization of optical lattices has paved the way to study strongly correlated many-particle systems with cold atomic gases [130, 131]; the *Bose-Hubbard model* (BH) is of central interest in this direction, since the dynamics of such systems has been shown to be mappable onto it [132] (see Subsec. 7.1.1). Moreover it is also a paradigm lattice model for the study of Josephson junction arrays [133] and superconducting films [134].

The BH model for spinless particles on a lattice is defined by Hamiltonian

$$\begin{aligned} \hat{H} &= \hat{H}_\epsilon + \hat{H}_t + \hat{H}_U \\ &= \sum_i \epsilon_i \hat{n}_i - \frac{t}{2} \sum_{\langle ij \rangle} \left(\hat{b}_i^\dagger \hat{b}_j + \hat{b}_j^\dagger \hat{b}_i \right) + \frac{U}{2} \sum_i \hat{n}_i \left(\hat{n}_i - 1 \right) , \end{aligned} \tag{7.1}$$

where the operator $\hat{n}_i = \hat{b}_i^\dagger \hat{b}_i$ counts the number of bosonic atoms at lattice site i; the annihilation and creation operators $\hat{b}_i$ and $\hat{b}_i^\dagger$ obey the canonical commutation rule $\left[\hat{b}_i, \hat{b}_j^\dagger \right] = \delta_{ij}$. The parameter U corresponds to the strength of the on-site repulsion of two atoms on lattice site i; t is the hopping matrix element between adjacent sites i and j; ϵ_i describes an energy offset of each lattice site. Localization is related to the single-particle bound states in the wells; the corresponding contribution $\hat{H}_\epsilon$ in Eq. (7.1) is thus proportional to the site population. On the other hand, the kinetic energy allows the bosons to delocalize; this corresponds to hopping contributions $\hat{H}_t$ that destroy a

particle on site i and create another one on site j. In the Hamiltonian of Eq. (7.1) only nearest neighbor interactions are allowed; this assumption is justified by the fact that it is the leading term in the tight binding approximation. More precisely, the hopping coefficients t_{ij} are proportional to the overlap between wavefunctions on sites i and j, thus they decay exponentially with the distance $|i-j|$. Finally, many-body systems are characterized by correlations and interaction between particles. The lowest order term is the on-site two-body interaction $\hat{H}_U$, which has to be proportional to $n_i(n_i-1)$, due to commutation rules of bosonic operators $\hat{b}_i$. The coefficient U is related to the appropriate microscopic model for interactions; for long-range interactions it has to be generalized to a non local matrix U_{ij}.

In absence of the hopping term, a uniform chemical potential $\epsilon_i = \mu$ fixes the particle number on each site to be equal to its integer part plus one. Once μ is fixed, the BH Hamiltonian of Eq. (7.1) is characterized by two energy scales: an on-site repulsion energy U between the bosons and an hopping energy t which allows bosons to delocalize. At zero temperature and in the limit $U \gg t$ bosons are localized because of the strong local interactions. In this case there is a gap in the spectrum for adding or subtracting a particle. This phase is called the *Mott insulator phase* (MI). In the opposite limit $U \ll t$ bosons are delocalized, therefore are in a *superfluid phase* (SF). A direct transition between the MI and the SF phase occurs at a given critical value of the ratio t/U, which depends on the chemical potential, in such a way that a lobe structure arises [135] in the $\mu - t$ plane (see Fig. 7.1): inside the lobes particles are localized on the lattice sites (MI), whereas outside the system is always globally superfluid (SF). At integer values of μ/U two different integer fillings are degenerate and thus superfluidity is present for an arbitrarily small hopping t. The higher is the Mott particle number, the higher are the bosonic hopping matrix elements involved, and thus the smaller is the lobe in the phase diagram. Dimensionality of the system can affect the form and the size of the lobes, but not this general structure.

We notice that the Superfluid-Insulator transition in BH models has been extensively studied both theoretically [133, 134, 135] and experimentally [136]. We also notice that the uniform potential picture catches the essential physical effects near the center of a shallow enough trapping potential, where local energy offsets are negligible. More generally, the spatial dependence of ϵ_i leads to a spatial dependent phase diagram; the system is locally a Mott insulator or a Superfluid according to the position of (t, ϵ_i) in Fig. 7.1. Henceforth we will restrict our analysis to the uniform case.

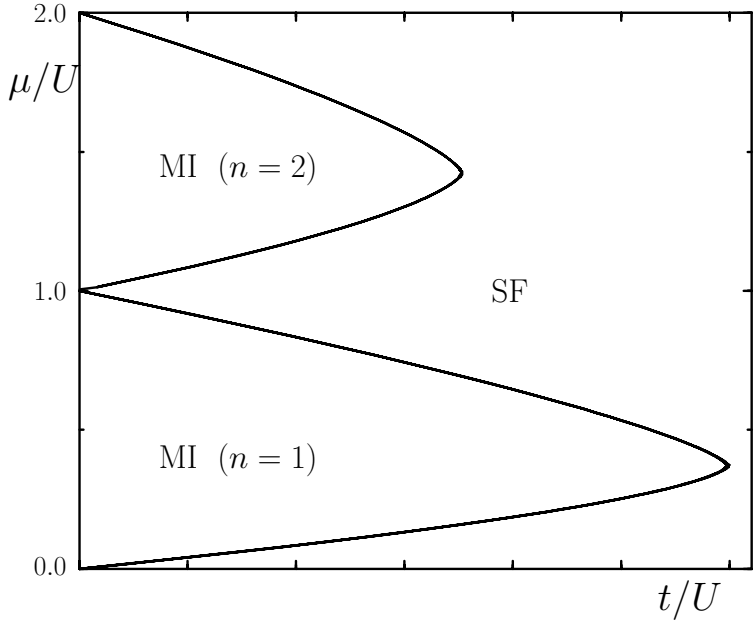

Figure 7.1: Qualitative phase diagram of the Bose-Hubbard model. Dimensionality effects are not taken into account here.

7.1.1 Cold atoms in optical lattices

The dynamics of an ultracold dilute gas of bosonic atoms in an optical lattice can be mapped into a Bose-Hubbard model, as shown in Ref. [132]. This setup has great advantages as compared to condensed matter systems, due to the possibility of a precise knowledge of the underlying microscopic models and an accurate control of the various couplings. The starting point in the derivation of the BH model in optical-lattice systems is the second quantized Hamiltonian operator for bosonic atoms in an external trapping potential:

$$\begin{aligned}\hat{H} &= \int d^3x \hat{\Psi}^\dagger(\mathbf{x}) \left[\frac{\hbar^2}{2m} \Delta_{\mathbf{x}}^2 + V_0(\mathbf{x}) + V_{\text{ext}}(\mathbf{x}) \right] \hat{\Psi}(\mathbf{x}) \\ &\quad + \frac{1}{2} \int d^3x \int d^3x' \hat{\Psi}^\dagger(\mathbf{x}) \hat{\Psi}^\dagger(\mathbf{x}') V_{2b}(\mathbf{x} - \mathbf{x}') \hat{\Psi}(\mathbf{x}') \hat{\Psi}(\mathbf{x}) \,, \end{aligned} \tag{7.2}$$

where $\hat{\Psi}(\mathbf{x})$ is a boson field operator for atoms in a given internal atomic state, $V_0(\mathbf{x})$ is the optical lattice potential, $V_{\text{ext}}(\mathbf{x})$ describes an external trapping potential, and $V_{2b}(\mathbf{x} - \mathbf{x}')$ accounts for two-body interactions. In

a typical axial symmetric magneto-optic harmonic trap the optical lattice potential has the form:

$$V_0(\mathbf{x}) = V_0 \sin^2(kx)\,, \tag{7.3}$$

where $k = 2\pi/\lambda$, and λ is the wavelength of the laser light, corresponding to a lattice period $a = \lambda/2$. The external potential is given by a slowly varying harmonic trap:

$$V_{\text{ext}}(\mathbf{x}) = \frac{m}{2}\Big[\omega_\parallel^2 x^2 + \omega_\perp^2 (y^2 + z^2)\Big]. \tag{7.4}$$

The ratio $\Omega = \omega_\parallel/\omega_\perp$ is inversely proportional to the ratio between the mean square sizes in the two directions. Transverse radius is estimated by the so called "oscillator length" $l_\perp = (\hbar/m\omega_\perp)^{1/2}$; the lattice structure has a recoil momentum $k_R = \pi/a$.

The theory of neutral bosonic atoms has been developed under a couple of basic assumptions: firstly the atoms are supposed to be confined to the lowest Bloch band of the periodic potential, then only binary collisions are taken into account, omitting the higher order ones (*dilute gas* approximation). Diluteness condition is fulfilled when the mean distance between particles is much larger than the typical range of the interatomic forces. The latter could be estimated with the s-wave scattering length a_s, that is the effective radius for a gas of hard spheres with the same scattering distribution at small energies. Under typical experimental setups this condition is always verified, since the diluteness parameter $\sqrt{na_s^3}$ (where n is the particle density) is very small ($\approx 10^{-3}$). Therefore interatomic forces can be modeled by two-body contact interactions of the form

$$V_{2b}(\mathbf{x} - \mathbf{x}') = g\delta(\mathbf{x} - \mathbf{x}'), \qquad \text{with} \quad g = \frac{4\pi\hbar^2 a_s}{m}\,. \tag{7.5}$$

Positive g indicates repulsion, negative one attraction: in experiments both cases can be treated. In the presence of a strong optical lattice and sufficiently shallow external confinement in the x direction, one can employ the *tight binding* approximation. The field operators can be expanded in terms of the single-particle Wannier functions localized at each lattice site $x_i = ia$. Single band approximation is satisfied in one-dimensional arrays if the radial waist $l_\perp$ of the system is negligible with respect to the lattice spacing a. Thus the excited bands are much higher in energy than any other term that appears in the Hamiltonian. In the harmonic limit the Wannier functions $\omega(\mathbf{x})$ factorize in the product of harmonic oscillator states in each direction,

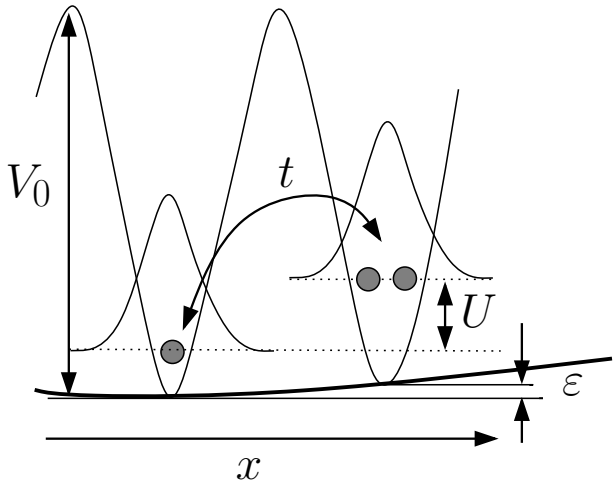

Figure 7.2: Realization of the Bose-Hubbard model in an optical lattice. V_0 is the optical lattice potential, U represents the on-site repulsion of two atoms on a lattice site, and t the hopping matrix element between adjacent sites. The offset ϵ of the bottoms of the wells is due to a trapping potential V_{ext}.

with the trapping potential almost constant between adjacent lattice sites. We thus have:

$$\hat{\Psi}(\mathbf{x}) = \sum_i \hat{b}_i \omega_x(x - x_i)\omega_y(y)\omega_z(z), \tag{7.6}$$

where the ω are supposed to be Gaussian.

Using this ansatz one can see that Eq. (7.2) reduces to the Bose-Hubbard Hamiltonian of Eq. (7.1), in which the coefficients are given in terms of superposition integrals of the Wannier functions, and their derivatives (details can be found, e.g., in Ref. [137]). Constant parts of the external potential, like zero-point energies due to harmonic approximation, are neglected. Using the recoil energy $E_R = \pi^2\hbar^2/(2ma^2)$ as scale unit ($\tilde{E} = E/E_R$) we get:

$$\tilde{U} = \sqrt{\frac{8}{\pi^3}}\frac{a_s a}{l_\perp^2}\tilde{V}_0^{\,1/4} \tag{7.7}$$

$$\tilde{\epsilon}_i = \frac{i^2}{\pi^2(l_\parallel/a)^4} \tag{7.8}$$

$$\tilde{t} = \left(\frac{\pi^2}{4} - 1\right)\tilde{V}_0 \exp\left[-\frac{\pi^2}{4}\sqrt{\tilde{V}_0}\right]. \tag{7.9}$$

We stress the fact that, apart from the external confining potential, both t and U can thus be controlled just by tuning the laser intensity V_0.

7.1.2 Spin degrees of freedom

Recent achievement of BEC of atoms with hyperfine states $S = 1$ and their entrapment in optical lattices by means of far-off-resonance optical traps has opened the exciting possibility to study spinor condensates (for a review, see Ref. [138]). Spin effects, typically difficult to observe in usual magnetic traps, are enhanced by the presence of stronger interactions and smaller occupation number, thus opening the possibility to have a rich variety of phases characterized by different magnetic ordering.

In s-wave approximation, the scattering between two identical bosons with hyperfine spin 1 is well described by the contact potential:

$$\begin{aligned} V_{2b}(\mathbf{x}) &= \frac{4\pi\hbar^2}{m}\delta(\mathbf{x})\big(a_0\mathcal{P}_0 + a_2\mathcal{P}_2\big) \\ &\quad \frac{4\pi\hbar^2}{3m}\delta(\mathbf{x})\big((a_0+2a_2)\mathbb{I} + (a_2-a_0)\mathbf{S_1}\cdot\mathbf{S_2}\big) \end{aligned} \tag{7.10}$$

where subscript labels denote the total spin of the incident pair; $\mathcal{P}_S$ are spin channel projectors, and a_0, a_2 are the s-wave scattering lengths. A generalization of the tight binding approach, explained in the previous subsection, is obtained by using the spin label for the operators $\hat{a}^\dagger_{i,\sigma}$ ($\hat{a}_{i,\sigma}$), which create (annihilate) a particle in the lowest Bloch band localized on lattice site i and having a spin-z component σ. Details of this calculations are given in Ref. [139]; here we just quote the results.

An extra term arises in the Bose-Hubbard Hamiltonian of Eq. (7.1):

$$\hat{H}_{S=1} = \hat{H}_\epsilon + \hat{H}_t + \hat{H}_U + \hat{H}_S, \quad \text{where} \quad \hat{H}_S = \frac{U_2}{2}\sum_i \left(\hat{\mathbf{S}}^2_{\mathbf{i}} - 2\hat{n}_i\right) \tag{7.11}$$

The total spin operator on a site is given by:

$$\hat{\mathbf{S}}_{\mathbf{i}} = \sum_{\sigma,\sigma'} \hat{a}^\dagger_{i,\sigma}\hat{\mathbf{T}}_{\sigma,\sigma'}\hat{a}_{i,\sigma'}, \tag{7.12}$$

where $\hat{\mathbf{T}}$ are the usual spin-1 operators for single particles. The sign of U_2 distinguishes between on-site ferromagnetic and anti-ferromagnetic behaviors.

The ratio between the interaction couplings is bound to be:

$$\frac{U_2}{U_0} = \frac{a_2 - a_0}{a_0 + 2a_2} \quad \longrightarrow \quad -1 < \frac{U_2}{U_0} < \frac{1}{2}\,; \tag{7.13}$$

the tunneling conserves the single particle spin, so there are three independent channels, with the same couplings. Atoms residing on the same lattice site have identical orbital wavefunction and their spin function must be symmetric; such a constraint implies that $s_i + n_i$ must be even [1]. The uniqueness of the completely symmetric state with fixed spin and number makes it possible to denote the single-site states with $|n_i s_i z_i\rangle$, where z_i is the z-projection of the i-th spin.

7.2 Phase diagram of the one-dimensional Spin-1 Bose-Hubbard model

In this section we present numerical data which determine the location of the Mott lobes in the phase diagram of the spinorial Bose-Hubbard model

[1] A simple argument which leads to the constraint is the following:
Let us consider n identical spin 1 bosons, whose state is labelled only by $z = 0, \pm 1$; the system wavefunction must be completely symmetric, therefore one is interested in the combinations which are invariant under the action of the permutation group $\mathbb{Z}_n$. The number of such states corresponds to the number of independent orbits of the group. An orbit of the group is labelled by the spin component numbers $n_0, n_\pm$. For a fixed magnetization $s^z \equiv n - m$ one has to satisfy the constraints $n_+ + n_0 + n_- = n$ and $n_+ - n_- = s^z = n - m$, that are equivalent to

$$\begin{cases} 2n_+ + n_0 = 2n - m \\ 2n_- + n_0 = m \end{cases}$$

which admit $[m/2] + 1$ independent solutions, identified by $n_- = 0, 1, \ldots, [m/2]$.
The lowering operator $\hat{S}^- = \sum_{p=1}^{n} \hat{S}_p^-$ is invariant under $\mathbb{Z}_n$, thus preserves the symmetry properties of a state. On the other hand, it is well known that from $|s,\, s^z = s\rangle$ it is possible to obtain all other states with the same total spin $|s,\, s^z\rangle$, by simply applying iteratively $\hat{S}^-$. For $m = 0$ the unique symmetric state has total spin $s = n$; when $m = 1$ only one orbit is present and the corresponding state cannot be other than the "son" $|n, n-1\rangle$ of $|n, n\rangle$. On the other hand, for $m = 2$ a new possibility opens: apart from $|n, n-2\rangle$, another independent symmetric state is present. It must have $s = n - 2$ since there is no possible "father" with higher spin. Thus, every time m is even, a new independent orbit appears, and it is possible to create a state with a total spin $s - m$. This concludes the proof, since all these such generated states evidently satisfy $s_i + n_i$ even.

described by Eq. (7.11) [127]:

$$\begin{aligned}\hat{H} &= \frac{U_0}{2}\sum_i \hat{n}_i(\hat{n}_i-1) + \frac{U_2}{2}\sum_i \left(\hat{\mathbf{S}}_i^2 - 2\hat{n}_i\right) - \mu\sum_i \hat{n}_i \\ &\quad - t\sum_{i,\sigma}\left(\hat{a}^\dagger_{i,\sigma}\hat{a}_{i+1,\sigma} + \hat{a}^\dagger_{i+1,\sigma}\hat{a}_{i,\sigma}\right) . \end{aligned} \tag{7.14}$$

Hereafter we will consider a uniform chemical potential ($\epsilon_i = -\mu \ \ \forall i$) , thus supposing an on-site energy offset equal for all lattice sites. In particular, we will show the even/odd lobe asymmetry in the spinor case, as discussed in Ref. [140]. From now on, U_0 is set as the energy scale unit: $U_0 = 1$. Furthermore, we discuss only the anti-ferromagnetic case ($0 < U_2 < 1/2$). This is a very important question, since up to now the location of the phase boundary of the spinor Bose-Hubbard model has been determined by mean-field and strong coupling approaches, but never with quantitative calculations; moreover in one dimension non-perturbative effects are more pronounced.

In absence of spin dependent coupling, a qualitative picture of the phase diagram can be drawn starting from the case of zero hopping ($t = 0$), where the ground state is separated from any excited state by a finite energy gap. For finite hopping strength, the energy cost to add or remove a particle $\Delta E_\pm$ (excitation gap) is reduced and, at a critical value $t_c^\pm(\mu)$, it vanishes. This phase is named the Mott insulator (MI). For large hopping amplitudes, the ground state is in a globally coherent superfluid phase (SF). When the anti-ferromagnetic coupling U_2 is different from zero, states with lowest spins (compatible with the constraint $n_i + s_i =$ even) are favoured. This introduces an even/odd asymmetry of the lobes. More precisely, the amplitude of lobes with odd filling is reduced as compared with the lobes corresponding to even fillings [140]. For example, in the first lobe at $t = 0$ the extra energy required to have two particles on a site (instead of one) is $U_0 - \mu$, while the gain associated to their singlet state (instead of triplet) is $2U_2$, thus lowering the chemical potential value $\mu_{\text{eff}} = \mu - 2U_2$ where the second lobe starts. On the other hand, having no particles on a site gives no gain due to spin terms, thus leaving $\mu_{\text{eff}} = \mu$, and so accounting for the nearly unvaried bottom boundary of the lobe.

In order to determine the phase diagram of Eq. (7.11) we use the finite-size DMRG [141] with open boundary conditions (see App. C). The DMRG has already been employed, for the spinless case, in Ref. [142]; here the presence of the spin degree of freedom makes the analysis considerably more

difficult. In the numerical calculations the Hilbert space for the on-site part of the Hamiltonian is fixed by imposing a maximum occupation number $\overline{n}_{max}$. Since the first lobe is characterized by an insulating phase with $n = 1$ particle per site, we choose $\overline{n}_{max} = 3$ in this case. Already at this level the dimension of the Hilbert space per site becomes $d = 20$. We have checked, by increasing the value of $\overline{n}_{max}$, that this truncation of the Hilbert space is sufficient to compute the first lobe. In each DMRG iteration we keep up to $m = 300$ states in order to guarantee accurate results. The numerical calculations of the second lobe ($n = 2$ particles per site) have been performed with $\overline{n}_{max} = 4$ (which corresponds to a local Hilbert space of dimension $d = 35$).

In the insulating phase the first excited state is separated by the ground state by a Mott gap. In the limit of zero hopping the gap is determined by the extra-energy $\Delta E_{\pm}$ needed to place/remove a boson at a given site. The finite hopping renormalizes the gap which will vanish at a critical value. Then the system becomes superfluid. The phase boundaries between MI and SF phase can thus be determined by evaluating the critical values $\mu_c^{\pm}(t)$ at which the extra-energy vanishes: $\Delta E_{\pm}(\mu_c^{\pm}(t), t) = 0$. From the structure of the system Hamiltonian, Eq. (7.14), it is clear that the gap between different fillings depends linearly on μ and on a function $g(t)$ of the hopping only:

$$\begin{aligned} \Delta E_{\pm}(\mu, t) &= g_{\pm}(t) \mp \mu \\ &= \Delta E_{\pm}(\mu_0, t) \pm (\mu_0 - \mu)\,. \end{aligned} \tag{7.15}$$

So, for any fixed t, the critical values $\mu_c^{\pm}(t)$ are given by

$$\mu_c^{\pm}(t) = \mu_0 \pm \Delta E_{\pm}(\mu_0, t), \tag{7.16}$$

and can be extracted from the gap at an arbitrary value of the chemical potential. This method has been employed for the spinless case first by Freericks and Monien [143], and then in Ref. [142], where it was combined with the DMRG. Here we use it for the spinor case:

Three iterations of the DMRG procedure have been performed, with projections on different number sectors; the corresponding ground states give the desired energies E_0, $E_{\pm} = E_0 + \Delta E_{\pm}$. As target energies we used those obtained by the mapping of the Bose-Hubbard system into an effective bilinear-biquadratic $S = 1$ spin chain, as described in Ref. [139]. We considered chains up to $L = 128$ sites for the first lobe, and $L = 48$ for the second lobe. The extrapolation procedure to extract the asymptotic values at the thermodynamic limit $L \to \infty$ was obtained by means of a linear fit in $1/L$, as discussed

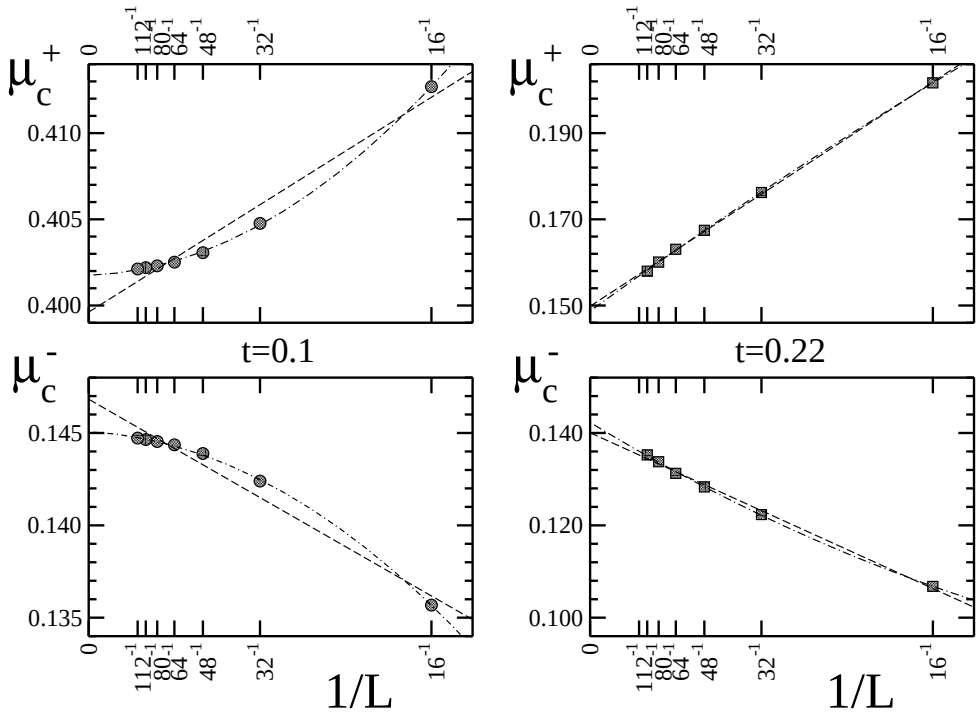

Figure 7.3: System size dependence of the critical chemical potential for the upper (μ_c^+) and the lower (μ_c^-) phase boundaries. Upper graphs correspond to the energy necessary to add a particle to the ground state of the insulator, lower ones to that of adding a hole. The extrapolation of the value at the thermodynamic limit has been obtained with a linear fit (dashed line) of numerical data. Quadratic fit (dashed-dotted line) is also shown to estimate minor corrections (within 1%). Here we set $U_0 = 1$, $U_2 = 0.2$, and two different values for the hopping t.

in [142] (an example is shown in Fig. 7.3). A comparison with a quadratic fit shows that $O(1/L^2)$ corrections are negligible on the scale of Fig. 7.4.

The plot of the phase diagram in the (μ, t) plane for different values of the spin coupling U_2 is shown in Fig. 7.4. The first lobe tends to reduce its size on increasing the spin coupling; in particular the upper critical chemical potential at $t = 0$ is $\mu_c^+(0) = 1 - 2U_2$, while the t^* value of the hopping strength over which the system is always superfluid is suppressed as U_2 increases. On the other hand, the second lobe grows up when U_2 increases. This even/odd effect, predicted in Ref. [140], is quantified in Fig. 7.4.

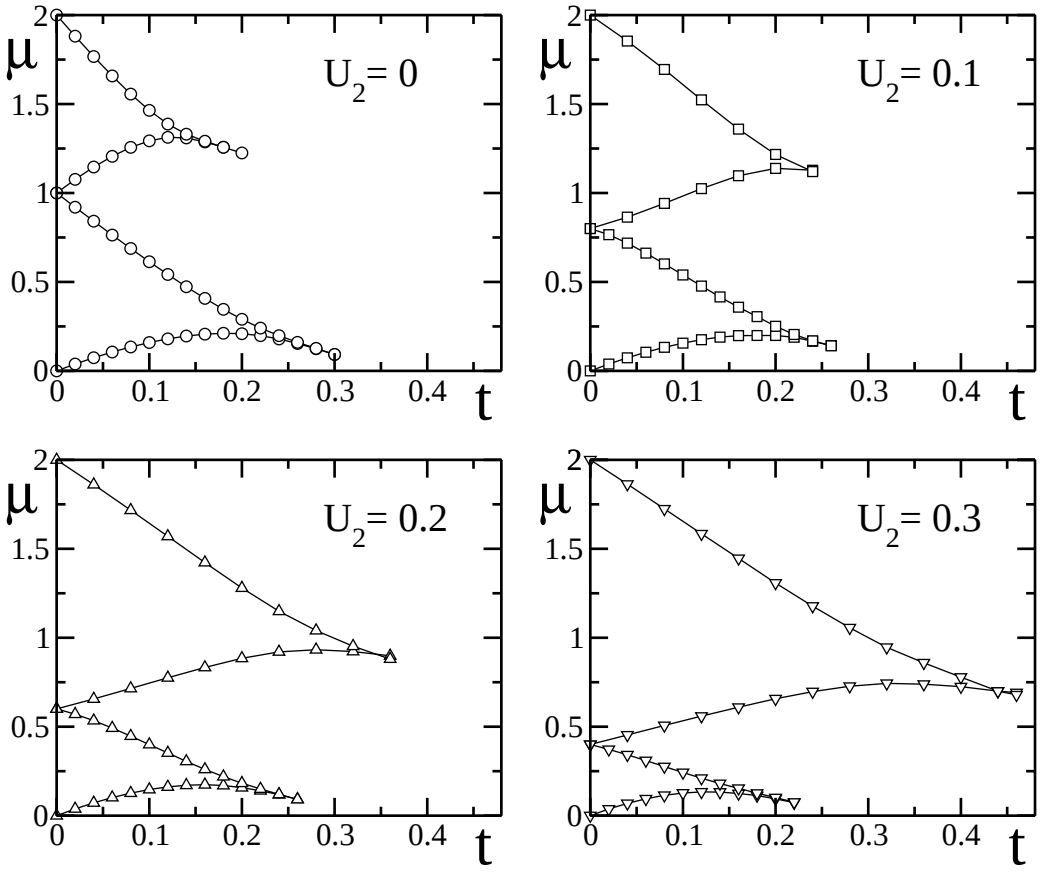

Figure 7.4: Phase diagram in the (μ, t) plane for the first two lobes of the one-dimensional Bose-Hubbard spin 1 model with nearest-neighbor interactions. The different panels correspond to different values of U_2: $U_2 = 0$ (upper-left), 0.1 (upper-right), 0.2 (lower-left), 0.3 (lower-right). The curves for $U_2 = 0$ coincide with the first two lobes for the spinless model computed in Ref.[142].

7.3 Magnetic properties of the first Mott lobe

We concentrate now on magnetic properties of the first Mott lobe of the spinor Bose-Hubbard model of Eq. (7.14). This model presents a rich variety of phases, characterized by different magnetic ordering. For spin-1 bosons it was predicted that the Mott insulating phases have nematic singlet [140] or dimerized ground state [144], depending on the mean occupation and on the value of the spin exchange. When the filling corresponds to one boson per site, the BH model can be mapped onto the $S = 1$ Heisenberg model with biquadratic interactions [139], which exhibits a rather rich phase diagram, including a long debated nematic-to-dimer quantum phase transition.

In the limit $t = 0$ the number of particles on each site is fixed to one, and the energy of the system does not depend on the spin orientation on different sites. In presence of small enough hopping $t \ll t_c^{\pm}(\mu)$ we expect that there still is one particle per site, but that boson tunneling processes induce effective interactions between the spins. Perturbative theory is valid when the coefficients in the expansion are much smaller than the unperturbed energy differences. Since first excited in the sector $N = L$ is higher than the particle-hole defect states ($N = L \pm 1$), such an expansion can be applied to the Mott state up to the phase boundaries. It can be shown that it is sufficient to consider second order expressions in the hopping strength t, that generate only pairwise interactions between atoms on neighboring sites [139].

The most general spin Hamiltonian for a chain of $S = 1$ particles that preserves $SO(3)$ symmetry can be written as:

$$\hat{H}_{\rm sp} = -\sum_{\langle ij\rangle} \left(J_0\, \hat{\mathbb{1}} + J_1\, (\hat{\mathbf{S}}_i \cdot \hat{\mathbf{S}}_j) + J_2\, (\hat{\mathbf{S}}_i \cdot \hat{\mathbf{S}}_j)^2 \right) . \tag{7.17}$$

The absence of higher order terms, such as $(\hat{\mathbf{S}}_i \cdot \hat{\mathbf{S}}_j)^3$, is due to the fact that the product of any three spin operators can be expressed via lower order terms. Parameterizing $J_1 = -\kappa \cos\theta$, $J_2 = -\kappa \sin\theta$, one obtains the following expression for the effective system Hamiltonian:

$$\hat{H}_{\rm eff} = \hat{H}_{\rm loc} - \mu L - J_0(L-1) + \kappa \sum_{\langle ij\rangle} \left(\cos\theta\, (\hat{\mathbf{S}}_i \cdot \hat{\mathbf{S}}_j) + \sin\theta\, (\hat{\mathbf{S}}_i \cdot \hat{\mathbf{S}}_j)^2 \right) \tag{7.18}$$

where $\hat{H}_{\rm loc} = \hat{H}_\epsilon + \hat{H}_U + \hat{H}_S$ accounts for the local terms in Eq. (7.11), and

$$\tan\theta = \frac{1}{1 - 2U_2}\,, \qquad \kappa = \frac{2t^2}{1 + U_2} \sqrt{1 + \tan^2\theta}\,. \tag{7.19}$$

The coupling constants are calculated with perturbative analysis: first order terms are absent, since hopping does not conserve local number of particles.

Let us now start from the two-site problem, in which the energy depends only on the pair total spin:

$S_{\rm tot}$	$\vec{S}_1 \cdot \vec{S}_2$	$(\vec{S}_1 \cdot \vec{S}_2)^2$	Energy/κ
0	-2	4	$-2\cos\theta + 4\sin\theta$
1	-1	1	$-\cos\theta + \sin\theta$
2	1	1	$\cos\theta + \sin\theta$

In the case of anti-ferromagnetic spin coupling $U_2 > 0$, the parameter θ varies in the interval $\theta \in [-3/4\pi, -\pi/2[$, therefore each bond tends to form a singlet-spin configuration ($S_{\rm tot}$), but singlet states on neighboring bonds are not allowed. A spin order will appear, whose precise nature depends on the lattice and dimensionality. In a 1D chain there are two possible ground states that may appear. A nematic state can be constructed by mixing states with total spin $S = 0$ and $S = 2$ on each bond. This construction can be repeated on neighboring bonds, thereby preserving translational invariance. This state breaks the spin-space rotational group $O(3)$, though time-reversal symmetry is preserved. On the other hand, a possibility to have $SO(3)$ symmetric solution stems from breaking translational invariance. Indeed, a dimerized solution with singlets on every second bond satisfy these requirements.

At mean field level a *nematic* solution can be written as

$$|N\rangle = \bigotimes_i |S_i = 1,\ m_i = 0\rangle\,; \tag{7.20}$$

its energy is $E^{(mf)}_{\rm nem} = 2\sin\theta\ (L-1)$. More generally, a nematic state is defined by the vanishing of any spin operator expectation value ($\langle \hat{S}^\alpha_i \rangle = 0,\ \alpha = x, y, z$), while some of the quadrupole operators have finite ones. The tensor $\hat{\mathcal{Q}}^{ab} = \langle \hat{S}^a \hat{S}^b \rangle - \frac{2}{3}\hat{\delta}^{ab}$ is a traceless diagonal matrix, indeed the off-diagonal terms are zero, due to invariance under spin reflections. Since it has two identical eigenvalues ($\langle (\hat{S}^x_i)^2 \rangle = \langle (\hat{S}^y_i)^2 \rangle \neq \langle (\hat{S}^z_i)^2 \rangle$), it can be written as $\mathcal{Q}^{ab} = Q\left(d^a d^b - \frac{1}{3}\delta^{ab}\right)$ using an order parameter

$$\langle \hat{Q} \rangle \equiv \langle (\hat{S}^z_i)^2 \rangle - \langle (\hat{S}^x_i)^2 \rangle = \frac{3}{2}\langle (\hat{S}^z_i)^2 \rangle - 1 \tag{7.21}$$

and a unit vector $\mathbf{d} = \pm\mathbf{z}$. However, since $[\hat{Q}, \hat{H}_{\rm eff}] = 0$, Coleman's theorem forbids to have $Q \neq 0$ in one-dimensional finite size systems, analogously

to what happens for the magnetization without external field. Therefore we characterized the range of nematic correlations in the ground state by coupling this operator to a fictitious "nematic field"

$$\hat{H}_\lambda \equiv \hat{H}_{\text{eff}} + \lambda \hat{Q} \tag{7.22}$$

and then by evaluating the nematic susceptibility χ_{nem} as a function of the system size:

$$\chi_{\text{nem}} \equiv -\left.\frac{\mathrm{d}^2 E_0(\lambda)}{\mathrm{d}\lambda^2}\right|_{\lambda=0} = \sum_\gamma \frac{|Q_{0,\gamma}|^2}{E_\gamma - E_0}\,, \tag{7.23}$$

where $E_0(\lambda)$ is the ground energy of $\hat{H}_\lambda$, $Q_{0,\gamma}$ is the matrix element between the ground and an excited state of $\hat{H}_{\text{eff}}$ (respectively with energy E_0 and E_γ).

The simplest *dimerized* state one can imagine is written as:

$$|D\rangle = \bigotimes_{i \text{ odd}} |S_i = 1,\ S_{i+1} = 1,\ S_i + S_{i+1} = 0\rangle\ , \tag{7.24}$$

and has energy $E^{(mf)}_{\text{dim}} = \frac{L}{2}\left(-2\cos\theta + 4\sin\theta\right) + \left(\frac{L}{2} - 1\right)\frac{4}{3}\sin\theta$. Dimerization could be described by looking at the differences in expectation values of the pair Hamiltonian $\hat{H}^{(ij)}_{\text{eff}}$ on adjacent links ($\hat{H}_{\text{eff}} = \sum_{\langle ij\rangle} \hat{H}^{(ij)}_{\text{eff}}$). Thus the order parameter D reads:

$$D \equiv \left|\langle \hat{H}^{(i-1,i)}_{\text{eff}} - \hat{H}^{(i,i+1)}_{\text{eff}} \rangle\right|. \tag{7.25}$$

In fact, on any finite chain some inhomogeneity exists, thus leading to a finite D_L even if $D = 0$. Quantitatively, an order parameter D_L could be defined by evaluating Eq. (7.25) in the middle of the finite size chain. The order parameter D has then to be extrapolated in the thermodynamic limit: $D \equiv \lim_{L\to\infty} D_L$ fact,

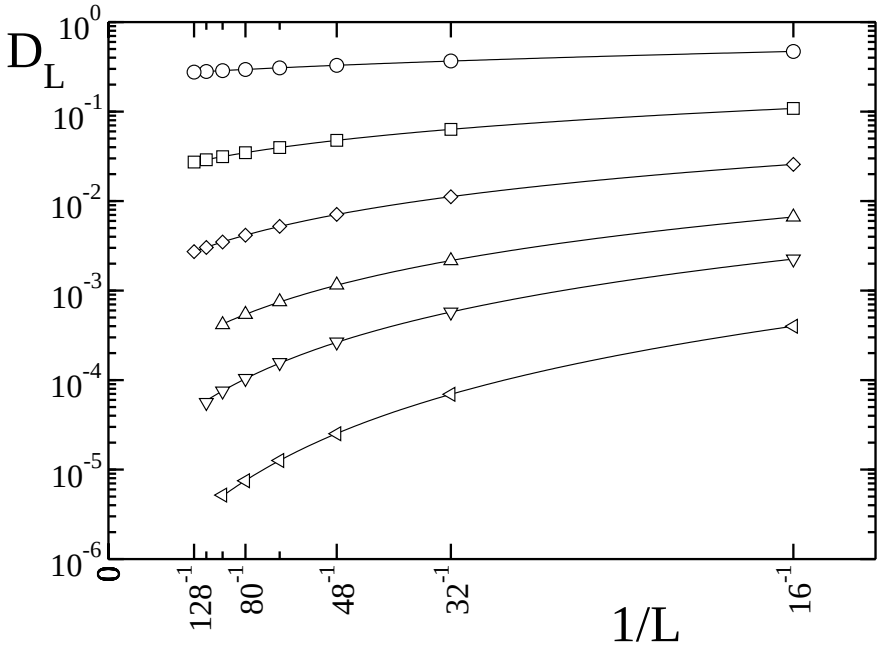

Figure 7.5: Finite size scaling of D_L for selected values of θ: -0.65π (circles), -0.7π (squares), -0.72π (diamonds), -0.73π (triangles up), -0.735π (triangles down), -0.74π (triangles left). In order to extrapolate the order parameter D, numerical data have been fitted with $D_L = D + cL^{-\alpha}$ (straight lines). DMRG simulations are performed with $m \simeq 140$ for $\theta > -0.73\pi$, $m \simeq 250$ for $\theta \leq -0.73\pi$.

making it difficult to detect the effective existence of the nematic phase. This interesting challenge has motivated numerical investigations with different methods [146, 147, 148, 149, 150]. Here we present new DMRG results which, in our opinion, clarify the magnetic properties of the first Mott lobe (for sufficiently small hopping) and consequently of the Heisenberg chain with biquadratic interaction.

According to our numerical calculation, there is no intermediate nematic phase, indeed we found a power law decay of the dimerization order parameter near $\theta_F = -3\pi/4$. The simulations of the bilinear-biquadratic model of Eq. (7.18) are less time and memory consuming than Bose-Hubbard ones, since the local Hilbert space has a finite dimension $d = 3$. The number of block states kept during the renormalization procedure was chosen step by step in order to avoid artificial symmetry breaking. This procedure insures

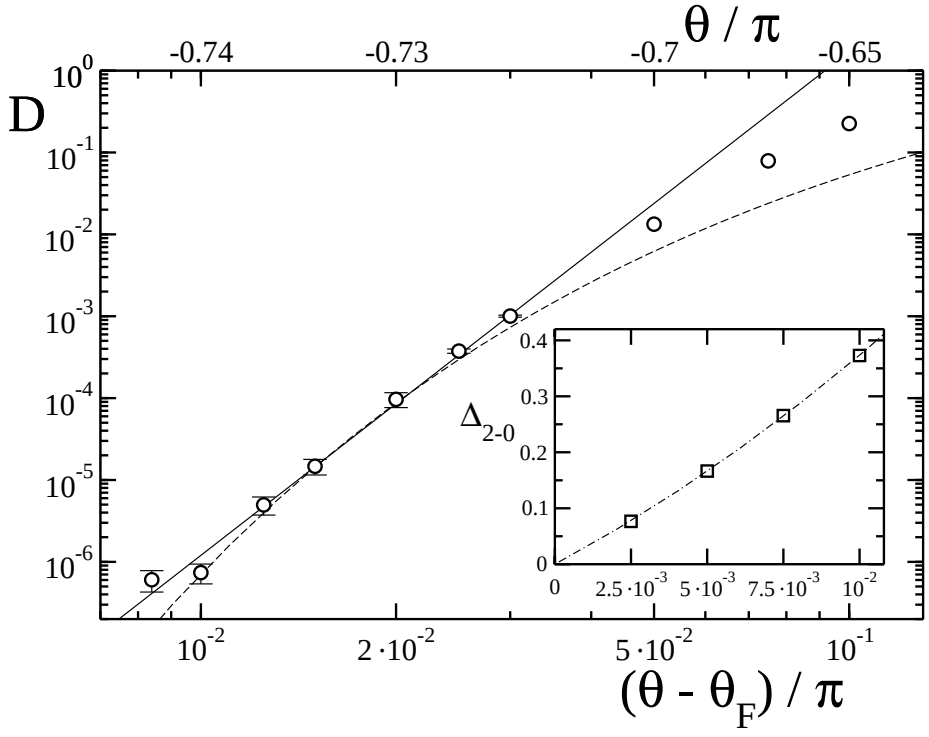

Figure 7.6: Dimerization order parameter D near the ferromagnetic boundary: solid line shows a power law fit $D \sim (\theta - \theta_F)^{\gamma}$ of numerical data with an exponent $\gamma \simeq 6.15$; dashed line shows an exponential law fit $D \sim \exp[-a/(\theta - \theta_F)^{-1/2}]$ with $a \simeq 2.91$. The linear fit is done over data for $\theta < -0.7\pi$, while the exponential fit is for $\theta \leq -0.73\pi$. DMRG calculations are performed with up to $m \simeq 300$ states. Inset: extrapolated scaled gap $\Delta_{2-0} = (L-1)(E_2 - E_0)$ at the thermodynamic limit, for some points at $\theta \leq -0.74\pi$. Dotted-dashed line displays a quadratic fit of data $\Delta_{2-0} \sim c_1(\theta\text{–}\theta_F) + c_2(\theta\text{–}\theta_F)^2$, where the linear coefficient $c_1 \simeq 9.3$ is consistent with the perturbative calculation in Subsec. 7.3.1, which gives $\tilde{c}_1 = 6\sqrt{2} \approx 8.5$.

that there are no spurious sources of asymmetry like partially taking into account a probability multiplet (see also Subsec. C.4.3). Here we considered up to $m \simeq 300$ states, and five finite-size DMRG sweeps in order to obtain stable results. Raw numerical data are shown in Fig. 7.5, where the finite size dimerization parameter $D(L)$ is plotted as a function of the chain length L. Finite size scaling was used to extrapolate D at the thermodynamic limit. After the extrapolation to the $L \to \infty$ limit, see Fig. 7.6, we fitted the dimer

order parameter with a power law

$$D = \left(\frac{\theta - \theta_F}{\theta_0} \right)^{\gamma} , \tag{7.26}$$

where $\gamma \sim 6.1502$ and $\theta_0 \sim 0.09177\,\pi$ (Fig. 7.6, solid line). We also tried to fit our data by an exponential law of the form

$$D = D_0\, e^{-a/\sqrt{\theta - \theta_F}} \tag{7.27}$$

as suggested in [146], with $a \sim 2.911$, $D_0 \sim 9.617$; this fit seems to work for narrower regions (Fig. 7.6, dashed line), however from our numerics we cannot exclude an exponential behavior of D in the critical region. The dimerized phase thus seems to survive up to the ferromagnetic phase boundary, independently from the chosen fitting form. This is also confirmed by the fact that the scaled gap between the ground state E_0 and the lowest excited state E_2 (which is found to have total spin $S_T = 2$) seems not to vanish in the interesting region $\theta > -0.75\pi$ (see the inset of Fig. 7.6). An hypothetical closure of this gap would have been a signature of a nematic ordered phase, since the nematic state has not well defined total spin, contrary to the dimerized chain.

To further characterize the behavior of the system, we analyzed the susceptibility of the chain to nematic ordering χ_{nem}. Numerical data presented in Fig. 7.7 show a power law behavior $\chi_{\mathrm{nem}}(L) \propto L^{\alpha}$ as a function of the size L. The exponent α (see the inset) approaches the value $\alpha = 3$ as $\theta \to \theta_F$. This can also be confirmed by means of a perturbative calculation around the exact solution available at θ_F (see Subsec 7.3.1). The only non vanishing $Q_{0,\gamma}$ is the one where $\gamma = |S = 2\rangle$, and scales $\sim L^2$. The energy difference goes like: $(E_\gamma - E_0) \sim L^{-1}$, therefore the conclusion follows from Eq. (7.23). The increase of the exponent for $\theta \to \theta_F$ indicates, as suggested in [149], that a tendency towards the nematic ordering is enhanced as the dimer order parameter goes to zero. On the other hand, we consider the fact that the value of 3 is reached only at the ferromagnetic boundary θ_F, thus supporting our claim against the existence of an intermediate proper nematic phase.

7.3.1 Perturbative analysis of susceptibility

Since both $\hat{H}$ and $\hat{Q}$ conserve the total spin, their expectation values do not depend on the projection along z, and we can henceforth restrict our

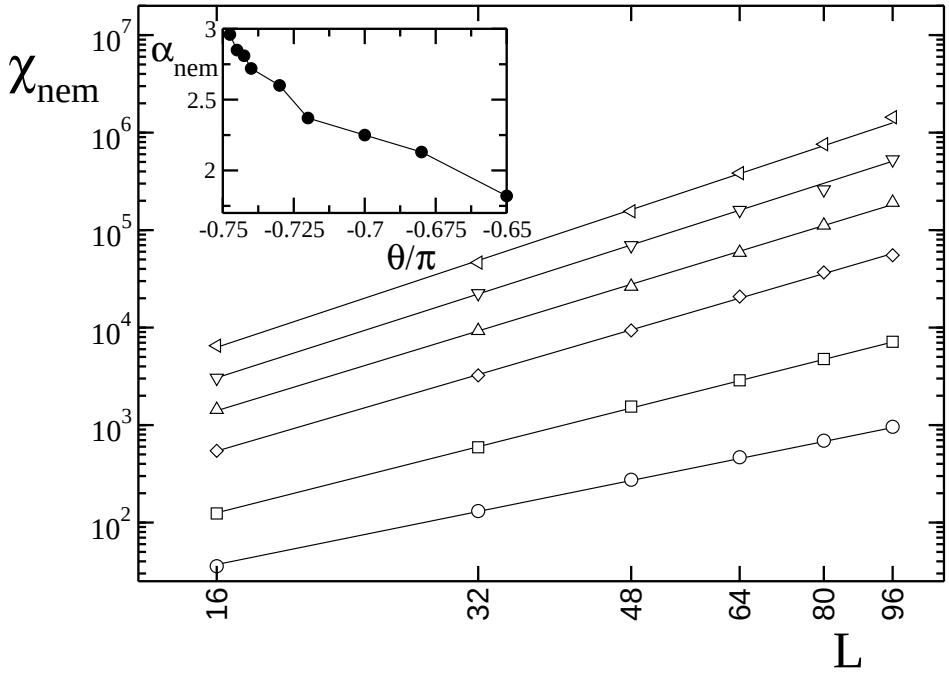

Figure 7.7: Nematic susceptibility $\chi_{\rm nem}$ as a function of the system size L. The various symbols refer to different values of θ: -0.65π (circles), -0.7π (squares), -0.73π (diamonds), -0.74π (triangles up), -0.745π (triangles down), -0.7475π (triangles left). Straight lines are the result of a power law fit $\chi_{\rm nem} = cL^{\alpha}$ of numerical data. In the inset the exponent α is plotted as a function of θ.

analysis to $S_z = 0$. At $\theta = \theta_F \equiv -3/4\,\pi$ the Hamiltonian on each link becomes a multiple of the sum of scalar product and its square. For a pair of nearest neighbor sites the generic state (with S_z fixed to 0) can be written in terms of a superposition of states with defined pair total spin, $|\psi_{i,i+1}\rangle = \sum_{S\pi}^{2}\rangle \quad \mathcal{T}|\otimes \quad \forall \quad \mathcal{T}\otimes \ / \quad \forall$

S

A further decomposition of $|S,0\rangle_L$ into the tensor products of single site states is useful; the only relevant thing is the number n_0 of sites with $s_z = 0$ ($n_0 + n_+ + n_- = L$ and $n_+ = n_-$): $|S,0\rangle_L = \sum_{n_0} c^{(L)}_{S,n_0} \mathcal{P}\{|n_0\rangle_L\}$. Indeed, the nematic operator $\hat{Q}$ is such that

$$\hat{Q}\,\mathcal{P}\{|n_0\rangle_L\} = \frac{L-3n_0}{2}\mathcal{P}\{|n_0\rangle_L\}\ . \tag{7.30}$$

Using explicit expressions for $c^{(L)}_{S,n_0}$ and the selection rules $\Delta S = 0, \pm 2$, one obtains the matrix elements $\langle S|\,\hat{Q}\,|S'\rangle$:

$$\begin{aligned}\langle S,0|\,\hat{Q}\,|S',0\rangle &= \delta_{S,S'}\, q_0(S)\,(L+3/2)^2 \\ &\quad +\delta_{S,S'-2}\, q_2(S)\,(L-S)\,(L+S'+1) \\ &\quad +\delta_{S,S'+2}\, q_2(S+2)\,(L-S')\,(L+S+1)\end{aligned} \tag{7.31}$$

On the other hand, the system Hamiltonian for $\theta = \theta_F + \delta$, apart from some constant, can be written as

$$\hat{H}_\delta = \cos\delta\,\hat{H}_0 + \sin\delta\,\hat{H}_p\,, \tag{7.32}$$

where

$$\hat{H}_0 = -\frac{1}{\sqrt{2}}\sum_{\langle ij\rangle}\left[(\hat{\mathbf{S}}_i\cdot\hat{\mathbf{S}}_j) + (\hat{\mathbf{S}}_i\cdot\hat{\mathbf{S}}_j)^2\right];\quad \hat{H}_p = \frac{1}{\sqrt{2}}\sum_{\langle ij\rangle}\left[(\hat{\mathbf{S}}_i\cdot\hat{\mathbf{S}}_j) - (\hat{\mathbf{S}}_i\cdot\hat{\mathbf{S}}_j)^2\right] \tag{7.33}$$

Energy differences that enter the susceptibility expression can be estimated with perturbative analysis for $\delta \to 0$:

$$\begin{aligned}E_\delta(L,S) &= \langle S|\,\hat{H}_p\,|S\rangle \\ &= -\sqrt{2}\left[(L-1) + \left((L+1) - \frac{S(S+1)}{L}\right)\delta + O(\delta^2)\right]\ .\end{aligned} \tag{7.34}$$

The ground state will thus have $S = 0$ and the only non-zero matrix element of $\hat{Q}$ in the susceptibility expression is $\langle 0|\,\hat{Q}\,|2\rangle$. Consequently, from Eq. (7.23), the scaling law of $\chi_{\rm nem}$ is obtained:

$$\chi_{\rm nem} \propto \delta^{-1}\,L^2\,(L+3) \tag{7.35}$$

and the asymptotic exponent 3 is recovered (see Fig. 7.7), as well as the discontinuity in θ_F (where the system is non-linear under the action of the

λ field). We stress that this result accounts also for the gap linear behavior with $(\theta - \theta_F)$ in the inset of Fig. 7.6.

As δ increases, higher orders in perturbation theory become relevant, and the scaling law is modified firstly by non-$1/L$ terms in the energy differences at susceptibility's denominator and secondly by different $Q_{\alpha,\gamma}$ contributions.

Conclusions

The seminal discoveries of fast quantum algorithms for solving important problems like factorization, searching, or the quantum simulation of physical systems on one hand, and the development of completely secure quantum cryptographic schemes on the other hand, have strongly indicated the desirability and the ultimate feasibility of the experimental realization of quantum information processing hardware. Technically, in spite of the recent great advances in nanotechnologies, this task is still very demanding, due to the extreme difficulty in controlling quantum systems at the nanoscale. This thesis work essentially lies in the context of the theoretical pioneering studies of feasibility of quantum information processing: its major investigative lines regarded the two main obstacles in every quantum information manipulation, i.e., imperfections in the system hardware and decoherence.

As far as concerning hardware imperfections, we first analyzed their effect on a quantum simulation of a classically chaotic system. We showed that random unitary errors in the quantum gates implementing an efficient quantum algorithm for the simulation of the sawtooth map are not affected by the dynamical behavior of the simulated system, in sharp contrast with the effects due to random perturbations in the parameters of the system's Hamiltonian. Then, we considered spin chains as quantum data buses for reliable state transfer. Perfect state transmission is possible in modulated chains, but imperfections are likely to corrupt it. We have studied the robustness of a communication protocol for perfect state transfer in presence of static disorder in the coupling strengths between the spins and in the local magnetic fields, showing that these imperfections destroy the transmission, above a given threshold. In particular, we showed that the state transfer fidelity, the fractal dimension of its temporal series, and the level spacing statistics of the system Hamiltonian can all be expressed, as a function of the level imperfection and the chain length, in a scaling form. Afterwards, we

considered imperfect transfer in unmodulated chains: we analyzed communication protocols in which a single quantum channel is used in order to admit multiple-qubit transfer in time. We computed the transmission rates of various protocols, showing that it is possible to exploit the effects of temporal correlations in order to boost the transmission efficiency.

Decoherence is the other main subject of this work. We first studied its role in a qubit coupled to a paradigmatic model of environment, such as a spin-chain bath. We considered the cases where the dynamics of the chain is determined by the Ising, XY, or Heisenberg Hamiltonians, analyzing what happens when the bath enters different phases and pointing out that the presence of criticality generally enhances the decoherence. We also showed how it is possible to engineer such type of baths by means of optical lattices, thus opening the possibility to experimentally test the temporal decay of coherences in a fully controllable and tunable environment. Subsequently we considered a completely different environment constituted by a fully deterministic single-degree-of-freedom quantum chaotic system. Despite the profound differences with a standard many-body bath with infinitely degrees of freedom, we showed that it can reproduce the dissipative coupling to a quantum oscillator bath, such as the Caldeira-Leggett model, by exploiting the complexity of its dynamical behavior. In particular, we studied the dynamics of entanglement between two qubits coupled to a kicked rotator model in the semiclassical limit; it has been possible to describe environmental interaction in terms of a random phase kick, so as to induce decoherence in the two-qubit system.

Finally, we reported some results concerning the numerical simulation of a one-dimensional strongly interacting lattice system, such as the spinorial Bose-Hubbard model. This represents a toy model for the study of cold atomic gases in optical lattices, which also have direct applications in quantum information processing. We evaluated the phase boundary between a Mott insulating and a Superfluid phase, and studied the magnetic properties of the insulating phase for odd fillings. Data have been obtained with the Density Matrix Renormalization Group algorithm, whose implementation in FORTRAN language has been developed within our group in Pisa during the last three years. This algorithm also admitted us to study the decoherence properties induced by an Heisenberg spin bath, which is not analytically solvable.

Appendix A

Fidelity

The notion of fidelity has been introduced long ago [80] in the context of the quantum chaos, in the attempt to characterize the stability of quantum motion under Hamiltonian system perturbations, and then subsequently used in a variety of situations (for a review, see [81]). For an initial pure state $|\psi_0\rangle$, it is defined as:

$$f(t) \equiv |\langle\psi_\epsilon(t)|\psi(t)\rangle|^2 = |\,\langle\psi_0|\,\hat{U}_\epsilon^\dagger(t)\,\hat{U}(t)\,|\psi_0\rangle\,|^2\,, \tag{A.1}$$

where the two state vectors $|\psi(t)\rangle$ and $|\psi_\epsilon(t)\rangle$ are obtained by evolving the initial state $|\psi_0\rangle$ under the unperturbed and perturbed evolutions $\hat{U}(t)$ and $\hat{U}_\epsilon(t)$, according to the Hamiltonians $\hat{H}$ and $\hat{H}+\epsilon\hat{V}$ respectively (ϵ accounts for the perturbation strength).

The fidelity (A.1) can have a dual interpretation: on one hand $f(t)$ is the probability that the states of unperturbed and perturbed time evolution are the same; on the other hand, due to unitarity of time evolutions, $f(t)$ is also the probability that after a composition of forward unperturbed and backward perturbed dynamics, i.e., and echo, one arrives back to the initial state (for this reason it is sometimes also called "Loschmidt echo"). The fidelity can also be written in terms of the expectation value of the so called "echo operator" $\hat{f}(t) = \hat{U}_\epsilon^\dagger(t)\,\hat{U}(t)$.

A.1 Quantum circuit for fidelity evaluation

The fidelity of quantum motion, Eq. (A.1), can be efficiently evaluated on a quantum computer [74], by using the scattering circuit [151] drawn in

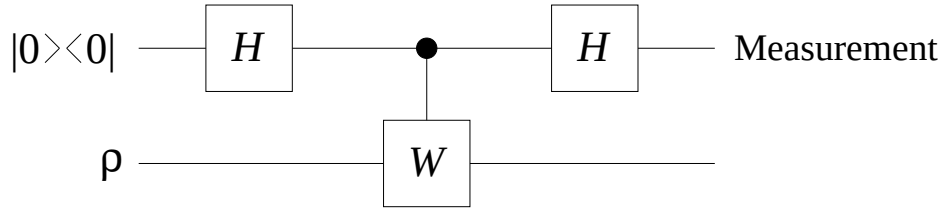

Figure A.1: Scattering circuit: the top line denotes a single ancillary qubit, the bottom line a set of n_q qubits, H the Hadamard gate, and W a unitary transformation.

Fig. A.1, that ends up with a polarization measurement of just the ancillary qubit. It can be shown that the expectation values of the Pauli spin operators $\hat{\sigma}_z$ and $\hat{\sigma}_y$ for the ancillary qubit are equal to

$$\langle \sigma_z \rangle = \mathrm{Re}\left[\mathrm{Tr}\left(\hat{W}\rho\right)\right] \qquad \langle \sigma_y \rangle = \mathrm{Im}\left[\mathrm{Tr}\left(\hat{W}\rho\right)\right], \tag{A.2}$$

where $\hat{W}$ is a unitary operator acting on n_q qubits, initially prepared in the state ρ. These two expectation values can be obtained, up to statistical errors, by running several times the scattering circuit. If we set $\rho = |\psi_0\rangle \langle\psi_0|$ and $\hat{W} = \hat{U}_\epsilon^\dagger(t)\,\hat{U}^t$, it is easy to see that

$$f(t) = |\,\langle\psi_0|\,\hat{U}_\epsilon^\dagger(t)\,\hat{U}^t\,|\psi_0\rangle\,|^2 = |\mathrm{Tr}\left(\hat{W}\rho\right)|^2 = \langle\sigma_z\rangle^2 + \langle\sigma_y\rangle^2. \tag{A.3}$$

Therefore, provided that the quantum algorithm implementing $\hat{U}$ is efficient, the evaluation of the fidelity on a quantum computer is also efficient.

A.2 Fidelity in quantum information

Recently, the fidelity has been adopted by the community of quantum information as a standard benchmark for the quality of any implementation of a quantum information device [1]. The main obstacle in producing quantum devices that manipulate individual quanta are errors in the system evolution, that can be due either to unwanted coupling with the environment or to internal imperfections. Namely, what typically happens is that the performance of a quantum protocol for applying a unitary operator $\hat{U}$ results in the actual faulty transformation $\hat{U}_\epsilon$, where ϵ measures the imperfection strength. If the fidelity (A.1) is close to one, the results of the quantum information

processing are close to the ideal ones, while, if f is significantly smaller than one, then quantum computation does not provide reliable results.

In order to engineer devices that are resistant to such perturbations, it is first necessary to understand the behavior of fidelity in different situations, so as to know how to maximize it. For this purpose, quantum error-correcting codes have been ideated, such to "control" and correct, in some limit, the disturbance induced both from decoherence and from internal hardware imperfections [1].

Up to now, we have just considered the effects of internal noise: decoherence generally induces a decay of the pure state $|\psi_0\rangle$ into a mixture $\rho(t)$, indeed the evolution of the (open) system alone is not unitary. The fidelity (A.1) can be easily generalized to the case in which the output state $|\psi_\epsilon(t)\rangle$ is substituted by a mixture $\rho(t)$:

$$f(t) = \langle\psi_0|\rho(t)|\psi_0\rangle\,. \tag{A.4}$$

If the initial state is also a density matrix, say σ_0, the fidelity is defined as:

$$f(\sigma_0,\,\rho(t);t) = \left(\mathrm{Tr}\sqrt{\sigma_0^{1/2}\,\rho(t)\,\sigma_0^{1/2}}\right)^2\,. \tag{A.5}$$

Notice that, in all cases, the fidelity is a real number between 0 and 1; if the two input states are equal (up to a global phase), then f is one; on the opposite case, if they are orthogonal, it is zero.

Appendix B

Level Spacing Statistics

In the field of quantum chaos, one of the most widely studied properties of complex quantum dynamical systems is the statistics of the energy levels. Generic classically integrable systems have levels that tend to cluster, and are not prohibited from crossing when a parameter in the Hamiltonian is varied; the typical distribution of the spacings of neighboring levels is an exponential one, just as if the levels arose as the uncorrelated events in a Poissonian random process. On the other hand, in classically non-integrable systems the levels are correlated such that crossings are strongly resisted.

Consider for simplicity a Hamiltonian system composed by an integrable part and a perturbation governed by a single parameter ϵ. The system undergoes a transition from regular to chaotic motion with increasing ϵ. A quite natural analysis on a perturbed system is to study how its energy levels depend on the perturbation parameter. Typically, for small values of ϵ the levels can cross each other, but as ϵ increases the levels begin to "repel" each other. This behavior is called *level repulsion* and is a generic feature of non-integrable systems [76]. We now try to give a simple and non rigorous explanation of this fact, by considering a simple argument based on the description of two energy levels that undergo a close encounter, under a variation of a parameter. These levels can be described within the nearly degenerate perturbation theory: assuming each of the two levels to be non-degenerate, one may deal with a 2×2 Hamiltonian $\hat{H}$ that lives in a two-dimensional Hilbert space. Its eigenvalues are given by:

$$E_{\pm} = \frac{1}{2}\left(H_{11} + H_{22}\right) \pm \sqrt{(H_{11} - H_{22})^2/4 + |H_{12}|^2}\,. \tag{B.1}$$

It is clear that, by simply varying one parameter, it is impossible to make

the square root vanish, hence the level spacing $|E_+ - E_-|$ can in general be minimized, but not made to vanish.

Notice that this argument works well in the case of two levels that belong to the same multiplets of quantum numbers, except from energy value. Indeed eigenvalues correspondent to different multiplets can become equal, as they do not feel each other (the matrix element H_{12} is equal to zero). Thus, to see level repulsion, one has to unfold the total spectrum and divide it into many subsets, each with one changing quantum number: the energy. In a quantum system which is classically integrable, this effect is not naturally seen, since a generic integrable system has d constants of motion, thus many different subsets. On the contrary, a non integrable one has a small number of symmetries. The probability that two already unfolded levels encounter each other is bigger and it is more frequent to see avoided crossings. When the perturbation destroys all the symmetries, the different subsets are mixed together and the spectrum is totally unfolded: no levels can cross each other any more, by varying just one parameter.

A quantitative way to analyze the level repulsion is the so called *Level Spacing Statistics* (LSS). Namely, it is the distribution $P(s)$ which gives the probability that the energy difference between two adjacent levels (normalized to the average level spacing) belongs to the interval $[s, s + ds]$.

This quantity has been widely used in the study of statistical properties of nuclear energy levels, which have very high densities of states. Assuming that the nuclear energy levels could be modeled by the eigenvalues of random matrices whose elements are drawn from a Gaussian ensemble, Wigner made the remarkable conjecture [152] that

$$P_G(s) = \frac{\pi}{2}\, s\, e^{-(\pi/4)\, s^2}\,. \tag{B.2}$$

Experimental data on nuclear energy levels amply confirmed this prediction. Notice that $P_G(s) \to 0$ as $s \to 0$, which implies the level repulsion. Notice also that the Wigner distribution is found only after having divided the levels by symmetry classes. Indeed, if the distributions from different classes are mixed together, a Poisson distribution

$$P_P(s) = e^{-s} \tag{B.3}$$

results, which corresponds to a completely random, uncorrelated organization of levels. It has been subsequently proved that for completely integrable systems the LSS is always Poissonian, provided the Hamiltonian is

non-degenerate. In that case, the most probable level spacing is thus zero, implying a strong clustering of levels [153].

A quite different distribution is expected in non-integrable systems: no rigorous demonstration is provided, but, depending on system symmetries, their LSS are expected to behave in such a way that:

$$\lim_{s\to 0} P(s) \sim s^{\gamma} \tag{B.4}$$

where $\gamma = 1, 2$ or 4, the three different cases corresponding to systems without any symmetry ($\gamma = 2$), with one anti-unitary symmetry (e.g. invariance under time reversal $\hat{T}$ with $\hat{T}^2 = 1$) and sufficiently high geometry ($\gamma = 1$), systems with Kramer's degeneracy (time reversal with $\hat{T}^2 = -1$) and no geometric symmetries ($\gamma = 4$). These characteristic behaviors can be understood in the framework of the Random Matrix Theory [96].

As an example, in Fig. B.1 we show the LSS for the quantum kicked rotator in two opposite situations. In the semi-integrable case, a Poissonian distribution of the LSS, Eq. (B.3) is found; in the chaotic regime instead a strong level repulsion is obtained.

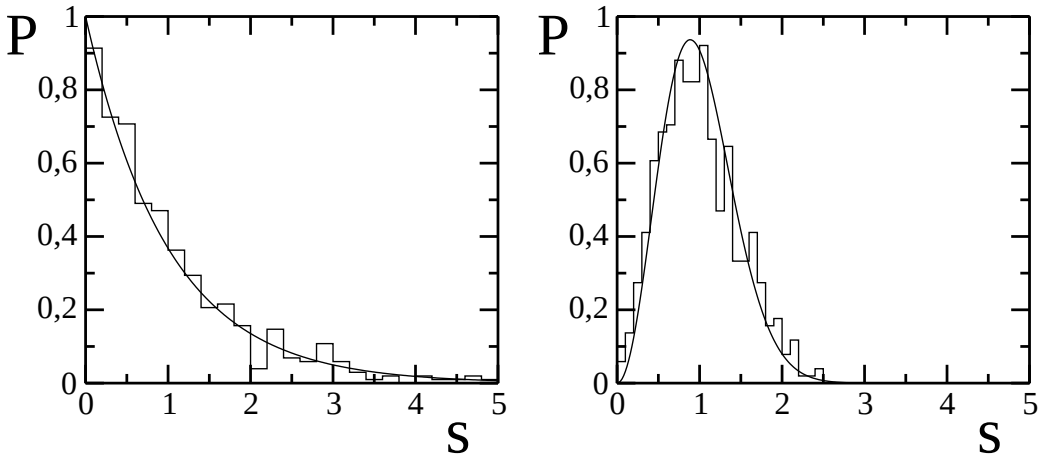

Figure B.1: Level Spacing Statistics in the quantum kicked rotator, for different dynamical regimes. The left side corresponds to a semi-integrable case ($K = 0.5$), while the right side to a chaotic case ($K = 5$). Straight lines indicate the theoretical distributions; on the left it is the Poissonian of Eq. B.3. Notice the level repulsion in the chaotic case.

Appendix C

Density Matrix Renormalization Group

The Density Matrix Renormalization Group (DMRG) in its first formulation given by White [141] is a numerical technique for finding accurate approximations to the ground state and the low-lying excited states of strongly interacting one-dimensional quantum lattice systems, such as the Heisenberg model or Bose-Hubbard models.

The simulation of a quantum mechanical system is generally a very hard task; one of the reasons is related to the number of parameters required to represent a quantum state, which usually grows exponentially with the number of constituents of the system (see Sec. 1.2). However, if one is interested in the ground state properties of a one-dimensional system, the number of parameters is limited for non critical systems, or grows polynomially for a critical one [126]. This means that it is possible to simulate them by considering only a relevant smaller portion of the entire Hilbert space. This is the key idea on which all the numerical renormalization algorithms rely. Starting from some microscopic Hamiltonian in a Hilbert space of dimension d, degrees of freedom are iteratively integrated out and accounted for by modifying the original Hamiltonian. The new Hamiltonian will thus exhibit modified, as well as new couplings; renormalization group approximations typically consist in physically motivated truncations of the set of couplings newly generated by the elimination of degrees of freedom. In this way one obtains a simplified effective Hamiltonian that should catch the essential physics of the system under study. The key for the success of these techniques rests on scale separation: in continuous phase transitions, for example, the diver-

ging correlation length sets a natural low-energy scale which dominates the physical properties; fluctuations on shorter length scales may be integrated out and summed up into quantitative modifications of the long-wavelength behavior [154].

In this appendix we describe the basics of the DMRG numerical method (for a more detailed exposition, we refer the reader to Refs. [155, 156]). The static (Sec. C.1) as well as the time dependent DMRG algorithms (Sec. C.3) will be explained. A section about the measurement procedure is also included (Sec. C.2). Finally, and in Sec. C.4 we discuss some technical issues regarding the implementation of a DMRG program code. In the last section the reader can find the schemes of the DMRG algorithms, both for static and time dependent case [1].

C.1 The static DMRG algorithm

As yet pointed out in the introduction, the tensorial structure of the Hilbert space of a composite system leads to an exponential growth of the resources needed for the simulation with the number of the system constituents. However, if one is interested in the ground state properties of a one-dimensional system, the number of parameters is limited for non critical systems or grows polynomially for a critical one [126]. This implies that it is possible to rewrite the state of the system in a more efficient way, i.e., it can be described by using a number of coefficients which is much smaller than the dimension of the Hilbert space. Equivalently, a strategy to simulate ground state properties of a system is to consider only a relevant subset of states of the full Hilbert space. This idea is at the heart of the so called *real-space blocking renormalization group*, which we briefly describe below, and is reminiscent of the renormalization group (RG) introduced by Wilson [154].

In the real space blocking RG procedure one typically begins with a small portion of a quantum system (a block $\mathcal{B}$ of size L, living on an m-dimensional Hilbert space), and a Hamiltonian which describes the interaction between two identical blocks. Then one projects the composite 2-block system (of size $2L$) representation (dimension m^2) onto the subspace spanned by the m lowest-lying energy eigenstates, thus obtaining a new truncated representation for it. Each operator is consequently projected onto the new m-

[1] Further material can be found at: `http://qti.sns.it/dmrg/phome.html`, where an open source version of the t-DMRG code written in FORTRAN 90 language is available.

dimensional basis. This procedure is then iteratively repeated, until the desired system size is reached. RG was successfully applied for the Kondo problem, but fails in the description of strongly interacting systems. This failure is due to the procedure followed to increase the system size and to the criterion used to select the representative states of the renormalized block: indeed, the decimation procedure of the Hilbert space is based on the assumption that the ground state of the entire system will essentially be composed of energetically low-lying states living on smaller subsystems (the forming blocks) which is not always true. A simple counter-example is given by a free particle in a box: the ground state with length $2l$ has no nodes, whereas any combination of two grounds in l boxes will have a node in the middle, thus resulting in higher energy.

A convenient strategy to solve the RG breakdown is the following: before choosing the states to be retained for a finite-size block, this one is first embedded in some environment that mimics the thermodynamic limit of the system. This is the new key ingredient of the DMRG algorithm; the price one has to pay is a slowdown of the system growth with the number of the algorithm's iterations: from the exponentially fast growth Wilson's procedure to the DMRG linear growth.

C.1.1 Infinite-system DMRG

Keeping in mind the main ideas of the DMRG depicted above, we now formulate the basis structure of the so called *infinite-system DMRG* for one-dimensional lattice systems. The typical scenario where DMRG can be used is the search for an approximate ground state of a 1D chain of neighbor interacting *sites*, each of them living in a Hilbert space of dimension D. As in Wilson's RG, DMRG is an iterative procedure in which the system is progressively enlarged. In the infinite system algorithm we keep enlarging the system until the ground state properties we are interested in (e.g. the ground state energy per site) have converged.

The system Hamiltonian is written as:

$$\hat{H} = \sum_i \sum_q J(q)\hat{S}_i(q)\hat{T}_{i+1}(q) + \hat{B}(q)\hat{V}_i(q) \tag{C.1}$$

where $J(q)$ and $B(q)$ are coupling constants, and $\{\hat{S}_i(q)\}_q$, $\{\hat{T}_i(q)\}_q$ and $\{\hat{V}_i(q)\}_q$ are sets of operators acting on the i-th site. The index q refers to

the various elements of these sets. For example, in a magnetic chain these can be angular momentum operators. For simplicity we will not describe the case of position dependent couplings, since it can be easily reduced to the uniform case.

The algorithm starts with a *block* composed of one site $\mathcal{B}(1, D)$ (see Fig. C.1a); the arguments of $\mathcal{B}$ refer to the number of sites it embodies, and to the number of states used to describe it. From the computational point of view, a generic block $\mathcal{B}(L, m_L)$ is a portion of memory which contains all the information about the block: the block Hamiltonian, its basis and other operators that we will introduce later. The block Hamiltonian $\hat{H}_B$ for $\mathcal{B}(L, m_L)$ includes only the local terms (i.e., local and interaction terms where only sites belonging to the block are involved). The next step consists in building the so called left *enlarged block*, by adding a site to the right of the previously created block. The corresponding Hamiltonian $\hat{H}_E$ is composed by the local Hamiltonians of the block and the site, plus the interaction term:

$$\hat{H}_E = \hat{H}_B + \hat{H}_S + \hat{H}_{BS} \; . \tag{C.2}$$

The enlarged block is then coupled to a similarly constructed right enlarged block. If the system has global reflection symmetry, the right enlarged block Hamiltonian $\hat{H}_{E'}$ can be obtained just by reflecting the left enlarged block; otherwise, if mirror symmetry does not hold, it must be built up independently. By adding the interaction of the two enlarged blocks, a *super-block* Hamiltonian $\hat{H}_{supB}$ is then built, which describes the global system:

$$\hat{H}_{supB} = \hat{H}_E + \hat{H}_{E'} + \hat{H}_{SS'} \; . \tag{C.3}$$

From now on, we refer to the sites S and S' as the *free sites*. The matrix $\hat{H}_{supB}$ should finally be diagonalized in order to find the ground state ψ_G, which can be rewritten in ket notation as:

$$|\psi_G\rangle = \psi_{a\alpha\beta b} \, |a\alpha\beta b\rangle \; . \tag{C.4}$$

Hereafter Latin indexes refer to blocks, while Greek indexes indicate free sites; implicit summation convention is assumed. From $|\psi_G\rangle$ one evaluates the reduced density matrix $\hat{\rho}_L$ of the left enlarged block, by tracing out the right enlarged block:

$$\hat{\rho}_L = \mathrm{Tr}_R \, |\psi_G\rangle \, \langle\psi_G| = \psi_{a\alpha\beta b} \, \psi^*_{a'\alpha'\beta b} \, |a \, \alpha\rangle \, \langle a'\alpha'| \; . \tag{C.5}$$

The core of the DMRG algorithm stands in the renormalization procedure of the enlarged block, which eventually consists in finding a representation in terms of a reduced basis with at most m (fixed *a priori*) elements. This corresponds to a truncation of the Hilbert space of the enlarged block, since $m_{L+1} = \min(m_L D, m)$ [2]. These states are chosen to be the first m_{L+1} eigenstates of ρ_L, corresponding to the largest eigenvalues. This truncated change of basis is performed by using the $m_L D \times m_{L+1}$ rectangular matrix $\hat{O}_{L\to L+1}$ (where the subscripts stand for the number of sites enclosed in the input block and in the output renormalized block), whose columns, in matrix representation, are the m_{L+1} selected eigenstates. To simplify notations, let us introduce the function $g(a,\alpha) = D(a-1)+\alpha$, which acts on a block index a and on the next free site index α and gives an index of the enlarged block running from 1 to $m_L D$. The output of the full renormalization procedure is a truncated enlarged block $\mathcal{B}(L+1, m_{L+1})$, which coincides with the new starting block for the next DMRG iteration. This consists in the new block Hamiltonian:

$$\begin{aligned} \hat{H}'_B &= \hat{O}^\dagger_{L\to L+1}\, \hat{H}_E\, \hat{O}_{L\to L+1} = \\ &= O^{*\,g(a,\alpha)\,c}_{L\to L+1}\, H_E^{g(a,\alpha)\,g(a',\alpha')} O^{g(a',\alpha')\,c'}_{L\to L+1}\ |c\rangle\langle c'| \end{aligned} \tag{C.6}$$

and in the local operators:

$$\hat{S}'_{L+1}(q) = \hat{O}^\dagger_{L\to L+1}\, \hat{S}_{L+1}(q)\, \hat{O}_{L\to L+1} \tag{C.7}$$

written in the new basis. These are necessary in the next step, for the construction of the interaction between the rightmost block site and the free site. The output block $\mathcal{B}(L+1, m_{L+1})$ includes also the matrix $\hat{O}_{L\to L+1}$ which identifies the basis states of the new block.

It is worth to emphasize that we can increase the size of our system without increasing the number of states describing it, by iteratively operating the previously described procedure.

We now summarize the key operations needed to perform a single DMRG step. For each DMRG step the dimension of the super-block Hamiltonian goes from $2L$ to $2L+2$, thus the simulated system size increases by 2 sites. The infinite-system DMRG, with reflection symmetry, consists in iterating these operations:

[2] If m is bigger than D^2 we do not truncate the basis at the first step. The truncation starts when $m < D^L$ and L is the number of spins in the enlarged block.

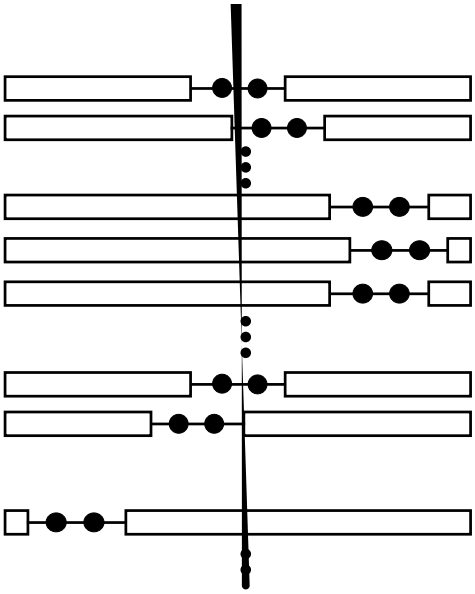

5. Renormalize all the relevant operators with the matrix $\hat{O}_{L\to L+1}$, thus obtaining $\mathcal{B}(L+1, m_{L+1})$.

Notice that at each DMRG step the ground state of a chain whose length grows by two sites is found. By contrast, the number of states describing a block is always m, regardless of how many sites it includes. This means that the complexity of the problem is a priori fixed by m and D (while D is imposed by the structure of the simulated system, $m \geq D$ is a parameter which has to be appropriately set up by the user, in order to get the desired precision for the simulation. In Sec. C.4 we will discuss how it is possible to extract the ground state of the super-block Hamiltonian without finding its entire spectrum, by means of efficient numerical diagonalization methods, like Davidson or Lanczos algorithms. We stress that at each DMRG step a truncation error $\epsilon_{\rm tr}$ is introduced:

$$\epsilon_{\rm tr} = \sum_{i>m} \lambda_i \tag{C.8}$$

where λ_i are the eigenvalues of the reduced density matrix ρ_L in decreasing order. The error $\epsilon_{\rm tr}$ is the weight of the eigenstates of ρ_L not selected for the new block basis. In order to perform a reliable DMRG simulation, the parameter m should be chosen such that $\epsilon_{\rm tr}$ remains small, as one further increases the system size. For critical 1D systems $\epsilon_{\rm tr}$ decays as a function of m with a power law, while for 1D systems away from criticality it decays exponentially, thus reflecting the entanglement properties of the system in the two regimes: a critical system is more entangled, therefore more states have to be taken into account.

C.1.2 Finite-system DMRG

The output of the infinite-system algorithm described before is the (approximate) ground state of an "infinite" 1D chain. In other words, one increases the length of the chain by iterating DMRG steps, until a satisfactory convergence is reached. However, for many problems, infinite-system DMRG does not yield accurate results up to the wanted precision. For example, the strong physical effects of impurities or randomness in the Hamiltonian cannot be properly accounted for by infinite-system DMRG, as the total Hamiltonian is not yet known at intermediate steps. Moreover, in systems with strong

magnetic fields, or close to a first order transition, one may be trapped in a metastable state favoured for small sizes (e.g. by edge effects).

Finite-system DMRG manages to eliminate such effects to a very large degree, and to reduce the error almost to the truncation error [141]. The idea of the finite-system DMRG algorithm is to stop the infinite-system algorithm at some preselected super-block length $L_{\max}$, which is subsequently kept fixed. In the following DMRG steps one applies the steps of infinite-system DMRG, but only one block is increased in size while the other is shrunk, thus keeping the super-block size constant. Reduced basis transformations are carried out only for the growing block.

When the infinite-system algorithm reaches the desired system size, the system is formed by two blocks $\mathcal{B}(L_{\max}/2-1,m)$ and two free sites, as shown in the first row of Fig. C.1b. The convergence is then enhanced by the so called "sweep procedure". This procedure is illustrated in the sequent rows of Fig. C.1b. It consists in enlarging the left block with one site and reducing the right block correspondingly in order to keep the length fixed. In other words, after one finite-system step the system configuration is $\mathcal{B}(L_{\max}/2,m)\bullet\bullet\mathcal{B}(L_{\max}/2-2,m)$ (where $\bullet$ represents the free site). While the left block is constructed by enlarging $\mathcal{B}(L_{\max}/2-1,m)$ with the usual procedure, the right block is taken from memory, as it has been built in a previous step of the infinite procedure and saved. Indeed, during the initial infinite-system algorithm one should save the matrices $\hat{O}_{i\to i+1}$, the block Hamiltonians $\hat{H}_B(i)$ and the interaction operators $\hat{S}_i(q)$ for $i=1,L_{\max}/2-1$. The finite-system procedure goes on increasing the size of the left block until the length $L_{\max}-4$ is reached. At this stage a right block $\mathcal{B}(1,D)$ with one site is constructed from scratch and the left block $\mathcal{B}(L_{\max}-3,m)$ is obtained through the renormalization procedure. Then, the role of the left and right block are switched and the free sites start to sweep from right to left. Notice that at each step the renormalized block $\mathcal{B}(i,m_i)$ has to be stored in memory. During these sweeps the length of the chain does not change, thus at each step the wavefunction of the previous one can be used as a good guess for the diagonalization procedure (see Subsec. C.4.2 for details). At each sweep the approximation of the ground state improves. Usually two or three sweeps are sufficient to reach convergence in the energy output.

Up to now we concentrated on a single quantum state, namely the ground state. It is also possible to find an approximation to a few number of states (typically less than 5): for example, the ground state and some low-excited state [141]. These states are called *target states*. At each DMRG step,

after the diagonalization, for each target state $|\psi_k\rangle$ one has to calculate the corresponding reduced density matrix ρ_k, by tracing the right enlarged block. Then a convex sum of these matrices with equal weights [155] is performed:

$$\rho = \frac{1}{n_k} \sum_{k=1}^{n_k} \rho_k \,. \tag{C.9}$$

Finally ρ has to be diagonalized in order to find the eigenbasis and the transformation matrices $\hat{O}$. In this way the DMRG algorithm is capable of efficiently representing not only the Hilbert space "around" the ground state, but also the surroundings of the other target states. It is worth noting that targeting many states reduces the efficiency of the algorithm because a larger m has to be used for obtaining the same accuracy. An alternative way could be to run as many iterations of DMRG with a single target state as many states are required.

C.1.3 Boundary conditions

The DMRG algorithm, as it has been depicted above, describes a system with open boundary conditions. However, from a physical point of view, periodic boundary conditions are normally highly preferable to the open ones, as surface effects are eliminated and finite-size extrapolation gives better results for smaller system sizes. In the presented form, the DMRG algorithm gives results much less precise in the case of periodic boundary conditions than for open boundary conditions [111, 155]. Nonetheless, periodic boundary conditions can be implemented by using the super-block configuration $\mathcal{B} \bullet \mathcal{B} \bullet$. This configuration is preferred over $\mathcal{B} \bullet \bullet \mathcal{B}$ because the two blocks are not contiguous, thus enhancing, for typical situations, the sparseness of the matrices one has to diagonalize and therefore maintaining the same computational speed of the algorithm for open boundary conditions [141].

C.2 Me4.3 C.2p

algorithm, although the symmetric configuration (with free sites at the center of the chain) usually gives the most accurate results. The procedure is to use the wave function $|\psi\rangle$ resulting from the diagonalization of the super-block (see the scheme in Sec.C.1.1, step 4), in order to evaluate expectation values.

We first concentrate on local observables $\hat{M}(i)$, living on one single site i. If one is performing the finite-system DMRG algorithm, it is possible to measure the expectation value of $\hat{M}(i)$ at the particular step inside a sweep in which i is one of the two free sites. The measure is then a simple average:

$$\langle\psi|\,\hat{M}(i)\,|\psi\rangle = \psi^*_{a\alpha\beta b}\,M(i)_{\alpha\alpha'}\,\psi_{a\alpha'\beta b} \tag{C.10}$$

where i is the first free site. In the special cases in which the observables refer to the extreme sites ($i = 1$ or $i = L_{\max}$), the measurement is performed when the shortest block is $\mathcal{B}(1, D)$, following the same procedure.

It is also possible to measure an observable expectation value while performing the infinite-system algorithm. In this case there are two possibilities: either i is one of the two central free sites or not. In the former case the measurement is performed as before, while in the latter one should express $\hat{M}$ in the truncated DMRG basis. At each DMRG iteration the operator $\hat{M}(i)$ must be updated in the new basis using the $\hat{O}$ matrix, as in Eq. (C.7): $\hat{M}(i) \to \hat{O}^\dagger\,\hat{M}(i)\,\hat{O}$. The measurement is then computed as:

$$\langle\hat{M}(i)\rangle = \psi^*_{a\alpha\beta b}\,M_{aa'}\,\psi_{a'\alpha\beta b} \tag{C.11}$$

if site i belongs to the left block and analogously if i belongs to the right block.

For non local observables, like a correlation function $\hat{P}(i)\,\hat{Q}(j)$, the evaluation of expectation values depends on whether i and j are on the same block or not. The most convenient way in order to perform such type of measurements is to use the finite-system algorithm. Let us first consider the case of nearest neighbor observables $\hat{P}(i)$ and $\hat{Q}(i+1)$. We can measure the expectation value $\langle\hat{P}(i)\,\hat{Q}(i+1)\rangle$ when i and $i+1$ are the two free sites. In this case the dimensions of the matrices $\hat{P}$ and $\hat{Q}$ are simply $(D \times D)$ and we do not have to store these operators in block representation. The explicit calculation of this observable is then simply:

$$\langle\hat{P}(i)\,\hat{Q}(i+1)\rangle = \psi^*_{a\alpha\beta b}\,P_{\alpha\alpha'}\,Q_{\beta\beta'}\,\psi_{a\alpha'\beta' b}\,. \tag{C.12}$$

In general, measures like $\langle\hat{P}(i)\,\hat{Q}(j)\rangle$ (where i and j are not nearest neighbor sites) can also be evaluated. This task can be accomplished by firstly

storing the block representation of $\hat{P}(i)$ and $\hat{Q}(j)$, and then by performing the measure when i belongs to a block and j is a free site or vice-versa. Analogously, it is possible to evaluate measures in the case when i belongs to the left block, while j to the right one. What should be avoided is the measure of $\langle \hat{P}(i)\,\hat{Q}(j) \rangle$ when i and j belong to the *same* block. Indeed, in this case the block representation of $\hat{P}(i)\,\hat{Q}(j)$ evaluated through those of $\hat{P}(i)$ and $\hat{Q}(j)$ separately is not correct, due to the truncation. Instead, such type of operators have to be built up as a compound object: in order to measure them, one has also to keep track of the block representation of the product $\hat{P}(i)\,\hat{Q}(j)$ throughout all the calculation, consequently slowing down the algorithm [141, 155].

The standard DMRG algorithm works better with open boundary conditions (see SubSec. C.1.3); this necessarily introduces boundary effects in the measure of observables. For example, in the case of spin $S = 1/2$ chains, open boundaries cause a strong alternation in the local bond strength $\langle \hat{\mathbf{S}}(j) \cdot \hat{\mathbf{S}}(j+1) \rangle$ at the borders, which slowly decays when shifting to the center [141]. In order to obtain a good description of the bulk system by using open boundary conditions, one generally has to simulate a larger system and then discard measurements on the outer sites; the number of outer sites over which measurement outcomes strongly fluctuate depends on the simulated physical system.

Finally, we stress that usually the convergence of measurements is slower than that of energy, since more finite-system DMRG sweeps are required in order to have reliable measurement outcomes (typically between five and ten). As an example, we quote the case of the one-dimensional spin 1 Bose Hubbard model [127], in which energies typically converge after 2 or 3 sweeps, while the measure of the dimerization order parameter requires at least five sweeps to converge (the convergence gets even slower when the system approaches criticality).

C.3 Time dependent DMRG

In this section we describe an extension of the static DMRG, which incorporates real time evolution into the algorithm. Various different time-dependent simulation methods have been recently proposed [110, 126, 157, 158], but here we restrict our attention to the algorithm introduced by White and Feiguin [110].

The aim of the time-dependent DMRG algorithm (t-DMRG) is to simulate the evolution of the ground state of a nearest-neighbor one dimensional system described by a Hamiltonian $\hat{H}$, following the dynamics of a different Hamiltonian $\hat{H}_1$. In few words, the algorithm starts with a finite-system DMRG, in order to find an accurate approximation of the ground state $|\psi_G\rangle$ of $\hat{H}$. Then the time evolution of $|\psi_G\rangle$ is implemented, by using a Suzuki-Trotter decomposition [159] for the time evolution operator $\hat{U} = e^{-i\hat{H}_1 t}$.

The DMRG algorithm gives an approximation to the Hilbert subspace that better describes the state of the system. However, during the evolution the wave function changes and explores different parts of the Hilbert space. Thus, the truncated basis chosen to represent the initial state will be eventually no more accurate. This problem is solved by updating the truncated bases during the evolution. The first effort, due to Cazalilla and Marston, consists in enlarging the effective Hilbert space, by increasing m, during the evolution [157]. However, this method is not very efficient because if the state of the system travels sufficiently far from the initial subspace, its representation becomes not accurate, or m grows too much to be handled. Another solution has been proposed in [110]: the block basis should be updated at each temporal step, by adapting it to the instantaneous state. This can be done by repeating the DMRG renormalization procedure using the instantaneous state as the target state for the reduced density matrix.

In order to approximately evaluate the evolution operator $\hat{U} = e^{-i\hat{H}_1 t}$ we use a Suzuki-Trotter decomposition [159]. The first order expansion in time is given by the formula:

$$e^{-i\hat{H}_1 t} \approx \left(\prod_{L=1}^{L_{\max}-1} e^{-i\hat{H}_1(L,L+1)dt} \right)^n , \tag{C.13}$$

where $n = t/dt$ gives the discretization of time t in small intervals dt, and $\hat{H}_{L,L+1}$ is the interaction Hamiltonian (plus the local terms) between site L and $L+1$. Further decompositions at higher orders can be obtained by observing that the Hamiltonian can be divided in two addends: the first, $\hat{F} = \sum_{L\,\mathrm{even}} \hat{H}_1(L, L+1)$, containing only even bonds, and the second, $\hat{G} = \sum_{L\,\mathrm{odd}} \hat{H}_1(L, L+1)$, containing only odd bonds. Since the terms in $\hat{F}$ and $\hat{G}$ commute, an even-odd expansion can be performed:

$$e^{-i\hat{H}_1 t} \approx \left(e^{-i\hat{F}\frac{dt}{2}}\, e^{-i\hat{G}dt}\, e^{-i\hat{F}\frac{dt}{2}} \right)^n . \tag{C.14}$$

This coincides with a second order Trotter expansion, in which the error is proportional to dt^3. Of course, one can enhance the precision of the algorithm by using a fourth order expansion with error dt^5 [160]:

$$e^{-i\hat{H}t} = \prod_{i=1}^{5} \left(e^{-ip_i \hat{F} \frac{dt}{2}} e^{-ip_i \hat{G}\, dt} e^{-i\, p_i \hat{F} \frac{dt}{2}} \right)^n + O(dt^5)\,, \tag{C.15}$$

where all $p_i = 1/(4 - 4^{1/3})$, except $p_3 = 1 - 4p_1 < 0$, corresponding to evolution backward in time.

Nonetheless, the most serious error in a t-DMRG program remains the truncation error. A nearly perfect time evolution with a negligible Trotter error is completely worthless if the wave function is affected by a relevant truncation error. It is worth to mention that t-DMRG precision becomes poorer and poorer as time grows larger and larger, due to the accumulated truncation error at each DMRG step. This depends on $L_{\max}$, on the number of Trotter steps and, of course, on m. At a certain instant of time, called the *runaway time*, the t-DMRG precision decreases by several order of magnitude. The runaway time increases with m, but decreases with the number of Trotter steps and with $L_{\max}$.

The initial wave function $|\psi_G\rangle$ can be chosen from a great variety of states. As an example, for a spin 1/2 chain, a factorized state can be prepared by means of space dependent magnetic fields. In general, it is also possible to start with an initial state built up by transforming the ground state as $|\psi_A\rangle = \sum_{i=1}^{L_{\max}} \hat{A}_i\, |\psi_G\rangle$, where $\hat{A}_i$ are local operators. The state $|\psi_A\rangle$ can be obtained by simply performing a preliminary sweep, just after the finite-system procedure, in which the operators $\hat{A}_i$ are subsequently applied to the transforming wave function, when i is a free site [110].

In summary, the t-DMRG algorithm is composed by the following steps:

1. Run the finite-system algorithm, in order to obtain the ground state $|\psi_G\rangle$ of $\hat{H}$.

2. If applicable, perform an initial transformation in order to set up the initial state $|\psi_A\rangle$.

3. Keep on the finite-system procedure by performing sweeps in which at each step the operator $e^{-i\hat{H}_1(L,L+1)dt}$ is applied to the system state (L and $L+1$ are the two free sites for the current step).

4. Perform the renormalization, following the finite-system algorithm, and store the matrices $\hat{O}$ for the following steps.

5. At each step change the state representation to the new DMRG basis using White's state prediction transformation [161] (see below).

6. Repeat points 3 to 5, until a complete dt time evolution has been computed.

White's state prediction transformation [161] has been firstly developed in the framework of the finite-system DMRG to provide a good guess for the Davidson or Lanczos diagonalization, thus enhancing the performance of the algorithm (see Subsec. C.4.2 for details). Here we briefly recall how it works, and adapt it to the time-dependent part of the DMRG algorithm. At any DMRG step, one has the left block $\mathcal{B}(L-1,m)$ and right block $\mathcal{B}(L_{\max}-L-1,m)$ description. To transform a quantum state $|\psi\rangle$ of the system in the new basis for the next step (corresponding to the blocks $\mathcal{B}(L,m)$ and $\mathcal{B}(L_{\max}-L-2,m)$) one uses the matrices $\hat{O}$: $\hat{O}_{L-1\to L}$ and $\hat{O}^{\dagger}_{L_{\max}-L-2\to L_{\max}-L-1}$. The first matrix transforms a block of length $L-1$ in a block of length L and it has been computed in the current renormalization. The second one transforms a block of length $L_{\max}-L-1$ in a block of length $L_{\max}-L-2$; this matrix is recovered from memory, since it has been computed at a previous step. The transformed wave function then reads:

$$\tilde{\psi}_{a\alpha\beta b} = O^{*\,g(a',\alpha')\,a}_{L-1\to L}\; O^{g(\beta,b)\,b'}_{L_{\max}-L-2\to L_{\max}-L-1}\; \psi_{a'\alpha'\alpha b'}\,. \tag{C.16}$$

Assuming this operation is already implemented, the t-DMRG algorithm introduces only a slight modification: at step L (i.e., when L and $L+1$ are the two free sites), instead of diagonalizing the super-block with the Davidson or Lanczos, one applies $e^{-i\hat{H}_1(L,L+1)dt}$ to the transformed wave function.

To compute the system time evolution using the first order Trotter expansion of Eq. (C.13), one should perform one half sweep for each time interval dt: at the j-th step one has to apply $e^{-i\hat{H}_1(j+1,j+2)dt}$, forming the usual left-to-right sweep. When arriving at the end of the chain, the system has been evolved of a dt time; one then goes on with the next time iteration, applying the corresponding evolution operators in a right-to-left sweep. Attention must be paid for the border links: at the first step both $e^{-i\hat{H}_1(1,2)dt}$ and $e^{-i\hat{H}_1(2,3)dt}$ have to be applied; an analogous situation happens at the last step. The procedure for one complete dt time evolution is depicted in

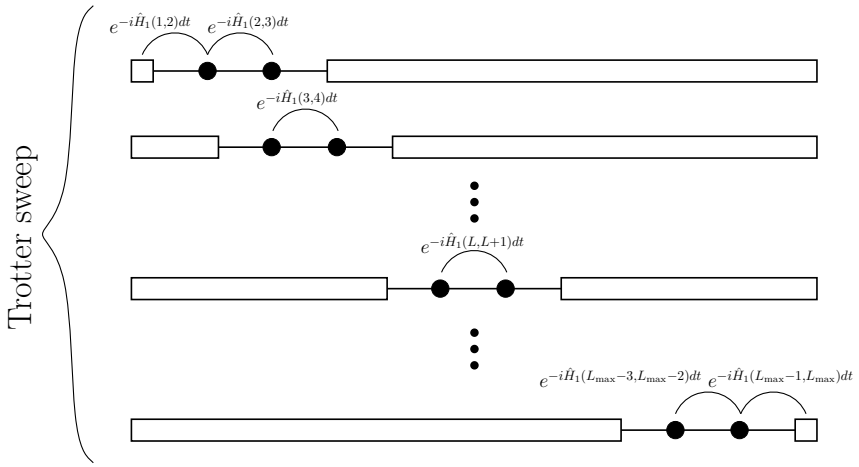

Figure C.2: Schematic procedure for the t-DMRG algorithm, implemented by using a first order Trotter expansion for the time evolution operator. In this case one half sweep is needed for each time interval dt; higher order expansions require more complicated schemes, with an increasing number of steps.

Fig. C.2. Notice that, since at each step the operator $e^{-i\hat{H}_1(L,L+1)dt}$ is computed on the two current free sites L and $L+1$ (or when the block is composed of just one site), its representation is given in terms of a $D^2 \times D^2$ matrix, and most remarkably it is exact. More generally, if the border block dimension is such that it can be treated exactly, it can be convenient to perform its evolution as a whole and then switch the sweep direction. As stated before, to increase the simulation precision, one can expand the time evolution operator to the second order Trotter expansion, as in Eq. (C.14). The implementation of this expansion requires 3/2 sweeps for each time interval dt: in the first $e^{-i\hat{F}\frac{dt}{2}}$ is applied, in the second $e^{-i\hat{G}dt}$, finally a third half sweep is needed to apply $e^{-i\hat{F}\frac{dt}{2}}$ again. In order to acquire further precision one may go to the fourth order (see Eq. (C.15)). In this case $5 \times \frac{3}{2}$ are needed, thus the computational time is respectively five times or fifteen times longer than the one needed by using Eq. (C.14) or Eq. (C.15).

Finally, we want to remark again that this algorithm for the time evolution is a small modification of the finite-system procedure: the main difference is the computation of a factor of the Trotter expansion instead of performing the diagonalization procedure at each step. This means that a typical t-DMRG sweep is much less time consuming that a finite-system one.

Notice also that the measurements are performed in the same way as in the finite-system algorithm.

To conclude this section, we provide a simple and intuitive example which explains how the time-dependent algorithm works. We consider the time evolution of the on-site magnetization of an excited state for a spin-1 Heisenberg chain [110]. In order to study the dynamics of this excitation, first we run the finite-system DMRG algorithm, thus obtaining the ground state $|\psi_G\rangle$ of a L-sites chain. We then perform a preliminary sweep to apply $\hat{A} = \hat{S}^+(j)$ on $|\psi_G\rangle$ for a single site j located at the center of the chain, namely we choose $\hat{A}_j = \delta_{j,L/2}\hat{S}^+(j)$. In this way we set up the initial state $|\psi_A\rangle$, that is a localized wave packet consisting of all wave vectors. We then perform the t-DMRG algorithm with $\hat{H}_1$ being the Heisenberg Hamiltonian, and instantaneously measure the local magnetization $S^z(j)$ for each site j: $\langle\psi(t)|\hat{S}^z(j)|\psi(t)\rangle$. The initial wave packet $|\psi_A\rangle$ spreads out as time progresses; different components move with different speeds, given by the corresponding group velocity (Fig. C.3).

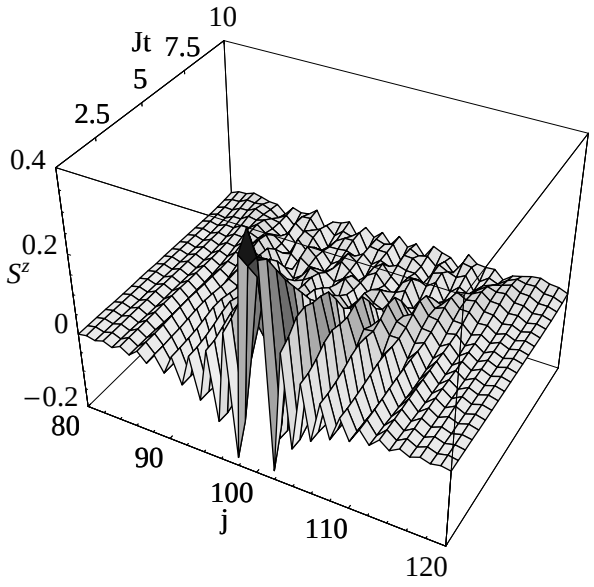

Figure C.3: Temporal evolution of the local magnetization $S^z(j)$ of a 200 sites spin-1 Heisenberg chain, starting from the excited state obtained by applying $\hat{S}^+(100)$ to the ground state of the chain. Here we used $Jdt = 10^{-1}$ as a Trotter slicing time, and a truncated Hilbert space of dimension $m = 15$.

C.4 Technical issues

In this section we explain some technicalities regarding the implementation of DMRG and t-DMRG code. They are not essential in order to understand the algorithm, but they can be useful to anyone who wants to write a code from scratch, or to modify the existing ones. Some of these parts can be differently implemented, in part or completely skipped, depending on the computational complexity of the physical system under investigation.

C.4.1 Hamiltonian diagonalization

The ground state of the Hamiltonian is usually found by diagonalizing a matrix of dimensions $(m\,D)^2 \times (m\,D)^2$. Typically the DMRG algorithm is used when one is only interested in the ground state properties (at most in few low-energy eigenstates). The diagonalization time can thus be greatly optimized by using Lanczos or Davidson methods: these are capable to give a small number ($\lesssim 10$) of eigenstates close to a previously chosen target energy in much less time than exact diagonalization routines. Moreover they are optimized for large sparse matrices, that is the case of typical super-block Hamiltonians, and they do not require as input the full matrix. What is needed is just the effect of it on a generic state $|\psi\rangle$, which lives in a $(mD)^2$ dimensional Hilbert space. The Hamiltonian in Eq. (C.1) can be written as:

$$\hat{H} = \sum_p \hat{A}(p) \otimes \hat{B}(p)\,, \tag{C.17}$$

where $\hat{A}(p)$ and $\hat{B}(p)$ act respectively on the left and on the right enlarged block. Thus, only this matrix multiplication has to be implemented:

$$\psi^{\rm out}_{a\alpha\beta b} = \sum_p \hat{A}(p)^{\,g(a,\alpha)\,g(a',\alpha')}\ \hat{B}(p)^{\,g(b,\beta)\,g(b',\beta')}\ \psi^{\rm in}_{a'\alpha'\beta'b'}\,. \tag{C.18}$$

In this way it is possible to save a great amount of memory and number of operations, since the dimensions of $\hat{A}(p)$ and $\hat{B}(p)$ are $(m\,D) \times (m\,D)$, and not $(m\,D)^2 \times (m\,D)^2$. As an example, a reasonable m value for simulating the evolution of a $L_{\rm max} = 50$ spin 1/2 chain ($D = 2$) is $m \sim 50$. This means that, in order to store all the $\sim 10^8$ complex numbers of $\hat{H}_{supB}$ in double precision, ~ 1.6 Gbytes of RAM is needed. Instead, each of the two matrices $\hat{A}$ and $\hat{B}$ requires less than 200 kbytes of RAM.

C.4.2 Guess for the wave function

Even by using the tools described in the previous paragraph, the most time consuming part of a DMRG step remains the diagonalization procedure. The step-to-step wave function transformation required for the t-DMRG algorithm, which has been described in the previous section, can also be used in the finite-system DMRG, in order to speed up the super-block diagonalization [161]. Indeed the Davidson or Lanczos diagonalization methods are iterative algorithms which start from a generic wave function, and then recursively modify it, until the eigenstate closest to the target eigenvalue is reached (up to some tolerance value, fixed from the user). If a very good initial guess is available for the diagonalization procedure, the number of steps required to converge to the solution can be drastically reduced and the time needed for the diagonalization can be reduced up to an order of magnitude.

In the finite-system algorithm the system is changing much less than in the infinite algorithm, and an excellent initial guess is found to be the final wave function from the previous DMRG step, after it has been written in the new basis for the current step. White's prediction is used to change the basis of the previous ground state with the correct operators $\hat{O}$, as in Eq. (C.16). The diagonalization can be speeded up also in the infinite-system algorithm, but in that case the search for a state prediction is slightly more complicated.

C.4.3 Symmetries

If the system has a global reflection symmetry, it is possible to take the environment block equal to the system block, in the infinite-system procedure. Namely, the right enlarged block is simply the reflection of the left one. To avoid the complication of the reflection we can consider an alternative labelling of the sites, as shown in Fig. C.4. In this case left and right enlarged blocks are represented by exactly the same matrix.

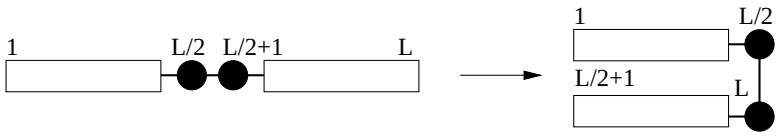

Figure C.4: Alternative labelling of sites to be used in the environment reflection procedure (in case of globally reflection-symmetric systems).

If other symmetries hold, for example conservation of angular momentum or particle number, it is possible to take advantage of them, such to considerably reduce the CPU-time for diagonalization. The idea is to rewrite the total Hamiltonian in a block diagonal form, and then separately diagonalize each of them. If one is interested in the ground state, he has to compare ground state energies inside each block, in order to find the eigenstate corresponding to the lowest energy level. One may also be interested only in the ground state with given quantum numbers (e.g. in the Bose-Hubbard model one can fix the particle number); in this case he first has to divide the operators for the left and right block into different symmetry sectors, then he diagonalizes the block Hamiltonian corresponding to the wanted symmetry values. Then the multiplication will take into account only the sectors' combination which preserves the total quantum number. When finding the reduced density matrix ρ, its eigenstates have also to be symmetry-labelled. Attention must be paid when truncating to the reduced basis: it is of crucial importance to retain whole blocks of eigenstates with the same weight, inside a region with given quantum numbers. This helps in avoiding unwanted artificial symmetry breaking, apart from numerical roundoff errors.

C.4.4 Sparse Matrices

Operators typically involved in DMRG-like algorithms (such as block Hamiltonians, updating matrices, observables) are usually represented by sparse matrices. A well written programming code takes advantage of this fact, thus saving large amounts of CPU-time and memory. Namely, there are standard subroutines which list the position (row and column) and the value of each non null element for a given sparse matrix.

C.4.5 Storage

A useful way to handle all the stored operators is to group each of them in a register, in which one index represents the length of the block. Operatively, we store all these operators in the fast-access RAM memory. However, for very large problems one can require more than the available RAM, therefore, in that case, it is necessary to store these data in the hard disk. The read/write operations from hard disk have to be carefully implemented, e.g., by performing them asynchronously, since a non optimal implementation may dramatically slow down the program performance.

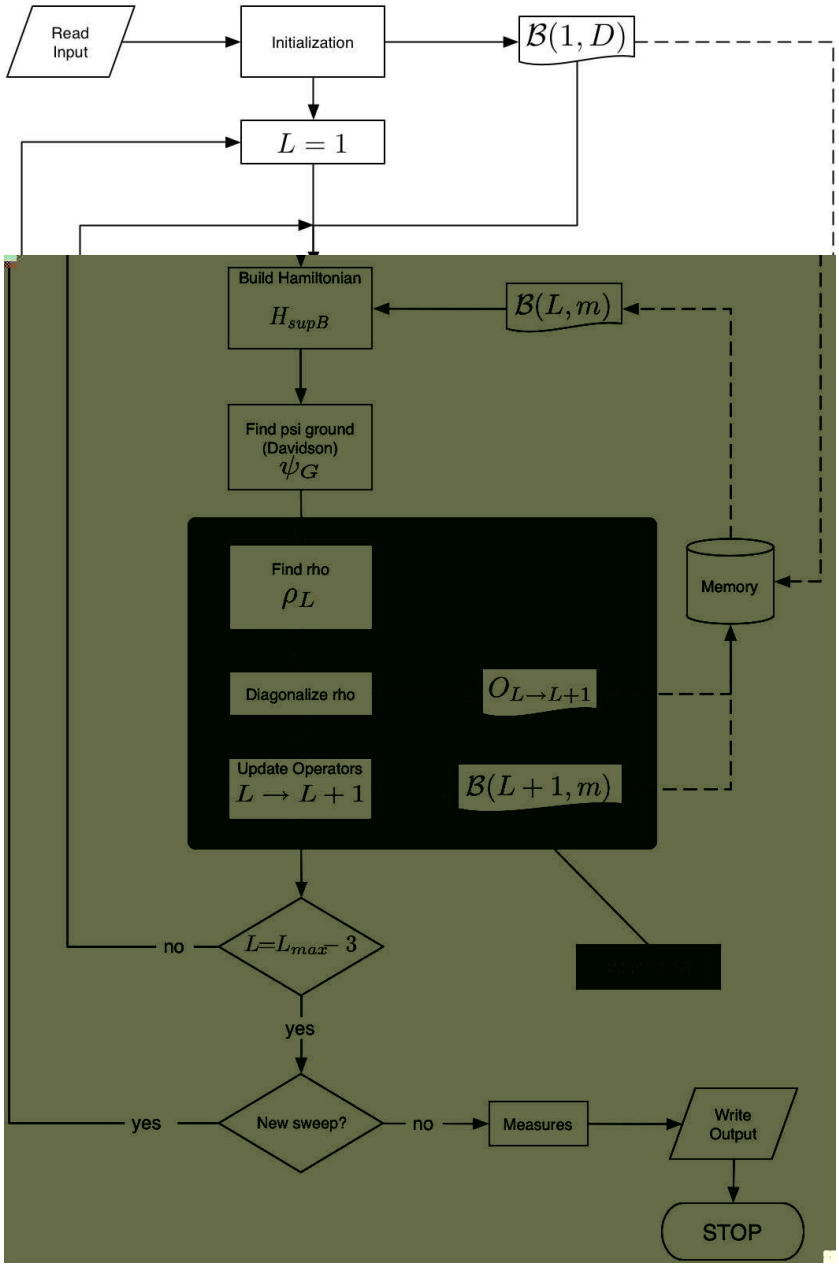

Figure C.5: Basic scheme of the infinite/finite DMRG algorithm. Here we assume reflection symmetry (the environment block is taken equal to the system block). The shadowed rectangle is the basic renormalization stage, also used in the t-DMRG algorithm (see Fig. C.6). Notations are the same as in the text.

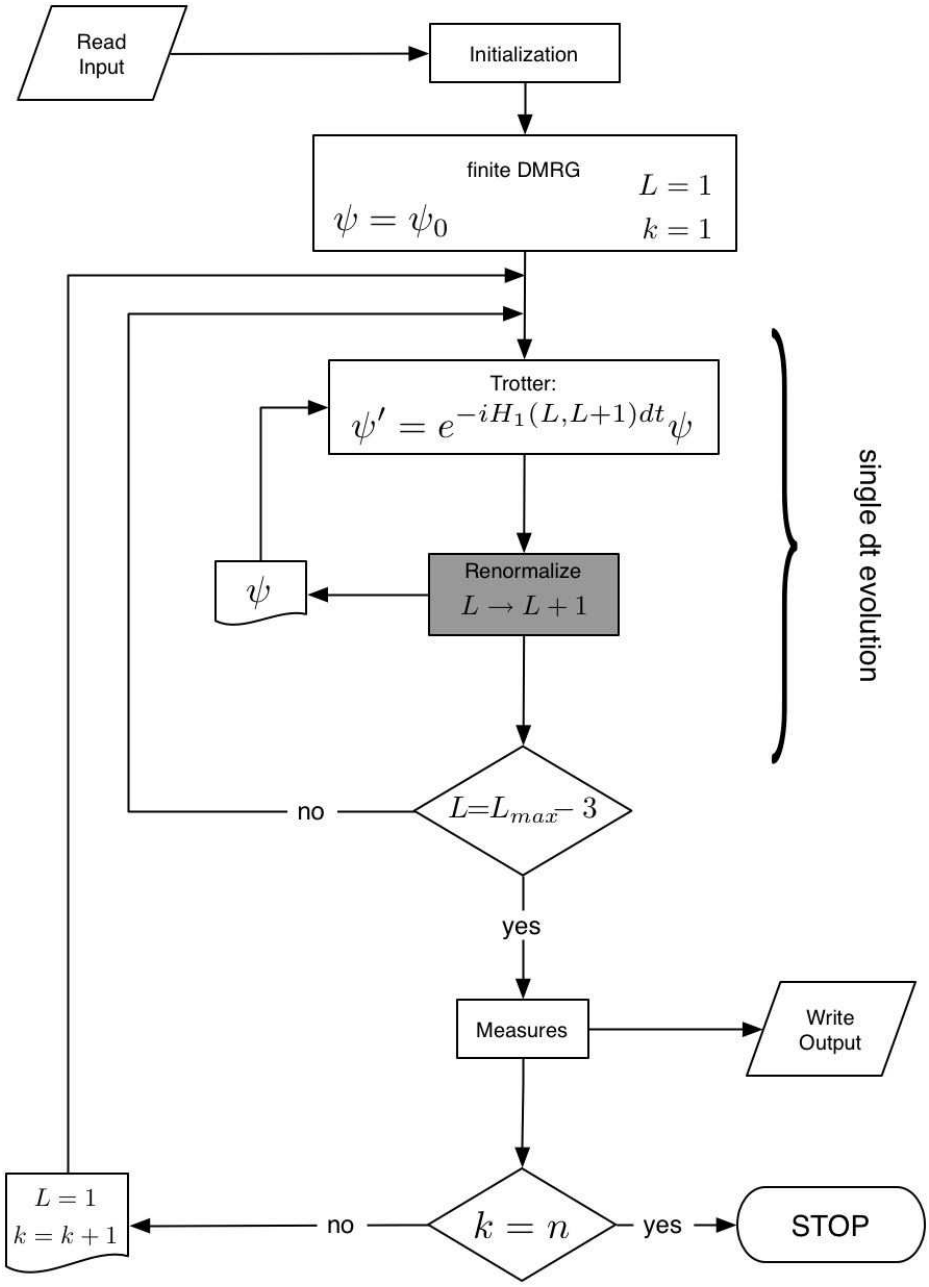

Figure C.6: Basic scheme of the time-dependent DMRG algorithm. The index k refers to the discretized time and $n = t/dt$.

Appendix D

Entanglement

Entanglement quantifies genuine quantum correlations that can be established between two or more subsystems of a quantum system, and it is definitely one of the most distinctive properties of quantum mechanics [162], lying at the basis of quantum information and quantum computation theory [1]. It is the key ingredient of quantum dense coding, quantum teleportation and of many quantum key distribution protocols; moreover, the efficiency of quantum algorithms which admit computational time and memory speedup with respect to their classical analogs is related to it [14].

Despite its crucial importance in quantum information processing, it is generally hard to give a quantitative characterization of it (for a review on the various entanglement measures see, e.g., Ref. [163]). Most of the present knowledge about entanglement properties concerns bipartite systems, that are composite quantum systems S of two subsystems A and B, that live in a Hilbert space $\mathcal{H}_S = \mathcal{H}_A \otimes \mathcal{H}_B$. In this Appendix we only deal with bipartite systems: we will examine a few peculiar cases in which entanglement can be quantified and operatively evaluated; namely, we will focus on pure states (Sec. D.1) and on generic mixed states of two qubits (Sec. D.2.1).

D.1 Entanglement in bipartite pure states

Any pure state $|\Psi\rangle \in \mathcal{H}_S$ describing a bipartite system S is *separable* if and only if it can be written as a tensor product of two pure states $|\phi\rangle_A \in \mathcal{H}_A$ and $|\xi\rangle_B \in \mathcal{H}_B$:

$$|\Psi\rangle = |\phi\rangle_A \otimes |\xi\rangle_B \ . \tag{D.1}$$

A non-separable state is *entangled*. As an example, in a two qubit system $|\uparrow\uparrow\rangle$ is a separable state, while the Bell state $\frac{1}{\sqrt{2}}(|\uparrow\uparrow\rangle + |\downarrow\downarrow\rangle)$ is entangled.

A bipartite wave-function $|\Psi\rangle$ is called "maximally entangled" if each of the reduced density matrices of the two subsystems is a multiple of the identity (i.e., $\mathrm{Tr}_B |\Psi\rangle\langle\Psi| = \mathrm{Tr}_A |\Psi\rangle\langle\Psi| = \kappa\, \mathbb{1}$). In that case all the information codified in $|\Psi\rangle$ is contained in quantum correlations between A and B: local operations on the two subsystems, or classical communication protocols between them (l.o.c.c. manipulations) cannot increase the knowledge of the state of the global system. Notable examples of maximally entangled pure states are the four two-qubit Bell states:

$$\begin{cases} |\phi^{\pm}\rangle = \frac{1}{\sqrt{2}} \left(|00\rangle \pm |11\rangle \right), \\ |\psi^{\pm}\rangle = \frac{1}{\sqrt{2}} \left(|01\rangle \pm |10\rangle \right) . \end{cases} \tag{D.2}$$

D.1.1 Schmidt decomposition

There exists a simple criterion in order to establish if a pure state of a bipartite quantum state is entangled or not, based on its Schmidt decomposition. Suppose $|\Psi\rangle$ is a pure state of a bipartite system S; then there exist orthonormal states $|i\rangle_A$ for subsystem A, and $|i'\rangle_B$ for subsystem B such that:

$$|\Psi\rangle = \sum_{i=1}^{k} \lambda_i |i\rangle_A |i'\rangle_B \ , \tag{D.3}$$

where λ_i are non-negative real numbers satisfying $\sum_{i=1}^{k} \lambda_i^2 = 1$, known as Schmidt coefficients. The number k of terms in Eq. (D.3) is called "Schmidt number". The state $|\Psi\rangle$ is separable if and only if $k = 1$.

The evaluation of the Schmidt number gives an immediate way to check if the state is entangled, but does not provide a quantitative measure of the "degree of entanglement". Indeed consider the wave function

$$|\Phi\rangle = \sqrt{1 - 2|\epsilon|^2}\ |0\rangle_A |0\rangle_B + \epsilon\, |1\rangle_A |1\rangle_B + \epsilon\, |2\rangle_A |2\rangle_B \tag{D.4}$$

which has a Schmidt number $k = 3$, irrespective of the value of ϵ. Nonetheless, as it can be intuitively seen, if $\epsilon \to 0$ the state $|\Phi\rangle$ converges to the separable state $|0\rangle_A \otimes |0\rangle_B$.

D.1.2 Von Neumann entropy

Despite the apparent limitations of Schmidt decomposition, the entanglement of a generic bipartite pure state $|\Psi\rangle \in \mathcal{H}_A \otimes \mathcal{H}_B$ can be unequivocally quantified and easily evaluated by computing the von Neumann entropy $S_{AB}(|\Psi\rangle)$, that is defined by:

$$S_{AB}(|\Psi\rangle) \equiv -\mathrm{Tr}(\rho \log_2 \rho)\,, \tag{D.5}$$

where ρ is either the reduced density matrix ρ_A of subsystem A, or ρ_B of subsystem B. It can be proved that $S_{AB}(|\Psi\rangle)$ is exactly the entanglement of $|\Psi\rangle$ in the sense described below.

Let us suppose to have n identical copies of the state $|\Psi\rangle$. We define $k_{\max}$ as the maximum number of maximally entangled states that can be extracted from the n copies, by only acting on them with l.o.c.c. manipulations. Similarly, let $k_{\min}$ be the minimum number of maximally entangled states that are required in order to generate the n copies of $|\Psi\rangle$ by means of l.o.c.c.. Since l.o.c.c. cannot create entanglement, $k_{\max} \leq k_{\min}$; moreover it can be shown that

$$\lim_{n\to\infty} \frac{k_{\min}}{n} = \lim_{n\to\infty} \frac{k_{\max}}{n} \equiv E(|\Psi\rangle) \tag{D.6}$$

where E is the entanglement of the state $|\Psi\rangle$, and it is given by the von Neumann entropy $S_{AB}(|\Psi\rangle)$.

D.2 Entanglement in bipartite mixed states

A generic mixed state of a bipartite quantum system $\rho \in \mathcal{H}_A \otimes \mathcal{H}_B$ is *separable* if and only if it can be written as an incoherent mixture of separable pure states:

$$\rho = \sum_i p_i \Big(|a_i\rangle_A \otimes |b_i\rangle_B \Big) \Big({}_A\langle a_i| \otimes {}_B\langle b_i| \Big)\,, \tag{D.7}$$

with $0 \leq p_i \leq 1$ and $\sum_i p_i = 1$. In all other cases the state is *entangled*. Finding such a decomposition for a given ρ, or proving that it does not exist, is generally a non-trivial task. Moreover, while for bipartite pure states entanglement is unequivocally quantified by the von Neumann entropy, the characterization for mixed states is still quite unclear and manifold. Indeed, in this last case there are many candidates as possible entanglement measures; all of them are typically very hard to compute for a generic density matrix ρ. We quote some of the most studied entanglement measures:

- *Entanglement cost*: estimate of the asymptotic number $k_{\min}$ of maximally entangled states used to extract n copies of ρ, minimized over all the possible l.o.c.c. manipulations

$$E_c(\rho) = \inf_{\text{l.o.c.c.}} \lim_{n\to\infty} \frac{k_{\min}}{n}\,; \tag{D.8}$$

- *Entanglement of formation*: average of the entanglement of pure states which form the mixture, minimized over all the possible decompositions

$$E_f(\rho) = \inf_{\text{dec.}} \sum_j p_j\, E(|\psi_j\rangle)\,, \tag{D.9}$$

  where $\rho = \sum_j p_i\, |\psi_j\rangle\, \langle\psi_j|$;

- *Relative entropy of entanglement*: distance of ρ from the nearest mixed separable state σ

$$E_r(\rho) = \inf_{\sigma\in\text{sep.}} \text{Tr}\left[\rho(\log_2\rho - \log_2\sigma)\right]\,; \tag{D.10}$$

- *Distillable entanglement*: estimate of the asymptotic number $k_{\max}$ of maximally entangled states that can be distilled from n copies of ρ, minimized over all the possible l.o.c.c. manipulations

$$E_d(\rho) = \inf_{\text{l.o.c.c.}} \lim_{n\to\infty} \frac{k_{\max}}{n}\,. \tag{D.11}$$

D.2.1 Entanglement of formation of an arbitrary state of two qubits

If the quantum system S is composed by two qubits, there exists a simple analytic prescription in order to evaluate the entanglement of formation $E_f(\rho)$ of a generic mixture $\rho \in \mathcal{H}_S$. First of all a "spin flip" transformation is required. For a pure state $|\phi\rangle$, its spin flipped state $|\tilde{\phi}\rangle$ is defined by:

$$|\tilde{\phi}\rangle = \hat{\sigma}_y\, |\phi^*\rangle \tag{D.12}$$

where * denotes the complex conjugation in the standard computational basis $\{|00\rangle\,, |01\rangle\,, |10\rangle\,, |11\rangle\}$. For a mixed state the spin flip is generalized by:

$$\tilde{\rho} = (\hat{\sigma}_y \otimes \hat{\sigma}_y)\rho^*(\hat{\sigma}_y \otimes \hat{\sigma}_y)\,, \tag{D.13}$$

where again the complex conjugate is taken in the standard basis.

Let us now define the *concurrence* C of the state ρ as [116]:

$$C(\rho) = \max(0, \lambda_1 - \lambda_2 - \lambda_3 - \lambda_4) \tag{D.14}$$

where λ_is are the eigenvalues, in decreasing order, of the Hermitian matrix $\sqrt{\sqrt{\rho}\,\tilde{\rho}\,\sqrt{\rho}}$ (equivalently the positive square roots of the eigenvalues of $\rho\,\tilde{\rho}$). Then, the entanglement of formation of ρ is a monotonic function of $C(\rho)$:

$$E_f(\rho) = \mathcal{E}(C(\rho)) \equiv h\left[\frac{1}{2}\left(1 + \sqrt{1 - C(\rho)^2}\right)\right], \tag{D.15}$$

where $h(x) = -x \log_2 x - (1-x)\log_2(1-x)$. Since $\mathcal{E}(C)$ is monotonically increasing and ranges from 0 to 1 as C goes from 0 to 1, one can also take the concurrence as a measure of entanglement, as well.

The demonstration of Eq. (D.15) is technical and quite tedious [116]; here we limit us to the case of pure states. For a state $|\Psi\rangle$ we have:

$$E(|\Psi\rangle) = S(\rho_A) = \mu_1 \log_2 \mu_1 - \mu_2 \log_2 \mu_2 \tag{D.16}$$

where (μ_1, μ_2) are the eigenvalues of ρ_A. It one expands the wave vector $|\Psi\rangle$ on the orthonormal basis of the four maximally entangled Bell states: $|\Psi\rangle = \alpha_1 |\psi^+\rangle + \alpha_2 |\psi^-\rangle + \alpha_3 |\phi^+\rangle + \alpha_4 |\phi^-\rangle$, one gets $E(|\Psi\rangle) = \mathcal{E}(C(|\Psi\rangle))$, where

$$C(|\Psi\rangle) = \left|\sum_{i=1}^{4} \alpha_i^2\right| = |\langle\Psi|\tilde{\Psi}\rangle| \tag{D.17}$$

is the concurrence of $|\Psi\rangle$. For example, apart from global phases, Bell states are left unchanged by the spin flip transformation, so their concurrence is one. At the other extremity, an unentangled pure state such as $|00\rangle$ is always mapped by the spin flip transformation into an orthogonal state, so that its concurrence is zero.

Publications

1. *Classical versus Quantum Errors in Quantum Computation of Dynamical Systems*
   D. Rossini, G. Benenti, and G. Casati,
   Phys. Rev. E **70**, 056216 (2004).

2. *From Perfect to Fractal Transmission in Spin Chains*
   G. De Chiara, D. Rossini, S. Montangero, and R. Fazio,
   Phys. Rev. A **72**, 012323 (2005).

3. *Phase Diagram of Spin-1 Bosons on One-Dimensional Lattices*
   M. Rizzi, D. Rossini, G. De Chiara, S. Montangero, and R. Fazio,
   Phys. Rev. Lett. **95**, 240404 (2005).

4. *Density Matrix Renormalization Group for Dummies*
   G. De Chiara, M. Rizzi, D. Rossini, and S. Montangero,
   `cond-mat/0603842` — J. Comput. Theor. Nanosci. (in press).

5. *Conservative Chaotic Map as a Model of Quantum Many-Body System*
   D. Rossini, G. Benenti, and G. Casati,
   Phys. Rev. E **74**, 036209 (2006).

6. *Information Transfer Rates in Spin Quantum Channels*
   D. Rossini, V. Giovannetti, and R. Fazio,
   `quant-ph/0609022` — Int. J. Quant. Inf. (in press).

7. *Decoherence Induced by Interacting Quantum Spin Baths*
   D. Rossini, T. Calarco, V. Giovannetti, S. Montangero, and R. Fazio,
   Phys. Rev. A **75**, 032333 (2007).

8. *Implementation of Quantum Communication Protocols in Josephson Junction Arrays*
   A. Romito, G. De Chiara, D. Rossini, and S. Montangero,
   Int. J. Quant. Inf. **4**, 519 (2006).

9. *Anti-ferromagnetic Spinor BECs in Optical Lattices*
   D. Rossini, M. Rizzi, G. De Chiara, S. Montangero, and R. Fazio,
   J Phys. B: At. Mol. Opt. Phys. **39**, S163-S175 (2006).

10. *Decoherence by Engineered Quantum Baths*
    D. Rossini, T. Calarco, V. Giovannetti, S. Montangero, and R. Fazio,
    J. Phys. A: Math. Theor. **40**, 8033 (2007).

11. *Dynamical Chaos and Decoherence*
    G. Casati and D. Rossini,
    Progr. Theor. Phys. Suppl. **166**, 70 (2007).

Bibliography

[1] M.A. Nielsen and I.L. Chuang; *Quantum Computation and Quantum Information*, Cambridge University Press (2000).

[2] J. Preskill, *Lecture notes for Physics 229: Quantum Information and Computation*, California Institute of Technology, Pasadena, CA, (1998), `http://www.theory.caltech.edu/people/preskill/ph229/`

[3] G. Benenti, G. Casati, and G. Strini, *Principles of Quantum Computation and Information*, Vol. 1: Basic Concepts, World Scientific, Singapore (2004).

[4] C.H. Bennett and D.P. DiVincenzo, Nature **404**, 247 (2000).

[5] N. Gisin, G. Ribordy, W. Tittel, and H. Zbinden, Rev. Mod. Phys. **74**, 145 (2002).

[6] I. Marcikic, H. de Riedmatten, W. Tittel, H. Zbinden, and N. Gisin, Nature **421**, 509 (2003).

[7] P. Shor, *Proceedings of the 35-th Annual Symposium on Foundations of Computer Science*, edited by Goldwasser, IEEE Computer Society Press, Los Alamitos, CA, p.124 (1994).

[8] L.K. Grover, Phys. Rev. Lett. **79**, 325 (1997).

[9] S. Lloyd, Science **273**, 1073 (1996).

[10] D.P. DiVincenzo, Science **270**, 255 (1995).

[11] L.M.K. Vandersypen and M. Steffen, Appl. Phys. Lett. **76**, 646 (2000); K.-A. Brickman, P.C. Haljan, P.J. Lee, M. Acton, L. Deslauriers, and C. Monroe, Phys. Rev. A ,R)er

L.M.K. Vandersypen, M. Steffen, G. Breyta, C.S. Yannoni, M.H. Sherwood, and I.L. Chuang, Nature **414**, 883 (2001);
S. Gulde, M. Riebe, G.P.T. Lancaster, C. Becher, J. Eschner, H. Häffner, F. Schmidt-Kaler, I.L. Chuang, and R. Blatt, Nature **421**, 48 (2003).

[12] Y. Nakamura, Y.A. Pashkin, and J.S. Tsai, Nature **398**, 786 (1999);
Y.A. Pashkin, T. Yamamoto, O. Astafiev, Y. Nakamura, D.V. Averin, and J.S. Tsai, Nature **421**, 823 (2003).

[13] W.H. Zurek, Phys. Today **44**, 36 (1991);
W.H. Zurek, Rev. Mod. Phys. **75**, 715 (2003).

[14] R. Horodecki, P. Horodecki, M. Horodecki, and K Horodecki, `quant-ph/0702225` (submitted to Rev. Mod. Phys.).

[15] A. Barenco, C.H. Bennett, R. Cleve, D.P. DiVincenzo, N. Margolus, P. Shor, T. Sleator, J.A. Smolin, and H. Weinfurter, Phys. Rev. A **52**, 3457 (1995).

[16] W.K. Wootters and W.H. Zurek, Nature **299**, 802 (1982).

[17] R. Feynman, Int. J. Theor. Phys. **21**, 467 (1982).

[18] R. Schack, Phys. Rev. A **57**, 1634 (1998).

[19] B. Georgeot and D.L. Shepelyansky, Phys. Rev. Lett. **86**, 2890 (2001).

[20] G. Benenti, G. Casati, S. Montangero, and D.L. Shepelyansky, Phys. Rev. Lett. **87**, 227901 (2001).

[21] G. Benenti, G. Casati, S. Montangero, and D.L. Shepelyansky, Phys. Rev. A **67**, 052312 (2003).

[22] A.A. Pomeransky and D.L. Shepelyansky, Phys. Rev. A **69**, 014302 (2004).

[23] Y.S. Weinstein, S. Lloyd, J.V. Emerson, and D.G. Cory, Phys. Rev. Lett. **89**, 157902 (2002).

[24] M.K. Henry, J. Emerson, R. Martinez, and D.G. Cory, Phys. Rev. A **74**, 062317 (2006).

[25] C.H. Bennett, G. Brassard, C. Crépeau, R. Jozsa, A. Peres, and W.K. Wootters, Phys. Rev. Lett. **70**, 1895 (1993).

[26] C.H. Bennett and S.J. Wiesner, Phys. Rev. Lett. **69**, 2881 (1992).

[27] L. Tian, P. Rabl, R. Blatt, and P. Zoller, Phys. Rev. Lett. **92**, 247902 (2004).

[28] D. Kielpinski, C.R. Monroe, and D.J. Wineland, Nature **417**, 709 (2002).

[29] S. Bose, Phys. Rev. Lett. **91**, 207901 (2003).

[30] M. Christandl, N. Datta, A. Ekert, and A.J. Landahl, Phys. Rev. Lett. **92**, 187902 (2004).

[31] C. Albanese, M. Christandl, N. Datta, and A. Ekert, Phys. Rev. Lett. **93**, 230502 (2004).

[32] M. Paternostro, G.M. Palma, M.S. Kim, and G. Falci, Phys. Rev. A **71**, 042311 (2005).

[33] M.J. Hartmann, M.E. Reuter, and M.B. Plenio, New J. Phys. **8**, 94 (2006); Y. Li, T. Shi, B. Chen, Z. Song, and C.P. Sun, Phys. Rev. A **71**, 022301 (2005);
T. Shi, Y. Li, Z. Song, and C.P. Sun, Phys. Rev. A **71**, 032309 (2005).

[34] T.J. Osborne and N. Linden, Phys. Rev. A **69**, 052315 (2004).

[35] F. Verstraete, M.A. Martín-Delgado, and J.I. Cirac, Phys. Rev. Lett. **92**, 087201 (2004).

[36] D. Burgarth and S. Bose, Phys. Rev. A **71**, 052315 (2005).

[37] D. Burgarth, V. Giovannetti, and S. Bose, J. Phys. A: Math. Gen. **38**, 6793 (2005).

[38] V. Giovannetti and D. Burgarth, Phys. Rev. Lett., **96**, 030501 (2006).

[39] A.Wójcik,T. Łuczak, P. Kurzyński, A. Grudka, T. Gdala, and M. Bednarska, Phys. Rev. A **72**, 034303 (2005).

[40] H.L. Haselgrove, Phys. Rev. A **72**, 062326 (2005).

[41] A. Romito, R. Fazio, and C. Bruder, Phys. Rev. B **71**, 100501(R) (2005).

[42] A. Romito, G. De Chiara, D. Rossini, and S. Montangero, Int. J. Quant. Inf. **4**, 519 (2006).

[43] S.C. Benjamin and S. Bose, Phys. Rev. Lett. **90**, 247901 (2003).

[44] E. Jané, G. Vidal, W. Dür, P. Zoller, and J.I. Cirac, Quantum Inf. and Comp. **3**, 15 (2003).

[45] L.-M. Duan, E. Demler, and M.D. Lukin, Phys. Rev. Lett. **91**, 090402 (2003).

[46] R.P. Feynman, R.B. Leighton, and M. Sands, *Feynman lectures on Physics*, Vol. 3, Addison-Wesley, Reading, MA (1965).

[47] J. Zhang, G.L. Long, W. Zhang, Z. Deng, W. Liu, and Z. Lu, Phys. Rev. A **72**, 012331 (2005).

[48] W.H. Zurek, Phys. Rev. D **24**, 1516 (1981).

[49] W.H. Zurek, Phys. Rev. D **26**, 1862 (1982).

[50] T. Pfau, S. Spälter, Ch. Kurtsiefer, C.R. Ekstrom, and J. Mlynek, Phys. Rev. Lett. **73**, 1223 (1994);
E. Buks, R. Schuster, M. Heiblum, D. Mahalu, and V. Umansky, Nature **391**, 871 (1998);
C.J. Myatt, B.E. King, Q.A. Turchette, C.A. Sackett, D. Kielpinski, W.M. Itano, C. Monroe, and D.J. Wineland, Nature **403**, 269 (2000);
K. Hornberger, S. Uttenthaler, B. Brezger, L. Hackermüller, M. Arndt, and A. Zeilinger, Phys. Rev. Lett. **90**, 160401 (2003);
L. Hackermüller, K. Hornberger, B. Brezger, A. Zeilinger, and M. Arndt, Nature **427**, 711 (2004).

[51] U. Weiss, *Quantum Dissipative Systems*, 2nd edition, World Scientific, Singapore (1999).

[52] N.V. Prokof'ev and P.C.E. Stamp, Rep. Prog. Phys. **63**, 669 (2000).

[53] A.O. Caldeira and A.J. Leggett, Ann. Phys. **149**, 374 (1983).

[54] W.G. Unruh, Phys. Rev. A **51**, 992 (1995).

[55] G.M. Palma, K.-A. Suominen, and A.K. Ekert, Proc. Roy. Soc. London A **452**, 567 (1996).

[56] S. Paganelli, F. de Pasquale, and S.M. Giampaolo, Phys. Rev. A **66**, 052317 (2002).

[57] L. Tessieri and J. Wilkie, J. Phys. A **36**, 12305 (2003).

[58] D.V. Khveshchenko, Phys. Rev. B **68**, 193307 (2003).

[59] V.V. Dobrovitski, M.I. Katsnelson, and B.N. Harmon, Phys. Rev. Lett. **90**, 067201 (2003).

[60] J. Lages, V.V. Dobrovitski, M.I. Katsnelson, H.A. de Raedt, and B.N. Harmon, Phys. Rev. E **72**, 026225 (2005).

[61] F.M. Cucchietti, J.P Paz, and W.H. Zurek, Phys. Rev. A **72**, 052113 (2005).

[62] C.M. Dawson, A.P. Hines, R.H. McKenzie, and G.J. Milburn, Phys. Rev. A **71**, 052321 (2005).

[63] H.T. Quan, Z. Song, X.F. Liu, P. Zanardi, and C.P. Sun, Phys. Rev. Lett. **96**, 140604 (2006).

[64] F.M. Cucchietti, S. Fernandez-Vidal, and J.P. Paz, Phys. Rev. A **75**, 032337 (2007).

[65] S. Camalet and R. Chitra, Phys. Rev. B **75**, 094434 (2007).

[66] M. Bortz and J. Stolze, `cond-mat/0612382`.

[67] D. Rossini, T. Calarco, V. Giovannetti, S. Montangero, and R. Fazio, J. Phys. A: Math. Theor. **40**, 8033 (2007); Phys. Rev. A **75**, 032333 (2007).

[68] H.-K. Park and S.W. Kim, Phys. Rev. A **67**, 060102(R) (2003).

[69] R. Blume-Kohout and W.H. Zurek, Phys. Rev. A **68**, 032104 (2003).

[70] L. Ermann, J.P. Paz, and M. Saraceno, Phys. Rev. A **73**, 012302 (2006).

[71] C. Pineda and T.H. Seligman, Phys. Rev. A **73**, 012305 (2006).

[72] J.W. Lee, D.V. Averin, G. Benenti, and D.L. Shepelyansky, Phys. Rev. A **72**, 012310 (2005).

[73] D. Rossini, G. Benenti, and G. Casati, Phys. Rev. E **74**, 036209 (2006).

[74] D. Rossini, G. Benenti, and G. Casati, Phys. Rev. E **70**, 056216 (2004).

[75] G. Casati and B.V. Chirikov, *Quantum Chaos*, Cambridge University Press (1985).

[76] F. Haake, *Quantum Signatures of Chaos*, Springer-Verlag, New York (1991).

[77] A. Lichtenberg and M. Lieberman, *Regular and Stochastic Motion*, Springer, Berlin (1983).

[78] S. Fishman, D.R. Grempel, and R.E. Prange, Phys. Rev. Lett. **49**, 509 (1982); Phys. Rev. A **29**, 1639 (1984).

[79] B.V. Chirikov, Phys. Rep. **52**, 263 (1979);
G. Casati, B.V. Chirikov, F.M. Izrailev, and J. Ford, *Stochastic Behavior in Classical and Quantum Hamiltonian Systems*, Lecture Notes in Physics, Vol. 93, Springer, Berlin, Heidelberg (1979).

[80] A. Peres, Phys. Rev. A **30**, 1610 (1984).

[81] T. Gorin, T. Prosen, T.H. Seligman, and M. Žnidaric, Phys. Rep. **435**, 33 (2006).

[82] Ph. Jacquod, P.G. Silvestrov, and C.W.J. Beenakker, Phys. Rev. E **64**, 055203(R) (2001).

[83] R.A. Jalabert and H.M. Pastawski, Phys. Rev. Lett. **86**, 2490 (2001).

[84] G. Casati, B.V. Chirikov, I. Guarneri, and D.L. Shepelyansky, Phys. Rev. Lett. **56**, 2437 (1986).

[85] A. Ekert and R. Jozsa, Rev. Mod. Phys. **68**, 733 (1996).

[86] F. Schmidt-Kaler, H. Häffner, M. Riebe, S. Gulde, G.P.T. Lancaster, T. Deuschle, C. Becher, C.F. Roos, J. Eschner, and R. Blatt, Nature **) 3314 042437 20)**

[94] G. De Chiara, D. Rossini, S. Montangero, and R. Fazio, Phys. Rev. A **72**, 012323 (2005).

[95] B. Georgeot and D.L. Shepelyansky, Phys. Rev. E **62**, 6366 (2000).

[96] T. Guhr, A. Müller-Groeling, and H.A. Weidenmüller, Phys. Rep. **299**, 189 (1998).

[97] M. V. Berry, J. Phys. A **29**, 6617 (1996).

[98] E.J. Amanatidis, D.E. Katsanos, and S.N. Evangelou, Phys. Rev. B **69**, 195107 (2004).

[99] A.S. Sachrajda, R. Ketzmerick, C. Gould, Y. Feng, P.J. Kelly, A. Delage, and Z. Wasilewski, Phys. Rev. Lett. **80**, 1948 (1998).

[100] C. Macchiavello and G.M. Palma, Phys. Rev. A **65**, 050301(R) (2005);
G. Bowen and S. Mancini, Phys. Rev. A **69**, 012306 (2004);
D. Kretschmann and R.F. Werner, Phys. Rev. A **72**, 062323 (2005);
V. Giovannetti, J. Phys. A: Math. Gen. **38**, 10989 (2005).

[101] D. Rossini, V. Giovannetti, and R. Fazio, `quant-ph/0609022` (to appear in Int. J. Quant. Inf.).

[102] V. Giovannetti and R. Fazio, Phys. Rev. A **71**, 032314 (2005).

[103] C.H. Bennett and P.W. Shor, IEEE Trans. Inf. Theory **44**, 2724 (1998).

[104] S. Sachdev, *Quantum Phase Transitions*, Cambridge University Press (2000).

[105] D. Jaksch, H.-J. Briegel, J.I. Cirac, C.W. Gardiner, and P. Zoller, Phys. Rev. Lett. **82**, 1975 (1999).

[106] O. Mandel, M. Greiner, A. Widera, T. Rom, T.W. Hänsch, and I. Bloch, Nature **425**, 937-940 (2003).

[107] D.G. Cory, R. Laflamme, E. Knill, L. Viola, T.F. Havel, N. Boulant, G. Boutis, E. Fortunato, S. Lloyd, R. Martinez, C. Negrevergne, M. Pravia, Y. Sharf, G. Teklemariam, Y.S. Weinstein, and W.H. Zurek, For. der Phys. **48**, 875 (2000).

[108] E. Lieb, T. Schultz, and D. Mattis, Ann. Phys. **16**, 407 (1961);
P. Pfeuty, Ann. Phys. **57**, 79 (1970).

[109] L.S. Levitov, H. Lee, and G.B. Lesovik, J. Math. Phys. **37**, 4845 (1996); I. Klich, in *Quantum Noise in Mesoscopic Physics*, Yu.V. Nazarov Ed., NATO Science Series, Vol. 97 (Kluwer Academic Press, 2003).

[110] S.R. White and A.E. Feiguin, Phys. Rev. Lett. **93**, 076401 (2004).

[111] M.C. Chung and I. Peschel, Phys. Rev. B **62**, 4191 (2000).

[112] A. Osterloh, L. Amico, G. Falci, and R. Fazio, Nature **416**, 608 (2002).

[113] T.J. Osborne and M.A. Nielsen, Phys. Rev. A **66**, 032110 (2002).

[114] G. Vidal, J.I. Latorre, E. Rico, and A. Kitaev, Phys. Rev. Lett. **90**, 227902 (2003).

[115] T. Stauber and F. Guinea, Phys. Rev. A **70**, 022313 (2004).

[116] W.K. Wootters, Phys. Rev. Lett. **80**, 2245 (1998).

[117] L. Amico, A Osterloh, F. Plastina, R. Fazio, and G.M. Palma, Phys. Rev. A **69**, 022304 (2004).

[118] E. Barouch, B.M. McCoy, and M. Dresden, Phys. Rev. A **2**, 1075 (1970); E. Barouch and B.M. McCoy, Phys. Rev. A **3**, 786 (1971).

[119] J. Kurmann, H. Thomas, and G. Müller, Physica A **112**, 235 (1982).

[120] O.F. Syljuåsen, Phys. Rev. A **68**, 060301(R) (2003).

[121] S. Daffer, K. Wódkiewicz, J.D. Cresser, and J.K. McIver, Phys. Rev. A **70**, 010304(R) (2004).

[122] D. Braun, Phys. Rev. Lett. **89**, 277901 (2002).

[123] C. Liverani and M. Martens, Commun. Math. Phys. **260**, 527 (2005); R. Artuso and A. Prampolini, Phys. Lett. A **246**, 407 (1998).

[124] A. Rechester and R. White, Phys. Rev. Lett. **44**, 1586 (1980); A. Rechester, M. Rosenbluth, and R. White, Phys. Rev. A **23**, 2664 (1981).

[125] H.J. Carmichael, *An Open Systems Approach to Quantum Optics* (Springer, Berlin, 1993).

[126] G. Vidal, Phys. Rev. Lett. **91**, 147902 (2003).

[127] M. Rizzi, D. Rossini, G. De Chiara, S. Montangero, and R. Fazio, Phys. Rev. Lett. **95**, 240404 (2005); J. Phys. B: At. Mol. Opt. Phys. **39**, S163-175 (2006).

[128] K. Southwell, *Ultracold Matter*: a collection of review articles, Nature **416**, pp. 205-246 (2002).

[129] B.P. Anderson and M.A. Kasevich, Science **281**, 1686 (1998);
F.S. Cataliotti, S. Burger, C. Fort, P. Maddaloni, F. Minardi, A. Trombettoni, A. Smerzi, and M. Inguscio, Phys. Rev. Lett. **293**, 843 (2001);
S. Burger, F.S. Cataliotti, C. Fort, F. Minardi, M. Inguscio, M.L. Chiofalo, and M.P. Tosi, Phys. Rev. Lett. **86**, 4447 (2001);
O. Morsch, J.H. Müller, M Cristiani, D. Ciampini, and E. Arimondo, Phys. Rev. Lett. **87**, 140402 (2001).

[130] A. Minguzzi, S. Succi, F. Toschi, M.P. Tosi, and P. Vignolo, Phys. Rep. **395**, 223 (2004).

[131] D. Jaksch and P. Zoller, Ann. Phys. **315**, 52 (2005).

[132] D. Jaksch, C. Bruder, J.I. Cirac, C.W. Gardiner, and P. Zoller, Phys. Rev. Lett. **81**, 3108 (1998).

[133] R. Fazio and H.S.J. van der Zant, Phys. Rep. **355**, 235 (2001).

[134] S.L. Sondhi, S.M. Girvin, J.P. Carini, and D. Shahar; Rev. Mod. Phys. **69**, 315 (1997).

[135] M.P.A. Fisher, P.B. Weichman, G. Grinstein, and D.S. Fisher, Phys. Rev. B **40**, 546 (1989).

[136] M. Greiner, O. Mandel, T. Esslinger, T.W. Hänsch, and I. Bloch, Nature **415**, 39 (2002).

[137] A. Albus, F. Illuminati, and J. Eisert, Phys. Rev. A **68**, 023606 (2003).

[138] D.M. Stamper-Kurn and W. Ketterle, *Proceedings of Les Houches 1999 Summer School, Session LXXII*, `cond-mat/0005001`.

[139] A. Imambekov, M. Lukin, and E. Demler, Phys. Rev. A **68**, 063602 (2003).

[140] E. Demler and F. Zhou, Phys. Rev. Lett. **88**, 163001 (2002).

[141] S.R. White, Phys. Rev. Lett. **69**, 2863 (1992);
S.R. White, Phys. Rev. B **48**, 10345 (1993).

[142] T.D. Kühner and H. Monien, Phys. Rev. B **58**, 14741(R) (1998);
T.D. Kühner, S.R. White, and H. Monien, Phys. Rev. B **61**, 12474 (2000).

[143] J. K. Freericks and H. Monien, Phys. Rev. B **53**, 2691 (1996).

[144] S.K. Yip, Phys. Rev. Lett. **90**, 250402 (2003).

[145] A.V. Chubukov, Phys. Rev. B **43**, 3337 (1991).

[146] G. Fàth and J. Sòlyom, Phys. Rev. B **51**, 3620 (1995).

[147] N. Kawashima, Prog. Theor. Phys. **145**, 138 (2002).

[148] A. Läuchli, G. Schmid, and S. Trebst, Phys. Rev. B **74**, 144426 (2006).

[149] D. Porras, F. Verstraete, and J.I. Cirac, Phys. Rev. B **73**, 014410 (2006).

[150] K. Buchta, G. Fàth, Ö. Legeza, and J. Sòlyom, Phys. Rev. B **72**, 054433 (2005).

[151] C. Miquel, J.P. Paz, M. Saraceno, E. Knill, R. Laflamme, and C. Negrevergne, Nature **418**, 59 (2002).

[152] E.P. Wigner, *Gatlinberg Conference on Neutron Physics*, Rep. ORNL-2309 p.57 (1957).

[153] M.V. Berry and M. Tabor, Proc. Roy. Soc. London A **356**, 375 (1977).

[154] K.G. Wilson, Rev. Mod. Phys. **47**, 773 (1975).

[155] U. Schollwöck, Rev. Mod. Phys. **77**, 259 (2005); U. Schollwöck and S.R. White, in G.G. Batrouni and D. Poilblanc (eds.): *Effective models for low-dimensional strongly correlated systems*, p. 155, AIP, Melville, New York (2006).

[156] G. De Chiara, M. Rizzi, D. Rossini, and S. Montangero, `cond-mat/0603842` (to appear in J. Comput. Theor. Nanosci.); see also `http://qti.sns.it/dmrg/phome.html`.

[157] M.A. Cazalilla and J.B. Marston, Phys. Rev. Lett. **88**, 256403 (2002).

[158] A.J. Daley, C Kollath, U. Schollwöch, and G. Vidal, J. Stat. Mech. P04005 (2004).

[159] H.F. Trotter, Proc. Am. Math. Soc. **10**, 545 (1959);
M. Suzuki, Prog. Theor. Phys. **56**, 1454 (1976).

[160] U. Schollwöck, J. Phys. Soc. Jpn. **74**, (Suppl.), 246 (2005).

[161] S.R. White, Phys. Rev. Lett. **77**, 3633 (1996).

[162] A. Einstein, B. Podolsky, and N. Rosen, Phys. Rev. **47**, 777 (1935).

[163] M.B. Plenio and S. Virmani, Quant. Inf. Comp. **7**, 1 (2007).